MSC-THESIS

Structural consolidation of historic monuments by interlocking cast glass components.

A computational analysis of interlocking cast glass brickwork

Author:
Erwin Jacobs

Structural consolidation of historic monuments by interlocking cast glass components.

A computational analysis of interlocking cast glass brickwork.

in partial fulfilment of the requirements for the degree of

Master of Science

in Building Engineering
at the Delft University of Technology

Erwin Jacobs

Delft
December 4th, 2017

Author
E.A.M. Jacobs
+31 6 83 97 0074
erwinjacobs@hotmail.com

University
Delft University of Technology
Faculty of Civil Engineering and geosciences
Master Building Engineering, Structural Design track

Graduation Committee

Chairman	Prof.ir. Rob Nijsse +31 15 27 85488 R.Nijsse@tudelft.nl Faculty CEG, B23-S2 1.36 Structural & Building engineering, ABT
Daily Thesis Coordinators	ir. Telesilla Bristogianni +31 15 27 89640 T.Bristogianni@tudelft.nl Faculty CEG, B23-S2 1.56 Structural & Building engineering
	ir. Faidra Oikonomopoulou +31 6 41 14 0976 F.Oikonomopoulou@tudelft.nl Faculty BK, B08-01+West 130 Architectural Engineering + Technology
Structural Coordinator	ir. Sander Pasterkamp +31 15 27 84982 S.Pasterkamp@tudelft.nl Faculty CEG, B23-S2 1.56 Structural & Building engineering Pieters Bouwtechniek
Computational Coordinator	ir. Cor Kasbergen +31 15 27 82729 C.Kasbergen@tudelft.nl Faculty CEG, B23-HG 6.52 Structural engineering
External Computational Coordinator	ir. Chris van der Ploeg +31 15 270 36 73 c.vd.ploeg@abt.eu Delftechpark 12, 2628 XH Delft ABT

TU Delft Delft University of Technology
Glass & Transparency Research Group

abt

4TU.Bouw

Acknowledgements

Towards the completion of this thesis as well as during my studies, various companies, individuals, friends and family have supported me. I hence would like to take a moment to thank all people involved.

First, I would like to thank my committee for sharing their expertise and knowledge on the various fields they represent. More specifically I would like to thank Rob Nijsse, for chairing the committee and providing me with the initial inspiration to do my thesis in structural glass during one of his lectures. Furthermore, I would like to thank my daily thesis supervisors, Telesilla Bristogianni and Faidra Oikonomopoulou. Having read and experienced your findings in the field of cast glass was truly inspiring. Thank you for helping me realise my prototypes and for your guidance throughout my thesis. Next I would like to thank Sander Pasterkamp, for sharing his passion and enthusiasm of evaluating monumental structures. I enjoyed looking into the reference projects in our meetings. Furthermore, I would like to thank Cor Kasbergen, for our pleasant discussions regarding both finite element analysis as well as travel destinations. Thank you for taking the time reviewing my work and models, even when the analyses ran long. Lastly, I would like to thank Chris van der Ploeg, thank you for keeping me sharp and to the point, and for your useful feedback throughout my thesis. Your guidance during my time in ABT was much appreciated.

Throughout my thesis some individuals also supported me in various ways. Hence I would like to thank Jeroen Coenders, for helping me setting up my thesis topic in the initial stage of my thesis. I would also like to express my gratitude to James O'Callaghan for his views on the proposed design solution. I would especially like to thank Lida Barou, for helping me cast my glass bricks in the laboratory. Lastly I would like to thank Ali Sarmad, for providing me with the point cloud of the Lichtenberg ruin.

I would like to express my gratitude to the company ABT, for hosting me and making their knowledge available to me. I hence would like to thank all its employees that helped me during my thesis. I especially would like to thank Kris Riemens, for his help during the finite element modelling of my design. Moreover, I would like to thank the rest of the DIANA-team for the pleasant atmosphere in their department, thank you Ersan, Joris, Lex, Ruxandra and Shayer! I really enjoyed my time there.

For implementing a new DIANA output for this research, I am very thankful to Gerd-Jan Schreppers, Emile van Varsseveld and Jantine van Steenbergen from TNO DIANA FEA. It was of essential importance for the evaluation of my geometries. Thank you furthermore for granting me a temporary license and allowing me to join one of your workshops.

In evaluating the ruin of Lichtenberg Castle, I would like to thank Pieter van Traa of Steunbeer BV. Your evaluation on site and your company's documentation were extremely helpful for my analysis of the tower. Moreover, I would like to thank Kevin Amendt, for providing me with a copy of Sprenger's analysis, which was one of the key literature pieces regarding the ruin. Furthermore, the information provided by the community of Stichting Oud Sint Pieter at the museum on site was very interesting and helpful. Thank you all!

Lastly, I would like to thank all my friends and family for their support. Especially I would like to thank my parents, John and Petra, for making my studies possible and supporting me throughout my studies. Of my friends I would like to especially thank Bjorn, Dennis, Fernando and Joris, for providing me with the needed non-study related intermezzos while studying.

Last, but definitely not least, I would like to thank Natália, for always being there for me and being my companion in all aspects of life.

Erwin Jacobs, 4th of December 2017, Delft

Abstract

The search for a transparent, reversible, and reusable consolidation system for monuments led to the ambition to test possible cast glass interlocking brick designs using numerical calculations. The focus of this research is hence the design, simulation and evaluation of a possible cast glass interlocking geometry using Finite Element Analysis (FEA). For this purpose, design criteria are formulated from literature; considering glass, polyurethane (used as interlayer) and interlocking systems. As interlocking systems are determined by their boundary conditions, a case study of a monument is chosen to provide additional design criteria. The goal of the case study is to provide a reversible and reusable restoration and consolidation alternative for the current invalid restorations.

The design criteria obtained then are combined into an initial geometry, whose parameters are varied to test their sensitivity to its shear capacity, using FEA. Christensen's failure criterion is used to locate prone areas in the geometry, and to evaluate the theoretical moment of failure. This output value combines the three principal stresses into a failure envelope, hence can generate contour plots to envision peak-stress-prone areas. This is important especially for glass structures, as they are prone to peak tensile stresses.

From the results design diagrams are created and applied on a conceptual cast glass interlocking consolidation design for the monument chosen as case study: The Lichtenberg Castle ruin.

The initial design is moreover prototyped to check its interlocking capabilities, residual stresses and deviations introduced by shrinkage.

Being able to evaluate possible geometries using FEA can decrease costs and time when searching for a new interlocking geometry. Prone areas are easily highlighted using the Christensen's failure criterion output. Hence peak stress sensitive or invalid geometries can be discarded before reaching the prototyping stage, which is time consuming and costly.

The creation of a methodology to predict this behaviour is hence valuable for further research on other cast glass geometries and can moreover be applied in any other field when analysing solid complex geometries.

Another goal is to find a cast glass brick design which not only can consolidate the monument of the case study, but is moreover applicable in other projects or configurations. The brick then is not a one-solution design, but can be reused in other projects.

The geometry hence is varied using Grasshopper plug-in for Rhinoceros. By exporting the geometry using a STEP-file, a solid can be loaded into DIANA FEA, where it can be analysed using their newly implemented output value of the Christensen's failure criterion.

The geometry of the monument is gained through a 3D laser scan, resulting in a point cloud. The point cloud is adapted using Autodesk Recap, then further processed in Rhinoceros.

The Christensen's failure criterion output is a proper and fast way to evaluate possible cast glass brick designs. Any compressive stresses on the interlocking brick geometry are beneficial for its shear capacity, as is an increase in interlocking amplitude or brick height. Increasing the amplitude however affects the allowable tolerance negatively, which is also the case for a decrease in brick height. Decreasing the brick height hence results in both negative effects.

The conceptual design for consolidation of the Lichtenberg Castle tower can replace the current interventions with equal or higher capacity, even for all conservative assumptions and simplifications. The design can still be altered less conservative after more experimental results and simulations come available.

The methodology applied can now be further developed and performed on other complex geometry designs. The presented multifunctional cast glass interlocking brick design, and its variations can be further investigated and applied in other projects.

Table of Contents

Nomenclature

2D	=	Two-dimensional
3D	=	Three-dimensional
ENCI	=	Eerste Nederlandse Cement Industrie
FEA	=	Finite Element Analysis
GH	=	Grasshopper, plug-in for Rhinoceros
IPO	=	Interprovinciaal Overleg
PU	=	Polyurethane
LHP	=	Light House Project
ShA	=	Shore A hardness
ShD	=	Shore D hardness

A	=	Amplitude	[mm]
A_i	=	Area of surface *i*	[mm^2]
C	=	Compressive strength	[MPa]
CHR	=	Christensen's Failure Criterion value	[-]
E_i	=	Young's Modulus of material *i*	[MPa]
f	=	stress	[MPa]
f_t	=	Tensile strength gap criterion	[MPa]
$f_{g;d}$	=	Design tensile strength glass	[MPa]
$f_{g;k}$	=	Characteristic tensile strength glass	[MPa]
F	=	External point load	[kN]
k_c	=	Coefficient for type of construction	[-]
k_{mod}	=	Coefficient for load duration	[-]
$R_{g;d}$	=	Design tensile strength glass	[MPa]
S	=	Shape factor	[-]
t_i	=	thickness of element *i*	[mm]
T	=	Tensile strength	[MPa]
γ_i	=	Safety factor	[-]
Δi	=	Certain change in parameter *i*	[unit equal to unit of *i*]
ε	=	strain	[-]
K_i	=	Bulk-modulus of material *i*	[MPa]
λ	=	Ratio deformed/original thickness	[-]
μ	=	Friction coefficient	[-]
ν_i	=	Poisson's ratio	[-]
π	=	Mathematical constant	
ρ_i	=	Density of material *i*	[kg/m^3], [T/mm^3]
σ_{ij}	=	Stress in ij-direction	[MPa]
τ_{ij}	=	shear stress in ij-direction	[MPa]
ϕ	=	Friction angle	[rad]

Chapter 1.

Introduction

Introducing the research topic, firstly the motivation for this line of research is presented, followed by the scope of the research and its scientific relevance. Research objectives are defined next, as well as the methodology used to reach these objectives. Lastly the structure of the thesis is clarified, for swifter navigation through the thesis.

Section 1.1. Motive

Throughout history many structures have not stand the test of time. Emerging technologies, political conflicts and acts of nature have shaped the built world we live in today. The structures that bore witness of earlier eras that did survive, we seek to protect, consolidate, and conserve for future generations to see.

For this purpose many local, national, and international organisations pursue to protect the often fragile displays of history, gathering funds for restorations and maintenance. The more damaged objects might even need consolidation, which is often the case for ruins. These consolidations are often in the form of steel ties or scaffolding, which are often an eyesore compared to the historical material, but necessary nevertheless.

Take for instance the Lichtenberg Castle ruin, shown here in Figure 1. The tower is the last remaining part of a once formidable castle (see Figure 1a), with historic records tracing it back to around 1212, when the first fortress was erected here for *Hugo de Pierrepont*, prince-bishop of Liège at that time. The castle has since been witness to a range of historical events, including being the headquarter of the Duke of Alva during the Eighty-year War with Spain (1568) and the reconquering by *Frederik Hendrik van Oranje* in 1632, as headquarters of colonel *Pinsen van der Aa*.

Throughout the centuries a series of unfortunate events have damaged the tower and lay destruction to its adjacent quarters. It is unknown what the cause of the wreckage was exactly, but the many sieges of Maastricht, underground quarries and erosion, as well as several strong earthquakes in the region might have had a hand in its downfall. There is a chance that the earthquakes in Verviers (1692, Belgium) and Düren (1756, Germany) were involved in its destruction, possibly in combination with underground flaws; such as erosion of the limestone or the quarries that have been there for centuries.

Nowadays the tower functions as a panoramic viewpoint over the river Maas and nearby ENCI-quarry. After the destruction of the castle, a fortified farm was built adjacent to the tower and later ENCI excavated a large part of Mount Saint Peter around the farm, creating an elevated peninsula towering over the river valley and quarry. The tower itself was consolidated with steel ties and a steel staircase in 1904, which in certain points are anchored into the walls. Since then, steel and limestone parts have been replaced occasionally. Old limestone was replaced both by new limestone and masonry brickwork. Some parts at the top of the wall are even covered in a layer of concrete, presumably to fix parts of the steelwork to the structure. The tower has become a patchwork of interventions, featuring several foreign materials as a consolidation or as a restorative measure.

Recent developments in cast glass technology might offer a more appropriate and homogeneous solution for monuments like the Lichtenberg Castle. Cast glass can be applied as a structural element, such as masonry bricks or columns, and therewith replace current opaque interventions with a transparent one. Besides transmitting more light into the monument, the monument can also be perceived in its former glory, as the elements can be cast to fit the current geometry of the structure, reviving historically lost details in a ghostly manner.

This principle can be visualised by reviewing the Crystal Houses project, designed by MVRDV and engineered by TU Delft and ABT (see Figure 2). In contrary to the fact that this was not a restoration project, it features the former appearance in a transparent ghostly way (Figure 2d). It seems that the upper part is levitating, while when one approaches the building the reflecting surfaces of the bricks highlight the sky, enforcing this sensation. Due to the adhesive connection, the tolerances on the bricks were incredibly strict. The glue moreover introduces a contamination when recycling.

For the TU Delft Glass & Transparency research group this led to the shift in focus from adhesively bonded masonry to an interlocking system of cast glass components, which can be dry-connected using a rubber interlayer. The glass components then can be reused for another purpose or recycled without any contaminants. Such a system is furthermore reversible, which is of high importance for monuments, as future techniques might prove to be more efficient or suitable interventions.

a

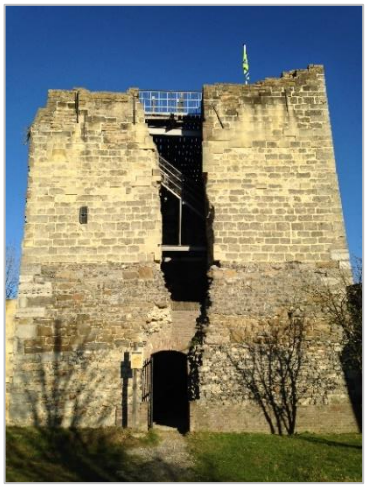

b

c

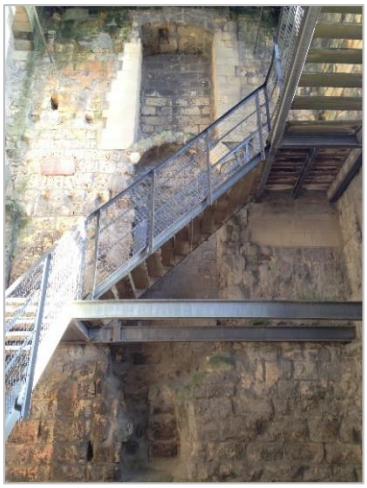

d

Figure 1: Lichtenberg Castle ruin, with a) Former appearance Lichtenberg Castle. Reprinted from (Haagen, 1650); b) inner courtyard façade and entrance to the tower (photograph by author); c) latest consolidation works on the tower (photograph by author); d) Inner staircase with embedded steel profiles (photograph by author).

a

b

c

d

Figure 2: Crystal Houses, with a) Casting of a brick; b) UV-light curing of an experimental set up; c) Façade reflections; d) Final design in street context. Reprinted from: (MVRDV, 2016).

Together with the Technical University of Eindhoven the research group gained a grant in the Lighthouse project (LHP) of 2016 for Restorative Glass. This grant led to the initial design idea of the Lichtenberg Castle consolidation, as shown in Figure 3. The design features three different heights of bricks, to mimic the different sizes of the stones used in the original wall. The design however focuses on the wall facing the courtyard, while it is the adjacent wall with the steel frame (Figure 1c) which prior to the current consolidation featured the most dangerous crack according to old drawings and the 3D scan. This will be further elaborated in *Chapter 3. Case Study: Lichtenberg Castle*.

In the 4TU.Bouw conference of 2017 the research group teamed up with researchers from the University of Twente and gained a grant for their Re^3 glass project. This project is a follow-up on the LHP2016 and focuses on a strategy to recycle a larger part of the glass waste line, by including glass with impurities and making cast glass interlocking elements. By optimizing the shape of the elements, the amount of material used can be reduced, and by dry connecting the elements they can be reused as well. As glass is infinitely recyclable this would create an infinite loop in which the glass never enters a waste line again, as is depicted in the infographic shown in Figure 4.

This thesis continues from the 2016 Lighthouse Project and uses the MSc thesis research conducted by Barou, *Transparent Restoration* (2016), as a starting point. So far, no detailed parametric and numerical analysis has been conducted on a cast glass masonry system, and gaining insight in parameter dependency can help determining potential beneficial brick designs or indicate flaw-prone areas.

Section 1.2. Scope

This thesis therefore primarily focuses on a parametric sensitivity analysis using numerical calculation software on a specific cast glass brick design. The results of these analyses are then used to find a conceptual solution for the Lichtenberg Castle.

The goal is to provide a method in evaluating possible future brick designs, and predict where stresses become critical using the finite element analysis software *DIANA FEA.* A newly implemented output value will be tested for *TNO DIANA* and used in the evaluation of the interlocking brick design to highlight flaw-prone areas. This output represents a test against the failure envelope as described by Christensen (2013), and uses the tensile and compressive strength of a given material and the principal stresses in a 3D geometry model. More about the Christensen's failure criterion is discussed further on in Section 2.1.5.

The evaluation method will be applied on a possible brick design which was especially designed for the case of the Lichtenberg Castle tower (as a brick design is mostly determined by its boundary conditions). This will illustrate the method's purpose and application on other possible interlocking brick designs for other or similar applications. Certain variations on the geometry are tested to discuss parameter dependency after rough analytical predictions. To highlight the reusable character, the brick will also be designed for its post-Lichtenberg life, in the sense that the design should be able to be applicable in other modifications.

As the shear key applied in the brick design needs to convey most of the loads acting on the system's boundary conditions, the shear key capacity is the focus of this thesis. Compression of the glass brick will be briefly discussed, but not further evaluated in the sensitivity study of the parametric brick design.

The scope is limited to the development of an evaluation methodology for a glass parametric brick, its parameter sensitivity study and a conceptual application on the existing structure. The only nonlinear effects taken into account are the interface properties defining the behaviour of contact between materials. Both glass and polyurethane are modelled as linear isotropic materials. For glass this is common practise, for polyurethane follow-up research is needed to validate the assumptions made

in this thesis. The polyurethane properties are derived from literature and the results of a representative test result. Other nonlinear effects such as creep of the system, thermal effects or deviations in the geometry are not taken into account in the simulations. The former two will not be discussed in order to limit the scope, the deviations in geometry will be evaluated from prototyping and in the discussion of the numerical results. By lack of sufficient experimental results, no other possible interlayer materials than PU for the interlayer are reviewed.

Regarding the new consolidation design, a concept is presented using the results gained from the numerical modelling. Furthermore, a possible connection system is designed to connect the glass system to the existing monument.

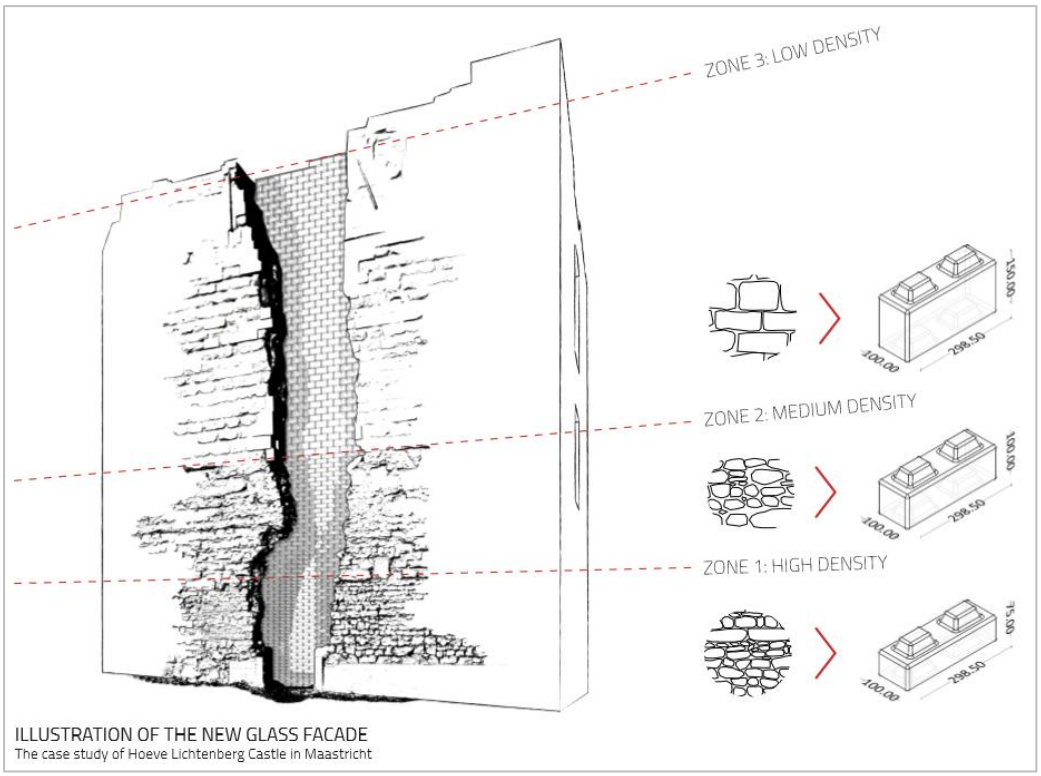

Figure 3: Restorative glass, granted 4TU.Bouw Lighthouse project 2016. Reprinted from (Restorative Glass Team, 2016).

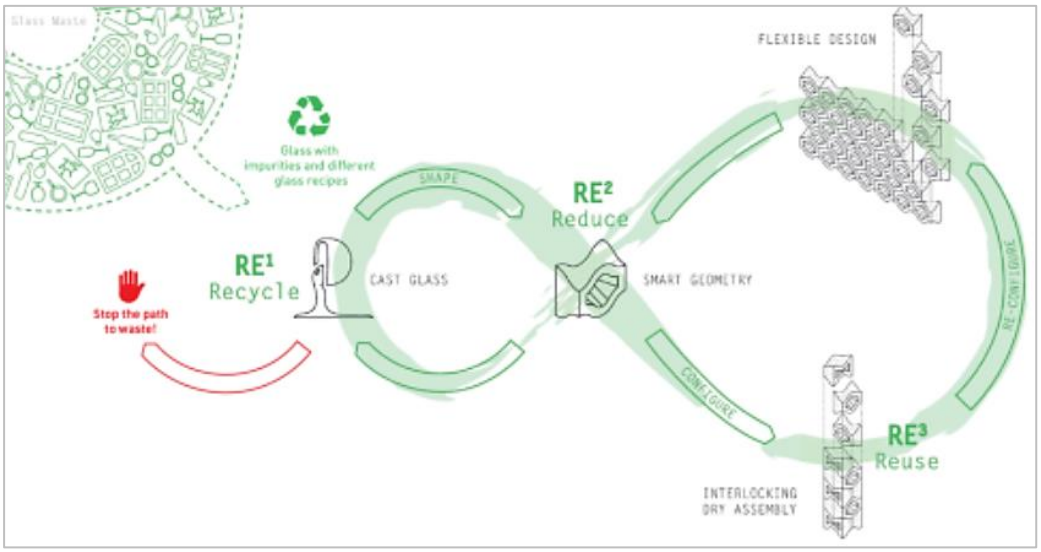

Figure 4: Re3 glass strategy, granted 4TU.Bouw Lighthouse project 2017. Adapted from (4TU Bouw, 2017).

Section 1.3. Relevance

With the data gained, it will be easier to determine which brick geometry theoretically can be pursued. As making prototypes of the glass bricks is a costly endeavour, the data can be used as a decision tool of determining whether a geometry has potential. Furthermore, the design diagrams derived from the data will provide an insight in the relation between geometric parameters, which can be used as a tool to either use one of the parametric possible designs for production, or to design new brick geometries derived from the data.

The computational methodology could be used for other applications as well. With alterations in the coding and properties it should be possible to investigate any complex geometry designed with Grasshopper in DIANA FEA. This could for instance be the case for complex steel nodes or other free-form designs.

Furthermore the glass brick can be of interest in other projects than merely monumental wall replacements. Think of temporary exhibitions or pavilions, internal division walls or columns. These are however not in the scope of this research, but can be explored using this thesis' results.

Section 1.4. Research objectives

The main research objective is to find out what an interlocking cast glass brick can do in matters of structural (shear) capacity and specifically when applied as a monumental consolidation. In this thesis, therefore the potential of the brick is analysed, and parameters are evaluated according to results gained from finite element analysis (FEA).

The following objectives can be distinguished:

- Formulate design criteria for an interlocking cast glass brick;
- Render design criteria to a fitting but multifunctional brick design;
- Generate geometries fit for inter-software exchange;
- Identify and evaluate the influence of deviations in leading parameters on brick shear capacity;
- Set up FEA protocol to investigate complex geometries;
- Discuss FEA results versus analytical expectations;
- Translate results into design values and compare 'perfect' model to reality;
- Create a conceptual consolidation design for implementation in the Lichtenberg Castle ruin.

Section 1.5. Methodology

The approach taken in this thesis can be described using four phases. Each phase yields input for the next phase. This is schematically shown in Figure 5.

Phase 1 consists of a brief literature review, considering the main ingredients of this thesis. Used materials are hence investigated, which in this case are (cast) glass and polyurethane (PU). Also important are interlocking geometries and the monument analysis.

Hence these topics yield boundary conditions and design criteria for the future interlocking cast glass masonry structure.

Phase 2 then considers the generation of this geometry. A parametric model is set up in the Grasshopper (GH) extension for Rhinoceros. Hence parameters can be changed to generate deviating geometries.

The monument is analysed using a point cloud, which is adapted to get ready for the new cast glass interventions. Hence current interventions need to be cut out, which is done using Autodesk Recap. The geometry is then generated in Rhinoceros in combination with its extension GH.

Phase 3 is the analysis of the geometries, which will be performed using TNO finite element software DIANA FEA. Generated geometries are exported in Rhinoceros using STEP-files, which can be imported as a CAD-file into DIANA FEA. Here the cast glass interlocking brick design is analysed, including certain parameter variations.

Phase 4 then concludes with the results of the research. Prototypes are made to discuss production and evaluate how the shape solidifies after casting. The finite element analysis results are transformed into design diagrams. These diagrams are then applied in a possible monument consolidation design for the Lichtenberg Castle ruin.

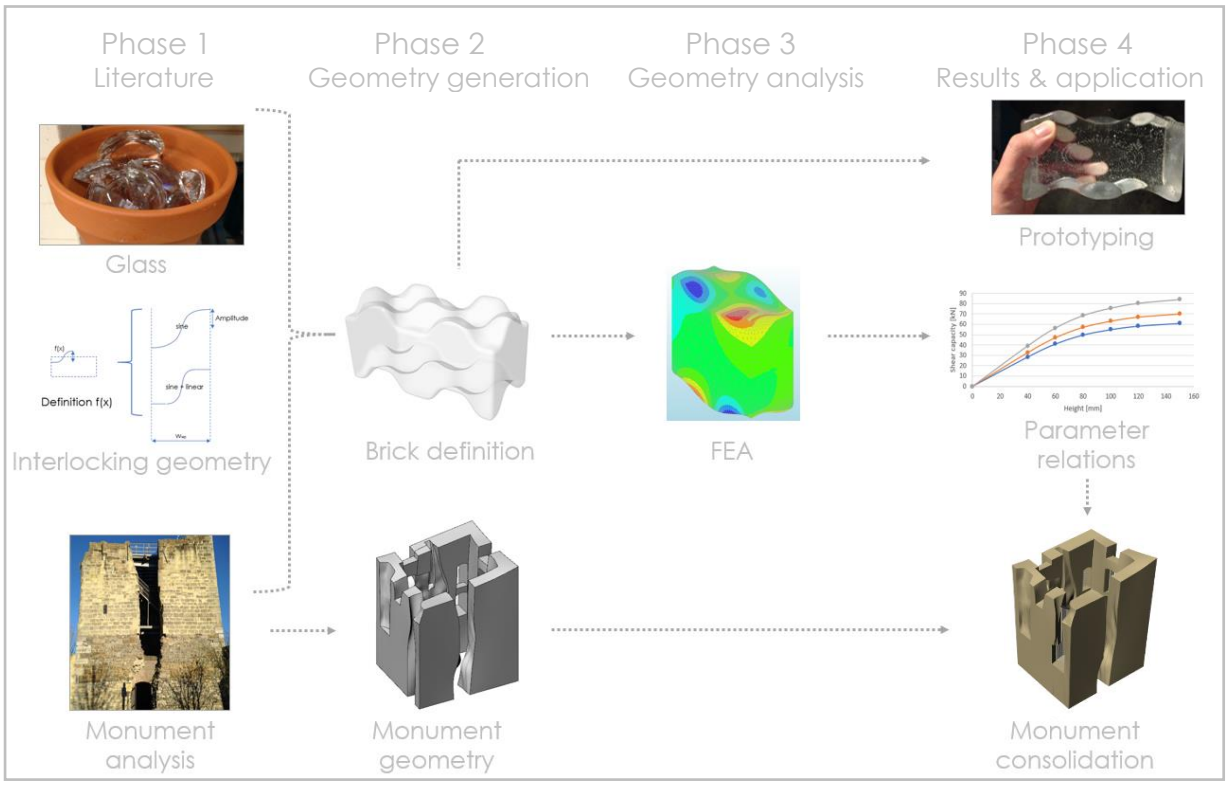

Figure 5: Methodology, flow of information throughout phases.

Section 1.6. Thesis Structure

The thesis structure follows closely the flow of information in this thesis, as is indicated in Figure 6. The literature study phase is divided into two chapters. In Chapter 2 the theoretic framework is discussed, which reviews literature on materials and interlocking geometry. Chapter 3 then reviews and analyses the subject of the case study: The Lichtenberg Castle. This also includes the monument geometry generation from the point cloud. The brick definition and parametric design is then discussed in Chapter 4, followed by the FEA protocol and settings presented in Chapter 5. The results of the finite element analysis and the resulting design diagrams. Discussion of the prototype takes place in Chapter 7 and implementation of the glass brick into the Lichtenberg Castle ruin in Chapter 8. Here also a possible connection design is presented. Lastly the thesis is concluded with the discussion, conclusions and recommendations in respectively Chapters 9, 10 and 11.

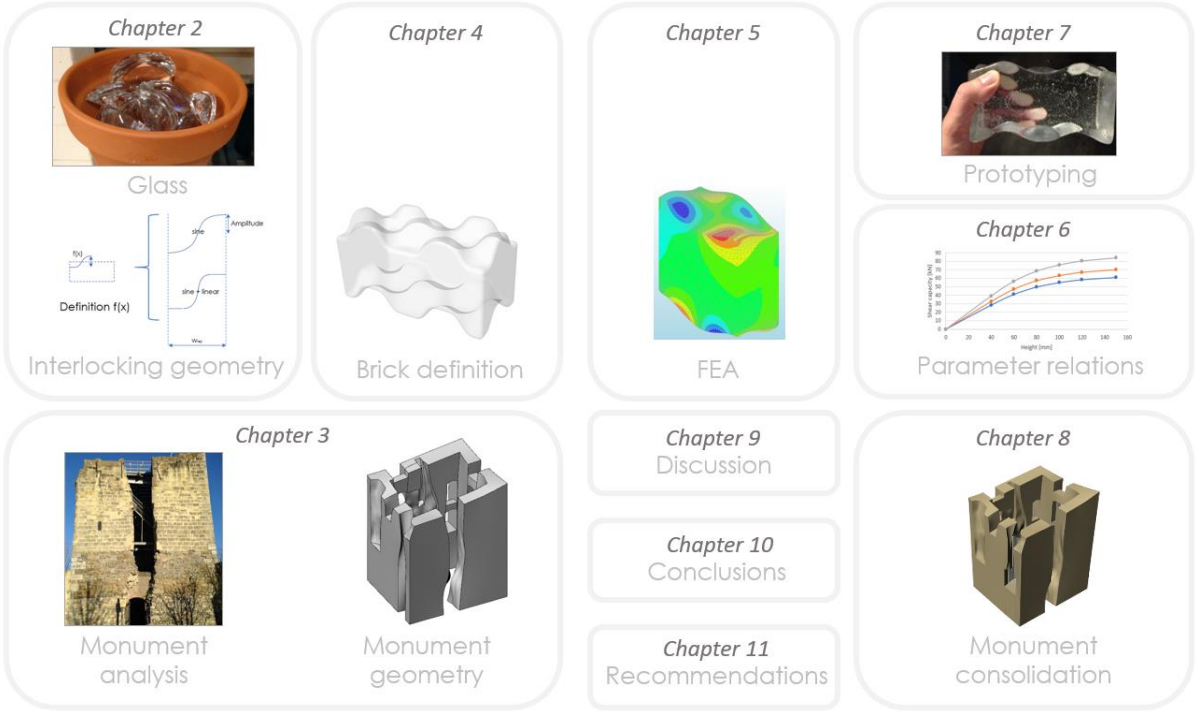

Figure 6: Thesis structure, overview of topics assigned to each chapter.

Chapter 2.

Theoretic Framework

In order to come to a new cast glass interlocking system for consolidation purposes it is important to gain knowledge from literature regarding the topics presented in this chapter. Hence the materials glass and polyurethane are briefly reviewed, as well as existing interlocking systems.

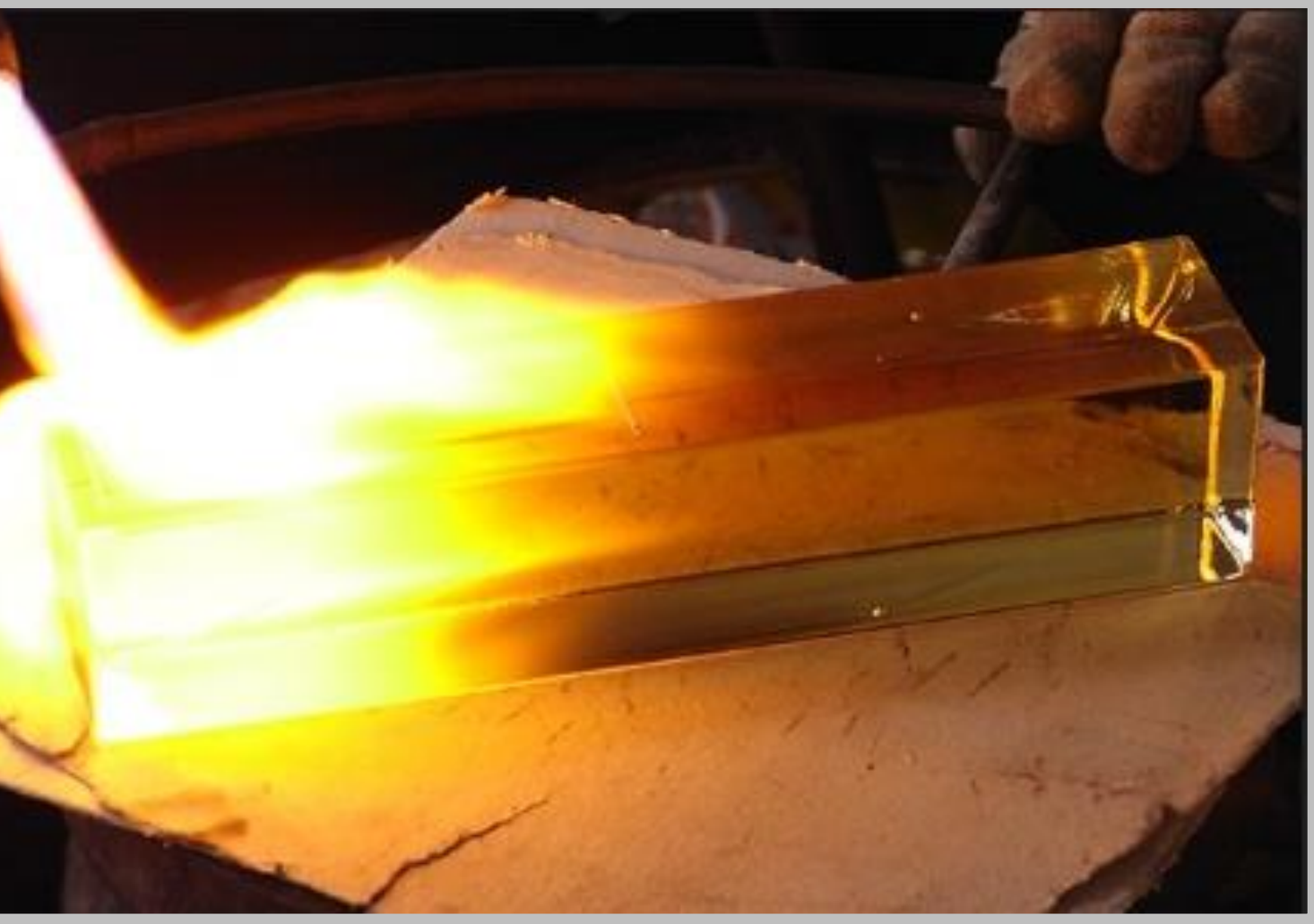

Post-processing of cast glass brickwork applied in the Optical Glass House in Hiroshima, Japan.
Reprinted from (Tadashi Oshima, 2012).

Section 2.1. The Material Glass

Glass is a peculiar material. Its most well-known properties are its transparency and its brittleness. Increasingly it is applied as a structural solution, and mostly laminated float glass elements are used. This thesis focuses on the application of cast glass instead, and investigates its applicability using finite element analysis. Hence it is important to gain an insight in the material itself.

This section therefore will discuss general topics on glass first, such as its classification and glass composition. Then the casting of glass and resulting residual stresses are reviewed, followed by mechanical properties such as the tensile strength, glass failure and its fracture mechanism.

2.1.1. Glass classification: An amorphous isotropic solid

Glass can be described as a liquid material that is gradually cooled down to its solid state, in which the molecules are in random order and non-crystallized. Glass therefore can be categorized as an amorphous isotropic solid (Schittich, Staib, Balkow, Schuler, & Sobek, 2007). Being an isotropic material, its properties therefore are equal in any direction.

The term 'random order' of an amorphous solid can however be misunderstood. An amorphous solid does not form a crystal lattice as is the case in crystalline solids, where the positions of atoms occur periodically in space. This phenomenon is defined as a long-range order, creating a macro structure of ever repeating patterns. Amorphous solids do not exhibit a long-range order, and atoms therefore seems to connect unstructured. This is however a misconception, as both crystalline and amorphous solids exhibit a short-range order, which defines the chemical bond length between atoms (Douglas & Zallen, 2016). The structure of an amorphous solid therefore is locally determined, simply lacking global conditions, whereas crystallized solids follow both local and global solidifying conditions. A 2D-representation of both molecule structures is given in Figure 7.

An amorphous solid is obtained when a material is cooled down rapidly enough to bypass crystallization, the rate of cooling down then varies for each material (Douglas & Zallen, 2016). This quenching, gives the material no chance to form a crystallized pattern the material will be 'frozen' in the amorphous state. For the material glass, this means that, to avoid crystallization, glass should be cooled down swiftly to its softening point (Oikonomopoulou, Bristogianni, Veer, & Nijsse, 2017). The softening point is graphically shown in Figure 8, where viscosity is plotted against temperature. This graph and the behaviour of molten glass is further discussed in Section 2.1.3.

From its molecular state glass also inherits its transparency. This can be explained with band theory, which states that within a solid, electrons are allowed to have certain energy bands (energy ranges electrons may have) and band gaps (ranges it may not have). Within glass, band gaps are quite large. Hence photons of visible light (wavelengths 400 to 700 nanometres) can pass through, as they have insufficient energy to be absorbed or reflected (Varshneya, 2016).

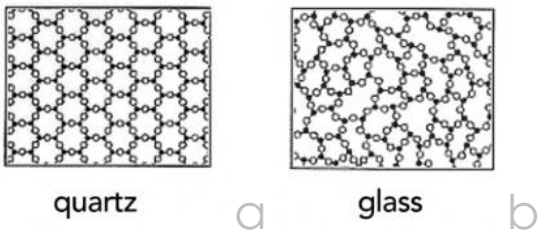

Figure 7: Molecule structures of a) a crystalline solid, quartz; and b) an amorphous solid, glass. Reprinted from (CMOG, 2011).

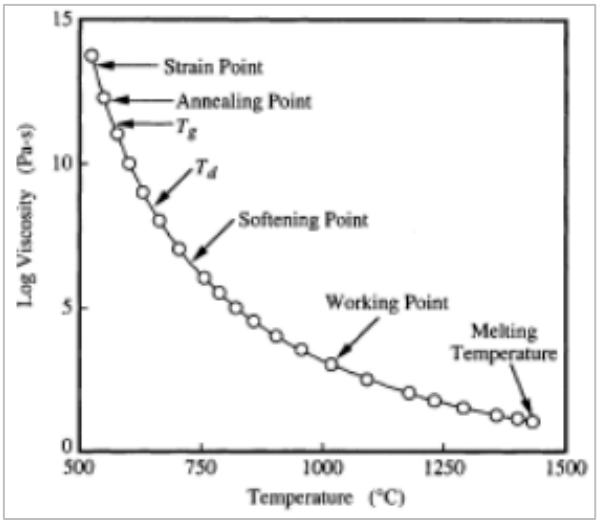

Figure 8: Characteristic points along viscosity curve from melting temperature until strain point. Reprinted from (Shelby, 2005)

2.1.2. Glass composition

Glass does not have a standard chemical formula. Its composition depends on the kind of glass applied and the properties desired. Two of those compositions are reviewed here: soda-lime glass and borosilicate glass.

The most common kind of glass is soda-lime glass, which consists mostly of silicon dioxides, with the addition of calcium, sodium, magnesium, and aluminium oxides (Schittich, Staib, Balkow, Schuler, & Sobek, 2007). A standardized composition for Europe is given in Table 1.

Using another composition, borosilicate glass can be manufactured, which replaces magnesium and calcium oxides with boron-oxides.

Comparing both kinds of glass, borosilicate glass has a significant lower thermal expansion coefficient, making it a better choice for applications that require increased fire protection (Schittich, Staib, Balkow, Schuler, & Sobek, 2007). It however also comes with higher tolerances, making it a less suitable choice for applications which only allow for small tolerances, as stated in a paper of Oikonomopoulou et al. (2014). Borosilicate glass furthermore has worse mechanical properties when compared to soda-lime glass and is more expensive in production. A comparison between both is given in Table 2.

There are other minor additions to the composition that can influence optical properties (colour, opacity, and transparency spectrum). Minor additions of these substances will however not influence the mechanical strength (Schittich, Staib, Balkow, Schuler, & Sobek, 2007).

Table 1: The composition of soda-lime glass according to European regulation in EN 572 part 1. Reprinted from (Stittich et al, 2007).

Composition of soda-lime glass		
Silicon dioxide	(SiO_2)	69%-74%
Sodium oxide	(Na_2O)	12%-16%
Calcium oxide	(CaO)	5%-12%
Magnesium oxide	(MgO)	0%-6%
Aluminium oxide	(Al_2O_3)	0%-3%

Table 2: Comparison between properties of float/cast soda-lie and borosilicate glass. Reprinted from (Oikonomopoulou, Veer, Nijsse, & Baardolf, 2014).

Properties of standardized float/cast soda-lime and borosilicate glass

	Units	Soda-lime	Borosilicate glass
Thermal resistivity	[m*°C/W]	0.909–1.11	0.769–0.909
Thermal expansion coefficient	10^{-6}/K	9.1–9.5	3.2–4
Tensile strength	MPa	30–35	22–32
Compressive strength	MPa	300–420	260–350
Young's modulus	GPa	68–72	61–64
Hardness	kg/mm²	440–485	84–92
Cost	€/kg	1160–1370	3430–5150
Typical Chemical Composition		73% SiO_2	80% SiO_2
		17% Na_2O	4% Na_2O
		5% CaO	13% B_2O_3
		4% MgO	2.3% Al_2O_3
		1% Al_2O_3	0.1% K_2O

2.1.3. Casting of glass: Poesia bricks

Glass does not have a set melting point. Instead it will slowly go back into a plastic-viscous state when heated until it reaches its fully liquid state. When casting glass, the production process is of the utmost importance to limit flaws and imperfections in the elements, as well as residual stresses due to the annealing process.

The process of casting glass will be described using the production of the *Poesia* cast-glass masonry bricks which were used in the Crystal Houses. This professional manufacturing technique is discussed in Oikonomopoulou et al. (2017), as well as a method to indicate residual stresses.

A more hands-down method to produce cast glass is applied in this thesis. It is only applicable for prototypes as the process is quite elaborate and imprecise. This method will be later discussed in Chapter 7.

Manufacturing of the Poesia bricks

The Crystal Houses bricks were manufactured by *Poesia* and the following production technique is discussed in Oikonomopoulou et al. (2017).

Glass first is molten past its melting temperature (see Figure 8) and then poured into a preheated steel mould. The moulds should be heated up to approximately 650-750˚C, lower temperatures will create a rough outer surface. If the steel has a higher temperature the glass would stick to the mould. The mould should also be coated prior to casting, to allow the glass to release from the mould easier.

The glass then is cooled down swiftly to around 720˚C, which is its softening point (see Figure 8). This to avoid the glass to crystallize, which would affect the transparency. When glass is at its softening point, the viscosity is low enough to not deform under its own weight (Shelby, 2005). The mould can then soon be removed.

After removal of the mould the brick is placed in an oven until it reaches its annealing point, which is around 545˚C. At this temperature a considered amount of stresses is relieved in just a few minutes (Shelby, 2005). The brick must be kept at this temperature for some time, to allow for the whole brick to reach the same temperature. Meanwhile the glass is able to relieve the residual stresses that come with non-uniform cooling down (Oikonomopoulou, Bristogianni, Veer, & Nijsse, 2017).

Annealing time can significantly increase by decreasing the element slenderness and increasing its mass. It is also influenced by practical matters in the oven, such as possible other nearby thermal masses and which surfaces are subject to cooling (Oikonomopoulou, Bristogianni, Veer, & Nijsse, 2017).

After reaching a uniform temperature in the glass, it can be cooled down towards the strain point (around 505 ˚C), after which any remaining residual stresses are locked into the glass. Due to natural shrinkage and necessity of low tolerances post-processing is necessary. These characteristic points are shown in a viscosity vs temperature diagram in Figure 8.

Residual stresses

The existence of residual stresses in the glass brick can be determined using polarized white light and a crossed polarized filter. When residual stresses are present in the brick, these areas will appear colourful due to the optical anisotropy glass exhibits when stressed (Oikonomopoulou, Bristogianni, Veer, & Nijsse, 2017). In Figure 9 this effect is shown for some bricks of the Crystal Houses project. On the left-hand-side side, isochromatic fringes appear indicating a substantial, yet unquantifiable, residual stress. On the right-hand-side a dark background indicates no residual stresses while the white areas reveal low residual stresses. Furthermore in all pictures a dark ellipsoid is recognisable in its centre. This is the result of the faster cooling down in the corners since it is subject to cooling from multiple sides. The core cools down somewhat later, creating residual stresses in the corner due to its natural shrinkage. The better the annealing process the fewer residual stresses remain. An even mass distribution also contributes to less residual stresses and a geometry approximating an ellipsoid is also favourable.

This method can also be used to monitor where stresses occur when loading the specimen. The isochromatic fringes then visibly appear three times, each time visualising a higher stress, while still being unquantifiable. This method therefore is merely used as an indicative tool.

It can be concluded that the annealing process is of the utmost importance and that the time needed for annealing is highly dependent on the geometry of the brick. Furthermore it might be favourable to apply geometries with curvatures, approximating an ellipsoid. In any case post-processing due to shrinkage and the necessity of low tolerances is inevitable unless all these effects can be taken into account by increasing controllability of the manufacturing process (e.g. taking this into account during mould design).

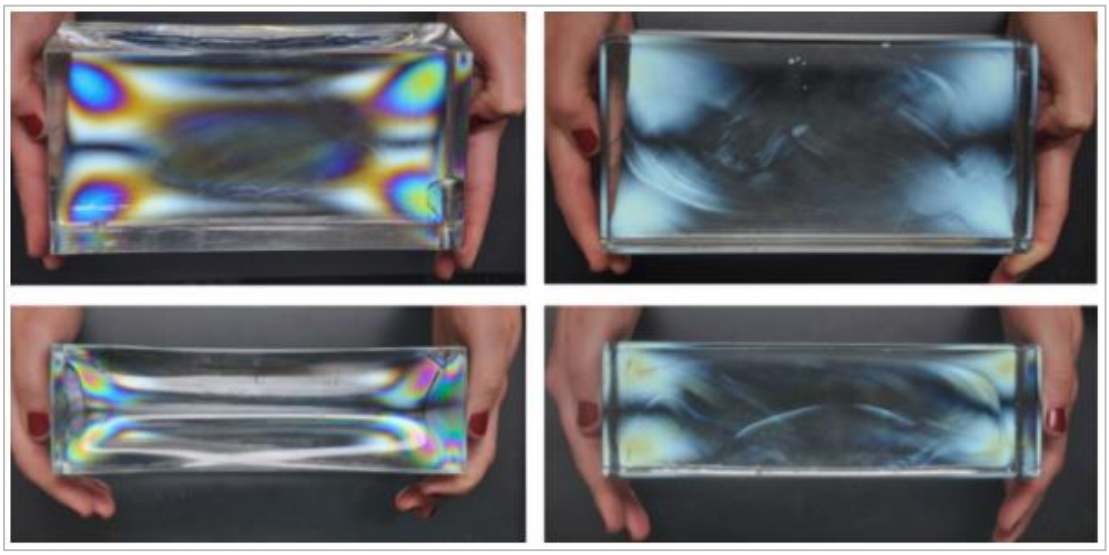

Figure 9: Residual stresses gained during the annealing process visualized by polarized light in the Crystal Houses project. Reprinted from (Oikonomopoulou, Bristogianni, Veer, & Nijsse, 2017).

2.1.4. Tensile strength of glass

Glass is a brittle material, yielding no warnings before failure in contrary to materials like steel (see Figure 10a). In this sense the material has more in common with unreinforced concrete than steel, as its failure mechanism is at the specific location where the peak stress exceeds its tensile strength. These peak stresses mainly occur at flaws in the material (micro-cracks or scratches) and locations where peak stresses are introduced (concentrated loads).

There is not much data related to cast glass available in literature. The structural application of cast glass masonry is relatively new and needs further investigation. Data from annealed glass panes are therefore compared with the limited data of cast glass. The results from experiments on 740 annealed glass panes are given in Figure 10b. It considers specimens from across nine factories in Europe. It initially shows how unpredictable glass is varying from approximately 30 MPa to 120 MPa. This range of results can be attributed to the amount and severity of flaws in the panes at a tensile stress prone location. In any case no value less than 30 MPa was recorded in these tests. The design strength of such a pane (short term horizontally annealed monolithic pane according to DIN 18008) is equal to 17.5 MPa (see Expression 2.1), which is well below the results of the tests. For permanent loads (k_{mod} = 0.25) the design strength is $f_{g;d}$ = 6.25 MPa.

$$f_{g;d} = \frac{k_{mod} * k_c * f_{g;k}}{\gamma_{m;g}} = \frac{0.7 * 1.0 * 45}{1.8} = 17.5\ MPa \qquad [\ 2.1\ ]$$

In which $f_{g;d}$ is the design strength [MPa]; k_{mod} the load duration factor [-]; k_c a coefficient for structure type [-] and $\gamma_{m;g}$ the partial safety factor for the resistance of the material factor.

When considering cast glass compression tests by Oikonomopoulou et al. (2014), which were carried out without intermediate layer to prevent peak stresses, none of the specimens failed before reaching a nominal stress of 20 MPa. This was caused due to unevenness of the surface compared to the stiffer steel plates (Oikonomopoulou, Veer, Nijsse, & Baardolf, 2014). The concentrated stresses (>20 MPa) then resulted into a local tensile failure instead of compressive failure.

It can be concluded that peak tensile stresses lead to premature failure of a glass element. The tensile strength design value is a conservative but safe value, as none of the specimen found in literature fails before reaching 20 MPa nominal stress (real tensile stress is concentrated and therefore higher). Hence the design value is considered a safe value.

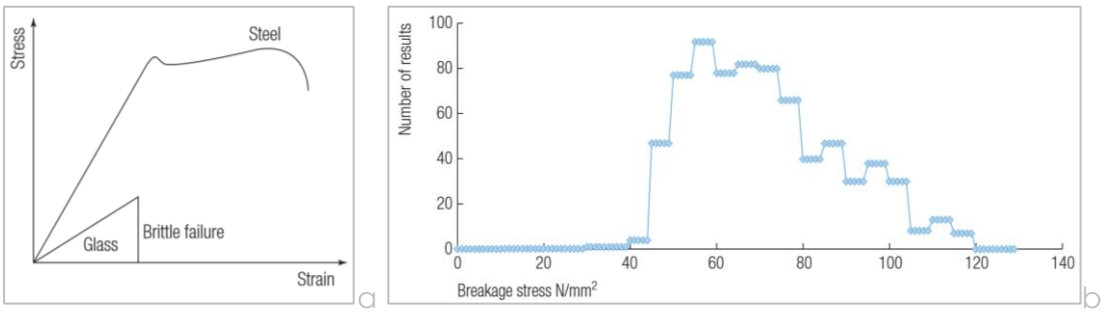

Figure 10: Stress/strain curves for steel and float glass (left) and test results of 740 annealed glass panes with a thickness of 6 millimetres (right). Reprinted from (O'Regan, 2015).

2.1.5. Failure criterion & fracture mode

As mentioned earlier, glass is a brittle material and highly sensitive to local peak tensile stresses. Its compressive strength (C) is 300-420 MPa, whereas its tensile strength (T) is about 30-35 MPa (Oikonomopoulou, Veer, Nijsse, & Baardolf, 2014) or 45 MPa (O'Regan, 2015).

Its failure behaviour can therefore not be described by single-property criteria Von Mises or Tresca, which use an equal strength for both compression and tensile strength and ductile behaviour (T=C). Other failure criterions like Drucker-Prager and Mohr-Coulomb do not provide a correct model for brittle materials as well. Drucker-Prager predicts unlimited compressive strengths for materials with T/C ≤ 1/3, whereas Mohr-Coulomb does the same for values of T/C ≤ 1/2 (Christensen, 2013).

In Christensen (2013) his endeavours to create a failure criterion that would be valid for all isotropic materials, he created the Christensen failure criterion. This criterion is given in Equation 2.2.

$$\left(\frac{1}{T}-\frac{1}{C}\right)(\sigma_1+\sigma_2+\sigma_3)+\frac{1}{2TC}[(\sigma_1-\sigma_2)^2+(\sigma_2-\sigma_3)^2+(\sigma_3-\sigma_1)^2]\leq 1 \qquad [\,2.2\,]$$

In which σ_1, σ_2 and σ_3 are the principal stresses (MPa); T is the tensile strength and C is the compressive strength.

The criterion includes extra conditions for brittle materials, which occur when T/C ≤ 1/2. These conditions are given in Equation 2.3.

$$\begin{aligned}\sigma_1 &\leq T\\ \sigma_2 &\leq T\\ \sigma_3 &\leq T\end{aligned} \qquad [\,2.3\,]$$

This extra condition creates a cut-off plane in the failure envelope, here shown in Figure 11. As depicted glasses are a brittle material with a ratio between tensile and compressive strength of about T/C = 1/8. For the characteristic strengths the following values can be assumed; T = 45 MPa and C = 360 MPa.

As mentioned before, failure is expected to occur near flaws or scratches in the glass. The dominant fracture mode for glass is crack opening due to tension (see Figure 12), whereas under compression the compressive strength generally prevents such fracture (Pepi, 2014). The Christensen failure criterion can then be used to predict where in the geometry the glass brick is most prone to failure by opening flaws under tension in that region.

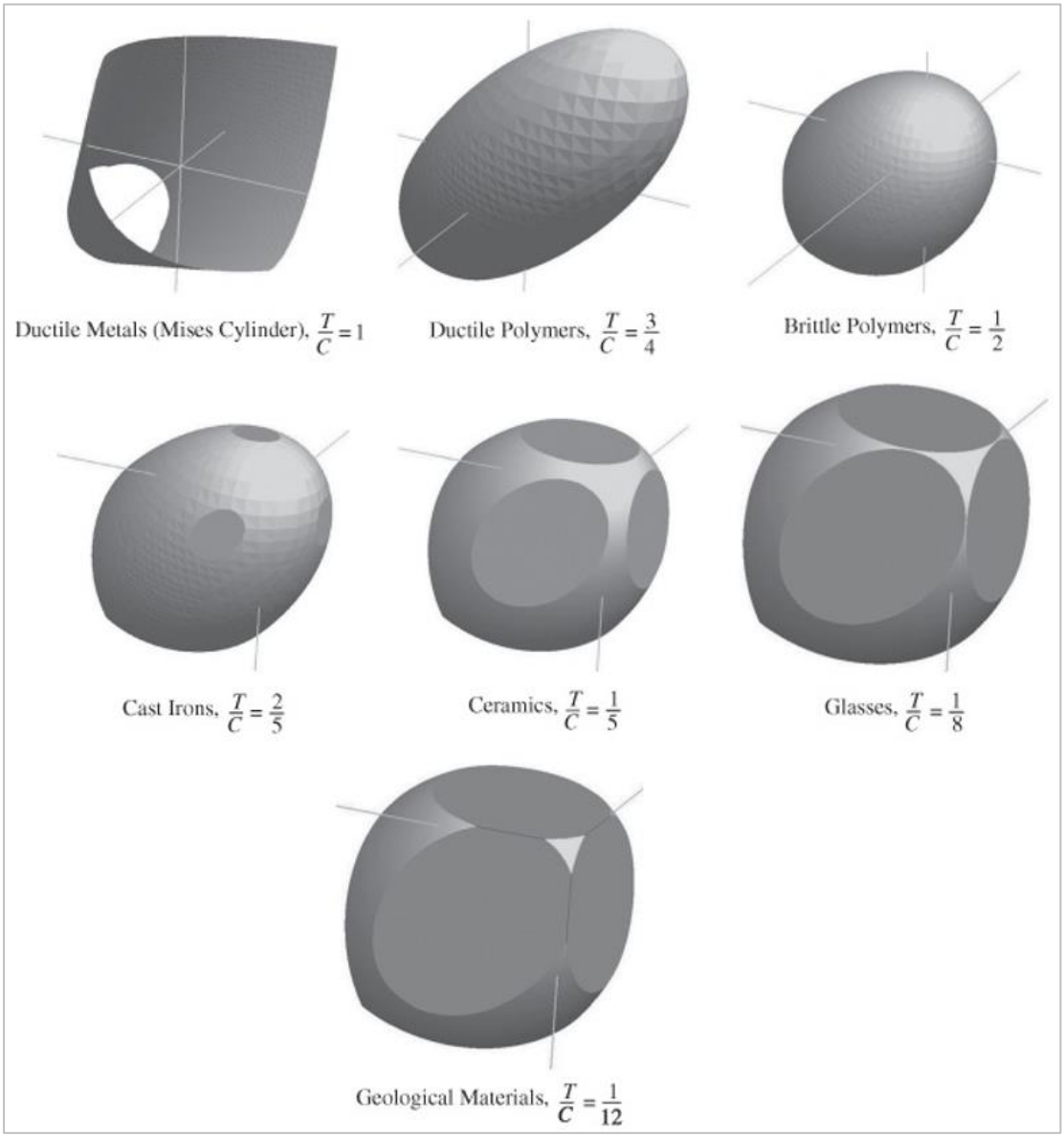

Figure 11: Failure envelopes of various materials according to Christensen failure criterion. Reprinted from (Christensen, 2013).

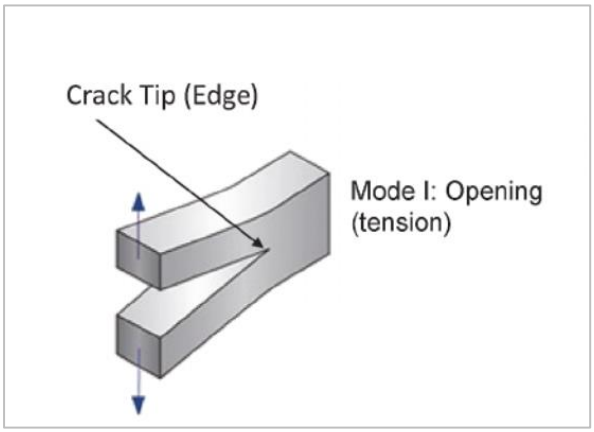

Figure 12: Fracture mode applicable to glass. Reprinted from (Pepi, 2014).

Section 2.2. Polyurethane (PU) interlayers

A direct glass-to-glass connection would introduce peak stresses that could lead to early failure. An interlayer therefore is placed in between the glass elements. As mentioned in the introduction, previous researches deemed polyurethane a suitable interlayer material (main advantages are its transparency, rigidity, durability, and UV-resistance).

There are however, due to the wide range of polyurethanes possible, different mechanical property results. This section therefore evaluates the previous researches on applicability and compares results with literature and manufacturer information available.

2.2.1. The material polyurethane

Polyurethane is the result of a reaction between diisocyanates and both short- and long-chain diols. A change in composition changes its physical properties, and polyurethanes can be processed into setting foams or elastomers; ranging from very soft and flexible to very rigid plastic-like elastomers. For the application as an interlayer, a transparent, semi-rigid elastomer is preferable, which can be casted into a mould. Therefore, the foams are disregarded and only the elastomers, both soft and rigid, are reviewed.

Polyurethane mixtures can roughly be divided into two categories, thermoset polyurethane and thermoplastic polyurethane. Both have their own characteristic properties.

Thermosetting polyurethanes react when components are mixed, which can already occur at room temperature. It is an exothermic reaction, and by adding more heat the curing of the plastic will be faster. Shaping the plastic can be done using compression moulding, rotational moulding, polymer casting or composite forming (CUAD, 2003). Moreover, they create chemical cross links, which increase its mechanical and thermal properties. The link however is irreversible (Huntsman, 2010) (see right-hand-side image of Figure 13). The solidified plastic cannot be melted, but will degrade instead.

Thermoplastic polyurethanes can be molten and therefore be recycled into a new mixture. Its components are heated up and can be shaped using extrusion, injection-, blow-, compression-, or rotational moulding. It is also possible to shape a solid plastic with machining (CUAD, 2003). Its mechanical properties are weaker than the thermoset plastics and by applying heat it can be molten and re-solidified (see Figure 14), which inherently reduces its thermal resistance.

On a molecular level both create a long chain of molecules during manufacturing. The amount of each component added influences the properties of the product. When the long-chain diol (or polyol) reacts with the diisocyanates it creates long flexible segments, while the short-chain diols create rigid segments when reacting with the diisocyanates (BASF, 2011). This principle is schematically visualised in Figure 15. Therefore, depending on the mixture, a larger or smaller quantity of rigid segments are created, influencing the overall rigidity and hardness of the polyurethane.

Depending on which polyurethane is applied (thermosetting or thermoplastic) either chemical or physical cross links are formed. The amount of cross links also highly influences the rigidity and hardness of the polyurethane.

Additives can be added to increase the properties of the polyurethane. For example, the producer BASF (2011) uses “glass fibres to increase rigidity” and “mould release agents, flame retardants, UV-stabilizers and plasticizers”. The polyurethane then can be elevated to the need of every application.

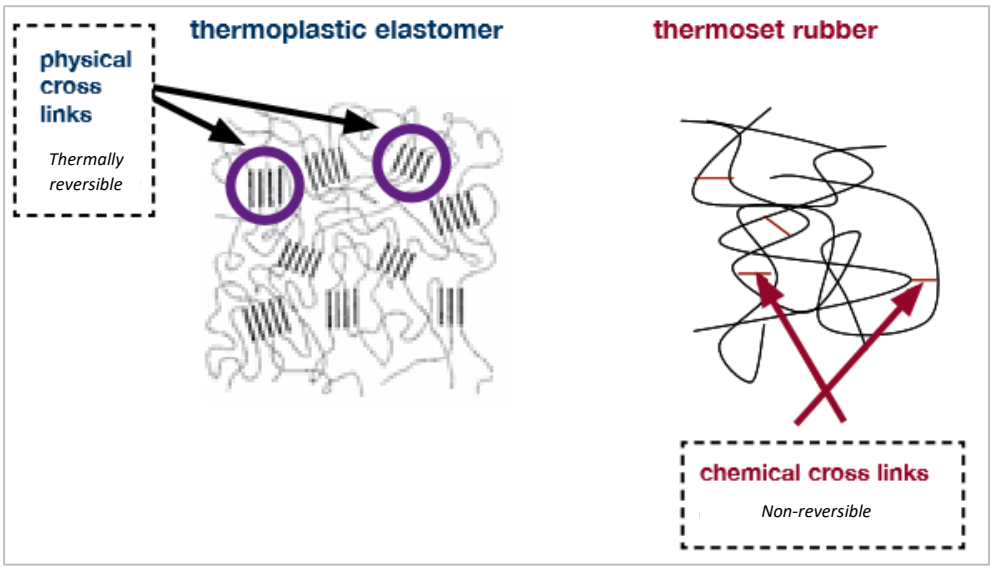

Figure 13: Differences between thermoplastic elastomers and thermoset rubbers. Reprinted from: (Huntsman, 2010).

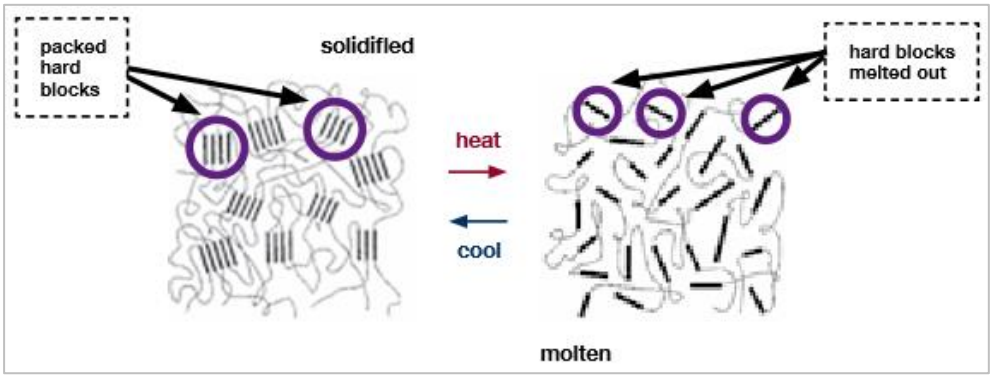

Figure 14: Solidified and molten polyurethane. Reprinted from (Huntsman, 2010).

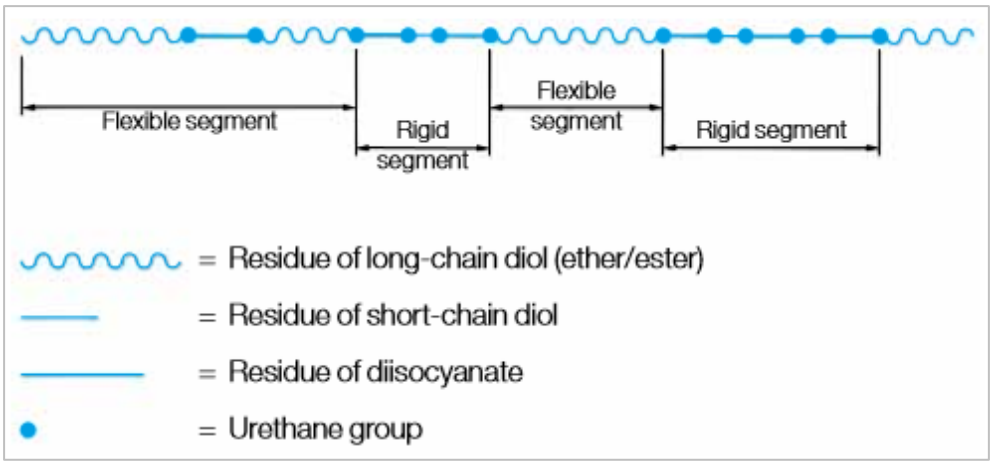

Figure 15: Structure of thermoplastic polyurethane. Reprinted from: (BASF, 2011).

2.2.2. Young's Modulus of PU in compression

As mentioned before, the mechanical properties highly depend on the mixture used while manufacturing the polyurethane. Generally, the Shore durometer scales are used to classify PU. Depending on this Shore hardness the material acts either similar to a rubber or a plastic. The range of possible cast urethanes is visualised in a schematic by manufacturer *Precision Urethane*, here shown in Figure 16. The polyurethane however remains an elastomer, keeping its elastic properties even for higher hardness values (up to 50 Shore D), which is unlike any other elastomers (Wright & Cumming, 1969). A lower Shore A (ShA) hardness can be achieved by other production techniques than casting.

The hardness of a material is its resistance to indentation and is measured with standardised tests. In theory the hardness can be calculated into a Young's modulus when in compression, as described by Johannes Kunz and Mario Studer in *Kunststoffe International* (Kunz & Studer, 2006). Tests are performed on different polymers, of which three are polyurethane. Each specimen has a thickness of 6 millimetres, conform standardised tests. The following formula is derived from these tests:

$$E_{PU;C} = \frac{1-\upsilon^2}{2*R*C_3} * \frac{C_1+C_2*Sh_A}{100-Sh_A} * (2.6 - 0.02 * Sh_A) \quad [MPa] \qquad [\ 2.4\ ]$$

In which $E_{PU;C}$ is the Young's Modulus of PU in compression [MPa]; υ is the Poisson's ratio [-]; ShA is the Shore A Hardness. The constants R, C_1, C_2, C_3 have the following values: R = 0.395 mm, C_1 = 0.549 N, C_2 = 0.07516 N, and C_3 = 0.025 mm and are derived from the Shore A test set up.

The article furthermore states that the minor effects of friction and deviations from the ideal Poisson's value (υ = 0.5) have sufficient small effects that they can be neglected. For other effects a correction factor is introduced, which is the last factor in Equation 2.4 (Kunz & Studer, 2006). The effect of thickness was also evaluated with minor deviations when increasing the thickness. No tests were performed using smaller thicknesses.

As smaller thicknesses than six millimetres will be used for the interlayer, other literature is consulted concerning the effect of smaller thicknesses on the Young's modulus. Bassi et al. (1987) states a reduction or increase of the Shore A value should be applied when using different thicknesses of polymers. Their correction diagram is given in Figure 17. It indicates smaller deviations when increasing the thickness, which would have merely a small effect on the Young's modulus as was also concluded in Kunz & Studer (2006). However, for smaller thicknesses the deviations are considerably larger, up to a reduction of six Shore A hardness when a two-millimetre 52 Shore A polymer is used.

Furthermore it is important to keep in mind that the above mentioned method merely regards compression by a standardised peak pressure on a polyurethane disk. When applied in a cast glass masonry system the material is restricted to deform under compression. Wright and Cumming (1969) therefore introduce a shape factor, which essentially is the ratio between one stressed area to the areas that are free to bulge out. For a rectangular object (l x w x t) this is equal to:

$$S = \frac{l*w}{2*t*(l+w)} \qquad [\ -\ ] \qquad [\ 2.5\ ]$$

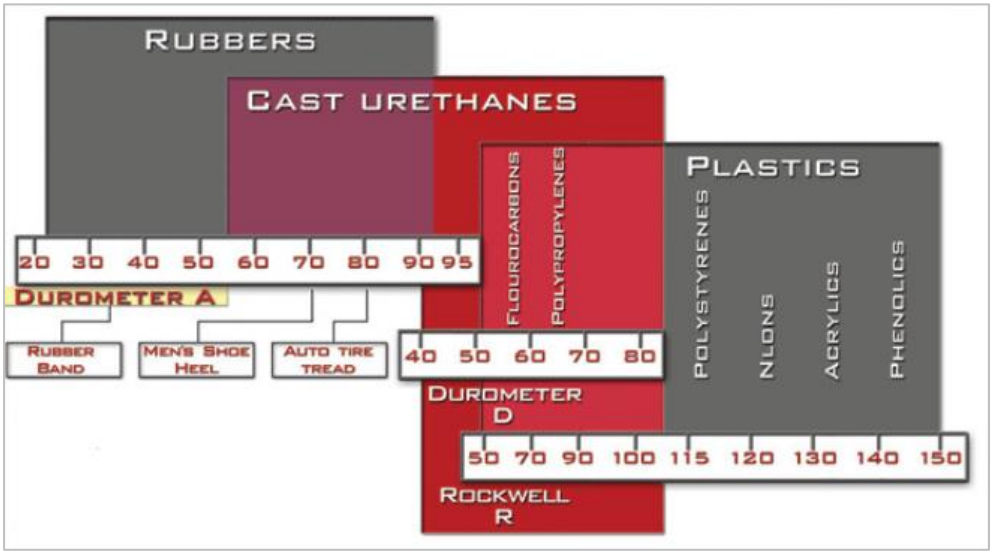

Figure 16: Hardness scales of rubbers, cast urethanes and plastics. Reprinted from (Precision Urethane, n.d.).

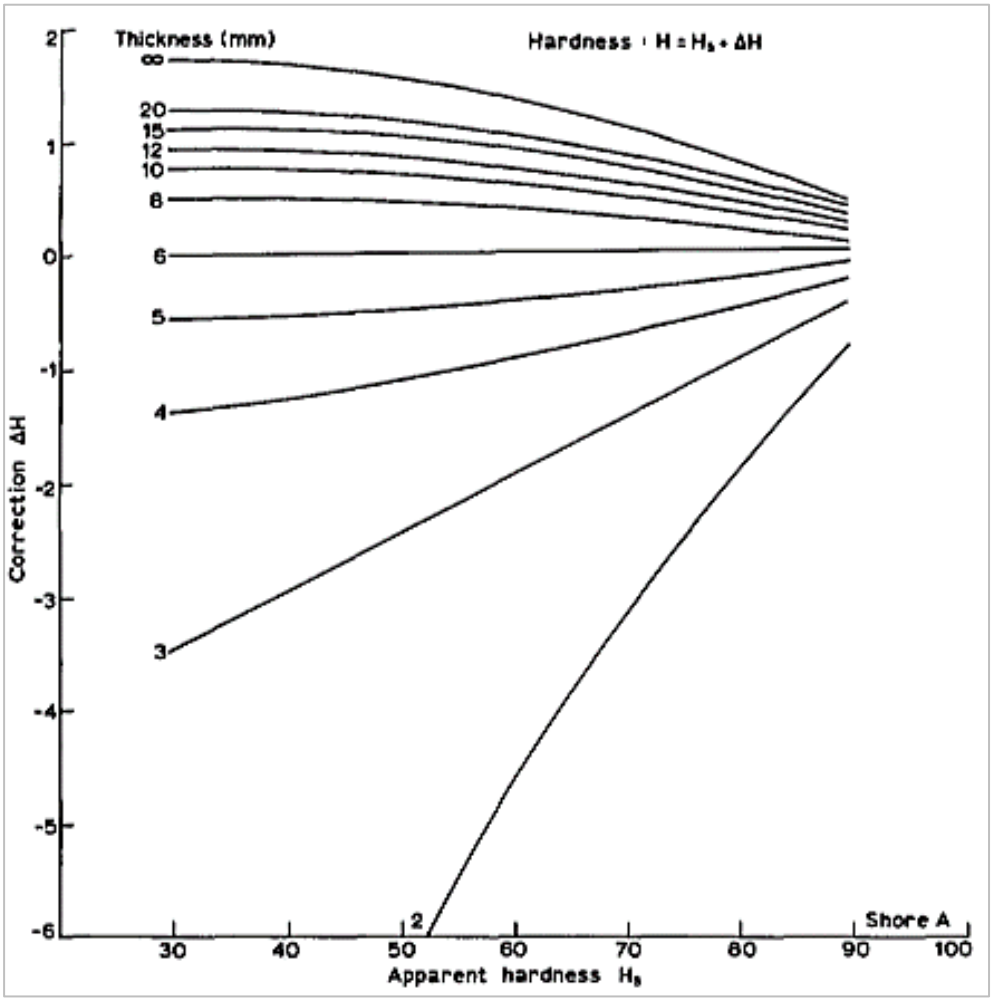

Figure 17: Correction diagram for a reduction or increase in hardness when using different thicknesses than 6 millimetres. Reprinted from (Bassi, Casa, & Mendichi, 1987)

This shape factor can then be used to incorporate incompressibility. Using Equation 2.7 the shape factor is incorporated into the recalculation of the Young's modulus for compression (Wright & Cumming, 1969). This shape factor is only applied when in compression, hence also the introduction of the minus sign (compare Equations 2.6 and 2.7).

$$f_t = G(\lambda - \lambda^{-2}) \qquad [\text{ MPa }] \qquad [\text{ 2.6 }]$$

$$f_c = -G(\lambda - \lambda^{-2})S \qquad [\text{ MPa }] \qquad [\text{ 2.7 }]$$

In which *f* is the stress applied on the non-deformed cross-section; G is the shear modulus; λ the ratio between the deformed thickness and the original thickness (defined in Equation 2.8); and S is the earlier mentioned shape factor (see Equation 2.5) (Wright & Cumming, 1969).

$$\lambda = \frac{t - \Delta t}{t} \qquad [\text{ MPa }] \qquad [\text{ 2.8 }]$$

The new Young's modulus incorporating the shape factor is found by determining the slope of Equation 2.7. Essentially, this slope is then equal to the Young's modulus. Hence its derivative is given in Equation 2.9.

$$E_{PU;c;S}(\lambda) = \frac{df_c}{d\lambda} = G(1 + 2\lambda^{-3})S \qquad [\text{ MPa }] \qquad [\text{ 2.9 }]$$

When λ is approximately 1 it can be seen that the Young's modulus near the origin is equal to 3*G*S. With the predicted deformation ratio under a certain given load (filling in fc, G and S into Equation 2.7) the new Young's modulus can be calculated in Equation 2.9.

To validate that this method of determining the compression Young's modulus is a realistic approach the method is applied on data from earlier researches. Compression data on polyurethane pieces is fairly rare in literature, generally tensile tests are applied as many applications of PU require sufficient tensile strength or elongation capacity. Some compression tests concerning PU have however been performed in previous theses by Haarhuis (TUe) and Aurik (TU Delft).

In Haarhuis (2010) cast PU elements were used as spacers for a glass structure. The elements were casted using a PUR480 resin from Intercol bv, which have a hardness of 30 Shore D (Intercol bv, 2017) (which is equivalent to 85 Shore A, see Figure 18). The average Young's modulus was 12 MPa for the smaller specimens (l x w x t = 10 x 10 x 5, S=0.5) and 18 MPa for longer specimens (l x w x t = 10 x 80 x 4.5, S=1.0). The specimens were then loaded until failure. The Young's moduli found were at a stress between 0 and 1.5 MPa (Haarhuis, 2010).

Using the methods described above a reduction of approximately 0.25 ShA could be applied for both thicknesses, which would result in a Young's modulus $E_{PU;c}$ of 15.6 MPa in accordance with an 84.75 Shore A polyurethane. Taking into account the shape factors the Young's modulus are $E_{PU;c;S=0.5}$ = 6.99 MPa and $E_{PU;c;S=1.0}$ = 12.04 MPa for respectively shape factor 0.5 and 1.0. Results are shown in Table 3.

The undershoot can be explained by the quadratic term in Equation 2.8, the calculated slope therefore is different from the linearly determined Young's modulus in the thesis. A linear approach (E=σ/ε) yields closer values to the results, respectively E = 9.38 MPa and E = 17.14 MPa for shape factors 0.5 and 1.

In Aurik (2017) a cast glass bridge has been designed, with arched bricks combined with a polyurethane interlayer. The Young's modulus of the interlayer sheets was determined in an experimental test on the compression of several bricks and interlayers. Two different

interlayers were applied, PU70 and PU90 (Shore A hardness), each with thicknesses ranging from one to four millimetres. The contact area of the glass and interlayer sheets were further identical for all test setups (l x w = 210x210mm). The specimens were loaded with a compressive force of 480 kN, which results into an applied stress of f_c=10.88 MPa (Aurik, 2017). Much higher Young's moduli were found, which could be attributed to the shape factor taking into account the incompressibility of the PU.

The expected Young's modulus according to the previous described method is presented in Table 4. The hardness was corrected due to the lower thicknesses than six millimetres and the initial Young's modulus was calculated for each thickness and hardness. Due to the small thicknesses and large contact areas the shape factors are relatively high. Still the results for both quadratic and linear predictions deviate significantly with the laboratory results. The predictions themselves seem closer with larger shape factors. This can be explained with the steepness of the compression stress – strain curve for higher shape factors. In Figure 19 diagrams are shown for this relation, including the effect of several different values of the shape factor. If the shape factor increases even more than the displayed values (as is the case with thin interlayers), it would increase the steepness of the curve ever more until it approaches linearity.

Due to the limited data available (each interlayer was tested once) and various other complications, it is difficult to draw conclusions from these results. The contact area was proven to be smaller than presumed in the calculations, especially in PU90, where the 1 and 2 millimetres samples had a contact area with less than 50% contact (hence probably the overshoot in estimated moduli). Furthermore, by stacking multiple glass blocks and interlayers the experiments had an increased chance in providing deviations or errors. Moreover, the PU interlayers were not cast by Aurik himself, but manufactured elsewhere. The deviating result of PU90 t = 3 mm he claimed could be due an inconsistent composition of the material (Aurik, 2017). The shape factor moreover might need an extra slenderness correction factor, as in very thin layers the actual bulging out area is smaller than the value taken into account.

In conclusion, the Young's modulus of PU in compression can be assumed linearly for very small deformation (Haarhuis, 2010) or for very large shape factors (Aurik, 2017). For smaller values of the shape factor a linear prediction seems adequate, while for larger shape factors the predictions undershoot the experimental results. This could be due to an overestimation of the area that can bulge out, which is very limited in thin interlayers.

Furthermore it is important that when using the material PU in practise it always should be evaluated extensively in the laboratory. Each mixture has its own properties and each applied thickness influences the Young's modulus significantly.

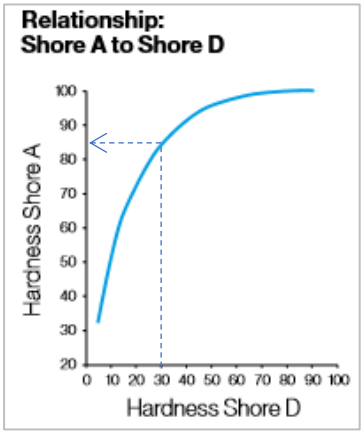

Figure 18: Relationship between Shore A and Shore D. Reprinted from (BASF, 2011).

Table 3: Comparison calculated Young's modulus with laboratory results of Haarhuis (2010).

Specimens	S [-]	E_{tests} [MPa]	$E_{PU;c;S}$ [MPa]	E_{linear} [MPa]
10x10x5	0.5	12	6.99	9.38
10x80x4.5	1	18	12.04	17.14

Table 4: Comparison calculated Young's modulus with laboratory results of Aurik (2017).

Specimens PU70	ΔShA	$E_{PU;c}$	S [-]	E_{tests} [MPa]	$E_{PU;c;S}$ [MPa]	E_{linear} [MPa]
210x210x1	-6*	7.46	52.5	-	415	403
210x210x2	-3	8.10	26.25	254	235	224
210x210x3	-1.5	8.45	17.5	315	171	159
210x210x4	-0.75	8.63	13.125	336	137	125
Specimens PU90						
210x210x1	-2*	19.04	52.5	185	1022	1007
210x210x2	-1	20.49	26.25	162	563	488
210x210x3	-0.5	21.31	17.5	516	395	383
210x210x4	-0.25	21.76	13.125	428	308	296

*no data available, determined by using trend of other thicknesses.

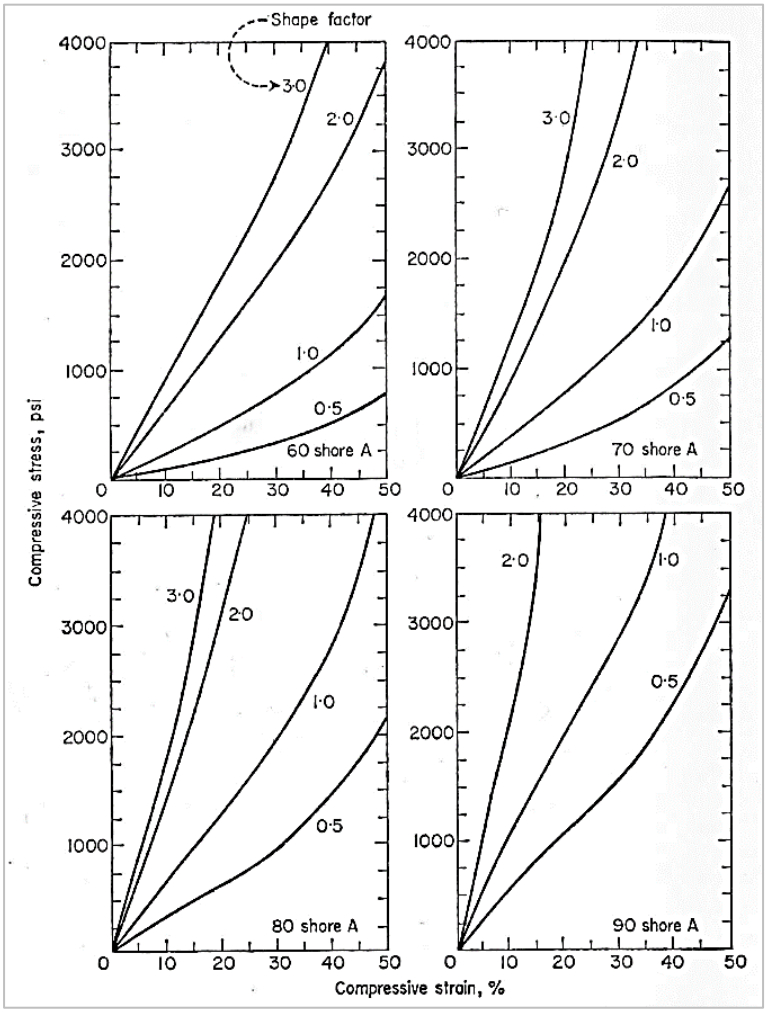

Figure 19: Influence shape factor on the compressive stress-strain diagram for various values for the Shore hardness. Reprinted from (Wright & Cumming, 1969).

2.2.3. Friction and Poisson's ratio of PU

In order to model the polyurethane properly, it is important to review some other properties of PU. Most importantly the friction angle, Poisson's ratio, and the density of PU.

Friction coefficient

The friction coefficient can be defined as the resistance of a material's surface to the sliding of another surface of the same or another material, in this case the friction coefficient between glass and PU. Considering PU as an incompressible elastomer, it is assumed to be comparable to rubbers. However, it is important to mention that the behaviour of a certain hardness of polyurethane should be tested in a laboratory, before applying in practise.

Experimental and numerical test results published in *Nature* by Tuononen (2016) could offer a base for a realistic value of the friction coefficient.

The experimental set up is given in Figure 20, and consists of a rubber element moving on a glass plate, observed by a high-speed camera and a force sensor. The results of the test are shown in Figure 21. There is no clear static friction coefficient, concluded by the absence of a peak value before complete detachment and full sliding. The dynamic friction coefficient can be set to μ_d = 2.0, determined from the converging curves in Figure 21. The middle of the contact area is last to detach, as is shown in Image 5 of Figure 21.

Comparing the experimental results to the numerical tests (setup in Figure 22), the contact pressure C_p concentrated in the centre of the model may explain this (see Figure 23). As detachment is initiated both contact pressure and shear stress increase on the right-hand-side of the sample, while the contact pressure in the centre remains. As there was no distinctive peak in the experimental phase, the friction coefficient input for the numerical model was $\mu = \mu_s = \mu_d = 2.0$.

Assuming the rubber applied in the article is representative for all elastomers, it can be concluded that $\mu = 2.0$ is a valid input for the friction coefficient. For practical use of the future interlayer this however should be validated with experimental tests.

Poisson's ratio

The interlayer in a masonry system will be subject to shear and mostly compression. Therefore it is important to take its incompressibility into account. This basically means the material is rigid when compressed and can only deform while retaining its volume. Any change to its shape will therefore result into bulging out of material where it can. The more it is restricted the less it will therefore deform.

Generally speaking all elastomers behave this way, however polyurethane retains these properties even for higher values of the hardness, making it so applicable for a wide range of applications (Wright & Cumming, 1969). Its Poisson's ratio can therefore be set to $\nu = 0.5$, which indicates incompressibility. To accommodate a small amount of compressibility the Poisson's value can be assumed slightly lower, for instance 0.48 or 0.49. The error in stress for $\nu = 0.48$ would be 2% for a compression strain of 0.5 and 4% for a compression strain of 1.0. For $\nu = 0.49$ the error would be even smaller, 1% for a strain of 0.5 and 2% for a strain of 1.0 (Qi & Boyce, 2005).

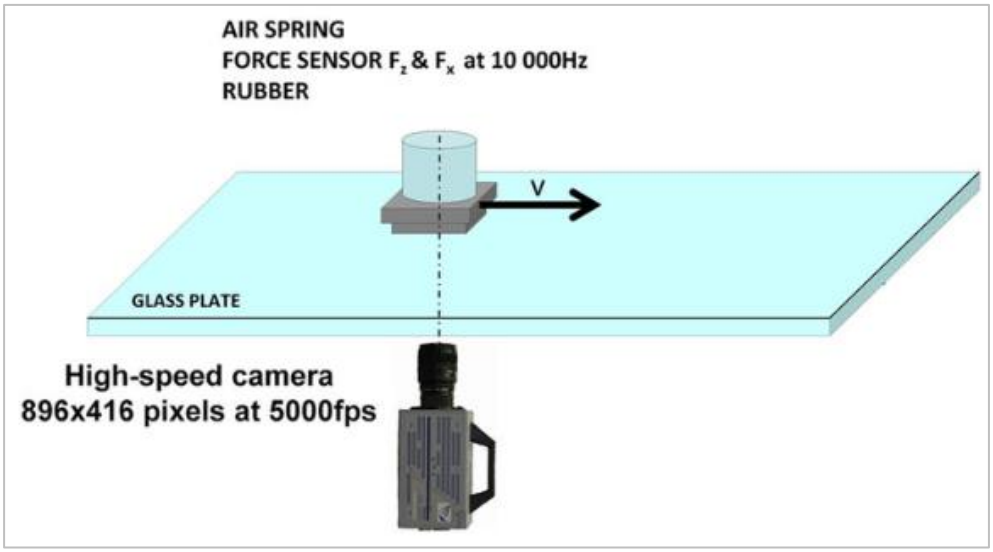

Figure 20: Experimental setup of a rubber element sliding over a dry glass plate observed by a force sensor and high-speed camera. Reprinted from (Tuononen, 2016).

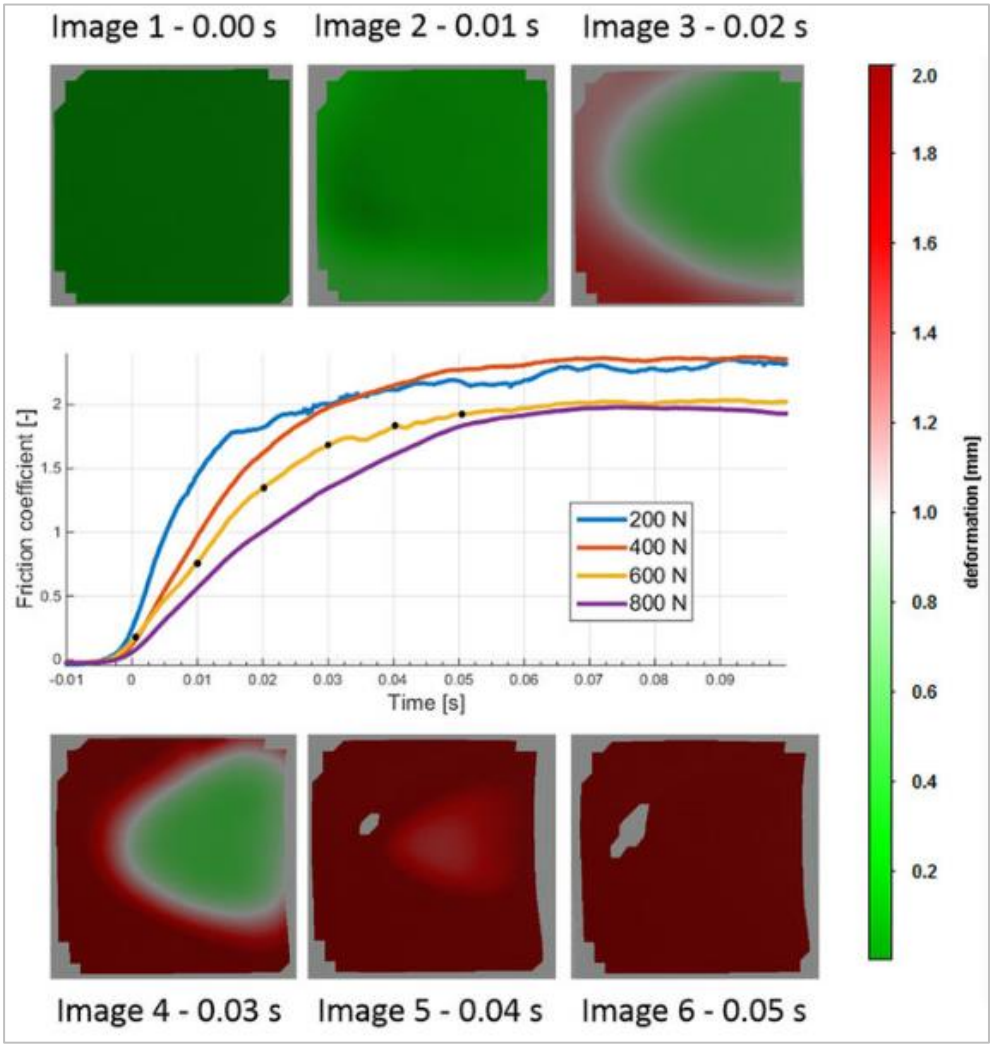

Figure 21: Experimental test results of a rubber element moving on a glass plate. Red areas show detachment of the rubber from the glass, snapshots are made on the black dots along the 600N-curve. Reprinted from (Tuononen, 2016).

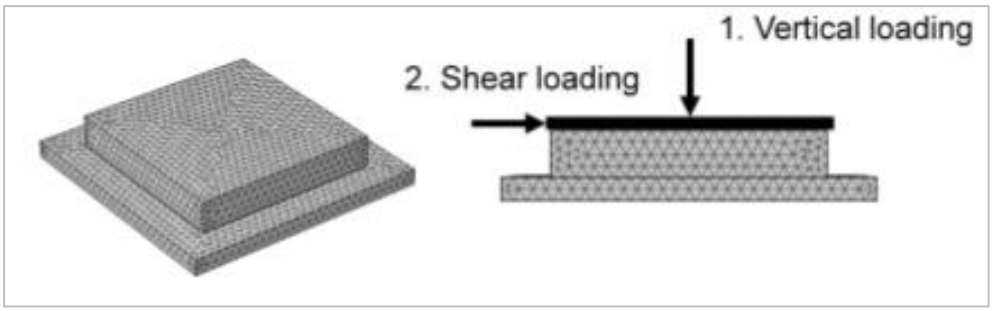

Figure 22: Numerical setup of a friction test of rubber on glass. Reprinted from (Tuononen, 2016).

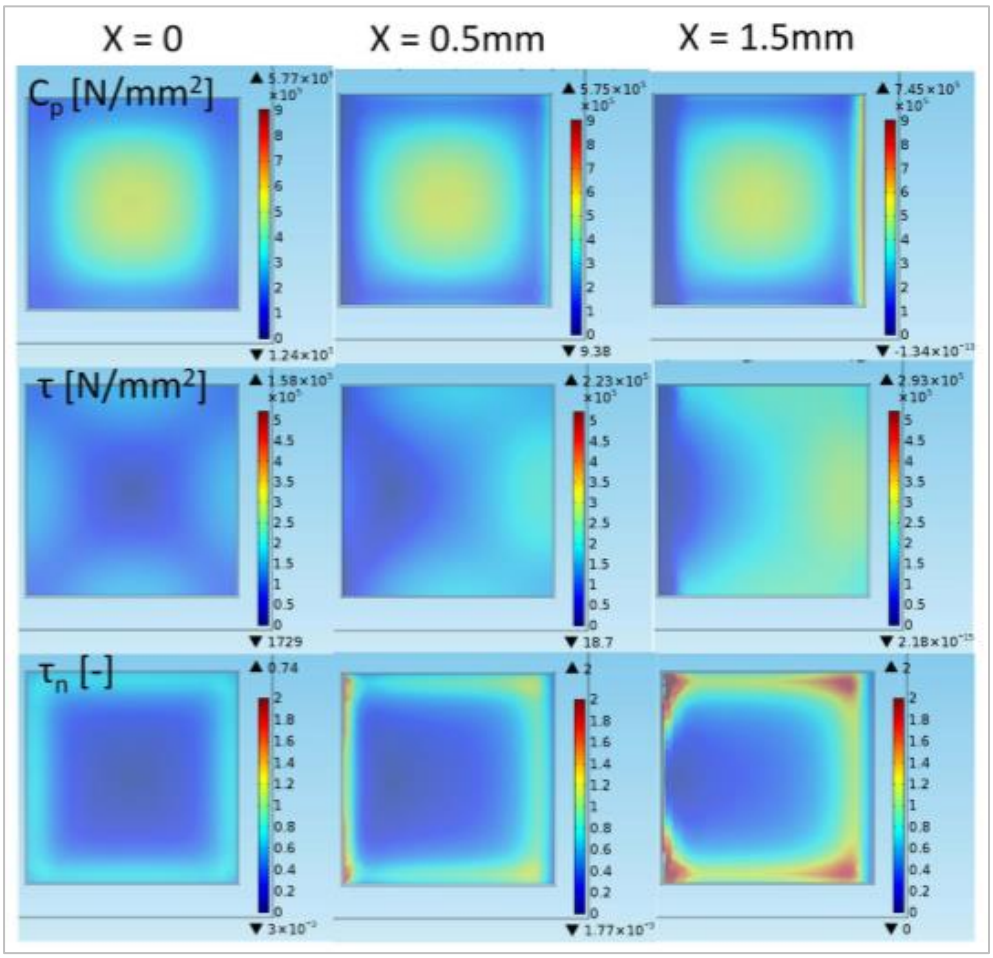

Figure 23: Numerical results of initiating detachment for μ=2.0, with Cp = contact pressure; τ = shear stress and τ_n= normalized shear stress. Reprinted from (Tuononen, 2016).

Section 2.3. Interlocking systems

Traditional masonry systems require an adhesive bond to achieve structural integrity. Without this bond the structure would be merely reduced to a pile of bricks when subject to most load conditions. It is hence the bond that makes a masonry wall successful structurally.

However, it comes with certain disadvantages. The adhesive bond binds the materials together, making it more difficult to reuse or recycle them, due to contaminations induced by the binding material. Especially in glass structures, using a material that is unlimitedly recyclable, a non-adhesive bond could not only clear a better path for recycling, it would even open the door for reusing the elements used.

Another disadvantage of an adhesive bond between glass elements is the low tolerance of deviations in the geometry, due to a very thin adhesive layer. In traditional masonry this problem is solved by applying a thicker viscous interlayer that can adapt to the geometry before hardening.

A solution to these problems might be provided by interlocking systems. The structural integrity in these systems solely rely on the combination of their function, geometry, boundary conditions and loading conditions. Shear forces between elements can be solved using **shear locks**, or by increasing the weight of the structure to increase **friction**. The boundary conditions describe the degrees of freedom the elements in the structure have.

To illustrate that these principles apply to all interlocking systems, a few systems will now be evaluated considering their function, geometry, boundary conditions and loading conditions.

2.3.1. Incan structures

Function:	*Load bearing walls*
Geometry:	*Tapered walls with trapezoid rock hewn bricks*
Boundary conditions:	*Foundations, previous upper structure*
Loading conditions:	*Wind, earthquakes, dead weight*

The Incas already used interlocking brickwork in their structures. By use of an interlocking system, and the use of tapered walls, the structures have a high resistance against earthquakes, making them last past many earthquakes the last 500 years (Cartwright, 2014). The trapezoid shape of the walls allows for greater stability and the heavy stones were held in place by their own weight and the weight of the stones in higher layers. Failure occurs when one of the boundaries of the system fails, for instance key stones that get removed or settlements in the soil, as can be seen in Figure 24.

Most of these ancient systems were severely over-dimensioned, and therefore it was easy to convey external loads, as they were relatively small in comparison with the weight of the walls. The Incan dry interlocking system moreover proved very resistant against earthquakes. A dry interlock system has certain damping properties as small movements are allowed, while masonry walls that are mortared, act like one monolithic system with no allowance for movements or damping properties.

Nowadays over-dimensioning can be reduced, as new developments make it possible to make more effective designs, reducing materials and cost. Structures as the Incan walls would be too time consuming and costly to apply nowadays. Therefore, current interlocking systems feature a uniform solution, applying a singular geometry for all its bricks or by having a flexible production technique such as 3D printing.

The Incan method for instance served as an inspiration for earthquake resistant columns, consisting of 3D printed interlocking elements made of sand. Due to its dry connection, it yields more resistance to earthquakes than when it would have been connected by mortar. Using hollow blocks increase assembly ease (MacLeod, 2014). 3D printed elements allow for more freedom in shape as it can be printed freely without the use of expensive moulds. Therefore, one can create a system of many differing geometries.

2.3.2. Masonry interlocking system

Function: *Load bearing walls*
Geometry: *Masonry bricks with shear keys*
Boundary conditions: *Foundations, upper structure*
Loading conditions: *Wind, dead weight, shear*

An example of a singular geometry structure is the masonry system shown in Figure 26. Using a singular design for all bricks allows it to make more slender structures than for instance done by the Inca. In order to properly convey the loads, shear locks have to be introduced in the geometry. These then also become prone regions in the design, as is depicted in Figure 26b. In-plane shearing then becomes an important failure mechanism. Due to the lower mass of the structure and loads other than its dead weight a key stone or reinforcement should be added to prevent uplifting of the upper brickwork.

The main reason for using an interlocking masonry system is faster assembly and earthquake resilience. Dry connections are beneficial due to the absence of curing the mortar, which decreases assembly time and therefore costs (Ali, Gultom, & Chouw, 2012).

Especially in earthquake prone regions these bricks might offer a solution, as the system is more resilient due to damping induced by the brickwork. The bricks designed by Ali et al. (2012) are one possible geometry for interlocking brickwork. This design also includes coconut fibre ropes as reinforcements throughout the height of the structure. During dynamic tests both structures with and without rope reinforcement were tested. The rope reinforcement made the structure stiffer, reducing relative uplifting of singular bricks, but having less damping properties than the structure without rope reinforcement (Ali, Briet, & Chouw, 2013)

2.3.3. Extra-terrestrial osteomorphic interlocking bricks

Function: *Load bearing walls, floors etc*
Geometry: *Masonry bricks with sinusoid shear keys*
Boundary conditions: *All boundaries*
Loading conditions: *Wind, dead weight*

Another potential application is the construction of extra-terrestrial structures. The osteomorphic blocks, as shown in Figure 27, can be created in situ and due to dry assembly no water is needed. The convex contact surfaces prevent high stress concentrations and give the stone self-adjusting properties (Dyskin, Estrin, Pasternak, Khor, & Kanel-Belov, 2005).

Dyskin et al. (2005) designed the bricks as a study to possible construction techniques on other planets. By forming the bricks from material available and by the absence of any interlayer or adhesive, the only thing needed to be transported from Earth would be the machines making the brickwork.

2.3.4. Interlocking system design principles

From previous examples the following design principles can be determined:

- Geometry design follows from function, boundary conditions and loading conditions;
- When using a singular design shear keys will be necessary, as well as key stones or reinforcement;
- Convex contact areas give self-adjusting properties as well as reduced stress concentrations;
- Failure occurs either in a global way (boundary or loading conditions failure) or locally (in the weaker spots of the brick design, for instance shear keys).
- Interlocking systems have damping properties when dry connected.

Figure 24: Inca megalithic interlocking stone walls (a), boundary induced failure (b). Reprinted from (Cervera, 2016).

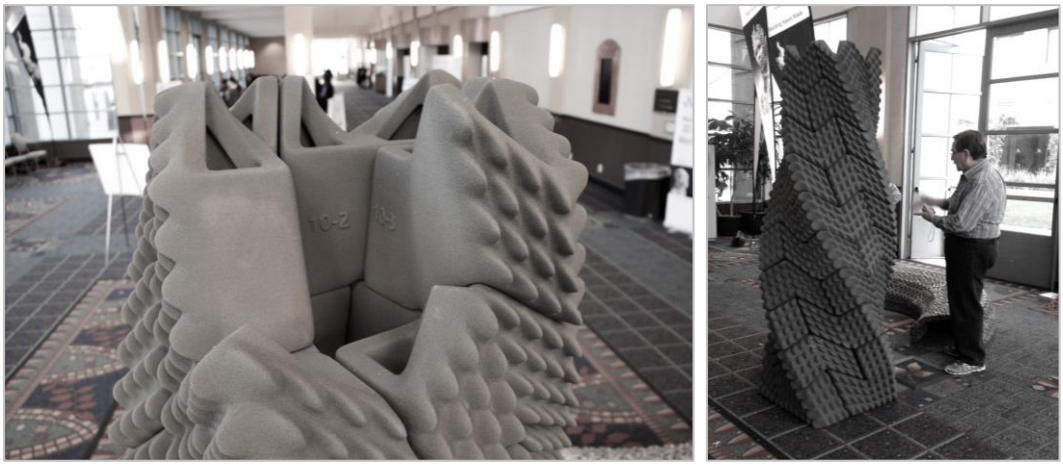

Figure 25: Interlocking 3D printed elements, designed to withstand earthquake based on Inca masonry interlocking systems. The slight in-plane angle combined with the interlocking system and no mortar interlayer increases the structural resistance against earthquakes. Reprinted from (MacLeod, 2014).

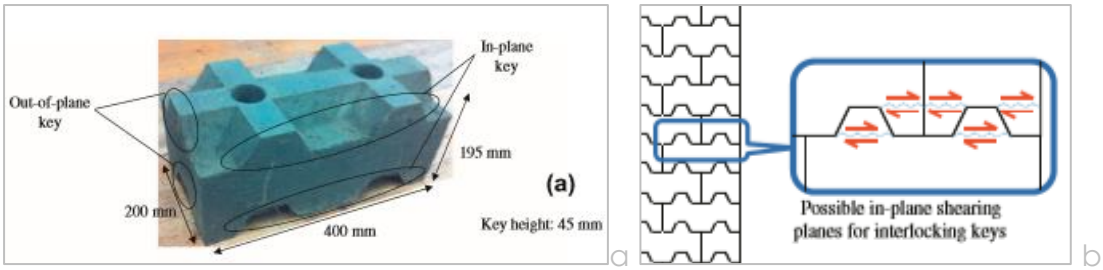

Figure 26: Interlocking brick with vertical reinforcement channels (a), possible shear failure (b). Reprinted from (Ali, Gultom, & Chouw, Capacity of innovative interlocking blocks under monolithic loading, 2012).

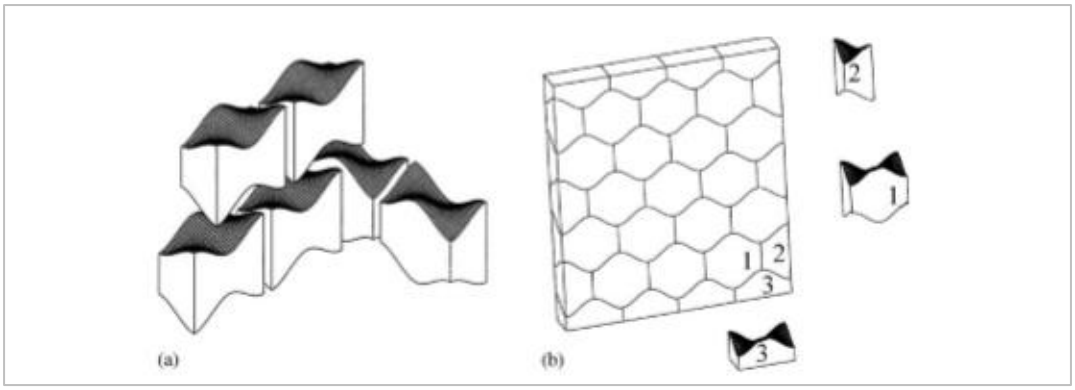

Figure 27: Topological interlocking bricks, as developed as potential extra-terrestrial construction technique. Reprinted from (Dyskin, Estrin, Pasternak, Khor, & Kanel-Belov, 2005).

Chapter 3.

Case Study: Lichtenberg Castle

In restoration, the first step is always to gather information from literature, drawings, and paintings. For a ruin like the Lichtenberg Castle tower it is especially important to gain insights in the original structure and to acquire knowledge considering potential causes for destruction. Both influence the restoration and consolidation method.

This chapter hence puts the ruin in a historic perspective and evaluates its current and former shape, both with respect to restoration and structural consolidation.

Castle Lichtenberg in 1670 by Valentijn Klotz. Reprinted from (Delemarre, 1966a)

Section 3.1. History of Lichtenberg Castle

The history of Lichtenberg Castle is for large parts unknown, yet the known historical events in the region indicate times of hardship and misfortune. The castle must have seen turbulent times and changed many a time of hand.

This section discusses the history of Lichtenberg Castle, starting with its origin and continuing with major events that might have had a hand in its destruction. Lastly images of the past are evaluated, in order to understand how the original castle used to look like.

3.1.1. The origin of Castle Lichtenberg

For fully grasping the importance of the castle one needs to understand the politics of the time in which it was constructed. Historian writer Perreau states that a "burgus" was constructed in 1212 by Hugo de Pierrepont, the then ruling prince-bishop of Liège (Sprenger, 1941). Therefore, the geopolitical state of the region in that time will be briefly discussed.

The Prince-Bishopric of Liège was at that time a sovereign state within the Holy Roman Empire. The political events leading up to the construction of the tower can be found in the book *"De Monumenten In De Gemeente Maastricht. Deel 1."* by *Van Nispen tot Sevenaer* (1974). It had gained the rights of coin and toll in Maastricht in the 10th century by the emperor of the Holy Roman Empire. The neighbouring state led by the Duke of Brabant however aspired full control of the trade route running from Ghent to Köln, and creating a closed Brabant territory. Gaining control of the city of Maastricht and its bridge passing the Meuse was essential for achieving this goal. The Duke foresaw problems with the Prince-bishopric of Liège and managed to install his own brother as bishop. When his brother got assassinated in 1192, the Duke gained control over the northern part of Maastricht through the German Holy Roman emperor Philips van Zwaben in 1204. This ensured the Duke's control over the region, including the before mentioned trade route. He then started to fortify his part of Maastricht by adding a wall protecting the highly valuable bridge crossing the Meuse.

The prince-bishop at the time, controlling the Liège part of Maastricht, was threatened by the increase of power of the Duke and saw the fortifications as an offense. He reacted by laying siege on the city in 1206 and managed to destroy the fortifications constructed by the Duke (Van Nispen tot Sevenaer, 1974a). The prince-bishop lost the siege as his part of the population could not put enough resistance against the Brabant residents (Sprenger, 1941). In the wake of the failed siege the prince-bishop decided to construct the tower, which later would be expanded and known as Lichtenberg Castle. Standing on top of Mount Saint Peter, it was a political statement of the prince-bishop to keep control in the region, as well as an overview of the river and the nearby city.

Furthermore, it is rumoured that the tower was built on top of the foundations of an old roman signalling post. It is viable as the city of Maastricht originated as a roman fortified encampment (Van Nispen tot Sevenaer, 1974a). It is known that the romans used such signalling posts on higher points to communicate, and they have been found elsewhere in the region. Its name is said to support this claim, argued to be derived from the Latin words 'Mons Lucis' (Sprenger, 1941). However, no evidence has been found so far, and perhaps future excavations will provide more answers. For now, this claim remains a theory.

3.1.2. Possible events leading to the destruction of Lichtenberg Castle

As the Middle Ages raged on, the tower was in the midst of various local historical events, many of which could have ravaged and destroyed parts of the castle. In chronological order, the more plausible events will be discussed in this subsection. The potential causes will later be evaluated in *Section 3.2. Potential causes of destruction*.

1267: Second Siege of Maastricht by Liège
In this siege prince-bishop Hendrik van Gelder of Liège attacked Maastricht, this time also destroying a fortified tower protecting the bridge crossing the Meuse (Van Nispen tot Sevenaer, 1974a). Possibly the knight that was currently residing in the Castle also participated in the siege, as this would have been an obligation from his lord. After the prince-bishop was abdicated he destroyed parts of the bishopric with flame and sword, it is unknown if the castle in Lichtenberg was involved in this matter (Sprenger, 1941).

1408: Fleeing of Bishop Jan van Beieren
In 1408 the bishop of Liège fell out of favour and had to flee to a more secure location, to hide from revolts in the bishopric. He fled to Maastricht and took refuge in its fortifications, in order to give his enemy no shelter and to see them coming from afar, he ordered the destruction of the whole village of St. Peter and the clearing of the nearby woods (Sprenger, 1941).

1465: Revenge after burning fleet of Huy
The villagers of St. Peter turned against the bishop when under Charles the Bold rebellions became a new standard. As Maastricht and Huy remained loyal to the bishop the villagers burned down the fleet of Huy, which was anchored at the Meuse and attacked the people of Maastricht. As revenge the Huy burned down the village, and declared it uninhabited from that moment on. It is unknown if the castle got damaged.

1568: Headquarters of Duke of Alba
At the start of the Eighty-Year War the Duke of Alba took headquarters in the Lichtenberg Castle (Van Nispen Tot Sevenaer, 1974b) when William of Orange revolted against the Spanish and tried to pass the Meuse for his conquest of Brussels. Alva did not let him pass and refused to be provoked into battle. This historical event is still sung in the 11th couplet of the Dutch national song, The Wilhelmus (Nederlands Maritiem Museum, 2017). It is unknown if the castle got damaged during this time. It is unlikely, as the armies never met at the castle, but in the hills surrounding Maastricht.

1632: Siege of Maastricht by Frederik Hendrik, Prince of Orange
During the siege of Maastricht by Frederik Hendrik, his colonel Pinsen van der Aa took Lichtenberg as his headquarters. From this siege many records exist and in Figure 28 a map is depicted from the collection of the Rijksmuseum. Figure 28a shows how heavily fortified not only Maastricht as a city was, but also its surroundings. One of these surroundings is the Lichtenberg Castle, depicted in Figure 28b. The letter G depicts the Quarter of Colonel Pinsen, the numbers depict the regiments under the command of the colonel. Other than these highly illustrative maps the piece of arts also features a detailed etching of the Lichtenberg Castle, which will be further discussed in subsection 4.1.3.

1673: Siege of Maastricht by King of France, Louis the XIV
Initially, when Louis the XIV attacked he passed through the Prince-Bishopric of Liège to attack the Republic of the Seven United Netherlands. In 1672 half of the village of St Peter, as well as a Spanish castle and nearby church were destroyed as they were blocking the line of fire. The stronger church tower was blown up with gunpowder (Van Nispen tot Sevenaer, 1974a).

1692: Earthquake Verviers
According to a study of earthquake risks in Flanders, an earthquake occurred in Verviers in 1692, with an estimated magnitude of 6.3 on Richter and damages ranging from scales VII-VIII on Mercalli near the epicentre, to scale VI in whole of Belgium and scale V in parts of France, Belgium, Germany and UK (Vanneste, et al., 2009).

1756: Earthquake Düren

The University of Cologne (2011) describes the earthquake of 1756 as the heaviest ever recorded in the German part of the lower Rhine area. With a Mercalli scale of VII-VIII numerous severe damages were recorded, especially near the epicentre, Düren, but also light damages were recorded as far west as Brussels. It moreover was mentioned in historical documents to be felt in London, Munich, and Amsterdam, underlining its magnitude. Damages near the epicentre were for instance failing masonry structures, falling chimneys and the collapse of mining shafts (Universität zu Köln, 2011).

Maastricht is located on the edge of the zone with the worst damages and therefore would have been subject to the earthquake with damaging consequences. Especially weak or instable structures would be vulnerable for large scale destruction. More about the earthquake risk and Mercalli scales is discussed in 3.2.3.

Figure 28: Part of a detailed map of the Siege of 1632, a) shows a heavily fortified Maastricht with fortified surroundings and b) zooms in on the Mount St Peter, indicating Castle Lichtenberg. Retrieved from Rijksmuseum, archive number RP-P-AO-16-127 (Visscher (II) & Cletcher, 1633)

3.1.3. Analysis of graphical representations of the castle

From before 1632 no graphical representations of the castle have been found during this thesis research. The earliest images found are those on strategical maps, more specifically maps depicting the siege of 1632. The castle in that time had already been expanded several times, and consisted of various towers and masses. Four of these images are shown in Figure 29. The quality of these small images of the castle are relatively poor, with exception of the one documented after the siege in 1633 (Figure 29d). In general some building masses can be recognised having a gabled roof, as well as two towers.

The map of 1633 also includes a detailed etching of the castle, which is one of the more valuable representations in determining which building mass is the nowadays ruin. This will be further discussed in 3.1.4.

Joris van der Haagen (1615-1669), member of an artist family and later dean of Saint Lucas Guild in The Hague (RKD, Joris van der Haagen, 2017), drew the castle from the other side, as is depicted in Figure 30. The round tower shows up in both drawings as the last building of the castle, as well as the larger masses with the gabled roofs. The structures in-between the round tower and the gabled roofed mass are not visible in Haagen's representation, however this could be due to the angle he chose to draw the castle in.

Valentijn Klotz (1650-1721) and Joshua de Grave (1643-1712) worked closely together in 1670 near Maastricht, and later would accompany Willem III and his State Army as engineers, to draw cityscapes and fortifications during the campaign against the French (RKD, Joshua de Grave, 2016) (RKD, Valentijn Klotz, 2016).

They both drew the castle around 1670, indicating the castle was still intact at the time. Their representation is given in Figure 31. All images indicate a crow-stepped gable of the larger building masses. The little tower is present as well, and in Figure 31a&b the smaller masses in-between the tower and the larger volumes are drawn as well.

The next representations are of Jan de Beijer (1703-1780), in 1740, which depict the nearby convent from two sides. This time the castle is half destroyed, and it seems that some building material is sticking out, as is shown in Figure 32a. The etching of de Beijer was also used in a topographic book, which is shown in Figure 32b&c. The original of the front view could not be retrieved in the databases.

Important to notice is that a significant part of the castle has disappeared. Only one of the crow-stepped gabled buildings remained, the other partially collapsed, with roof beams still sticking out. The cylindrical tower has disappeared, and the small volumes that connected it to the still standing gabled building is reduced to a mere ruin. An event between 1670 and 1740 therefore must have been the cause for this partial destruction.

These representations are the last that indicate the ruin differently from the shape it has nowadays. Currently the tower is part of a 19th century fortified farm. In 1939 the authorities for monument care let the farm be drawn up by one of their draughtsmen, which gives a detailed overview of how the farm has looked like over the last century. In Figure 33 the drawing of the farm seen from the inner courtyard is shown. Mind that both the ENCI and Steunbeer renovations have not been carried out here and that the staircase placed in 1904 is not shown here.

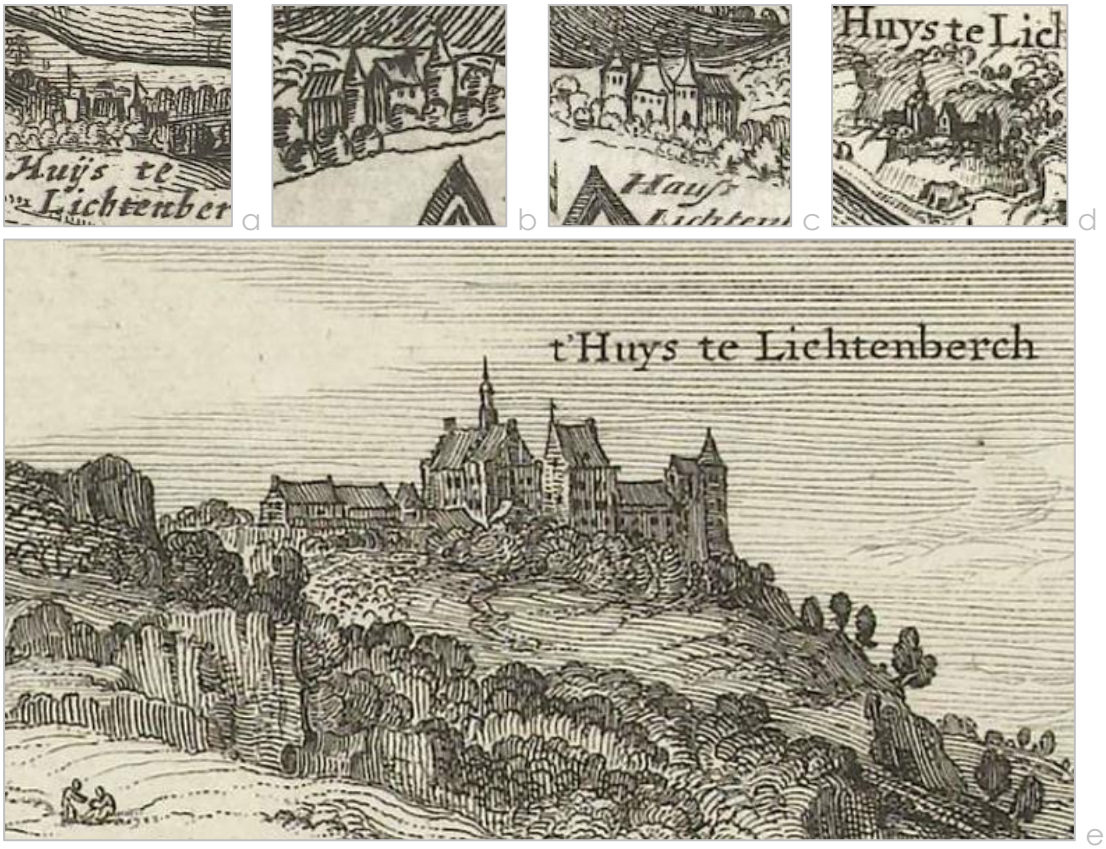

Figure 29: Castle Lichtenberg as depicted on strategical maps in the years 1632 (a,b,c) and 1633 (d,e). Reprinted from a; b (Anonymous, Belegeringe ende Overwinninge der Stercke Stadt Mastricht, 1652); c (Anonymous, Belegering van Maastricht, 1632); d & e (Visscher (II) & Cletcher, 1633).

Figure 30: Castle Lichtenberg as depicted by Joris van der Haagen in 1650. Reprinted from (Haagen, 1650).

Figure 31: Archived drawings from a) Valentijn Klotz (1670), Josua de Grave (1668),Val. Klotz (1670), Josua de Grave (166?) all showing extended masses and featuring a small tower. Adapted from respectively: (Delemarre, 1966a); (De Hoog, 1914a); (Delemarre, 1966b); (De Hoog, 1914b).

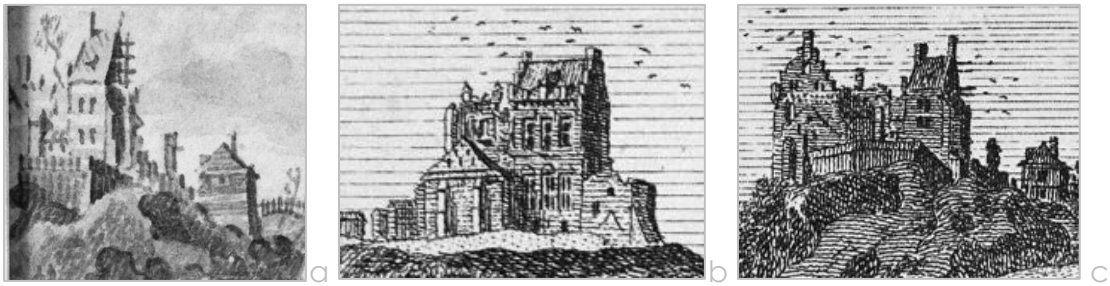

Figure 32: Representations of the castle in 1740; a) the original by Jan de Beijer (1740) and b & c) reproductions from both sides in a book of Spilman. Adapted from a) (Delemarre, 1966c); b & c (Spilman & De Beyer, 1740).

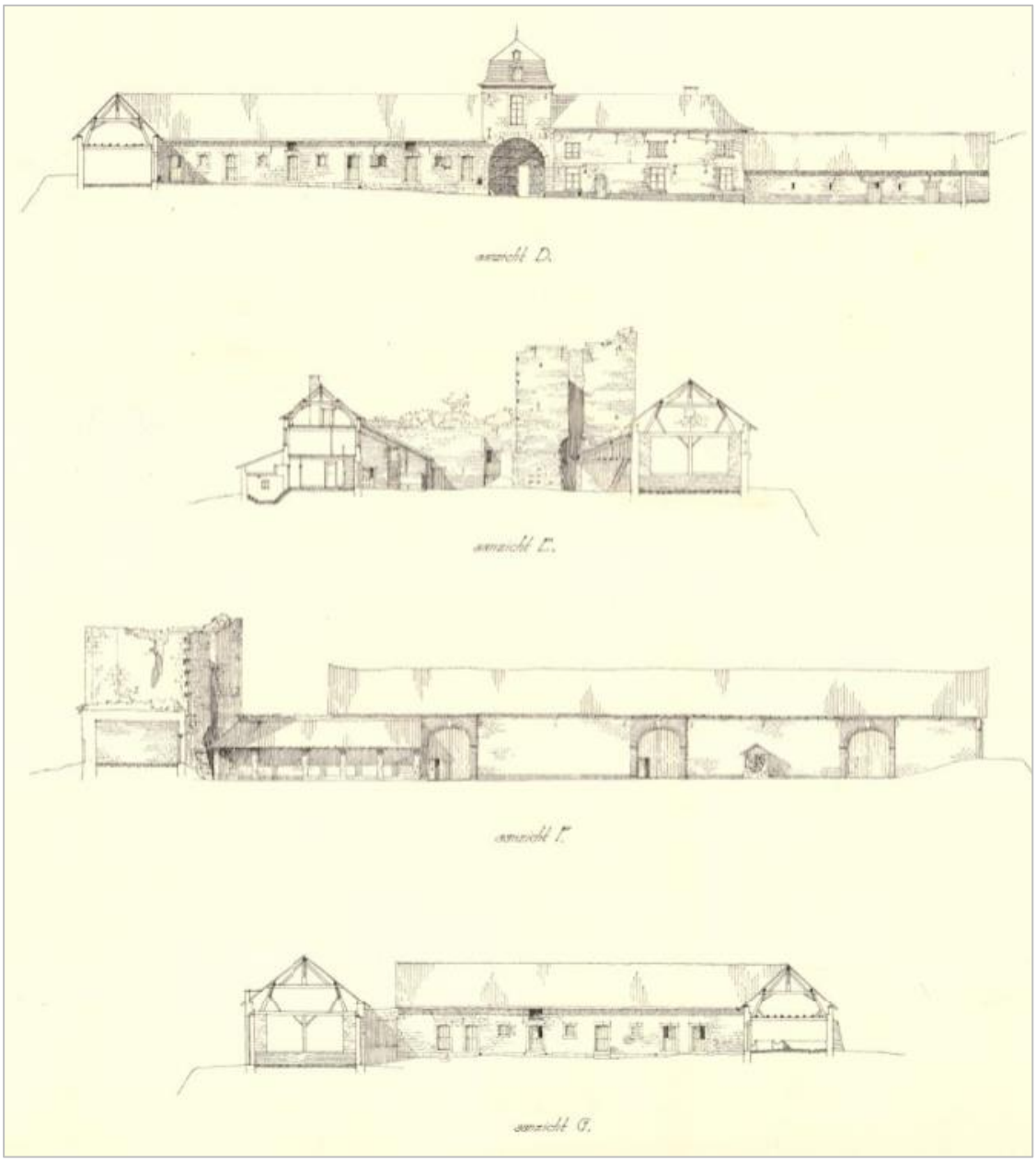

Figure 33: Drawing of the 19th century Lichtenberg fortified farm. Reprinted from (Verheus, 1939).

3.1.4. Determination of ruin in context of the castle

In the previous paragraph it is difficult to locate which building mass is the current day's ruin. For restoration purposes it is however important to know to which level a monument can be restored. Known details or structures can then be restored to its previous form where possible. This paragraph will therefore provide an analytical breakdown of the previous images to state a hypothesis about how the current buildings relate to the former castle. It is important to mention this is merely a motivated hypothesis, archeologic research is necessary in order to proof it.

Unrenovated state versus historical images

Due to prior renovations many details are lost in the nowadays ruin, however photographs in the beginning of the 20th century provide an insight in those details. The two most important images are shown in Figure 34. They display clearly how other structures previously were connected to the ruin. Hence it can be noted that the tower used to have adjacent structures in both the north and the east side (De Steunbeer BV, 2012).

On the eastern façade (Figure 34a) two diagonal lines can be interpreted as a former roof structure (marked yellow), the gaps below those lines indicating roof beams. In Figure 35a a drawing from the ruin in 1850 is shown. It features a smaller building with buttresses. It is smaller in scale than the imprint on the wall but that can be an artistic impression of the whole (as the distant buildings are also out of scale to make the view more imposing).

A small building also appears to be attached in a decoration of a war map in 1633, marked yellow in Figure 36. It seems different in shape with a pointier roof. It could therefore be an artistic impression or the predecessor of the buttressed building.

In any case the images seem consistent in direction and façade of the buttressed building. Hence it can be derived that the ruin was part of the larger step-gabled volume, which disappeared partly from the images before 1740.

More indications for this setting can be found on the northern façade (Figure 34b). There is a noticeable colour difference near the door openings of the ruin. This can be attributed to the fire that once occurred according to Sprenger (1941). Limestone colours orange when in contact with fire. It means that during the fire this part of the wall was protected. It is known that in 1740 (Figure 35b), one of the stepped-gabled wings was still intact, and in all previous images the two wings seem to touch in some way. These doors therefore probably were used to commute between buildings. Hence it can be deducted that the fire occurred before 1740 and that the spared wing protected this part of the wall from orange marks.

A diagonal mark can be seen which could indicate there used to be some sort of a roof structure. The indents in the wall then indicate where an attic floor might have been. Lower, another set of indents indicate another floor. This can be explained with Joris van der Haagen's representation of the castle, where the roof of one building is extended backwards (marked green in Figure 34b and Figure 37).

Joris van der Haagen also indicates two chimney-like structures. From details inside the ruin a former embedded flue is visible (marked orange in Figure 38a), which corresponds with the left-hand-side chimney in Figure 37. The other chimney-like structure then probably corresponds to cylindrical markings in the western wall, as shown in Figure 38b. Another possibility is that this would be the small rooftop tower, however that seems unlikely as in most pictures it is depicted in the middle of the roof, whereas in the ruin it is located far to the side of the building.

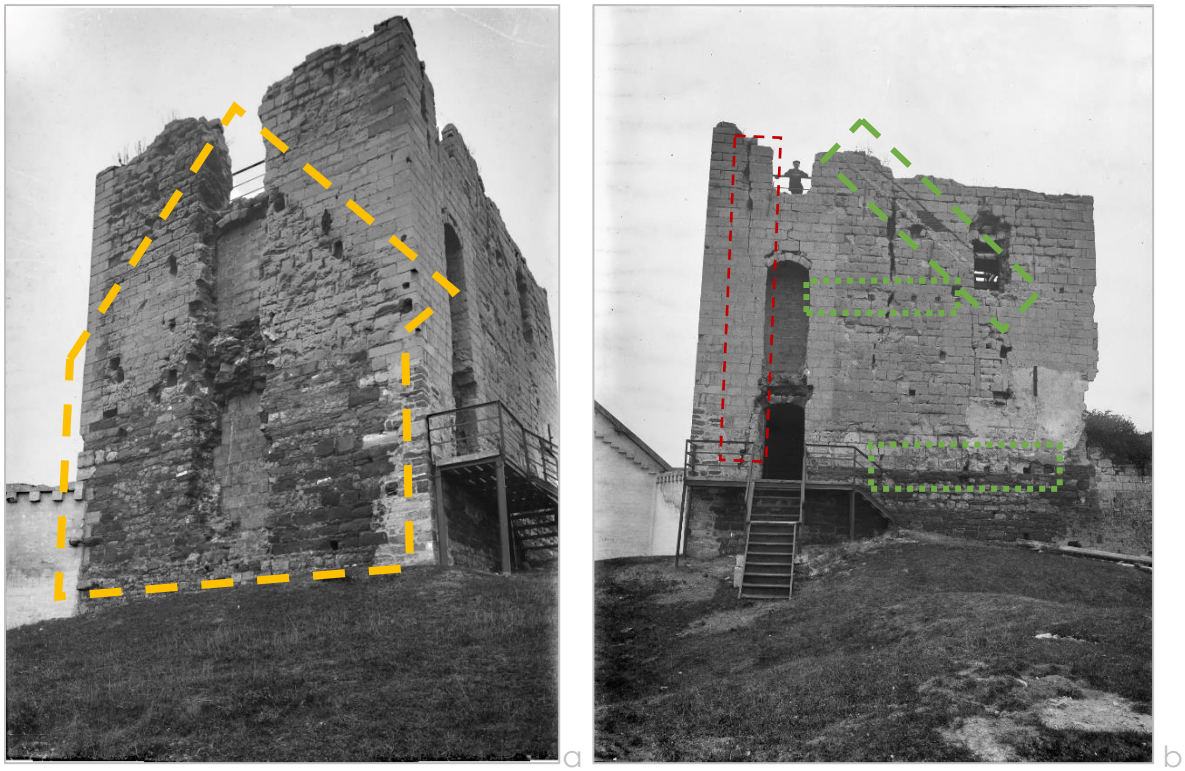

Figure 34: East (a) and north (b) side of the building. It clearly shows markings of former roof lines and cavities were beams used to be. These walls therefore also served as separation wall between two buildings and openings served as passages to different parts of the castle. Source says these pictures are taken in 1893, which cannot be as the inner staircase was firstly constructed in 1904 (Sprenger, 1941). Probably these pictures are therefore dated soon after the staircase was constructed. Adapted from a) (Anonymous, ruïne Ligtenberg, 1893a); b) (Anonymous, ruïne Ligtenberg, 1893b).

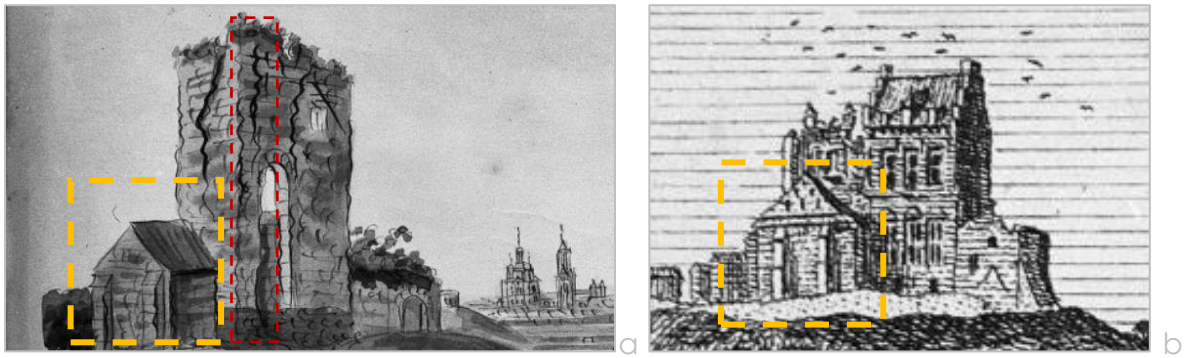

Figure 35: a) A reproduction drawing of the ruin in 1850 by Van Gulpen, featuring a small structure on the eastern side of the ruin which is quite out of scale compared to the markings shown in Figure 34; b) part of an etching by Hendrik Spilman in 1740 also shows the same buttressed building. Adapted from a) (Delemarre, 1958); b) (Spilman & De Beyer, 1740).

Figure 36: Decorative image from a decorative war map, also depicting a small building. Adapted from (Visscher (II) & Cletcher, 1633).

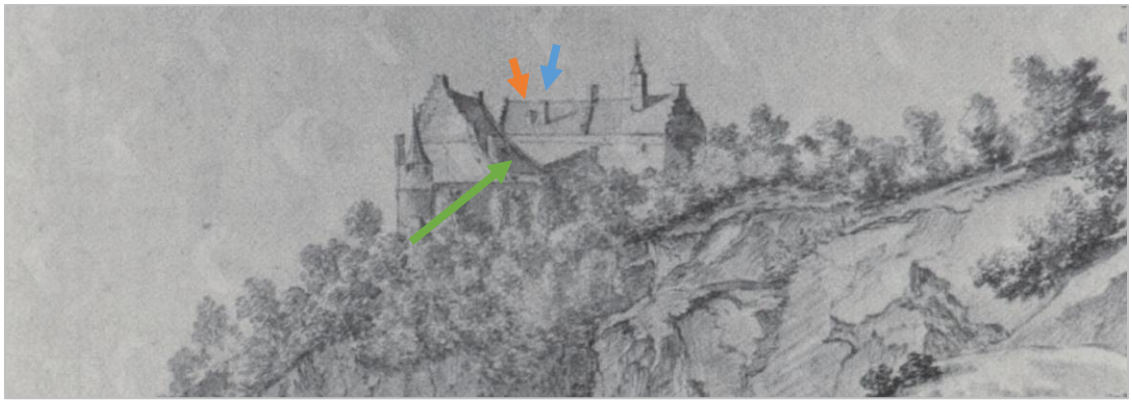

Figure 37: The castle in 1650, indicating the building to be extended backwards (marked green) and two chimney-like structures. Adapted from (Haagen, 1650).

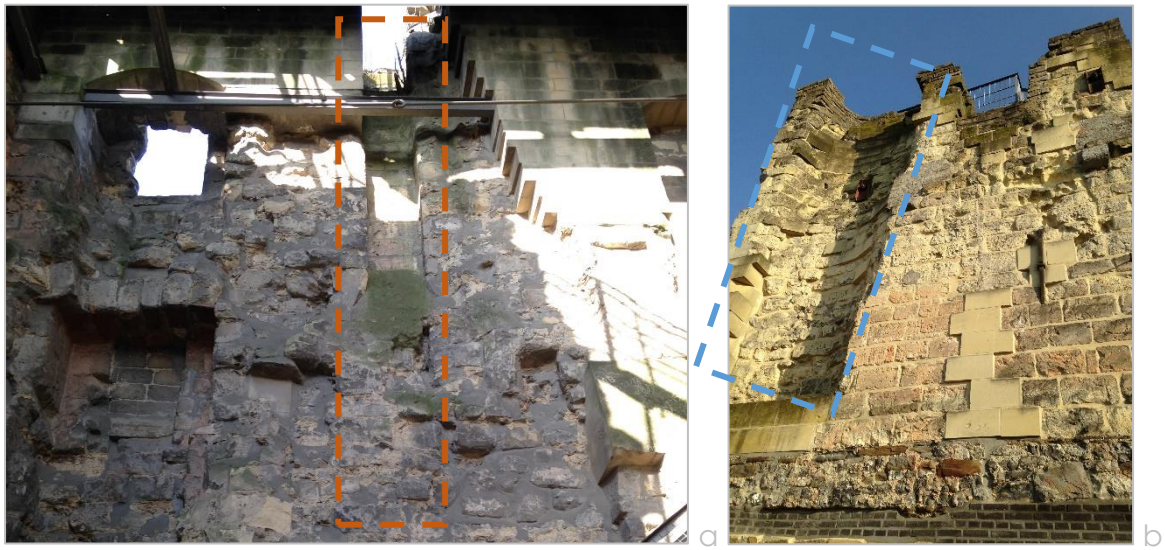

Figure 38: a) Markings inside the ruin of an embedded fireplace flue and b) a cylindrical marking in the west façade. Photographed by author.

Plan of the castle

Now the location of the ruin is analysed, it is important to point out certain other aspects of the plan of the castle. In Figure 35b we see a small ruin on the right-hand-side of the surviving wing of the castle. Both Figure 36 and Figure 31a indicate a much larger string of buildings towards the cliffs. Moreover, in all drawings and photographs after 1670 the hillside seems steeper, and not accommodating at all for any former structures. It is therefore a hypothesis that this part of the castle collapsed into valley, possibly by an earthquake, collapsed quarry or underground erosion.

In Figure 36 there are also some low-rise buildings to the left of the castle. These seem to be aligned with the nowadays stables. From the keystones it is known that these parts of the farm were constructed in the 19th century. It is therefore probable that the current stables are built on top of the old ones.

The same is probably true for the gatehouse, of which a previous version might be visible in Figure 32, just behind the half-destructed wing of the castle.

These statements are merely deductions based on the available literature and graphical images. Archaeological research for old foundations could make these hypotheses conclusive.

Section 3.2. Potential causes of destruction

From the previous section it can be concluded that the first partial destruction of the castle occurred between 1670 and 1740; and the second destruction somewhere between 1740 and 1850. The later period is also the time that the new farm was erected on the property, in the early 19th century. Furthermore, it was mentioned that markings on the ruin indicate a fire had raged in parts of the castle, after which only one wing survived, as was indicated in images of 1740.

The potential causes of the collapse of (parts of) the castle will be briefly discussed within the timeframes mentioned above and supported with background information. There are three distinctive subjects that could have caused the destruction. Firstly the castle could have been damaged or destroyed during a siege or war. Secondly it is important to review the state of the regional complications of the underground, which are subject to erosion and the complications induced by man-made mining channels. Lastly, in each of the two timeframes a major earthquake was recorded in historical documents. Perhaps in combination with the underground state of the mountain, this could have had a hand in the downfall of Lichtenberg Castle.

3.2.1. Damages gained through sieges and political conflicts

The last images showing the castle intact date back to 1670 (Figure 31) and the first partly destructions are shown in images from 1740. The only siege that could have done damage to the tower is therefore the siege of Louis the XIV in 1672, and the events connected to the Franco-Dutch war.

It is known that in the area many structures were destroyed to open the line of fire prior to the siege in 1672, or to prevent the opponent to occupy strategic locations. With that in mind the castle of Valkenburg was also blown up with gunpowder in 1672, to prevent it to fall in the hands of the French. In the area of Saint Peter, the village was destroyed and several buildings blown up with gunpowder.

It is however important to notice, that the castle at that time was not under the Republic of the Seven United Netherlands rule, but under the rule of the Prince-Bishopric of Liège. The Prince-Bishop was pro-France, and allowed them to pass through his lands. The castle moreover is distinctively far away from the city of Maastricht, more southern than the village. It is known that the French shot down onto the city more northern on the mountain, which in 1701 led to the construction of Fort Saint Peter by the Dutch Republic and therefore was a far more strategic location in the area.

Therefore, it seems unlikely that the French would have destroyed a castle of one of their allies, especially if it would not have been standing in the line of fire to the city of Maastricht (as was the case with the village and other structures blown up more northward). It is however plausible that the Republican troops of the Netherlands destroyed it to prevent the French to use the castle as a stronghold, as they had done with the castle in Valkenburg.

It is moreover important to note that much has been documented of these wars: sieges; losses; material damages and new constructions are mostly accounted for in old documents. From the castle none of those records have been found, as also mentioned by Sprenger (1941). As less important structures are mentioned in these documents, it is unlikely that the siege had anything to do with the destruction of the castle, it however cannot be ruled out. Perhaps future literature findings can provide a conclusive answer.

3.2.2. Collapse of underground quarries or erosion of underground layers

Below the possible influence of the old mineshafts and erosion is briefly reviewed.

Limestone quarries and old mines

Even before ENCI started excavating, there already were quarries using the resources of the St. Pietersberg and its surroundings. The region is rich of limestone and flint, which were used as building materials for new constructions.

On occasion of the *International Symposium on Flint* arranged by the *Maastricht Museum of Natural History* in 1969, dr. D.G. Montagne wrote an article considering the use of flint in these regions throughout all ages. He states that about 5000-6000 year ago, people started to take flint stones from the surface in these regions and use them as tools. When bigger tools were demanded for agriculture around 3000BC, they also started mining the flint in vertical mine shafts east of the Maas, near *Rijckholt*. Flint kept on being used for tools until the material was replaced by its successor: bronze. Only in the second half of the 19th century flint stones gave new perspectives due to new technologies, which gave use to flint of lesser quality (which were for that reason discarded by our prehistoric ancestors). This resulted in large scale mining in the Jekerdal, which is in the near vicinity of the ruin (Montagne, 1969).

The use of the limestone in this region probably began with the Roman Empire, which called the soft yellow stone *marga* which later led to the use of the word *mergel* (marl) by the local population. The romans used this word to describe all soft chalk containing sedimentary rocks (Felder, 1989).

Underground mine shafts therefore have been a long tradition, and even run underneath the castle, as is shown in Figure 39, a detail from a mineshaft map in the Lichtenberg museum. All mines underneath the castle are considered dangerous and cannot be entered (Natuurmonumenten, 2014). A part of the system already collapsed. This already occurred around 1700 according to some volunteers in the Lichtenberg museum. In the research for this thesis no literature has been found to support this statement. In Figure 40 the sinkhole still imprints its signature in the landscape. On the edge of the sinkhole the farm can be seen, as well as the tower. As mentioned in Paragraph 3.1.4. the castle used to be larger in the direction towards the sinkhole. This sinkhole might therefore have a causal relationship with the destruction of this part of the castle.

Erosion and karst formations

In soils consisting of slabs of limestone and layers of flint, erosion can pose quite a problem. Limestone is highly vulnerable for dissolving in water, especially water with higher acidity. Flint however is much more durable, and non-permeable. This leads to water washing out the limestone, creating vertical channels in the soil, until it reaches a flint bank from which the water will remove limestone horizontally. This principle is shown in Figure 41a. Eventually the weight of the upper layers can result into the collapse of the soil.

Another soil failure mechanism occurs when erosion creates deep karsts, which in time are filled with other sediments. Due to this erosion the surface of the ground keeps on settling in time, creating a larger displacement on ground level. This mechanism is shown in Figure 41b.

In the region of the castle, three layers of limestone formations can be identified. The deepest layer is the Formation of Vaals, and is characterized by low to no chalk content (Felder, 1989). The middle layer is the Formation of Gulpen (roughly 90m thick) followed by the Formation of Maastricht which is topped-off with a layer of loess and sand (see Figure 42a).

The horizon of Lichtenberg is marked as a transition between two formations in an article by Felder (1989) in *Grondboor en Hamer*. Both Figure 42a & b indicate several layers of flint that could cause settlements or sinkholes due to erosion. Furthermore Figure 42a shows the location of the mineshafts, which are brought into context with the ruin in Figure 43.

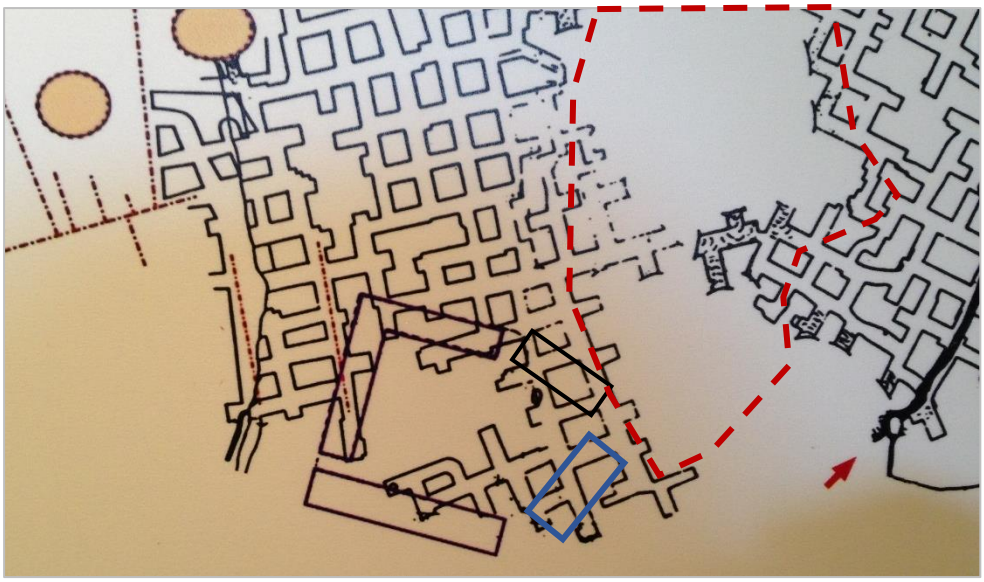

Figure 39: Mineshafts running underneath the farm and ruin, red line indicates nearby sinkhole, blue line the castle ruin. Adapted photograph taken from Lichtenberg museum.

Figure 40: Photograph clearly showing the contours of the sinkhole. Reprinted from (Natuurmonumenten, 2014).

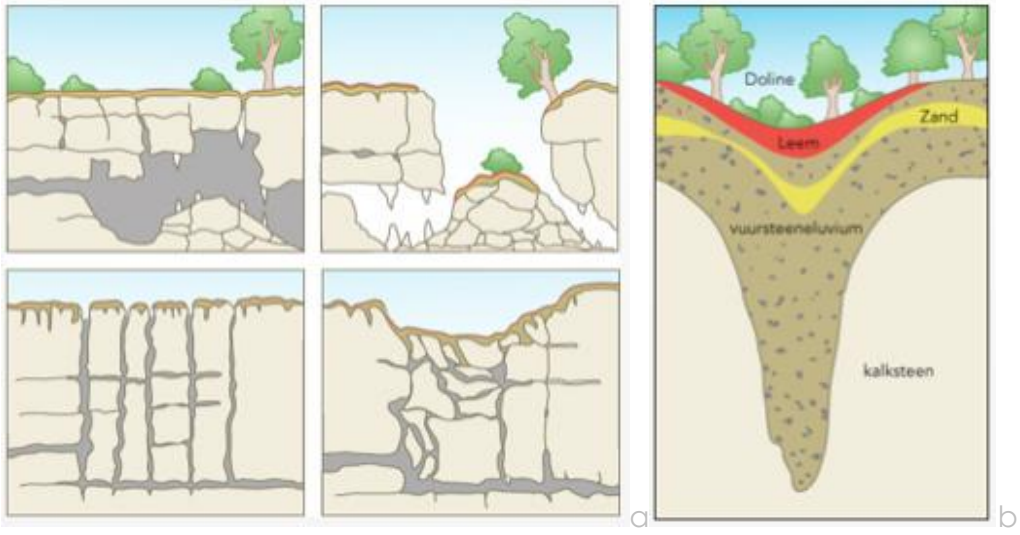

Figure 41: a) Collapse mechanism due to erosion in the limestone rich areas on the St. Pietersberg and b) karst formations creating settlements. Reprinted from: a) (Bosch, Ontstaan van instortingsdolines (boven) en erosiedolines (onder)); b) (Bosch, CO2-doline met geologische orgelpijp in het Vijlenerbos).

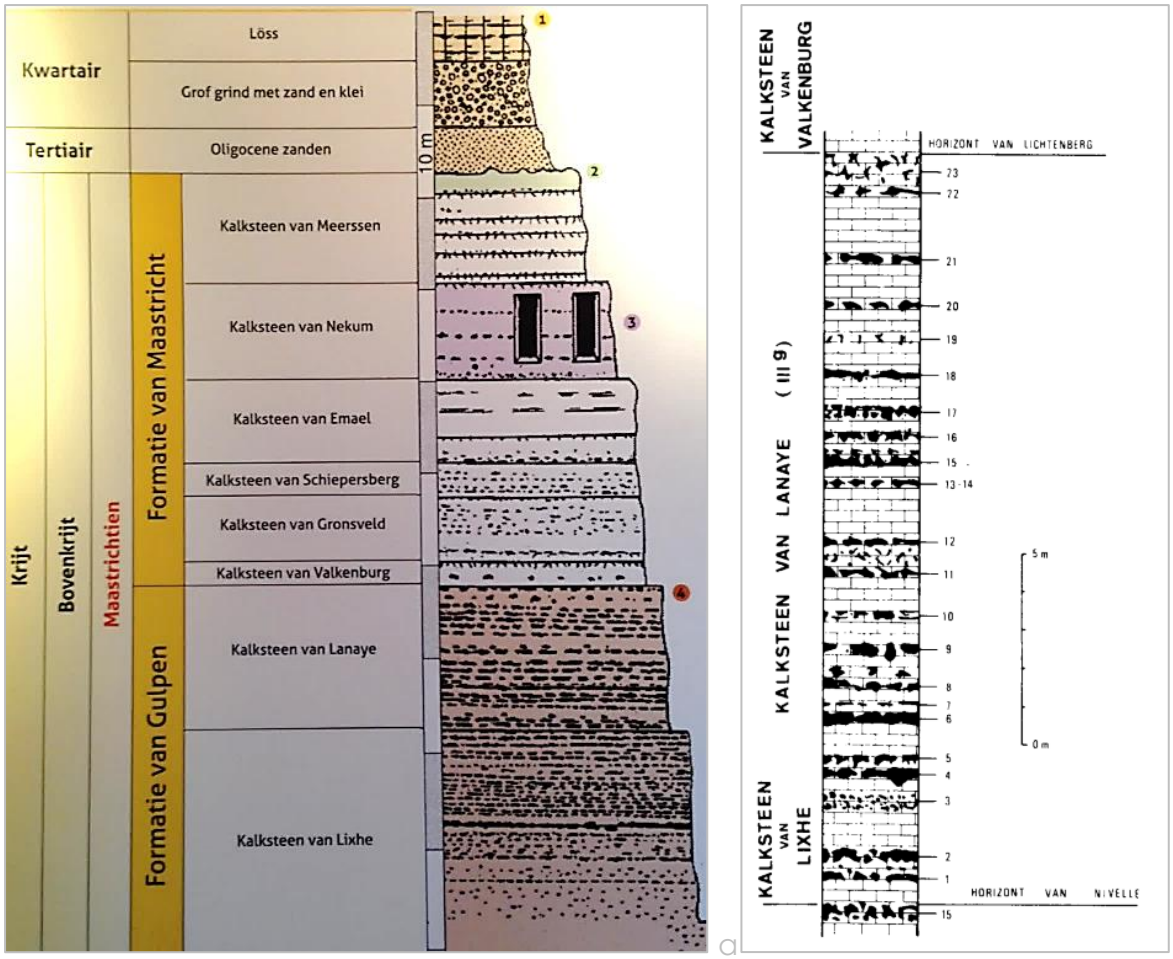

Figure 42: a) Layers of limestone as depicted in the Lichtenberg museum; b) Lithological composition of the limestone of Lanaye (IIIg) till the horizon of Lichtenberg, including all layers of flint numbered (Felder, 1989).

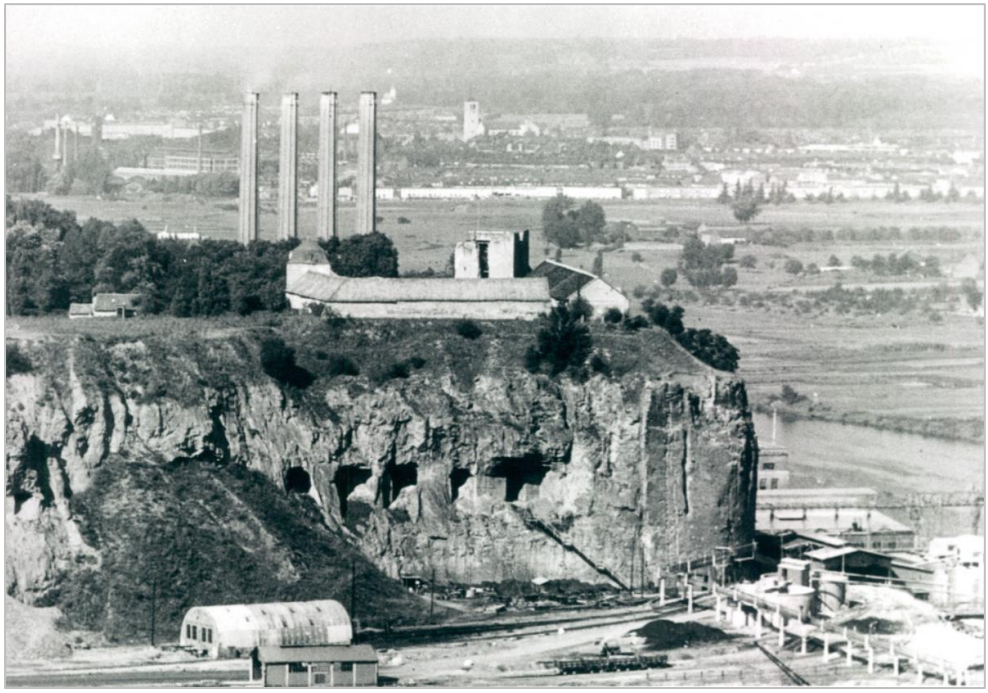

Figure 43: Archive picture indicating the location of the layer of Nekum and its historical mining shafts underneath the farm area. Reprinted from (Spee, s.d.)

3.2.3. Damage obtained during nearby earthquakes

As two major earthquakes were recorded in historical documents to have occurred in the timeframes the castle was destroyed, it is important to assess the risk of earthquakes in this area. This could lead to potential hypotheses for the destruction of the castle.

Risk maps & Mercalli scale

For measuring earthquakes two scales are commonly used; the Richter scale and the Mercalli scale. Whereas the Richter scale measures the magnitude of the earthquake in the epicentre, the Mercalli scale measures the consequences of a certain earthquake on any given location. The further from the epicentre, the less effects will be felt and the lower the magnitude on the Mercalli scale.

The Mercalli scale, which reaches up to XII in roman digits, measures the impact on people and buildings on a certain location. Whereas scale I is not even being felt by people and only noticeable on seismometers, scale XII is exceptionally catastrophic (IPO, n.d.).

In the Netherlands, however, only scales V to VIII can be expected according to *Interprovinciaal Overleg* (IPO), which is an organisation of the Ministry of Internal Affairs and the Ministry of Infrastructure and Environment. The scales indicate the following intensity of damages and perception by people:

V:	Quite Strong	Vibrations felt by all, sleeping people wake up, suspended objects sway.
VI:	Strong	People startle, objects in houses fall, trees move, damage to weak buildings.
VII:	Very Strong	Damage to many buildings, chimneys fall, waves in ponds, ringing bell towers.
VIII:	Destructive	Damage to most buildings, weak buildings partly destroyed. (IPO, n.d.)

As depicted in the risk maps in Figure 44, the VIII scale is only depicted as a risk in the far east in Kerkrade (near the German border). Scale VII is considered a potential risk in the central area and scale VI west of Maastricht. The ruin is located in the VII zone and therefore it is probable it will be subjected to a potentially very strong earthquake in the future.

These risks are based on earlier earthquakes in the Netherlands, Belgium and Germany, their magnitudes and their effect on people and the built environment. An overview from the KNMI of all earthquakes from 1900 till 2014 is given in Figure 45. Whereas in Groningen earthquakes occur due to gas extraction, the southern provinces experience natural earthquakes induced by tectonic activity near the *Rur-graben*, which is created by the tectonic faults called *Peelrandbreuk* and *Feldbissbreuk* (KNMI, 2014).

In 1992 one of these earthquakes occurred near Roermond, which inflicted scale VII effects in a wide spread region around the epicentre. The magnitude of the earthquake was 5.8 on Richter's scale (KNMI, n.d.). As Figure 45 depicts, there have been multiple tectonic earthquakes since 1900 in the area around Maastricht with differing magnitude.

Earthquakes between 1670 and 1850 near the castle

Near the area in which the Lichtenberg castle was built two major earthquakes could be found in literature with Mercalli scales varying from VI-VIII. These were the 1692 earthquake in Verviers (Belgium) and the 1756 earthquake in Düren (Germany).

According to a Belgium research team the Verviers earthquake resulted in VI consequences in the whole of Belgium and VII-VIII consequences closer to the epicentre (see Figure 46), including southern Netherlands up to nowadays Sittard (Vanneste, et al., 2009). Even in London the earthquake was felt and recorded in historical documents.

The University of Cologne reports chimneys falling as far west as Liège after the Düren earthquake, which would include also the Lichtenberg Castle. Furthermore, mine shafts and buildings of poor structural quality collapsed near the epicentre (Universität zu Köln, 2011).

It can therefore be concluded that earthquakes are a real risk in this region and could have had a hand in the downfall of the Lichtenberg, possibly in combination with poor underground stability due to mines or erosion. The possibility exists that the Verviers earthquake may have caused initial damage to the castle. The Düren earthquake may have been the finishing blow to parts of the ruin after it already had burned down.

The sinkhole (± 1700) could indicate such a hypothesis to be plausible, as from graphical analysis it could be determined that there used to be a wing extending the nowadays ruin for double its length, of which a part would have ended up in the sinkhole. As for the northern wing and its extended building masses, they might have been subject to a landslide, perhaps as a result of one of the earthquakes. As shown in a photograph from 1900 (Figure 47), the area could not have accommodated such a structure, leading to the conclusion that parts of the mountain must have disappeared at a certain time (and before the excavation by ENCI).

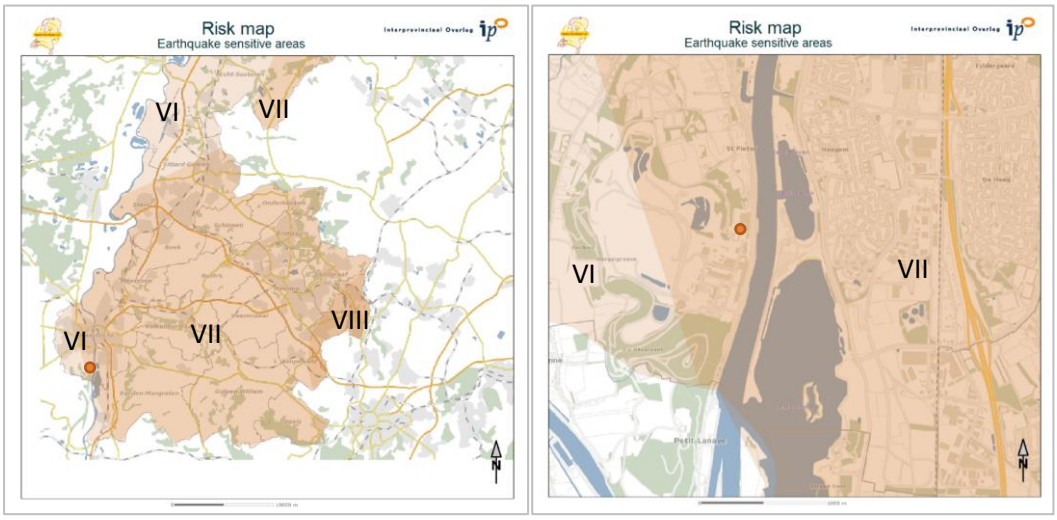

Figure 44: Earthquake sensitive area risk maps of Southern part of the province of Limburg, the ruin is depicted with a small orange dot and has a risk of experiencing scale VII effects on the scale of Mercalli (risk maps generated from risicokaart.nl, a site maintained by two Dutch ministries and IPO (Interprovinciaal Overleg).

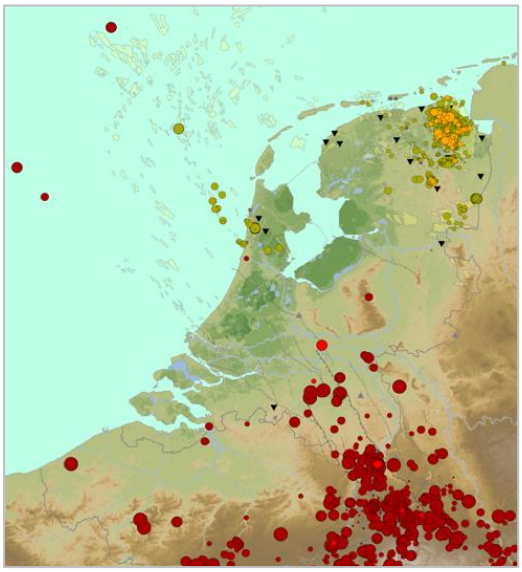

Figure 45: KNMI chart of earthquakes, which occurred between 1900 and 2014. Red circles depict natural earthquakes, of which the light red ones occurred in 2014. Green dots depict induced earthquakes, of which the yellow ones are gas extraction related earthquakes in 2014. The size of the dots indicates the magnitude of an earthquake. Reprinted from: (KNMI, 2014)

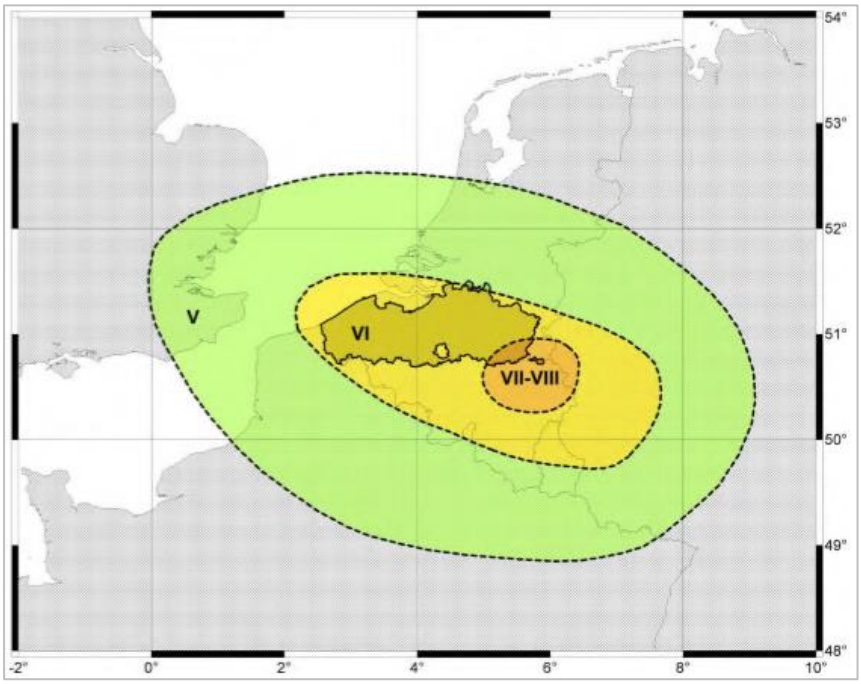

Figure 46: Earthquake scales of Mercalli according to Belgium research group during the Verviers earthquake in 1692. As can be depicted the Lichtenberg castle was directly afflicted by this earthquake. Reprinted from: (Vanneste, et al., 2009).

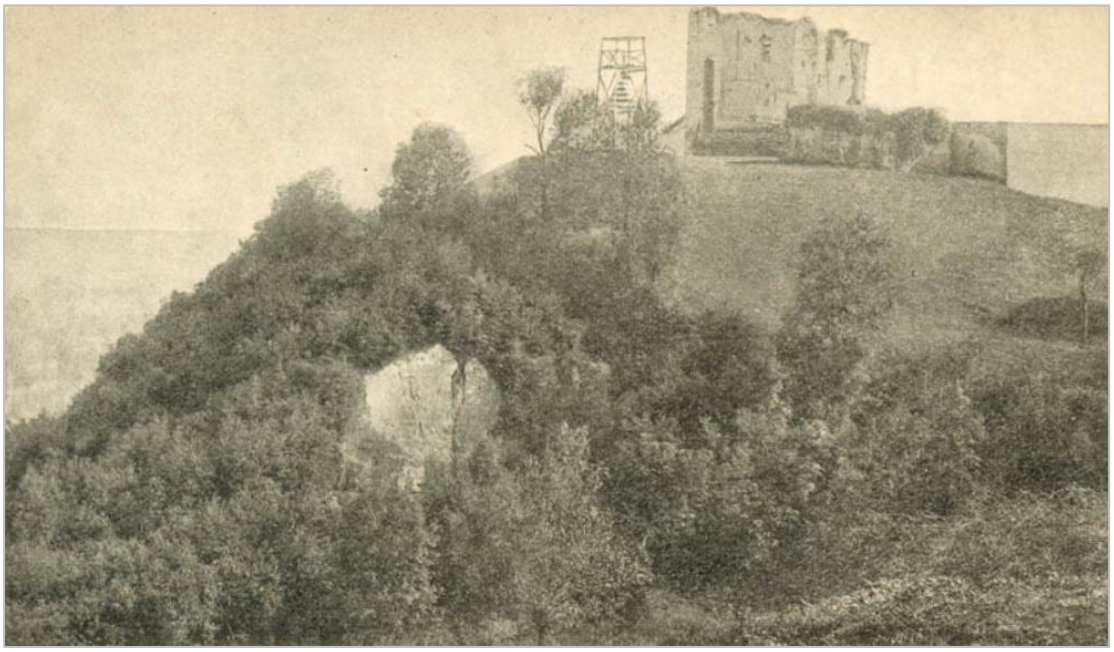

Figure 47: Photograph from 1900, depicting the ruin and its surroundings. Reprinted from (GAM, 1900).

Section 3.3. Forensic assessment of the ruin

In order to determine the critical damages to the ruin, an analysis is made discussing material usage and replacement; current and former cracks; and current interventions. From this boundary conditions can be derived for the new cast glass system at the location of the most critical damage.

3.3.1. Material usage and properties

It is believed the tower originally was constructed with locally found flint, coal-sandstone and marl stones. Historical research gives indication that the original stronghold was destroyed after which a new castle was erected on its foundations.

Drs. J. Sprenger indicates in 1941 in *Maasgouw* that the flint and coal-sandstone were reused from a former structure dating from the 11th till the early 13th century, as it was common practice to use coal sandstone in those times. By analysing the Namensche cornerstones he concluded them to be from around 1300. This he depicted from how the stones were cut, which is similar to the stones found in the city walls of Maastricht, which were being constructed in this time. The marl inner part and upper part then serve as a reinforcement, presumably due to improvements in military techniques a thicker wall was preferred. These parts presumably date back from the 15th century, as several details indicate (Sprenger, 1941). One of those details is for instance a gothic niche, as is shown in Figure 48. This also fits the historical analysis of a destructive event in the 15th century after which reconstruction and strengthening would have been a logical next step.

Revisiting the claim that marl was used during construction, some remarks should be made. Officially, according to geology definitions, marl is a mixture of chalk and clay, with 35 – 65% of calcium carbonate (Felder, 1989). As the article of Felder in *Grondboor en Hamer* states, the 'marl' in the southern parts of Limburg has such a high percentage of chalk it belongs to the category limestone rather than marl. The local limestone at the location of ENCI (cement factory neighbouring the ruin) features a $CaCO_3$-percentage varying between 95 and 98%. Furthermore this area features eighteen large flint deposits, consisting of larger chunks than found elsewhere in the region. The density varies strongly in this region, the higher layers vary between 1300 and 1500 kg/m^3 while deeper layers and higher layers more eastern from the location feature a density from 1400 to 1560 kg/m^3. Assuming that mostly higher layers were used during construction, the highest density of this layer will be used in further calculations. The density of all limestone in the structure is hence set to 1500 kg/m^3.

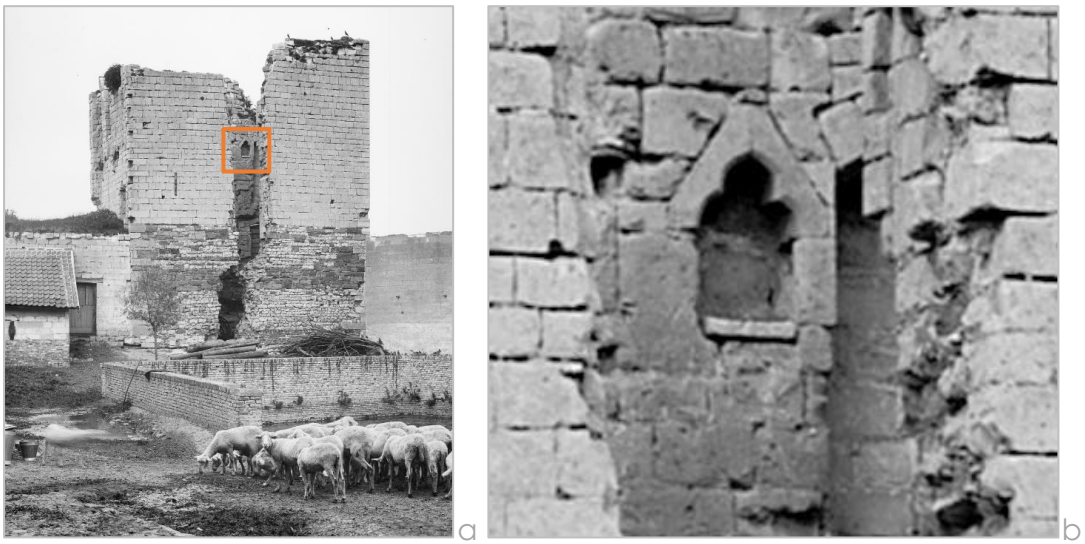

Figure 48: Gothic niche indicates this part dates from the 15th century, visible in a picture made in 1904; a) complete picture; b) zoomed in detail of the gothic niche (Anonymous, Ruine Ligtenberg, 1904).

3.3.2. Current tissue replacement and lost detailing

From field and graphical research, it can be determined which limestone parts have been added later. The additions of limestone parts have been categorized into three periods of time. The results in Figure 49 show which additions have been made in between the technical drawings of 1881 and 1904, the presumed additions by both ENCI (probably post-WWII) and Steunbeer bv (company contracted for restoration and responsible for newest additions). The image also presents where brickwork was added as a cheaper alternative for the limestone. Lastly also details that were lost in restoration and preservation efforts have been marked.

Secondly it is also important to identify the markings within the structure to see where floors have been and other details that were characteristic for the monument. Due to many former restorations markings inside the current structure have been lost. The only sources of information found are some technical drawings from both 1881 and 1904, which provide an insight in the state of the ruin in that time.

The interior markings show traces of different systems. Therefore it is plausible that parts have been removed during the time it was still intact. It may even be that the removal or change of parts have led to cracking and ultimately failing of the flooring system of the upper floors.

Take for instance the arches that likely once spanned from the south to the north wall (see Figure 50). Probably they once formed the base of the tower's structure. The traces connecting the vault to the walls run along the full northern and southern wall. The remarkable part is that all four sides appear to have some sort of opening or detailing. The two little niches in the eastern and western part could indicate this room was actually in use, as it probably would have evaded the vault's radius. A possible entrance could have been the lower seemingly open part in the northern wall. However, in the northern wall a gothic niche appears, drawn similar to the other gothic niches but not to the other niches on the ground floor. They can therefore be made in different times. Problematic is that this niche seems to abruptly disrupt the vault, as also the doorlike opening does in the southern wall. It is a possibility that the owners tried to remove the vault to make better use of the space, followed by adding a new wooden floor to replace the stone structure (see indents just above the arch). They therefore might have added the opening in the southern wall to make use of the new space and added a gothic niche. These, of course, are only speculations, but they might evolve into a viable hypothesis in how the structure got to its current state.

Both the upper floors are also indicated with marks into the stone. Primary beams are only regular at one side. This might indicate staircases were disrupting these beams and there was some sort of replacement structure for this. This can also be concluded from the girder indents (marked yellow) which show a jump in the eastern inner wall. The upper floor was still a functional floor and the last storey of the tower. This can be concluded from half a window in Figure 34b.

Then there are some more indents scattered over the eastern and western wall. Those in the western wall were not given in the drawings in 1881 but were visible in the drawings of 1904 by Sprenger. They might have been used for other supports. However it is remarkable that many are close to the cracking pattern of one of the cracks in the western wall.

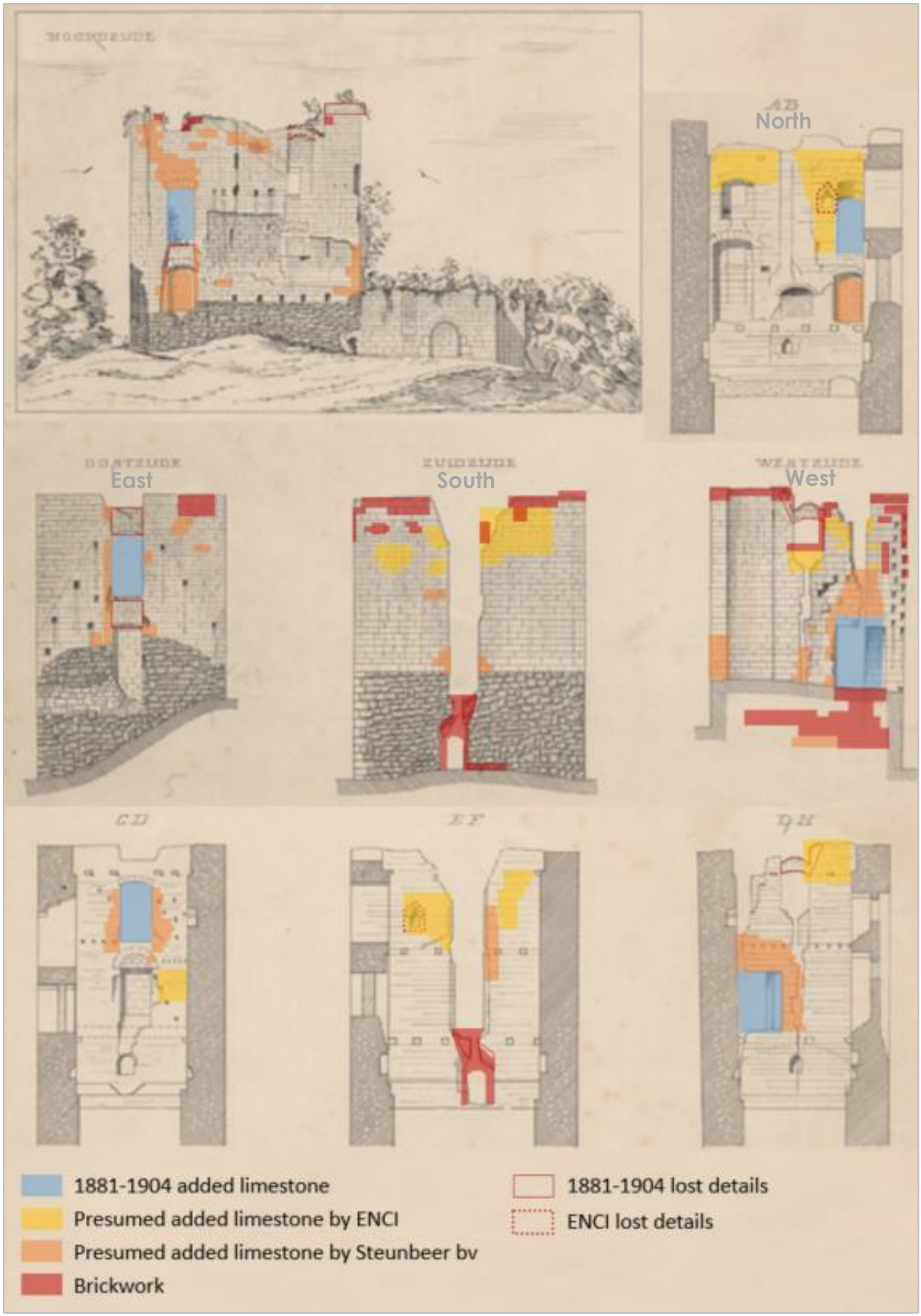

Figure 49: Limestone and brickwork additions since 1881. Including also known details which disappeared. Adapted from (Anonymous, Gevelaanzichten en plattegronden, 1881a), (Anonymous, Gevelaanzichten, 1881b).

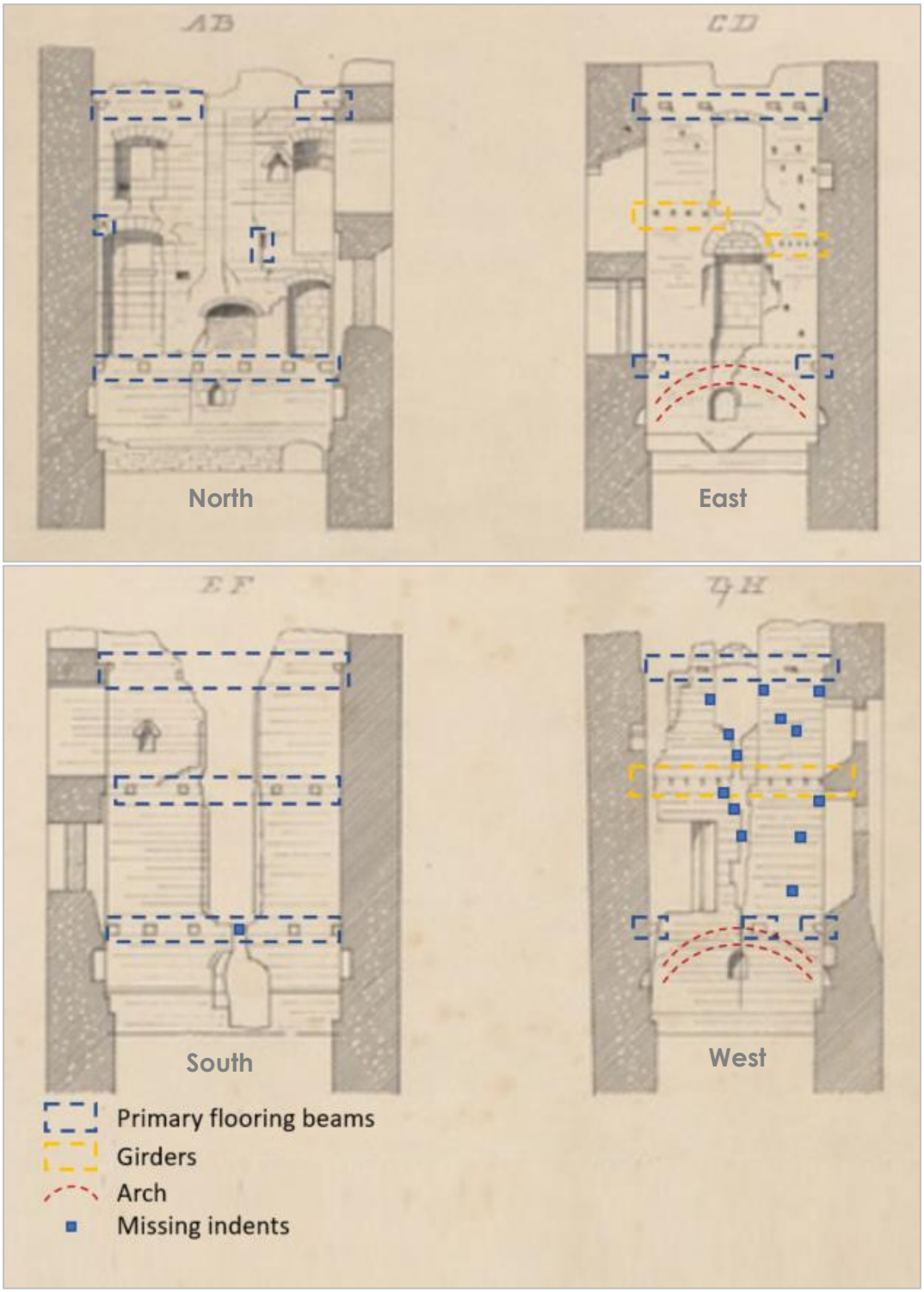

Figure 50: Analysis of inner wall markings. Adapted from (Anonymous, Gevelaanzichten en plattegronden, 1881a).

3.3.3. Crack identification and evaluation

Both current and former cracks must be identified and evaluated to understand the current state of the monument and its tendency to move. For those cracks a selection of hypotheses will be discussed. In Figure 51 six major cracks have been identified, these are summarized in Table 5 including their possible causes, weak spots, and current interventions.

Earthquake damage is a potential cause for all the cracks. As earlier discussed, there is a possibility that movements in the soil might have destroyed the other parts of the castle, leaving only the current tower ruin. It is reasonable to assume that with the destruction of adjacent parts, the remaining tower got damaged as well.

As for crack A, no weak spots are found, but partial settlement of the ground, taking also in consideration the weak spots near crack B and C is a possibility. When the upper ground profile is considered (red striped line in Figure 51) it is plausible a settlement of the ground might have occurred in this pattern as well, which would suit the crack pattern of cracks A, B and C. At the location of Lichtenberg Castle there are several scattered flint layers in the ground (Felder, 1989), which are much harder than the regular larger layers of limestone (see Figure 51). If, during an earthquake there were certain shifts in the ground, it might have affected the ground underneath the ruin as well. Uneven movements or the presence of a flint layer might have caused such a crack pattern during an earthquake.

Crack D is the result of an out-of-plane wall translation. When analysing the old drawings, it can be observed that the draughtsman recorded damages at equal heights as the windows in the eastern side. Moreover, the width of the crack is the same as the width of the windows in the eastern wall. Hence it is plausible that similar windows were present in this south wall, whose arches fell down after the rotation. Regarding the door opening it is unsure to say if it used to be there in older times. The flint would have protected the ground levels from intrusion, as the limestone is quite soft and easy to puncture. Combined with the arched markings in the wall it is unlikely this passage existed in older times. In any case this crack is not so much a crack as it is a direct result of the rotation of the wall, with partial collapse of the window bridges as a result. This mechanism is shown in Figure 52.

Crack E might be the direct cause of the wall rotation. It seems someone added a higher entrance to the tower cutting through the corner of the wall of the south and west side of the tower. The Düren earthquake might have caused propagation of the crack or further settlement of the soil, which then led to the wall's rotation.

The earlier earthquake might have caused crack F, or might have been caused by the internal collapse following wall rotation. There are many indications of indents in the wall that could have contributed to this mechanism.

Table 5: Crack identification, considering hypothetical causes, weak spots, and current interventions.

Crack	Hypothetical cause	Weak spots	Current intervention
A	-Earthquake damage	None found	Renewed limestone brickwork
B	-Earthquake damage -Settlement ground -Missing adj. building	Indents from former parts Former chimney inside (Van Nispen Tot Sevenaer, 1974b)	Filled with mortar
C	-Earthquake damage -Settlement ground -Missing adj. building	Window opening	Renewed limestone brickwork
D	-Wall rotation	Former windows	Steel ties to hold wall into place
E	-Earthquake damage -Later added passage	Door opening through corner	Steel frame, added and renewed limestone brickwork
F	-Earthquake damage -Internal collapse	Indents from former parts Window opening	Renewed limestone brickwork

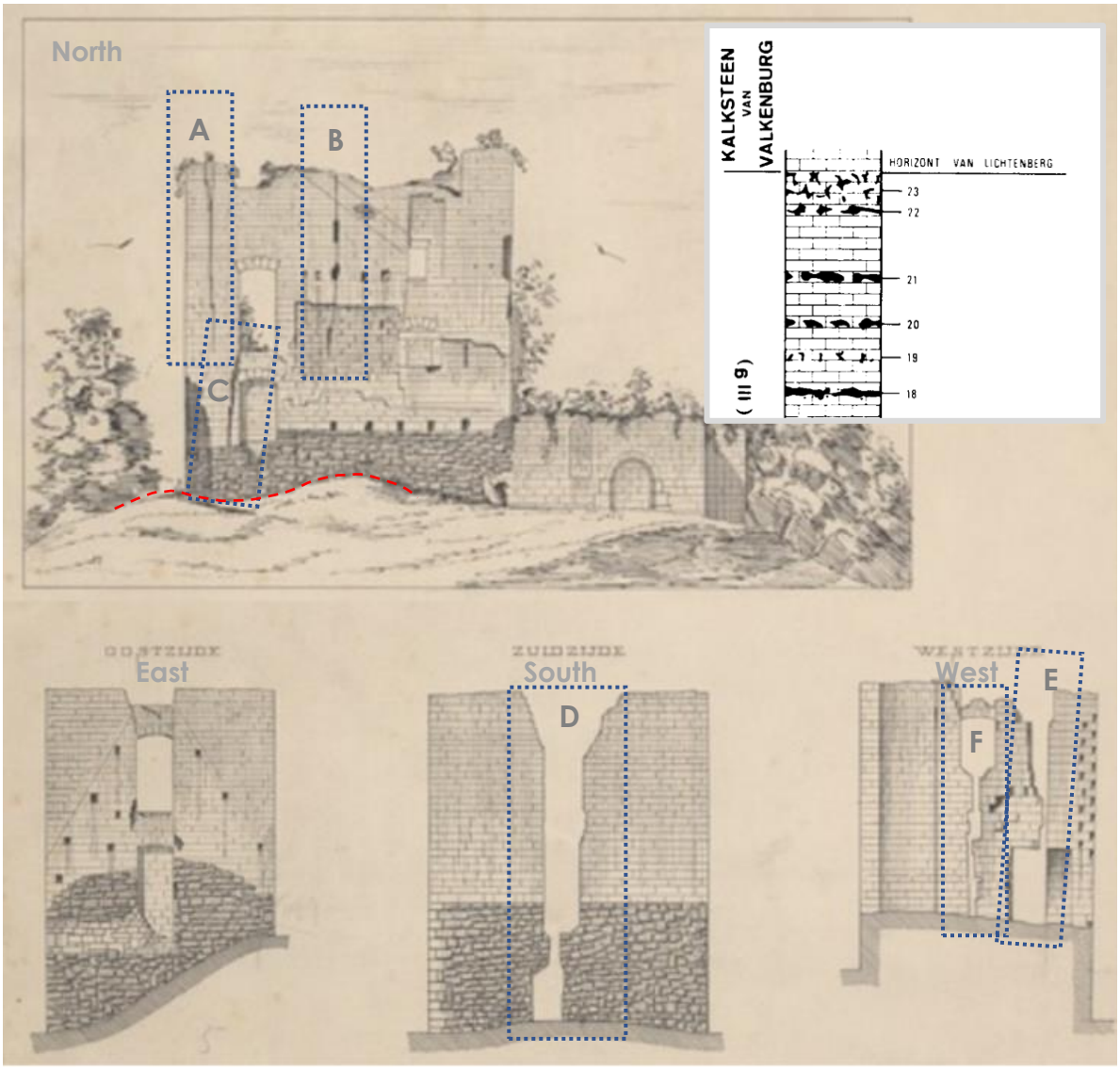

Figure 51: Crack identification. Adapted from (Anonymous, Gevelaanzichten, 1881b). Incorporated in this figure also a lithology near Lichtenberg Castle, limestone with layers of flint (black), retrieved from (Felder, 1989).

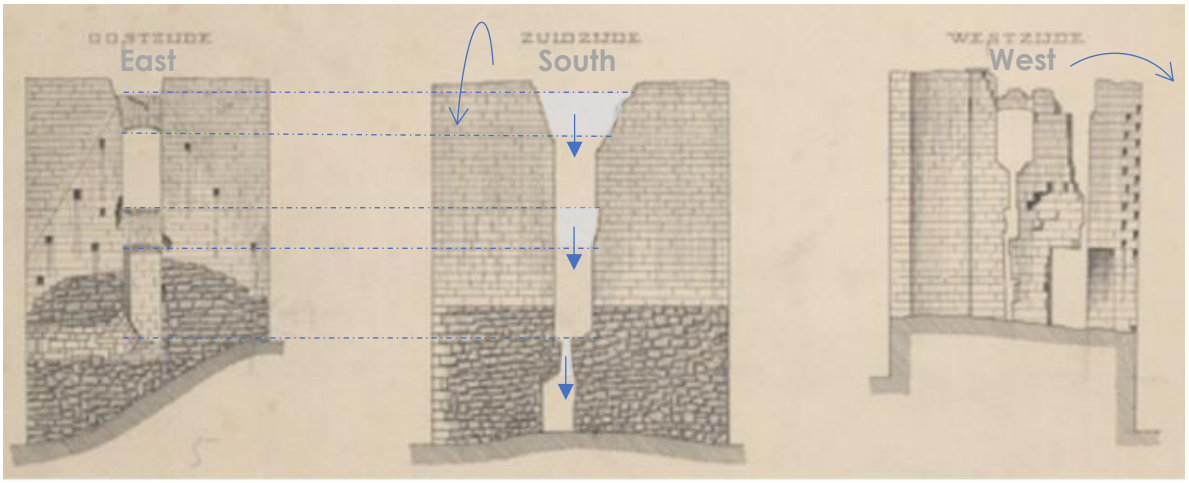

Figure 52: Mechanism failure of southern wall, arches above openings collapsed after out of plane translation of part of the wall. Adapted from (Anonymous, Gevelaanzichten, 1881b).

3.3.4. Current consolidations

In the past, the ruin underwent many structural interventions. The most radical was the reallocation of the tower in 1904. In this year, the ruin was transformed into a lookout tower, which also consolidated the tower, using a steel- or wrought iron structure embedded and anchored into the limestone walls. As far as known the structure had only one intervention at that moment, a tensile rod spanning the north and south wall, as shown in Figure 53a.

The earliest staircase had its entrance at the northern side and featured the staircase also partially outside (see Figure 34b). Parts of this staircase may have been renewed during its lifetime, as photographs dating from both 1928 and 1936 show loos steelwork, which could indicate renovation or renewal practices being carried out. In any case, at a certain point the lower part of the staircase was added, and certain anchor plates were renewed. This probably occurred during the time the ENCI was the owner. They also carried out some partial restorations and probably are responsible for the brickwork arch that now gives entrance to the ruin, as well as the brickwork in the top section of the ruin (see Figure 49).

Most of the profiles of the steelwork are embedded into the limestone. Some of them are also anchored with steel bars puncturing the thick wall. In Figure 54 all steel ties are given that might contribute towards the stability of the tower (highlighted in red). Other profiles are merely embedded in order to support loads acting on the staircase. In green, support structures are shown for restored limestone additions, which could not be supported by the ruin structure itself. These however do not contribute to any lateral stability.

It is unknown which quality the forged steel/wrought iron structure had. In literature it can be found that the maximum yield stress during the period of 1840-1940 is equal to f_y = 500 N/mm^2 (Van Maarschalkerwaart, 1996). There are no indications of yielding deformations. Unless more information comes available this yielding stress is the safest assumption for calculating the capacity of the interventions, which in the new design should be met by a glass structure. All the current interventions are assumed to have the same yielding capacity as the measured tie on the field visit. This tie is the tensile rod spanning near the staircase, and measures 31.8 millimetres in diameter. Hence the capacity of both ties is assumed to be about 40kN before yielding. This is however a very conservative value.

$$P = f_y * A$$

$$P = f_y * \frac{1}{4}\pi D^2$$

$$P = 500 * \frac{1}{4}\pi * 31.8^2 = 39711.3\ N \approx 40kN$$

Figure 53: a) 1904 picture featuring a single intervention (see red circle); B) picture of measured tie rod. Adapted from: a) (Anonymous, Ruine Ligtenberg, 1904); b) photograph by author.

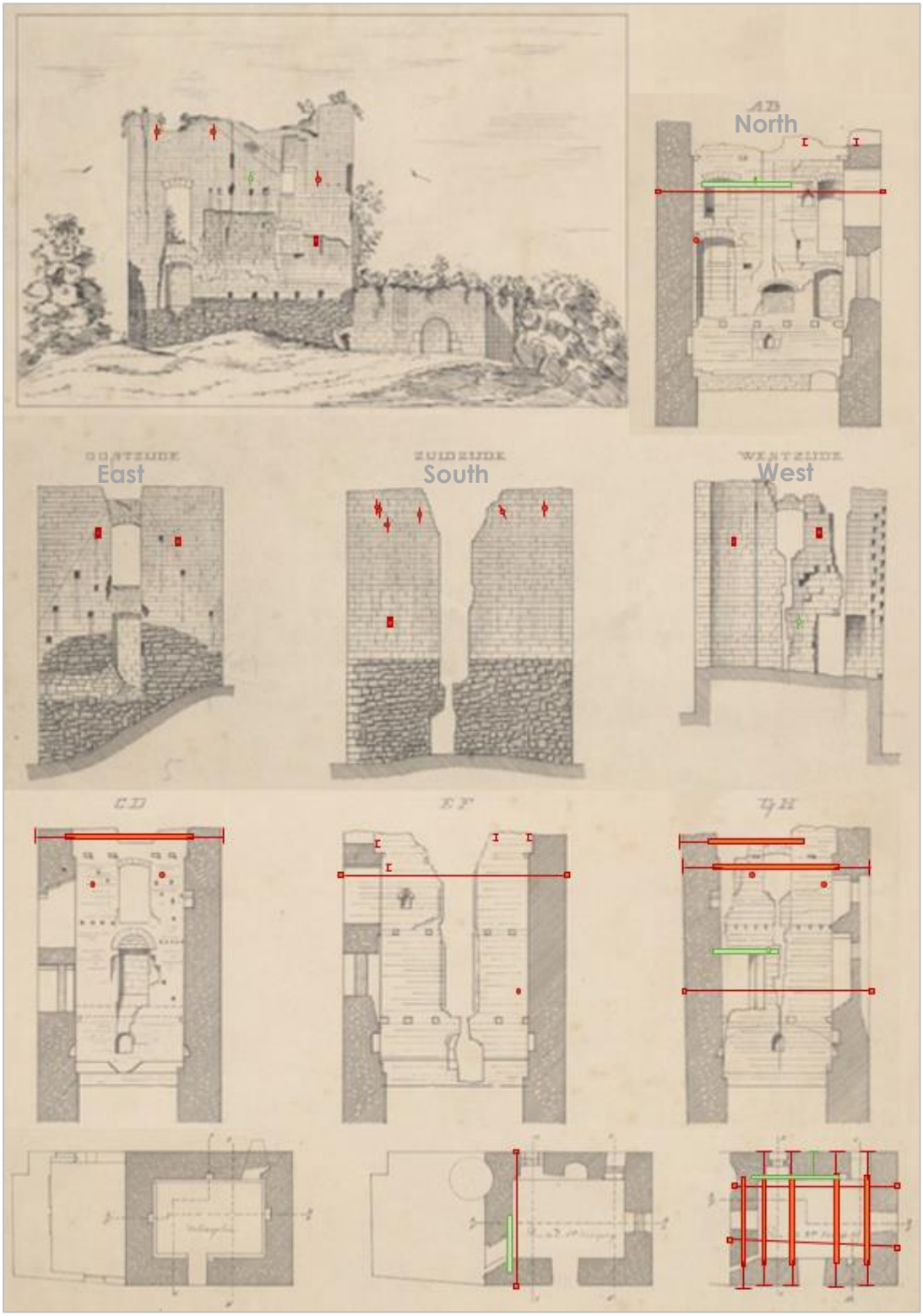

Figure 54: Active interventions in the ruin of Lichtenberg, red interventions secure stability, green interventions only support reconstructed limestone masonry. Adapted from (Anonymous, Gevelaanzichten en plattegronden, 1881a), (Anonymous, Gevelaanzichten, 1881b).

3.3.5. Critical element in the ruin

Of all damages the rotated wall and corner crack is the most critical in the ruin. This can also be depicted from the amount of steel interventions in this part of the wall (see south view in Figure 54). Five steel rods are applied here, of which most of them in the top edge of the wall. Assuming each has a capacity of F = 40 kN, this is what the interlocking cast glass brick wall must be able to meet as a system.

Hence the focus for a possible cast glass brick geometry will revolve around design criteria and principles coming from this critical wall in the structure. A brick design that fits this wall is hence expected to be applicable for the rest as well.

Section 3.4. Restoration boundaries

Aging, deterioration of materials and historical events alike, all have had their impact on the still existing historical objects. Protected by a monumental status, they are cultural heritage meant for future generations to see. However, due to these harmful influences, material quality decreases, and for the badly damaged structural integrity might become a problem. The latter is especially the case for ruins, as a past destructive event might have damaged important structural parts, leaving it vulnerable for possible future impacts.

A solution is to restore the monument to its former glory, or at the very least to consolidate the structure in order to preserve it. For this it is important to review the restoration principles, to define restoration, and to determine the boundaries of a possible restoration or consolidation design. The principles discussed in this chapter are therefore directly reflected on the Lichtenberg Castle

3.4.1. Definition restoration

Brandi (2005) defines restoration as "the methodological moment in which the work of art is appreciated in its material form and in its historical and aesthetic duality with a view to transmitting it to the future". It implies that the moment of restoration should reflect on the subject's history and its material form as is. The current state of the materials therefore should be kept intact as much as possible, so as long as this state is not harmful for the overall structural integrity. The goal of restoration is to preserve the historical tissue and shape for future generations to see, by taking into account its history and shape throughout the history.

In the case of a ruin, restoration should be limited to conserving the structure as it is, with the focus on preserving the material as is (Brandi, 2005). It therefore solely should use interventions that consolidate the structure, with as less impact as possible to the current material. The ruin therefore should still be a ruin in perception, with preferably a non-visual intervention.

3.4.2. The Venice Charter in context of Lichtenberg Castle

The Venice Charter, drawn up in 1964 by the International Council on Monuments and Sites (ICOMOS), gives some guidelines regarding valid restorations and conservation activities. In this charter articles 5, 6 and 8 to 13 are applicable on a ruin, such as the case study of Lichtenberg Castle. A restoration plan should therefore be valid and in accordance with these articles. Therefore, these articles will now be discussed and put into context with the Lichtenberg Castle ruin.

Article 5 states that conservation of a monument should be accompanied with a "socially useful purpose" (Gazzola, et al., 1964). Within this socially useful purpose it is only allowed to make alterations if this does not consider the "lay-out or decoration of the building".

Regarding the tower, the exact past lay-out is unknown, but some details of the past have been uncovered in old drawings and therefore could be brought back, as well as the floors of which the location is known. As for the socially useful purpose, the tower will accompany the nearby museum as either exhibition hall or lookout tower (as is its current use).

Article 6 considers the setting of the monument. It states that if a "traditional setting exists, it must be kept" and that "no new construction, demolition or modification which would alter the relations of mass and colour must be allowed" (Gazzola, et al., 1964).

As for the tower, the ruin is the only remnant of the traditional setting. The rest of the castle was lost in time. The new setting is that of a farm, and this has remained the setting for such an amount of time, that this new setting has become monumental as well. Therefore, it is important that no large mass will be added that can distract from either of the two monumental settings. Reconstructing the whole castle therefore would disturb the setting of the monumental farm.

Article 8 states that important parts may only be removed from the monument if the reason is to safeguard the monument. Only when otherwise the monument would be endangered important details can be sacrificed to preserve the monument. For the tower, the small gothic niches have been sacrificed in time and replaced by solid blocks of limestone, without any intention of keeping these historic details. This intervention therefore is considered invalid, as the details could have been restored in new limestone as well. The markings of flooring indents are a similar case in which important marks of the past have been replaced with smooth limestone brickwork. Only when these details were sacrificed because of immediate danger of propagating cracks or similar damages these interventions would have been valid. If there is a possibility to bring these details back whilst maintaining the structural integrity it would be a valid intervention.

Article 9 is the first article considering restoration, whereas the previous articles focused on the conservation of monuments. It states that the purpose of restoration "is to preserve and reveal the aesthetic and historic value of the monument and is based on respect for original material and authentic documents". It further states that "it must stop at the point where conjecture begins" (Gazzola, et al., 1964) and that any intervention necessary for preserving or consolidating the monument should be distinguishable from the older parts. Translating this to our castle ruin tower, it is important to follow the results from the forensic research described in Appendix B. Only information as depicted in old documents or drawings, or conclusions drawn from this can be taken into account. In this respect the door on ground floor level in the southern wall is due to the other markings in the monument an invalid restoration, as no proof has been found which indicates when this door was constructed. The presence of window openings in the southern wall cannot be proven, but is a viable hypothesis, as long as it remains merely a hypothesis that these windows cannot be restored as no proof exists in documentation or in historic visual representations. Many of the other door- and window openings are currently closed with limestone brickwork. In order to recover the historical layout, it can be argued that these openings should be either a void or fitted with a transparent solution if necessary for consolidation of the monument. Moreover, a glass solution would be both distinguishable and be able to fit in due to its transparency.

Article 10 states that newer techniques may be used "where traditional techniques prove inadequate" provided that "the efficacy of which has been shown by scientific data and proved by experience" (Gazzola, et al., 1964). This article validates the steel intervention structure of architect Sprenger, as traditional techniques would not be able to preserve the tower as is. An interlocking glass solution strives to be an improvement of valid interventions using new technologies. This thesis therefore aspires to be the first step in proving the efficacy of this new way of intervening in monuments, that on many levels is a more valid intervention technique than currently used techniques.

Article 11 states that all "valid contributions of all periods to the building of a monument must be respected" and that "the revealing of the underlying state can only be justified in exceptional circumstances and when what is removed is of little interest and the material which is brought to light is of great historical, archaeological or aesthetic value" (Gazzola, et al., 1964). As is depicted in the forensic analysis of the tower (Appendix B), there are many parts that can be considered valid contributions to the tower. Basically all limestone contributions are valid, as they feature the same material. However, when used as an intervention they may be altered to fit new interventions. Whereas the steel intervention of architect Sprenger is a valid intervention, the contribution to the original is one that is invalid. Material use and general shape makes all steel IPE profiles foreign to the mass and general

look of the tower. The brickwork added by ENCI and Steunbeer bv are also an invalid contribution, as these parts could have been applied in limestone, which would add to the whole. Moreover, it covers parts that are made of original limestone, which now are lost to the eye.

Article 12 then states that the "replacements of missing parts must integrate harmoniously with the whole, but at the same time must be distinguishable from the original so that restoration does not falsify the artistic or historic evidence" (Gazzola, et al., 1964). This article indicates that the replaced parts must be in harmony as well as in contrast to the original. For the former interventions it can be concluded that newly added limestone gives a certain contrast due to difference in discolouring and the application of whole blocks as the original blocks are mostly damaged and worn. Other interventions as masonry brickwork and the steel beams are less in balance and therefore more in contrast than harmonious. A cast glass system could be shaped in such a way to be harmonious while also maintaining contrast with the original, as a ghostly appearance of the past.

Article 13 lastly states that "additions cannot be allowed except in so far they do not detract from the interesting parts of the building, its traditional setting, the balance of its composition and its relation with its surroundings" (Gazzola, et al., 1964). This article is a very strong argument to use glass instead of other available materials. As a transparent material the visitor can choose to solely focus on the structure as it used to be, perceiving the monument in light as the transparency also allows for more light to enter the monument, whereas the current steel solution distracts from the ruin and together with limestone intervention blocks most of the potential light entering the monument.

3.4.3. Restoration decisions on the Lichtenberg Castle ruin

It is impossible to fully restore the whole castle. This due to settlements near the tower (which is assumed to have been the cause of the destruction of part of the castle) and due to the excavations by ENCI Moreover the more recent farm setting of the site has become monumental as well, hence adding large masses or structures would violate this monumental setting as well. The ruin should still be perceivable as a ruin.

Using glass as an intervention material, the perception of the monument remains a ruin, whilst also displaying parts of its former glory. Many of the markings in the ruin have disappeared throughout time in repeated restorations. These were part of the ruin, and bore the marks of its history.

Hence it is possible that ornamental details can be brought back using cast glass elements, such as gothic niches or floor indents where structural elements used to be. These are however not part of the focus of this research, hence these topics are not further pursued.

The parts of the wall that used to feature an opening, such as a door or a window, however can be brought back using cast glass interlocking brickwork. The glass masonry system then consolidates the structure, even more than the current limestone parts, as they would simultaneously replace the steel rod interventions.

Regarding the current status of the materials in the monument, any concrete, masonry brickwork or steel can be removed without a problem regarding restoration principles. These are foreign materials to the structure and hence can be replaced with glass.

The current tissue replacements that are performed using limestone can be adapted if this is deemed necessary for the structure, or if new information marks them as invalid interventions. On this notice, also the closed doors and windows can be opened up again and filled with glass, as this is a more valid intervention. Examples are shown in Figure 55.

Figure 55: Examples of materials to be replaced: a) brickwork entrance; b) steel frame, regular masonry and limestone wall; c) concrete topping and masonry with embedded steel; d) limestone fillings for former doors and window openings. Photographs by author.

Section 3.5. Ruin geometry and structural analysis

The ruin geometry is retrieved from a point cloud and processed in a solid geometry. This geometry is then simplified for applying the new cast glass interventions.

3.5.1. From point cloud to simplified model

Retrieving important measures from a complex geometry, as is the case for the ruin, can be a challenging process. For another research a partial point cloud was made of the ruin, which provides for exact coordinates for all points created with the laser scan. All measurements and derived geometries are hence based on the data in this point cloud.

The translation of the point cloud to a useable geometry was a challenging process. Point clouds can be loaded in Rhinoceros; however the large amount of data makes processing slow and the chance on crashes higher. Autodesk Recap was hence used for altering the point clouds and dividing them into smaller groups of points.

This post-processing of the point cloud is shown in Figure 56. Characteristic points in the geometry are marked in Rhinoceros and connected to outline the boundaries of the solids. Using Autodesk Recap the point cloud is divided into parts that fit within these outlines. Patching the surface untrimmed but including the point cloud partition then results into a boundary surfaces. Using the Grasshopper (GH) command '*boundary volumes*' a solid is created which in turn can be exported to DIANA FEA using STEP-files.

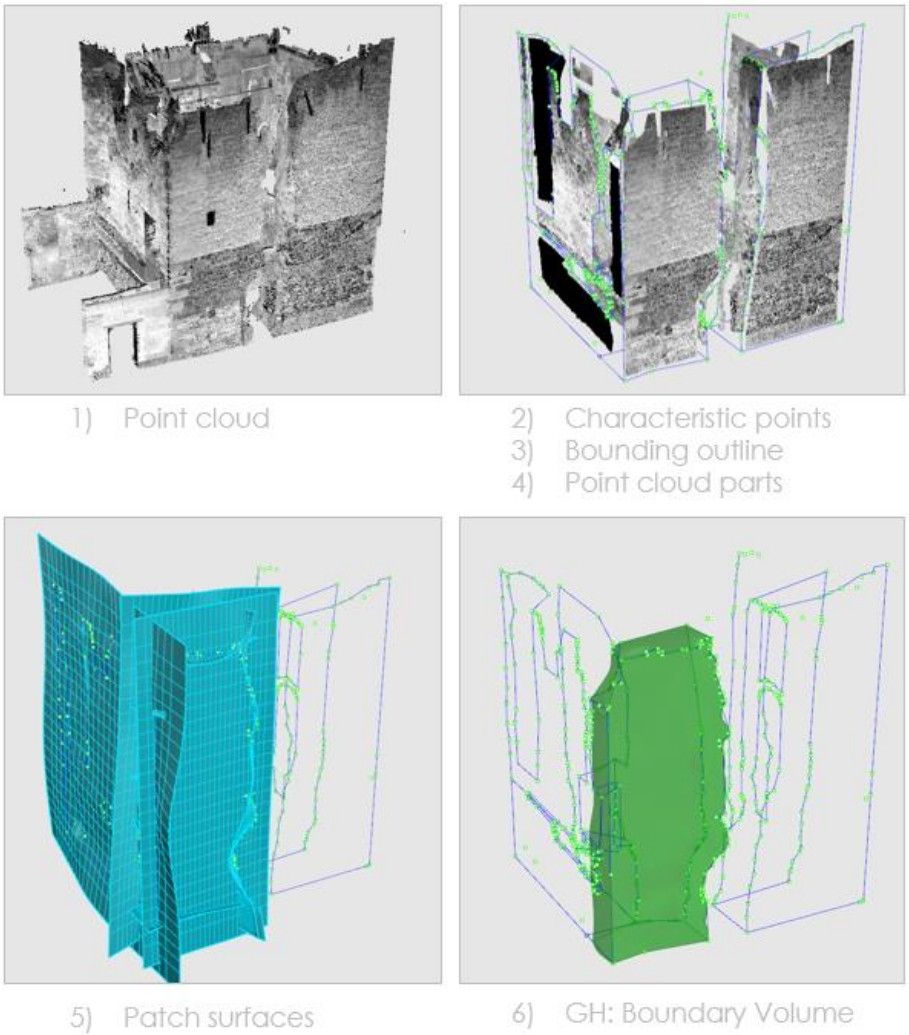

Figure 56: Retrieving solids from a point cloud.

The resulting ruin geometries are shown in Figure 57. Due to missing parts in the point cloud certain surfaces did not have point cloud partitions included in their surface, moreover Rhinoceros did not fill in the blanks, hence the geometry would differ from reality.

With a complete point cloud, this model could be used for finite element purposes to predict for instance new cracks, or even model existing cracks. This however deviates too far from the scope of this thesis and could be investigated on its own.

Hence the model is simplified even more to gain global measurements and is adapted to fit in the new ruin consolidation design. This simplified model is shown in Figure 58 and is used as a base for any measurements illustrations. The values of for instance steel rod locations are retrieved from the original point cloud.

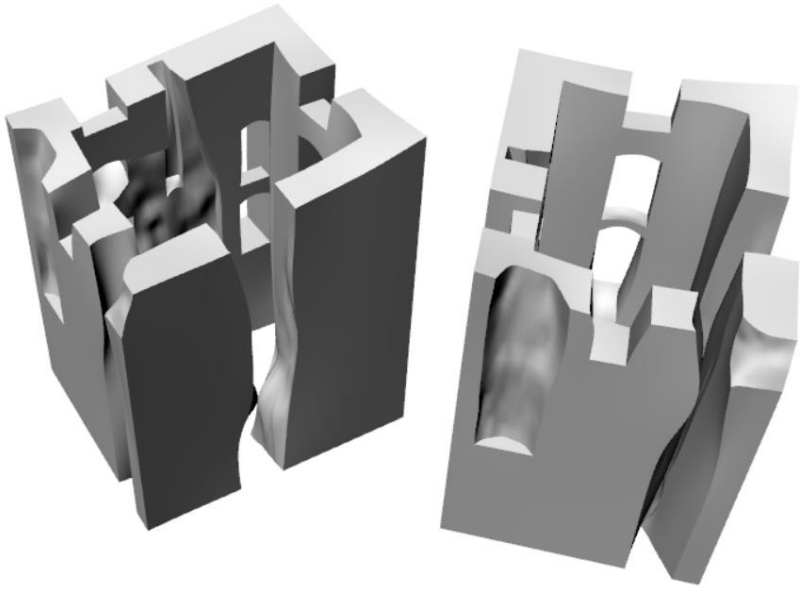

Figure 57: resulting model from patched surfaces.

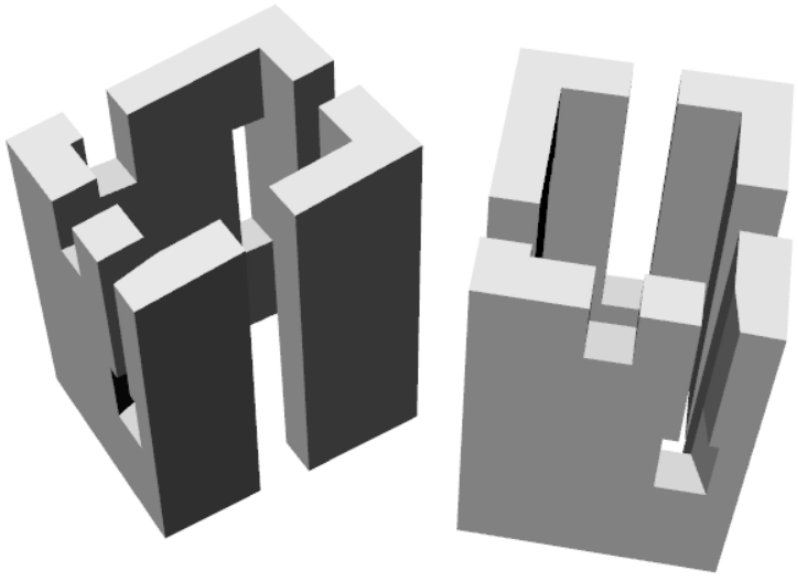

Figure 58: Simplified model with lower detail level.

3.5.2. Replacement of monument interventions

The current interventions of the ruin have to be replaced by a cast glass interlocking system. Hence the following assumptions and simplifications are made. From old technical drawings it can be depicted that the crack once ran fully through the wall until the bottom. Partly this was still the case prior to Steunbeer bv restoration work. Their interventions on this part of the wall are shown in Figure 60. These interventions will be removed for application of the glass system.

Assuming the lower half is still weakened and does not contribute to the structural system, the rotated wall is kept only in equilibrium by the forces resulting from the interventions.

The tower is expected to have been built on top of existing foundations of an even older structure, which was set to the rock. However, as foundation details could not be found in the literature available, none is assumed to exist. This results into a simple model with a certain rotational stiffness on the bottom, as is depicted in Figure 59.

The new glass intervention should hence have the same capacity in the rotational centre as the current interventions.

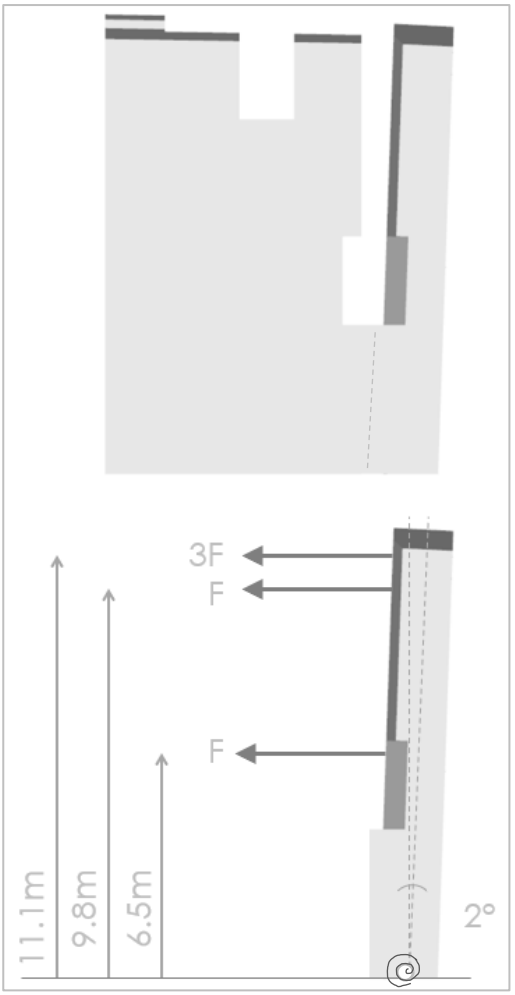

Figure 59 Simplified model including intervention locations.

A quick calculation shows that the resulting moment capacity from the interventions is equal to:

$$M = \sum F * h$$

In which F is the capacity of the interventions and *h* the height as was depicted from the point cloud. The top three tensile rods are applied on the same height, hence 3F.

This results in a total capacity of:

$$M = 1.984\, MNm$$

The applied glass system hence should also result in a capacity of at least 2 MNm at the rotational centre.

It is moreover worth to notice that the assumptions stated in this section are quite conservative, in reality it is expected that the foundation and adjacent wall both also contribute positively to the stability of the system.

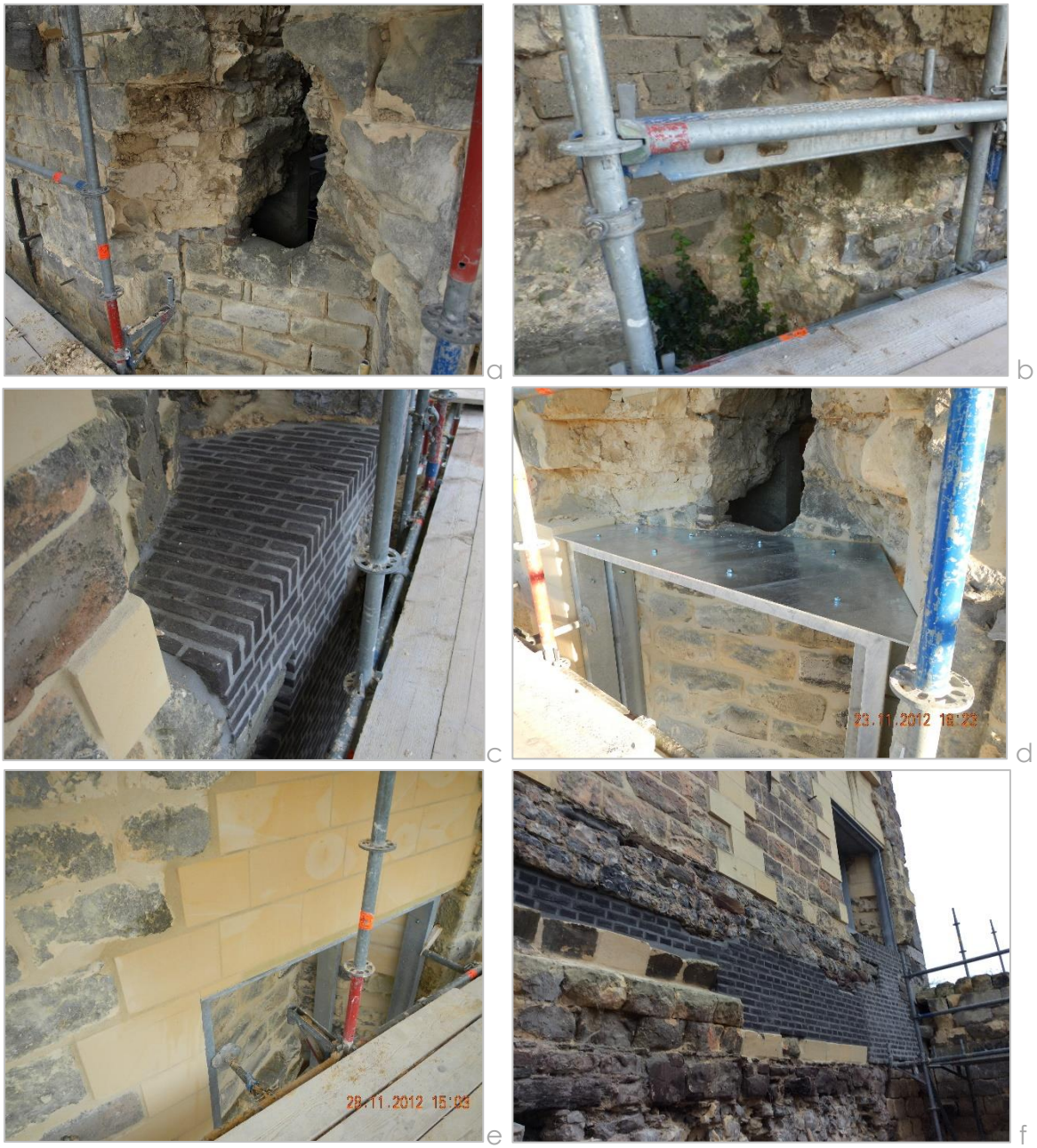

Figure 60: Restoration/consolidation works performed by Steunbeer bv: a) prior to intervention, limestone wall to replace; b) bottom of the limestone wall filling in the crack; c) masonry base for intervention; d) frame support system introduction; e) tissue replacement and addition; f) complete intervention applied. Reprinted with courtesy of Steunbeer bv.

3.5.3. Acting loads on the structure

To put this simplified capacity in perspective, simplified loads are calculated for the structure. Firstly, the initial tilt of the wall is a loading condition that will always be present. The tilt hence results into an initial permanent loading when compared to the rotational centre. Secondly there is the wind loading on the structure. Only wind loading in the most negative direction is considered, as this would increase the tilt of the wall. Lastly there is also an earthquake load to take into account. For this load a simplified calculation is made, only applied on the inclined wall. Hence a difference in frequency between this wall and the other may enhance the earthquake effects.

Initial tilt

The permanent loading implied due to the initial tilt can be calculated as an eccentricity of the mass centre of the wall in respect to the rotational centre of the wall. Hence the following moment can be derived around the rotational centre for a tilt of $\alpha = 2°$ and a wall density of $\rho = 1500$ kg/m^3.

$$M_{initial} = F * e = \rho * h * w * d * g * \frac{1}{2} h * \sin(\alpha)$$

$$M_{initial} = 1500 * 12 * 4 * 1.6 * 9.81 * \frac{1}{2} * 12 * \sin(2) = 0.237\ MNm$$

Wind load

The wind load is calculated according to the NEN-EN 1991-1-4. Two wind directions have a negative effect on the already tilted wall. These are suction due to a North-Western wind or due to a South-Western wind, here indicated in Figure 61.

The tower is located in wind area III and hence has a basic windspeed of $v_{b,0} = 24.5$ m/s^2. Due to the location of the tower, on a cliff top, terrain orography should be taken into account. The values used for determining these factors are shown in Figure 62. For the two wind-directions under review this results in a $c_{0;NW} = 1.51$ and $c_{0;SW} = 1.22$.

The tower's terrain classification can be set to terrain category II: Unbuilt area, as there is only low vegetation and a lower farm complex near the tower. On other sides there is an abyss of approximately 57 metres. The roughness factor resulting from this classification is equal to: $c_r(z = 12) = 0.86$.

The following mean wind speeds are hence applicable for both wind directions:

$$v_m(z) = c_r(z) * c_0(z) * v_b$$

$$v_{m;NW}(12) = 0.86 * 1.51 * 24.5 = 31.8\ m/s$$

$$v_{m;SW}(12) = 0.86 * 1.22 * 24.5 = 25.7\ m/s$$

This is equivalent to an extreme wind thrust of $q_p(12) = 1.3$ kN/m^2 and 1.0 kN/m^2 for respectively the NW and SW directions. Without a roof or look-out plateau the structure can be perceived as a chimney, which inner suction would be beneficial to the wind loads. To be conservative this is not taken into account, and the before mentioned extreme wind thrusts are conservatively taken over the whole height of the wall. Calculating the effects on the tilted wall then result in the following moments for both walls:

$$M_{wind} = \frac{1}{2} h * c_s c_d * \sum_{elements} c_{pe,10} * q_p(z_e) * A_{ref}$$

In which $c_s c_d$ is conservatively taken as one, wall areas are retrieved from the geometric model and $c_{pe,10}$ factors are chosen according to the Eurocode. This yields the following moments for both walls:

$$M_{wind;NW} = 0.188\ MNm$$
$$M_{wind;SW} = 0.266\ MNm$$

Hence a South-Western wind is normative.

Earthquake load

Due to the high mass of the inclined wall, the earthquake load has shown to be normative. An earthquake with an acceleration of 0.12*g can be expected in this region (Vanneste, et al., 2009). A rough estimation of this load is calculated below:

$$F = m * a$$
$$F = \rho_{limestone} * h * b * d * a = 1500 * 12 * 4 * 1.6 * 0.12 * 9.81 = 0.136\ MN$$

This force considered from the rotational centre results into an acting load of 0.814 MNm. It is however important to notice that in the case of an earthquake the other adjacent wall might move differently and hence can increase the load on the cast glass system. A more detailed earthquake analysis of the whole ruin is necessary to give definitive conclusions considering earthquake loading.

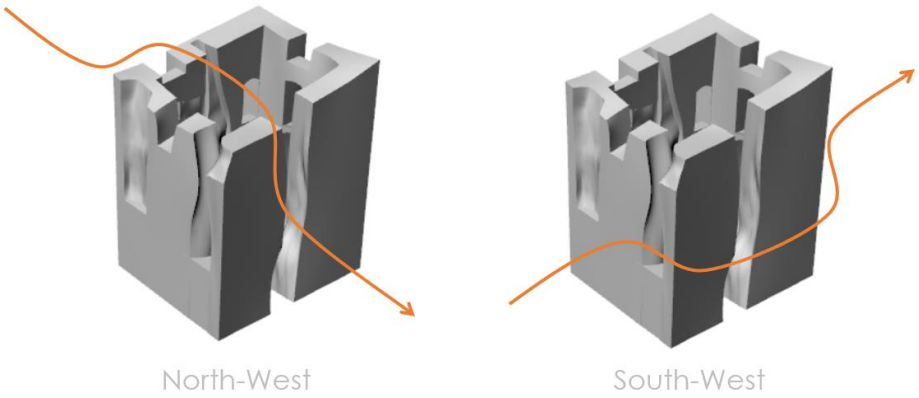

Figure 61: Unfavourable wind-directions, suction due to a North-Western wind or due to a South-Western wind.

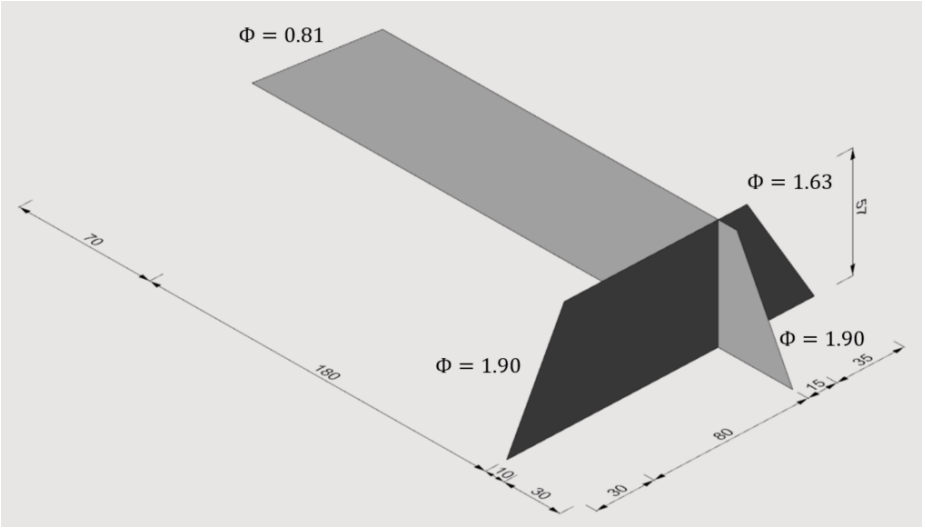

Figure 62: Terrain orography values assumed for wind calculations.

Chapter 4.

Parametric definition of a glass brick

From the previous chapters certain design criteria can be determined. Hence a new design of a cast glass brick can be derived from these design limits and choices. The generation of this geometry is done parametrically, and variations can be created automatically with Grasshopper (GH). The expectations of parameter variations hence are discussed as well as the critical brick in the design.

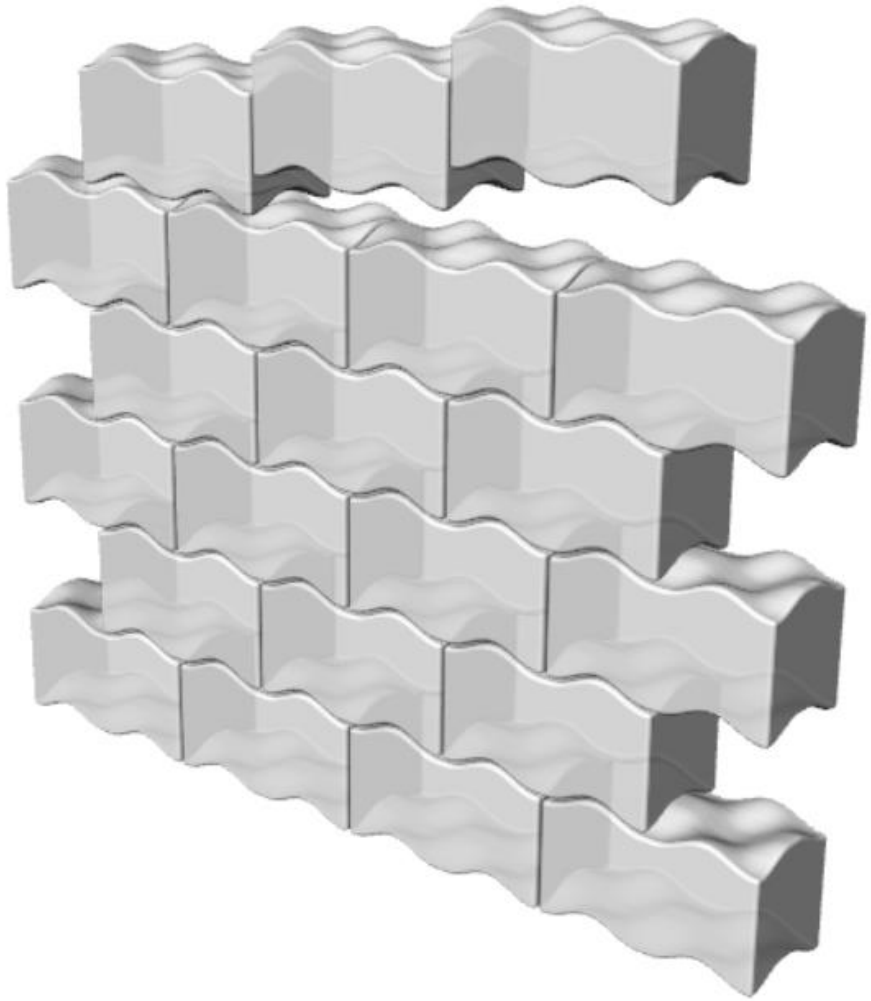

Section 4.1. Parametric approach

The geometry of a cast glass interlocking brick will influence its mechanical properties. Due to various design limits and choices the geometry is bound to be too complex to calculate by hand. Hence calculations will be done using Finite Element Analysis (FEA) software, in this case DIANA FEA.

To determine the optimal values for the dimensions of the glass interlocking brick a parametric model is set up for the initial design, which then is investigated using a sensitivity analysis, by varying certain leading parameters.

Hence the parametric approach is best described as visualised in Figure 63. The design limits and choices follow from the literature study and case study investigation. These are then translated into an initial design, from which certain parameters will be further investigated in Chapter 5.

The determination of which parameters to investigate follows from analytical predictions, as well as the ranges that will be reviewed.

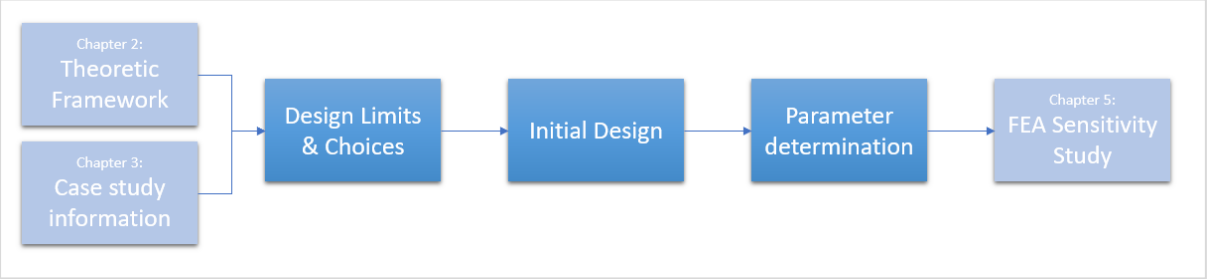

Figure 63: Parametric approach as discussed in this chapter.

Section 4.2. Design limits and choices

As mentioned in Chapter 2, an interlocking system is subject to its function, boundary conditions and loading conditions. The geometry of a brick in this system therefore follows the design limits and choices that flow from these conditions.

4.2.1. Functional design limits, material aspects and reusability

The function of the interlocking cast glass brick will be a consolidation measure, and therefore a structural intervention in the monument. Its shape therefore is largely dependable on the loading conditions. There are however several functional aspects and practicalities to take into account.

Constructability & multifunctionality

A masonry system is generally build from bottom to top, stacking brickwork to create a wall. To accommodate vertical stacking of elements it is important that no locks intervene with the assembly, hence the vertical contact faces between bricks remain flat. To achieve a smooth planar wall, the other vertical faces remain flat as well.

Using flat surfaces for all vertical faces moreover increases the systems multifunctionality, as different configurations can be used while assembling the bricks (e.g. double walls or columns). The interlocking geometry therefore is only applied to the remaining two faces, the top and bottom face.

For easy assembly and cheaper manufacturing the geometry therefore should be repetitive, each brick therefore is preferred equal in size. This allows for making reusable moulds and a standardised production technique. Assembly becomes easier as each brick can take any place in the structure, instead of predefined locations, as is the case with systems featuring multiple geometries.

Using a single geometry also provides better prospects for reusability, as there is not only one valid configuration. Take for instance the in Chapter 2 mentioned Incan structures. Each stone had to be manufactured individually to fit exactly the structure, reusing them would only be possible in the same configuration, or one would have to alter the stones. For glass this would mean re-melting and re-casting. A standardised brick geometry would allow for other assemblies then the initial configuration.

Material aspects

Regarding the overall shape it is important to take some material factors into account. Glass is known to prefer an ellipsoid shape, increasing internal residual stresses when it is forced to solidify in pointy edges. The design therefore should focus on a more convex geometry, with as few as possible sharp turns or edges.

To prevent more residual stresses when annealing the glass, it is important to keep the cross-sectional area equal throughout the brick. This way the brick can gradually cool down uniformly and residual stresses can be reduced.

Damage and failure of the system

If due to an extreme loading event damage is initiated in the system, there should be a warning mechanism in place. This warning mechanism should occur in the system and not in the historical tissue of the monument.

Summarizing the design limits and choices regarding functionality, reusability and material aspects, the design should have:

- flat vertical faces;
- smooth convex curvatures and preferably approaching an ellipsoid;
- equal thickness/height throughout;
- as few as possible sharp turns or edges;
- a warning mechanism before failure should be placed in the system;
- a multifunctional character, for reusability (e.g. multiple possible configurations).

4.2.2. Boundary and load conditions of the system

The boundary conditions are important for interlocking systems, as a failure in the boundary conditions could lead to a failure of the system. As mentioned in Chapter 3, the most dangerous crack in the ruin is at the western side, as depicted in Figure 64. The new system should prevent further leaning over of the southern wall.

Wall-to-wall connection

The system should be able to convey the wind load on the adjacent wall and counter the load induced by the initial inclination. Both create a pulling effect in the plane of the wall. This boundary condition therefore can also be considered a load condition, and is the leading condition for the geometric design as the interlock geometry should be able to convey these loads. A shear lock should therefore be introduced in the in-plane direction.

The wall-to-wall connection should at least accommodate the same strength when compared to the current steel interventions. These are calculated in Chapter 3.

The sides of the system should be anchored into the walls, to connect the system to the original structure. These connections should be rigid enough to convey the loads properly onto the interlocking bricks, while ensuring minimal (visible) intervention to the original monument. Furthermore, the connection on the system side should be weaker than the connection in the historical tissue, to prevent further damage to the monument.

Keystone
Due to the pulling forces, uplifting is expected to pose a problem, as they will try to lift the interlocking brick from its place. A keystone element therefore is necessary to keep the whole interlocking system in place. This keystone should not restrict movement in the in-plane direction, as that could influence the expected damping properties of an interlocking system, any restriction of movement would increase the rigidity of the system (Ali, Briet, & Chouw, 2013). An in-plane sliding connection of the keystone is therefore preferable, while restricting out-of-plane movements. This also accommodates thermal expansion of the bricks and the structure around the new intervention.

Bottom connection
In the bottom an in-plane sliding connection is also preferable, for the same reasons as the keystone connection. Perpendicular to the plane movement should be restricted. The bottom connection should be levelled and designed in such a way that it remains level throughout its lifetime as well.

Wall surface
The wall surface is subject to wind loads and impact loads. Therefore there should be shear resistance of the bricks in the out-of-plane direction as well. Shear locks therefore should be introduced in this direction.

To summarize the following design limits follow from boundary and loading conditions:
- Shear locks should be applied both in in-plane and out-of-plane directions;
- An anchored connection should be applied for wall-to-system connections, which:
    - is weaker on the system side;
    - rigid enough to convey loads acting on adjacent wall;
    - should have at least the same capacity as current interventions;
- Sliding connections for both keystone and bottom connection;
- Keystone should prevent uplifting from occurring;
- Bottom connection should be level and remain so.

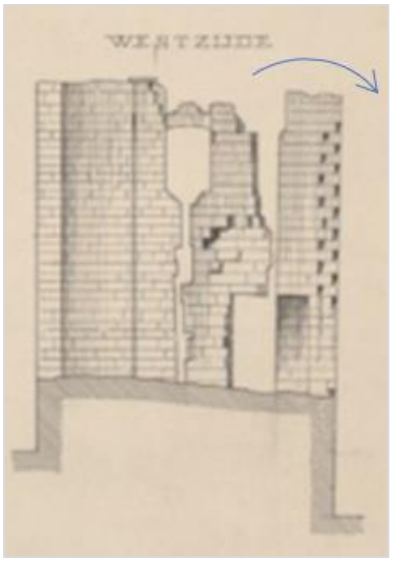

Figure 64: Critical crack in western wall of Lichtenberg ruin. Adapted from (Anonymous, Gevelaanzichten, 1881b).

Section 4.3. Parametric geometry definition

This section explains how the design criteria are translated into a potential brick design and how variations on this design then are generated through parametric modelling in Grasshopper.

4.3.1. Translation design limits and choices to initial design

The previously discussed design limits provide sufficient input for a new brick design. A rough flow of the design process is shown in Figure 65.

Starting point is set to a flat regular masonry brick. The vertical faces remain planar for easy assembly and to allow for different configurations. This leaves the top surface for geometry variations.

To keep a homogeneous thickness throughout the brick the geometry deviation on the top is equal to the geometry deviations at the bottom. Symmetry is applied to keep the geometry singular and easy to assemble.

A smooth and gradual geometry works well for preventing peak stresses to occur, moreover the material glass prefers ellipsoid shapes. Hence the interlocking geometry applied follows a sine curve. Applying this shape in one direction provides a locking mechanism in that direction.

To achieve an interlock in both directions the geometry should be altered in the other direction as well. Therefore a sine function is applied in this direction as well.

The design idea behind that, is that when shear forces are applied onto the geometry, the deformation tendency determines the opposing geometry. This design principle is shown in Figure 66. The middle cross-section therefore is an inverse of the edge geometry, hence introducing a 3D stiffness effect. This repeating inverse/non-inverse geometry is clarified in Figure 67a. The resulting interlock geometry is shown in Figure 67b.

This design principle promotes its multi-functionality. The brick geometry should be able to be used in multiple configurations. By keeping the sine function constant in both directions, symmetry allows for this multifunctionality. Hence the geometry can be used for single and double walls, or even columns, as depicted in Figure 68.

Lastly edges should be rounded to prevent any sharp turns in the geometry, which then leads to the final brick design. Assumed initial dimensions are 300 millimetres in width, and 150 millimetres both in depth and in height.

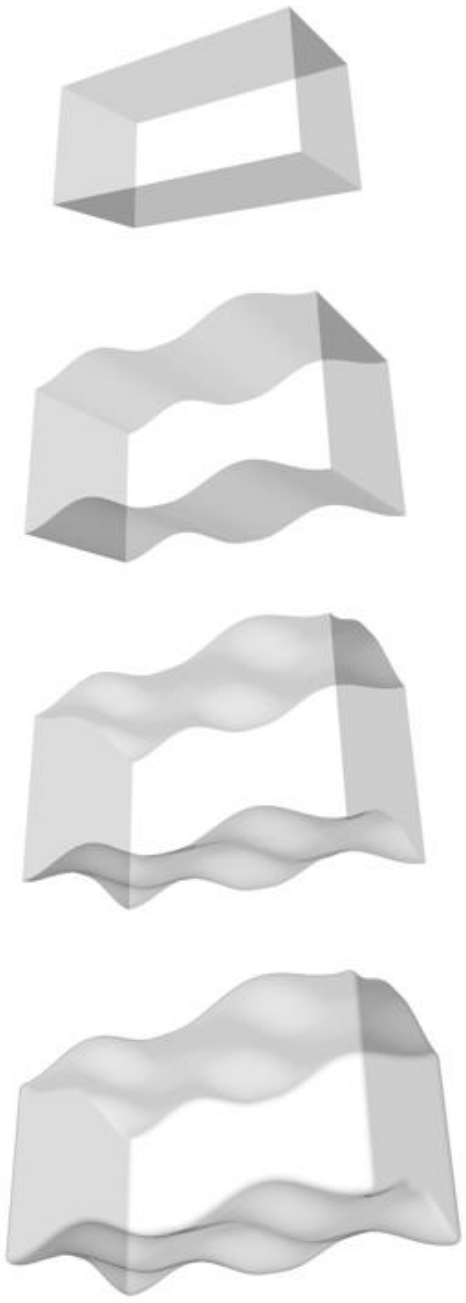

Figure 65: Design flow from masonry brick to interlocking brick geometry.

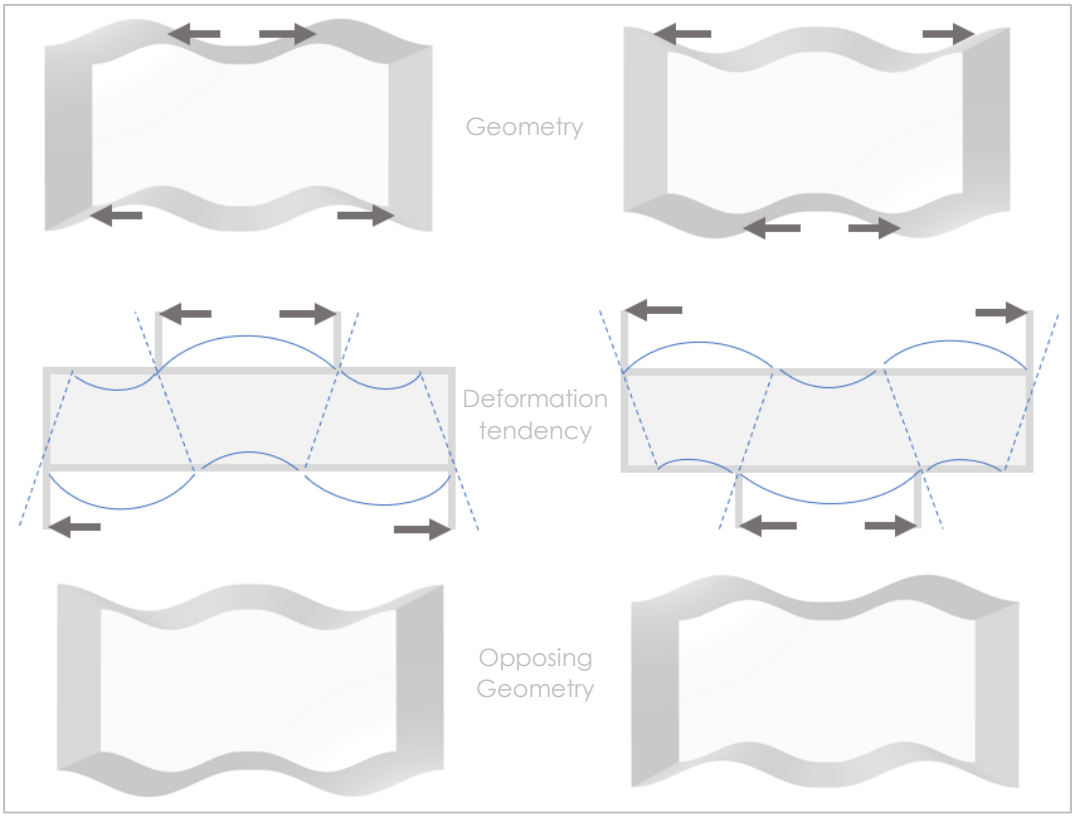

Figure 66: Geometry design principle, tendency to deform strengthened by opposing geometry.

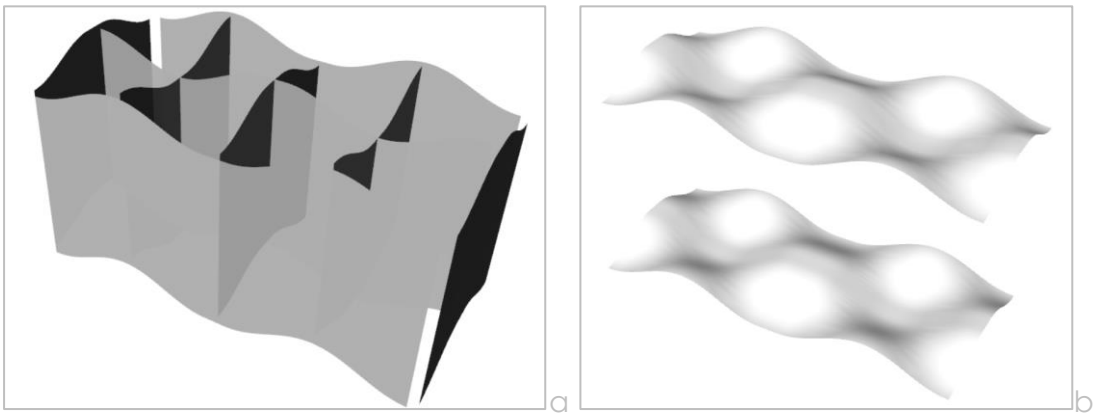

Figure 67: a) Repeating cross-sections and inverse cross-sections; b) Resulting interlock geometry planes.

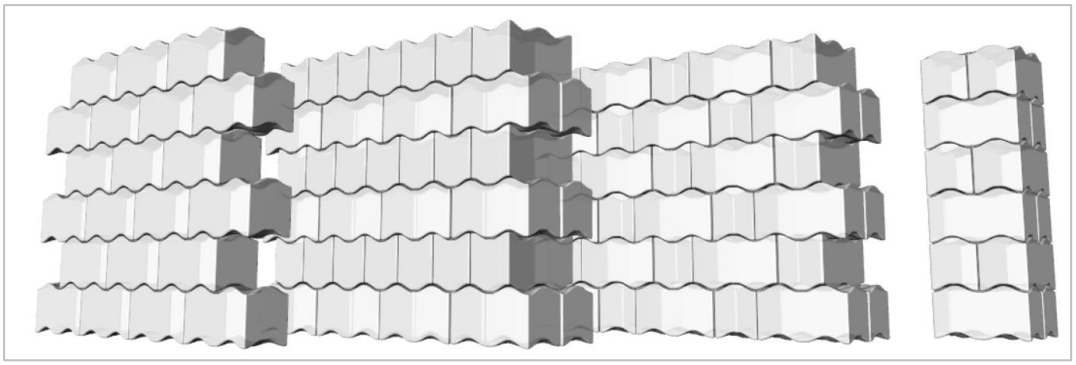

Figure 68: Possible assembly sequences due to the multifunctional geometric design, from left to right: single layer masonry wall in running bond; double wall using English bond; double wall using Flemish bond; column configuration.

4.3.2. Variable parameters in the design

Below decisions are made whether to vary certain parameters in the design. All parameters discussed are graphically shown in Figure 69 and the decisions made here will influence the parametric model generation in Grasshopper as well as the analytical predictions of the effects of the parameters on the performance of the geometry.

Interlock definition

The initial design is based on decreasing peak stresses by adding a gradual curvature in the interlock geometry. Consequently, the interlock formulation is one of the primary parameters which will influence the capacity of the glass interlocking brick.

Within this interlock definition, various parameters might affect the performance of the interlock. Its amplitude for instance is expected to highly influence the shear capacity and uplifting behaviour. A higher amplitude would increase the contact area for stresses to spread on, while reducing the uplifting behaviour by increasing its slope.

Another way to influence the geometry is to apply linear parts in combination with the sine function. This would be beneficial for post processing, as the increase of flat surfaces are easier to polish while maintaining the overall geometry.

Hence the amplitude and a sine/linear geometry combination will be reviewed as variable parameters.

Overall dimensions

The overall dimensions of the geometry are other parameters that influence the overall capacity of the brick. However, due to the multifunctional nature of the brick, it is important that the ratio between width and depth remain the same. This way different configurations will be possible.

The height however can be varied freely and is hence an interesting parameter to investigate, as it is expected that this parameter influences the failure mechanism based on brick slenderness. A shear key failure is desired, as this is expected to lead to the chipping off of one of the keys, instead of fully splitting a brick. Hence the height is taken on a higher value, equal to its depth.

Interlayer thickness

The interlayer thickness itself will not be varied in the research, as the performance of the interlayer is a different research on its own. The option is however already built in for future use. For now, a thickness of four millimetres is taken as an assumption, based on experimental results in Aurik (2017). More experimental research is necessary to gain a full overview of the working of the PU interlayers.

Radius edges

As there cannot be any sharp corners or edges to prevent peak stresses to occur during assembly, the whole brick geometry will be given rounded edges. This offset can be chosen parametrically, but will not be further evaluated in this thesis as it is expected to have minor influences in the modelling. A radius of six millimetres is chosen as an assumption.

Number of interlocks

The number of interlocking curvatures can be increased, however post processing would be more intensive and the chance on deviations is higher with each interlock. Given that the chosen geometry is already quite complex, it is chosen not to vary further on base of bigger problems during post-processing and deviations. It is however interesting to revisit this topic when complex glass bricks can be made with very slim tolerances.

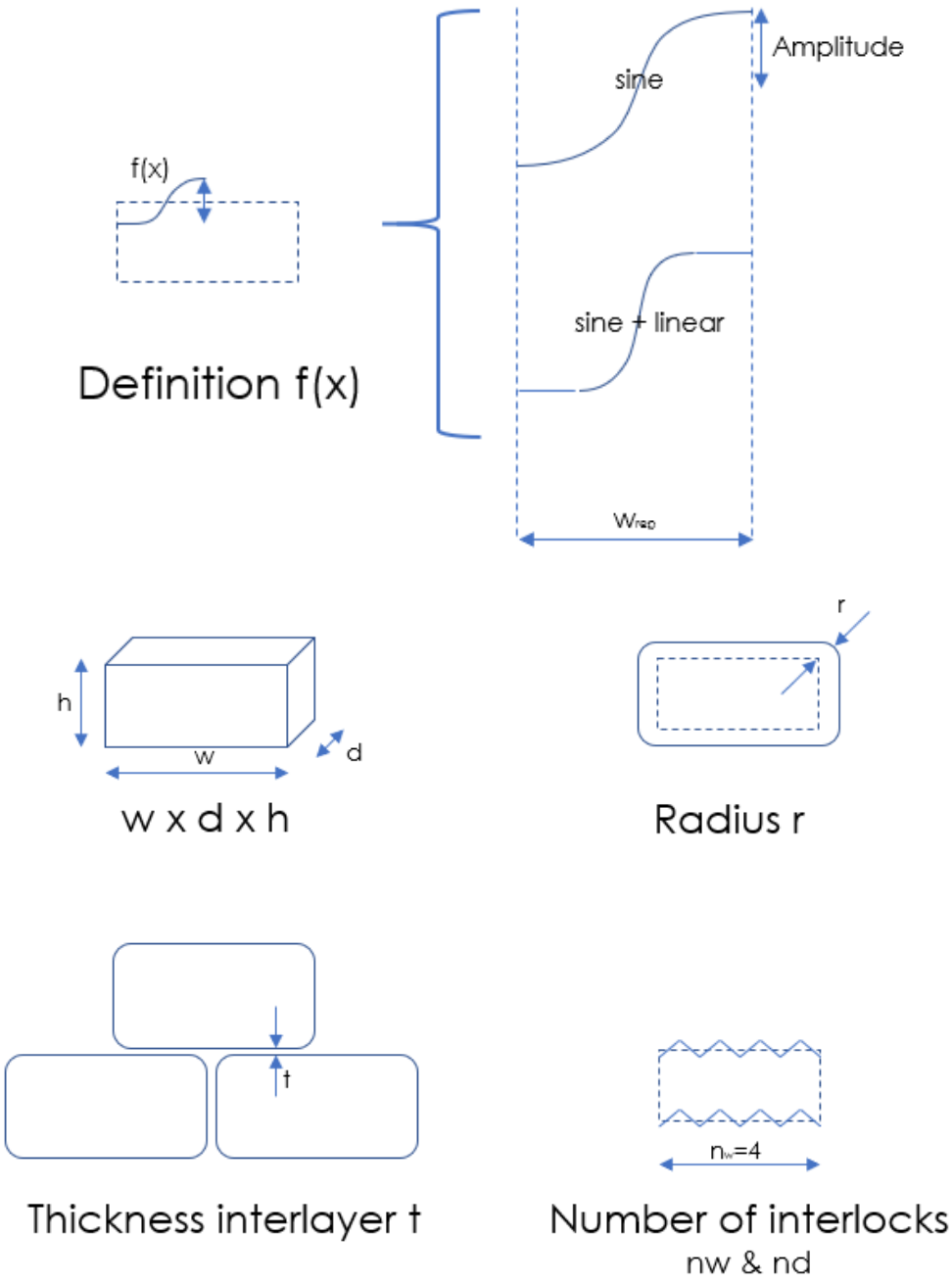

Figure 69: Possible parameters to investigate.

4.3.3. Parametric model generation in Grasshopper

The geometry is generated through the Grasshopper plug-in for Rhinoceros. This plug-in allows for automatic generation of new geometries by changing certain input parameters. The parameters discussed in the previous paragraph for instance. Hence it is a great tool to generate geometries of which the most beneficial dimensions are not certain yet or when multiple geometries are needed for sensitivity studies of the parameters. The working of grasshopper itself is further not discussed in this thesis, internet provides plenty tutorials and information on this topic. Here the most important principles behind the modelling are discussed. The GH-script used in this thesis is reviewed in detail in Appendix A.

Interlock definition

The model revolves around setting up the interlocking geometry and therefore forms the base of the parametric model. Therefore, first the sine function is introduced, including some horizontal lines to implement the interlayer thickness. This small adjustment needs to be applied in order to fit the geometries correctly together in masonry patterns. The initial sine curve and its linear additions are shown in Figure 70a. The geometry is then mirrored multiple times to gain the edges of the interlocking geometry.

Defining the bounding surfaces

When the edges are defined in both directions, the edges are moved into place according to the parameters for brick dimensions as shown in Figure 70b. The surfaces in the curved edges are generated with a 'Sweep-2-curves' command, which basically plots a surface between two lines according to a cross-sectional curve definition. For planar surfaces or singular curved surfaces, a 'loft' command is sufficient for generating the geometry. The resulting surfaces are shown in Figure 71.

For the top and bottom surface the process is somewhat more complicated. The top and bottom surface shown in Figure 71 has been cut from a larger geometry to exactly fit into the brick design. This larger geometry is created using the 'network surface' command, which basically plots a surface from the given curves. By adding more curve geometries, it is ensured that the geometry has exactly the right curvature at the location of the cuts. Hence the surfaces will match exactly. The process leading up to creating the larger surface geometry is shown in Figure 72, including the spacing of the curves (due to the implementation of the interlayer thickness).

Generating a solid

The surfaces are then all collected and put through a 'boundary volume' command. This command creates a solid from input surfaces, but only works when the surfaces combined create a closed geometry.

Certain combinations of parameters therefore do not result into valid solids. This mostly occurs when higher curvatures are generated, or when higher amplitudes are combined with greater linear/sine ratios in the case of linear-sine combination geometries.

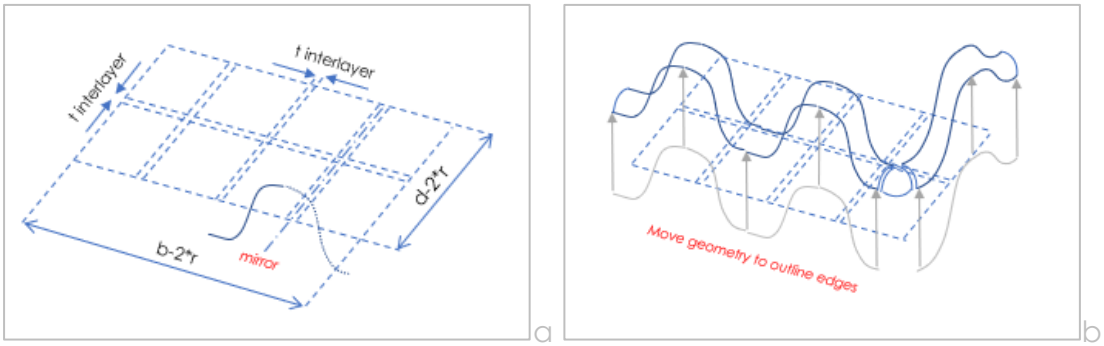

Figure 70: Defining the interlock a) initial curve and mirroring; b) moving geometry in final position.

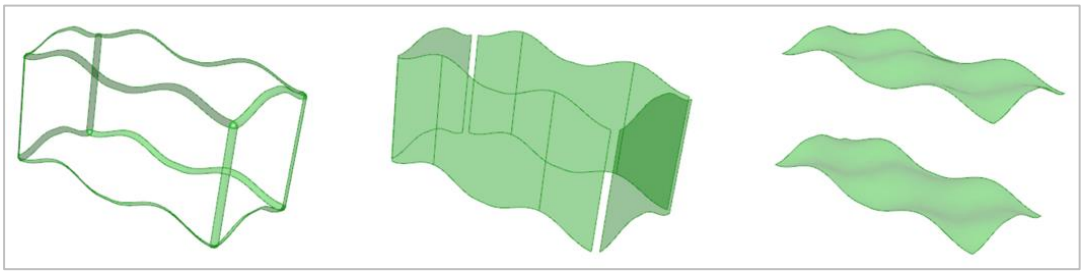

Figure 71: From edges to surfaces of the curved edges, flat vertical surfaces and top/bottom interlocking geometry.

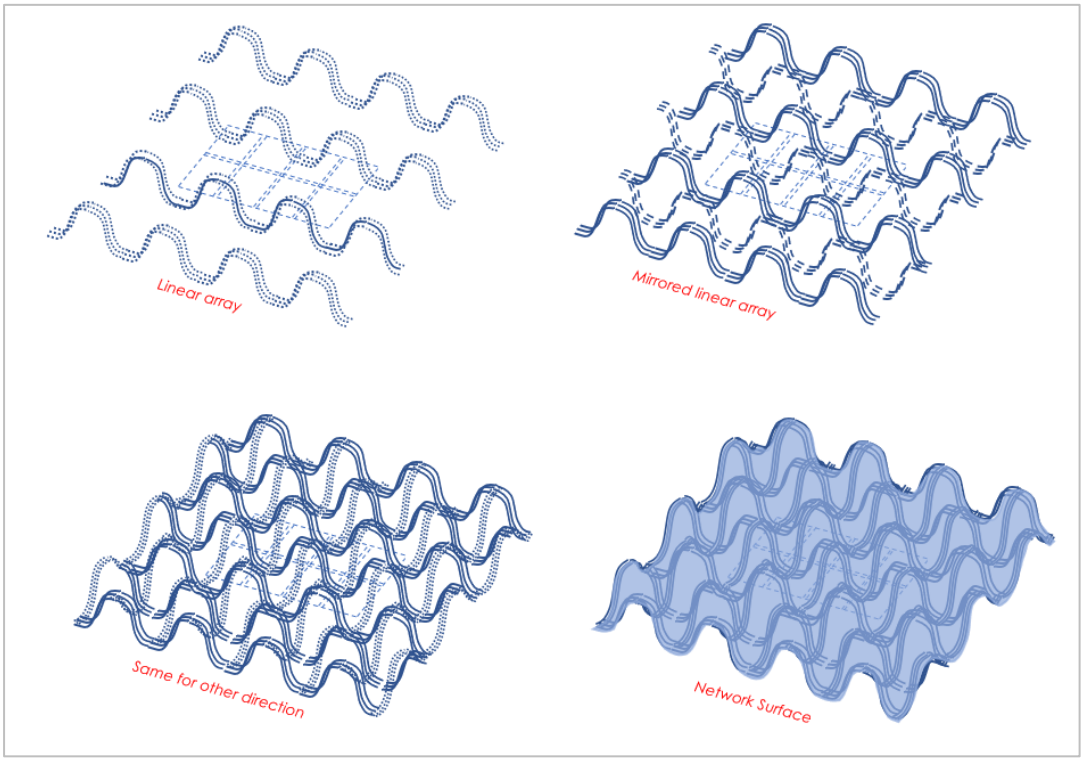

Figure 72: Defining the interlocking geometry for the top and bottom surfaces.

Section 4.4. Parameter variation expectations

Prior to calculating the influences of the parameters with a finite element model, coarse analytical expectations are determined using simplified calculations. This section will provide an insight in the expected working of the model. The modelling moreover calculates a perfect brick; therefore the expectations take this into account. However in reality, the bricks will have certain deviations from the perfect geometry, even after post-processing. Hence on these effects will also be commented.

4.4.1. Effect of the height of parametric brick

The height of the brick is expected to have direct influence on the failure mode of the glass brick. A too thin brick of glass would gain more stresses due to eccentric loads (failure through bending), while higher bricks are more resistant to this, leading to shear key failure (failure through shear).

These failure mechanisms are expected to occur in the most flaw-prone area, as will be gained from the Christensen's failure criterion. The upper boundaries will be determined from a simplified hand calculation using the characteristic strength of glass. It is expected that the real value lies somewhere below, as the combination of the principal stresses in the Christensen's criterion lead to failure before reaching this characteristic value.

Bending failure

The 3D geometry would be subject to an eccentric load at the top and bottom plane of the geometry. Assuming the full force going into the upper shear lock, and concentrated halfway the shear lock. The height will be expressed in multiplications of the amplitude. This simplified representation of the reality is shown schematically in Figure 73.

The local peak stress is equal to:

$$\sigma = \frac{F}{b * h} + \frac{F * e}{\frac{1}{6} * b * h^2}$$

Filling in the simplified model proportions gives:

$$f_{g;k} = \frac{F}{b * Ax} + \frac{F * \frac{1}{2}Ax}{\frac{1}{6} * b * (Ax)^2}$$

Filling in the initial parameters: A = 10mm; b = 150mm; and σ = 45 MPa yields:

$$45 = \frac{F}{150 * 10x} + \frac{F * 5x}{\frac{1}{6} * 150 * (10x)^2}$$

$$F_{max} = 16875 * x\ [N]$$

The maximum shear force hence increases linearly with the amount of amplitude multiplications applied for the height.

Deviations from the original cross-section in reality would not influence the resulting value much, however any surface flaw in the interlock would introduce (tensile) peak stresses around this flaw and hence initiate earlier failure of the glass brick. Proper manufacturing and post-processing to reduce these flaws and discontinuities are therefore key to approaching this calculated value.

Shear key failure

The same principle is applied for a shear key failure. As the geometry is perfect and thus without deviations from this perfection, all shear keys will resist shear key failure simultaneously. Concentrating the shear force once again halfway the interlock geometry, the maximum shear force can be determined as follows, using the area of the three resisting interlock cuts as shown in Figure 74 and assuming a maximum tensile stress in one principal stress direction.

$$\tau = \frac{\sigma_1 - \sigma_3}{2} = \frac{45 - 0}{2} = 22.5\ [MPa]$$

$$F_{max} = \tau * A_{shearing} = 22.5 * 7922 = 178252\ [N] \qquad [\ 4.1\ ]$$

This value therefore is a linear ceiling value for the maximum applied force. In reality this value will differ from the modelled capacity. Natural shrinkage of the material while cooling down can deform the geometry slightly to a less proper fit. The shearing keys will then be loaded unevenly, hence one of the shear keys will fail earlier than the others in reality. The polyurethane layer is meant to make up for some of these deviations, and spread resulting peak stresses more evenly from brick to brick.

These areas are moreover very prone to flaws, even when globally the area would be under compression, a flaw could introduce local peak stresses and highly influence the brick's capacity. Proper manufacturing and post-processing again are key to higher capacities of the brick. Perhaps after a study on the influence of shrinkage on the geometry, the geometry can be slightly adapted to gain the required shape after cooling down. This however would require a high control on the manufacturing process and probably many iterative castings to gain a relative perfect brick. To indicate some deviation problems prototypes are manufactured, but with regard to time testing and adapting the geometry input to account for this shrinkage is not in the scope of this thesis.

The deformation of the polyurethane interlayer at a Christensen's value of CHR = 1 can indicate how much of a geometry deviation can be countered by spreading the load through the polyurethane. The lower this interlayer deformation, the smaller the deviations can be and the closer the geometry should be to a perfect state. Hence larger deformations of the interlayer at a Christensen's value of one are preferred to small rigid deformations.

Moreover it is worth to notice that the interacting forces on the geometry are not at all in a horizontal manner (i.e. global X-direction). The geometry will react from a horizontal distributed load perpendicular to the surface (normal direction) and along the surface (tangential direction). This normal direction is different throughout the whole contact surface due to the interlock geometry. Hence crack propagation coming from a flaw will most likely initiate in this normal direction and then go for the weakest route through the glass. The shearing area in this case is higher than presented above, and consequently the shearing capacity as well. The principal stresses however are in reality also not equal to 45 and 0, but somewhere in between, which then would lower the capacity. Hence the value determined above is just an indicative value to predict the order of magnitude in a simplified manner.

Resulting expectation graph

Combining both values as a maximum result coming from the test the following graph can be drawn as a ceiling value for the results expected from the model, see Figure 75. Due to the assumption of a maximum tensile stress, the results from the tests are expected to be somewhat below these lines, as in the Christensen's failure criterion 3D effects are taken into account.

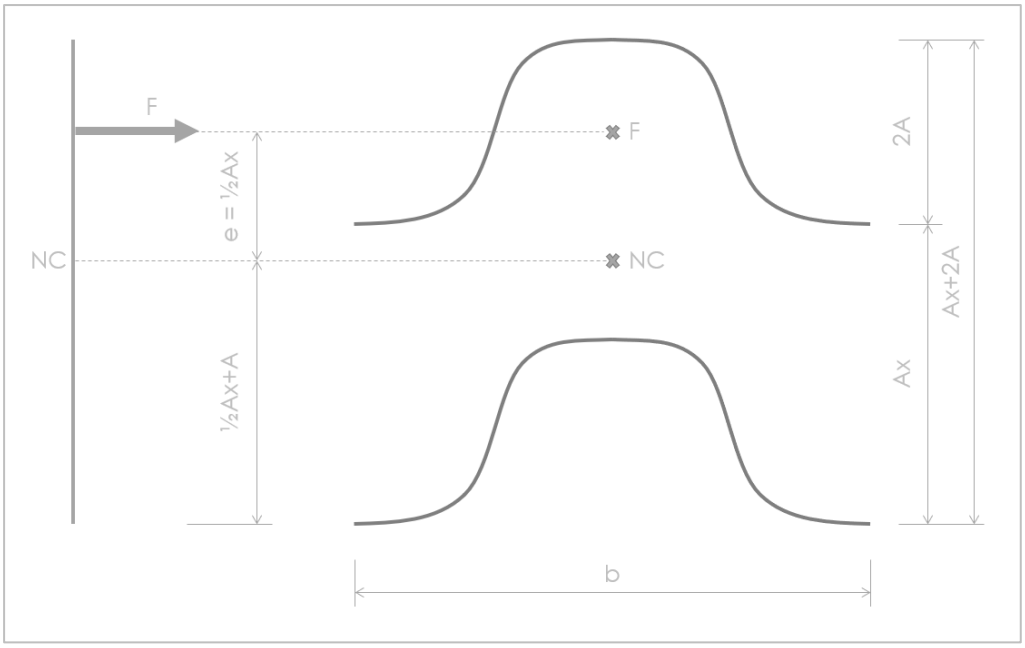

Figure 73: Schematic showing the simplified representation of bending failure occurring in the geometry.

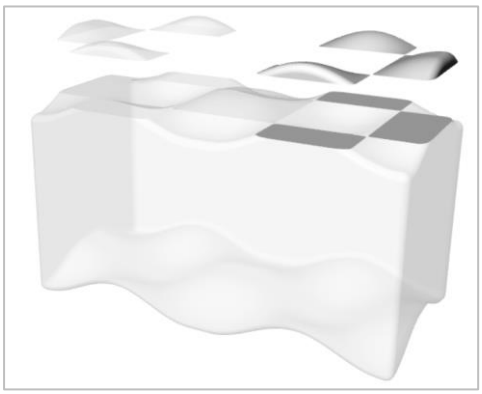

Figure 74: Shear failure area determination, in grey the shearing surfaces for the simplified calculation.

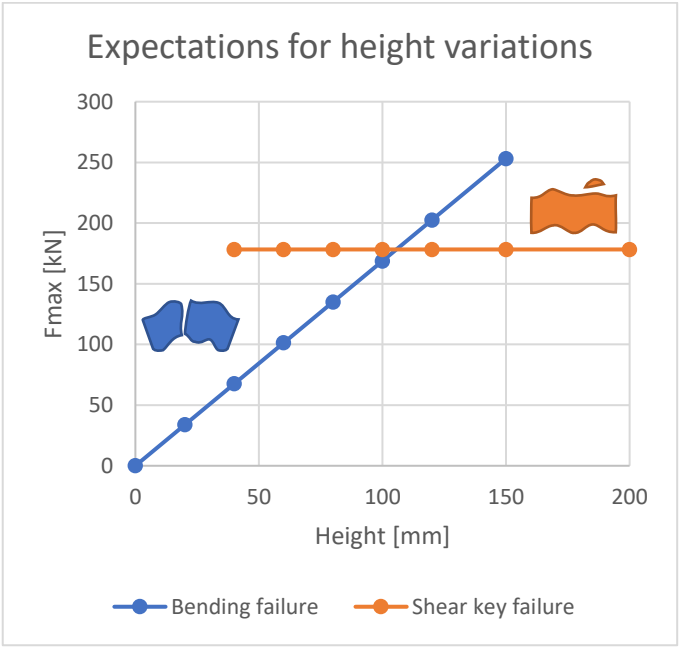

Figure 75: Graph indicating ceiling values for bending and shear key failure mechanisms.

4.4.2. Amplitude shear key

The shear key's amplitude is expected to have a certain amount of influence on the shear capacity of the brick. Increasing the amplitude would result in a larger contact area for the bricks, hence the load applied is spread over a larger surface. This consequently would lead to a higher capacity, as a higher load needs to be applied to reach a maximum peak stress somewhere on the surface.

However, it is difficult to quantify this effect due to the complex geometry. Hence the prediction is based on the parameter range tested (see section 4.5). From these models the contact surface is retrieved using Rhinoceros, and a prediction is based on the previously calculated shear key failure (Equation 4.1) times the ratio of contact surfaces between the amplitude deviating geometries and the initial geometry. This yields the values given in Table 6. Converting these values into a graph the image in Figure 76 is obtained, providing with the expected capacities for the shear strength when deviating the amplitude.

Due to an increase in amplitude, the uplifting behaviour would be affected as well. Keeping all other dimensional parameters equal, an increase in the amplitude would increase the steepness of the curve as well. With increasing steepness, a larger quantity of the force will be taken by the geometry normal to the surface, and a smaller portion by traction. This principle is drawn up for a small amplitude and a larger amplitude in Figure 77 in the case of equilibrium.

Hence a smaller amplitude leads to the need for a higher frictional capacity. However this capacity is limited, the friction coefficient as retrieved from literature (See Section 2.2.3.) indicates that the following should be true for equilibrium:

$$F_f \leq \mu_s * F_n$$
$$F_f \leq 2.0 * F_n$$

This means that the traction vector should be twice smaller than the length of the normal vector. As is depicted in Figure 77 this principle does not hold for the small amplitude at that location on the curve. Hence the weight of upper layers and the keystone should add additional force to keep the interlocking bricks in place.

For the larger amplitude the friction at this point of the curve is sufficient to keep the geometry in place. However, in reality the geometry is subjected to a distributed horizontal load, meaning that each point on the interlocking curve will have different directions normal- and tangent directions. Moreover, this phenomenon occurs in both directions (3D effects). Making it difficult to predict the behaviour taking into account friction.

A rough quantitative estimation can however be made when excluding friction and concentrating the expected shear capacity again halfway the amplitude. The force will then be conveyed in two directions: by traction parallel to the steepness at that point (which results in uplifting) and by compression normal to the geometry. This can be illustrated similar to Figure 77, only changing the friction and normal force directions. The uplifting force will initially slide along the steepness curve at this point and hence change direction as the upper brick slides along the interlock geometry. The model however will not read reaction forces in this direction. The uplifting forces therefore need to be decomposed and calculated into the global z-direction. For the amplitudes under investigation this would yield the predictions as shown in Table 7 and graphically in Figure 78.

Hence it is expected that for smaller amplitudes the need of a vertical load increases to prevent uplifting from occurring. Higher amplitudes are expected to be more resistant to uplifting and moreover have a higher shear capacity as the contact surface increases.

Table 6: Shear capacity prediction for various values for the amplitude.

Amplitude	Area contact surface [mm²]	Ratio	Shear capacity [kN]
5	40324	0.960	171.1
10	42004	1.000	178.3
11	42455	1.011	180.2
12.5	43201	1.028	183.3
15	44610	1.062	189.3
20	47996	1.143	203.7

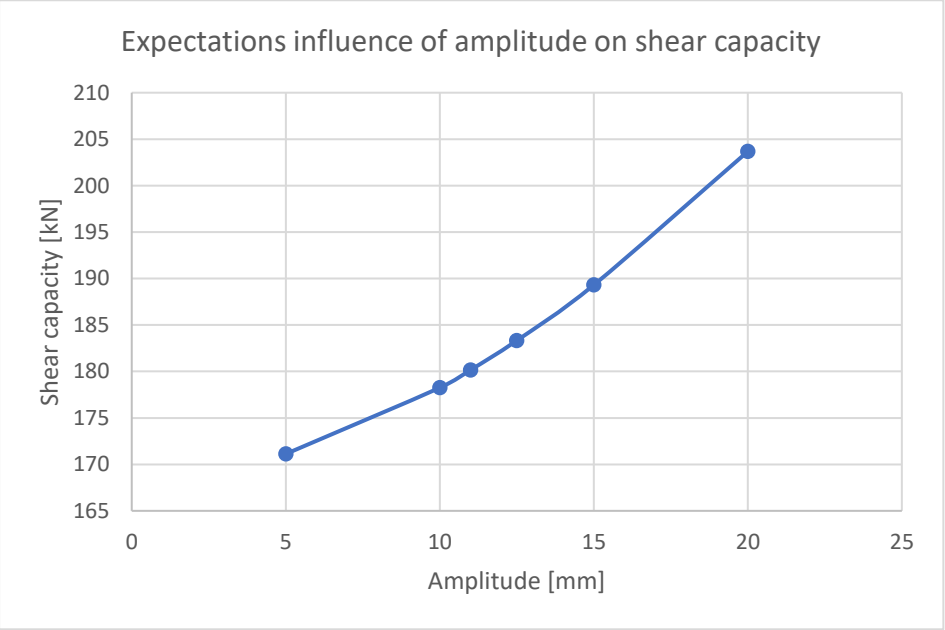

Figure 76: Graph of the expectation of the influence of the amplitude on shear capacity of the brick.

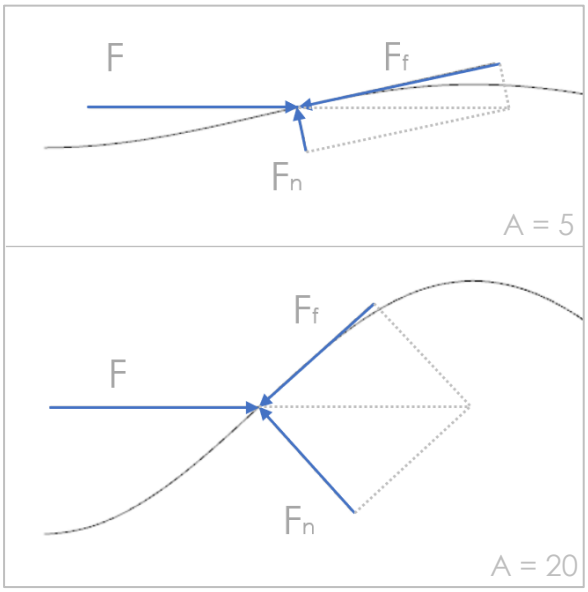

Figure 77: Necessary normal and friction forces for achieving equilibrium given interlock definitions with amplitudes of respectively A = 5mm and A = 20mm; and a horizontal force acting somewhere along the curve. Dead weight and weight upper structure not accounted for.

Table 7: uplifting and reaction force predictions for various values for the amplitude.

Amplitude	Shear capacity [kN]	Angle [°]	Uplifting force [kN]	Reaction force [kN]
5	171.1	13.0	166.7	37.5
10	178.3	24.8	161.9	67.9
11	180.2	26.9	160.7	72.7
12.5	183.3	30.0	158.7	79.4
15	189.3	34.7	155.6	88.6
20	203.7	42.7	150	102

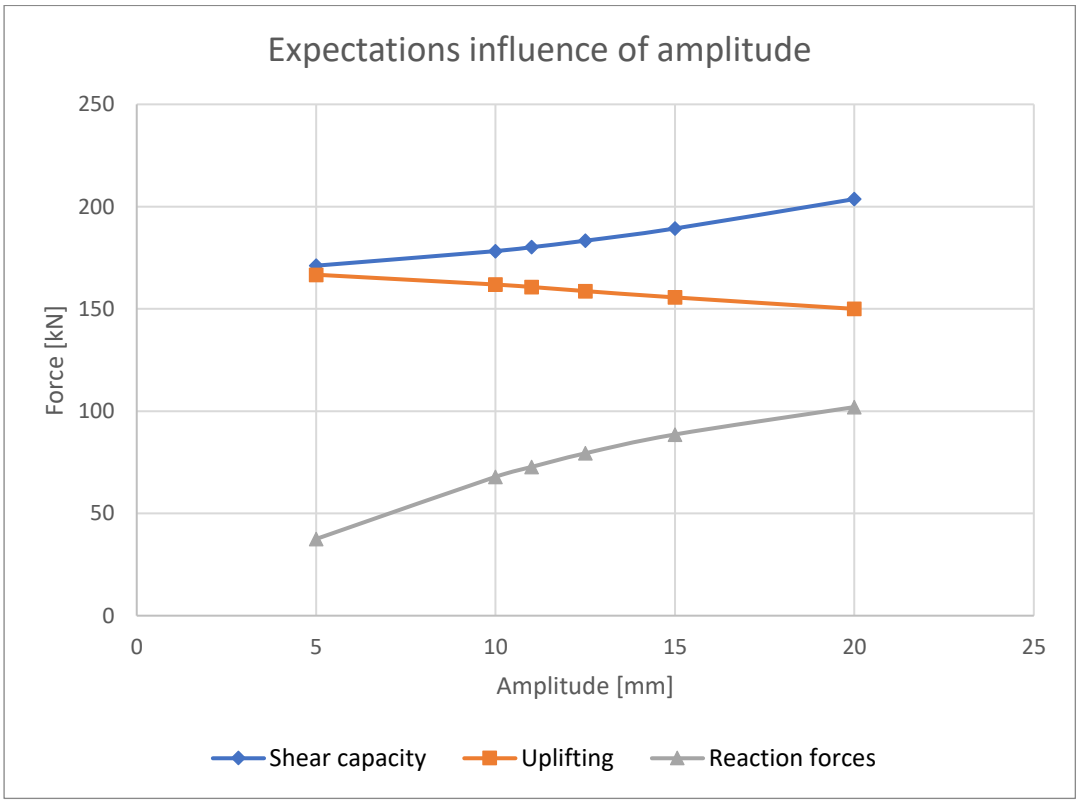

Figure 78: Expectations on shear capacity, uplifting and reaction forces for the amplitudes under investigation.

4.4.3. Interlocking curve variations

With post-processing of the bricks in mind, it might be an interesting side-step to investigate interlocking curve variations. By adding a linear part to the interlock definition more flat surfaces are created which will be easier to polish. An impression of the difference between sine-bricks and linear-sine-bricks is given in Figure 79. Both bricks have similar steepness halfway the interlocking geometry.

The addition of these linear parts however come at a price. In the previous paragraph it was mentioned that a higher amplitude would increase the shear capacity. By topping of this amplitude with a linear function one gains an increase in steepness without gaining the beneficial interlocking contact area. The increase of steepness then would work beneficial, as less vertical force is needed to compensate for uplifting effects.

In Table 8 the quantitative predictions are presented. By increasing the linear percentage of the interlock it indeed shows a decrease in uplifting force when maintaining the same shear capacity.

It is hence expected that when comparing the linear-sine-combination bricks with the regular sine-bricks they will have fewer shear capacity but still have a beneficial influence on uplifting effects.

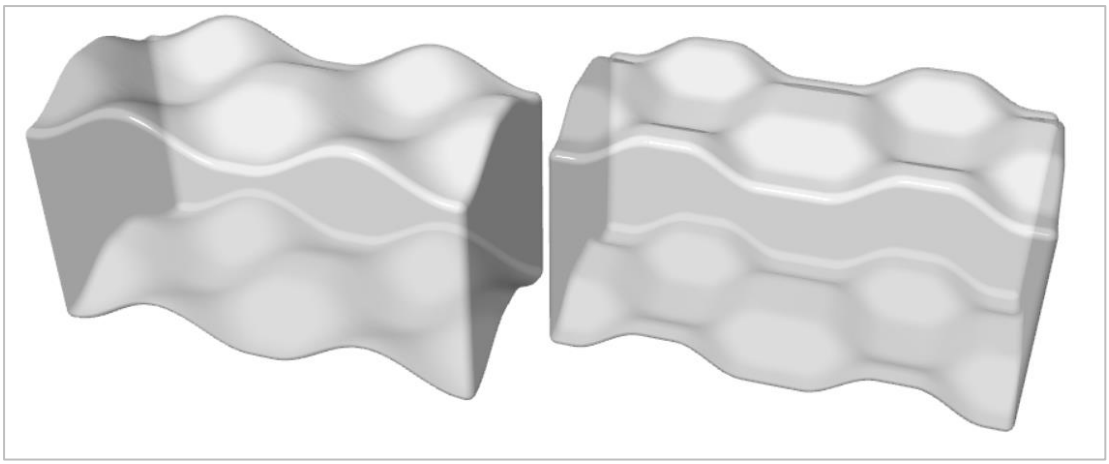

Figure 79: Comparison sine-brick (left) with linear-sine-combination brick (right).

Table 8: Predictions for certain amplitude values and linear-sine combinations.

Parameter	Shear capacity [kN]	Angle [°]	Uplifting force [kN]	Reaction force [kN]
A = 10 0%	178.3	24.8	161.9	67.9
A = 11 10%	180.2 178.3	26.9 27.2	160.7 158.6	72.7 72.5
A = 12.5 20%	183.3 178.3	30.0 30.0	158.7 154.4	79.4 77.2
A = 15 32%	189.3 178.3	34.7 34.2	155.6 147.5	88.6 82.9

4.4.4. Normative brick

The loads on a brick in a masonry cast glass interlocking wall are not equal for each brick. Their location in the wall determines which loads they are subjected to, and hence it can be assumed there is a certain brick that is normative for the design. The normative brick.

To find this normative brick it is important to review the system which will be applied. A sketch of the masonry wall system is shown in Figure 80a. First it is important to understand that the shear force is only introduced by the pulling of the monument wall at the anchors. This anchor will be connected to certain half bricks on the edges, as is highlighted in Figure 80b. These anchor bricks and their connection (which are further discussed in detail in Chapter 8) hence introduce the load into the system.

The vertical spacing of the anchors determine how each brick is loaded. In Figure 80 it is assumed that an anchor is placed every four layers of brickwork. The distribution of the initial load is then spread throughout the system. Hence the first whole glass bricks only carry half of the applied force in the anchor. This principle of spreading out is shown in Figure 80c for an anchoring every four layers. If the anchoring would be applied at every half brick near the edge, all glass edge bricks would have to convey the full initial force through the system. However it is expected that there should be sufficient distance between the anchors to not weaken the wall too much.

The second principle that influences the choice of the normative brick lies in the behaviour of the material glass. Glass is very strong under compression, and any added compression is expected to prestress the brick with compressive stresses. Hence the further down the wall, the more a brick is compressed due to the weight of the upper layers. Consequently the brick first needs to overcome this initial compression prior to being affected by tensile stresses. Moreover tensile opening of a flaw is not expected to occur as long as the surface is under compression (Pepi, 2014).

It can be concluded that the normative brick is in the upper region, and near an anchor. Therefore no prestress or keystone will be applied in the model, alternatively a slider is placed to be able to evaluate the forces acting on such a sliding keystone (see Figure 81). For modelling purposes the brick is loaded symmetrically. This will be beneficial when setting up the model in Chapter 5. To validate that this is the normative brick a compression test will also be evaluated in Chapter 6 for the initial model.

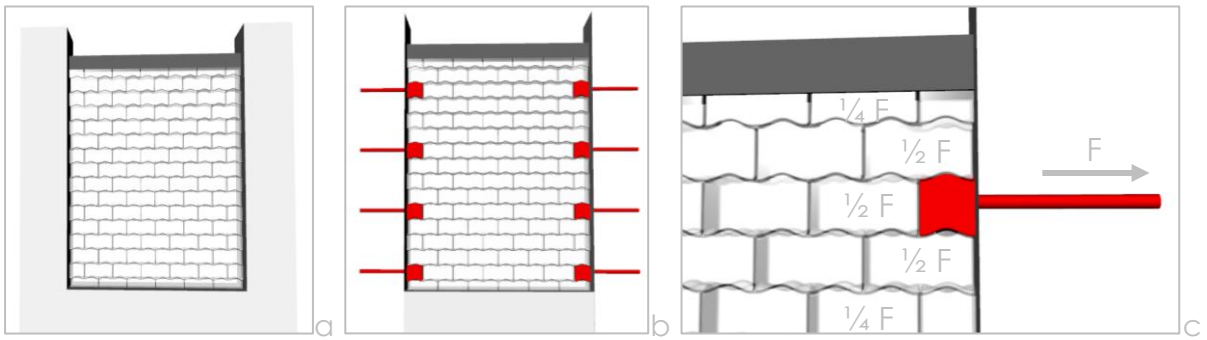

Figure 80: Wall structure principle, a) cast glass interlocking masonry wall example; b) highlighted anchors at a certain spacing in the brickwork; c) close-up of the top anchor and keystone with force partitions conveyed through the shear locks.

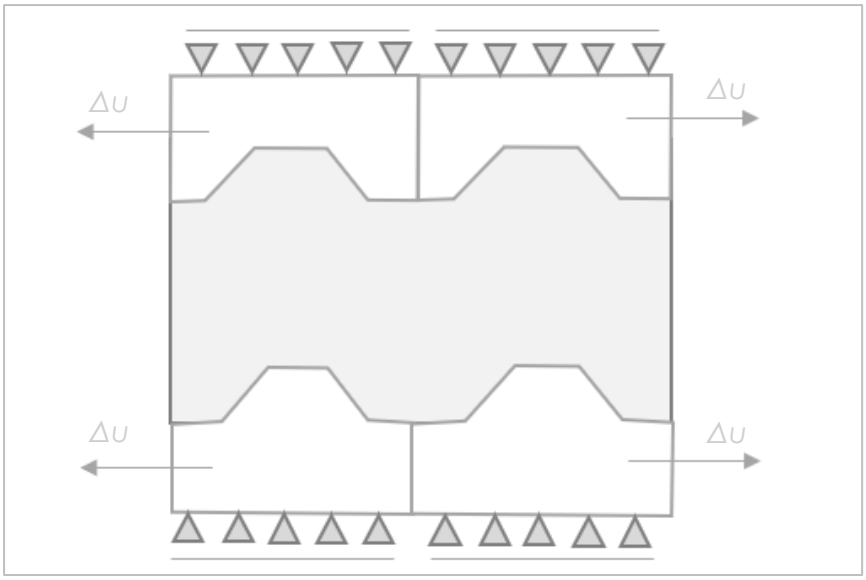

Figure 81: Rough sketch of modelling test set up.

Section 4.5. Parameter ranges tested

A selection of models is generated using the GH-file with various parameters. The ranges tested will be discussed below and are based on practical considerations as well as the limits of the GH geometry generations and DIANA importation. An overview of the parameter ranges tested is shown in Figure 82. The initial geometric model is shown at A = 10, Linear-Sine = 0% and H = 150.

Amplitude variations

The amplitude will be tested with a range from 5mm to 20mm. The initial model was chosen to have an amplitude of 10 millimetres. One value below the initial model is tested, however this model had some complications when generating the geometry. For lower amplitudes than the initial value the GH-file would create geometries with larger tolerances, which resulted into a higher needed input for "coincidence tolerance" in DIANA. For many other amplitudes this would lead to an ill-fitted mesh, however for A = 5mm the mesh could be fixed while maintaining the before mentioned tolerance issues. For other values in between no valid meshes were generated and hence no other values are calculated.

The higher values A = 15mm and A = 20 are tested to evaluate the influence of the amplitude, the values A = 11mm, A = 12.5mm and also including the A = 15mm variation are introduced to compare with the Linear-Sine variations. The values correspond with a similar steepness halfway the sine curve.

Linear-Sine variations

These variations are chosen on the capacity of the Grasshopper script. With the initial amplitude the model could only be given linear segments up to 16% on each side of the curve, hence the variations stop at a total linear percentage of 32%. The steepness of the variations 10%, 20% and 32% correspond respectively with the amplitude variations of A = 11, A = 12.5 and A = 15mm.

Height variations

The parameter variations for the height are chosen according to the predictions made in Section 4.4.1. Higher bricks than 150mm would become increasingly impractical, as the initial brick design is already a heavy brick (± 16.8 kg) which potentially could lead to assembly issues.

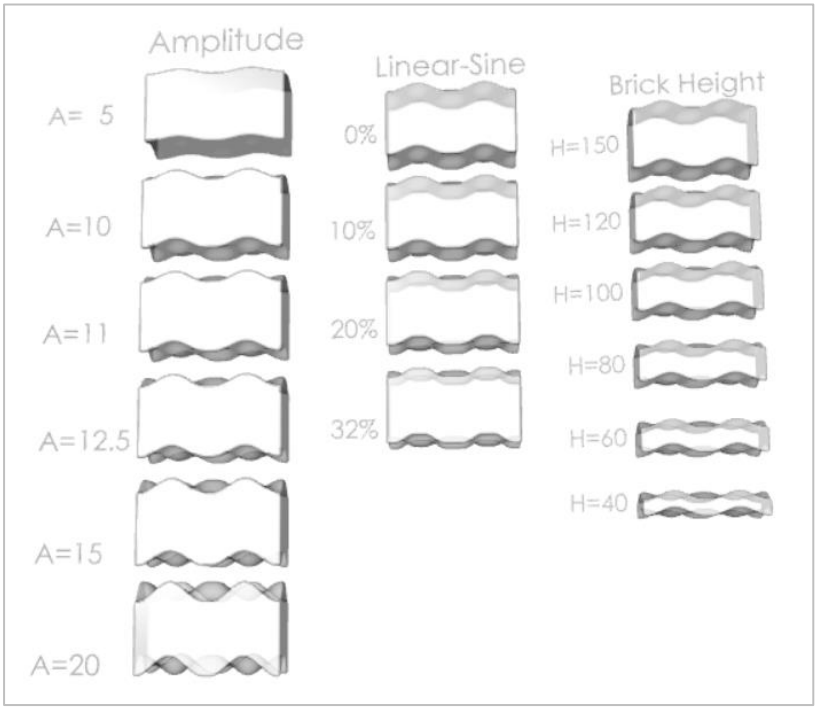

Figure 82: Overview parameter ranges tested.

Chapter 5.

FEA protocol and model input

This chapter explains how the FEA models are set up and which values are used as an input. It is the base of every finite element analysis and hence its principles and assumptions are here discussed.

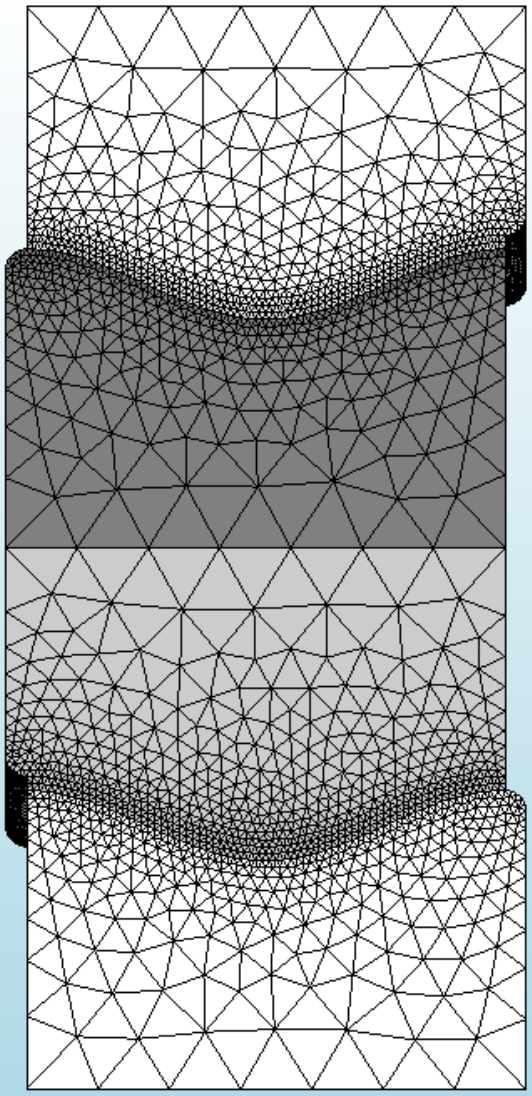

Section 5.1. Principles of the finite element model

A finite element model is always merely an approximation of the reality. How close the results will relate to realistic values is completely dependent on the modelling approach, boundary conditions and assumptions made.

The principles of the finite element model therefore describe how these modelling choices came about. Limitations of the model will be explained, and assumptions are supported by either literature or experimental results.

5.1.1. Goal and approach of the finite element model

The parametric geometry designed in the previous chapter is of high complexity, and therefore difficult to analyse by conventional methods. Hence finite element modelling is applied to evaluate the structural capacity of the designed brick, and to predict sensitive areas in the geometry.

The software used is DIANA FEA. For evaluating glass sensitivity, a new output was created by the developers at DIANA: The Christensen's failure criterion output. Besides its application for glass it can be applied for any other material, by varying its tensile and compressive strength.

The criterion combines the principal stresses into a failure envelope, and for brittle materials such as glass also applies a brittle cut-off. Hence the criterion can evaluate when tensile surface stresses become critical. The contour plots then directly show sensitive areas in the design, and indicate where peak stresses occur. The criterion is given below in Equation 5.1.

$$\left(\frac{1}{T}-\frac{1}{C}\right)(\sigma_1+\sigma_2+\sigma_3)+\frac{1}{2TC}[(\sigma_1-\sigma_2)^2+(\sigma_2-\sigma_3)^2+(\sigma_3-\sigma_1)^2]\leq 1 \qquad [5.1]$$

For the tensile strength the characteristic strength of annealed float glass is used: T = 45 MPa. As Christensen (2013) states a T/C = 1/8 for glass, its compressive strength is set to C = 360 MPa. In reality the value for the compressive strength can be significantly higher, but to satisfy the criterion set by Christensen the earlier mentioned value will be applied. Hence it is not needed to extensively review the influence of compressive stresses on the geometry, as the leading fracture mechanism occurs only by tensile peak stresses (Pepi, 2014).

The characteristic shear strength of the geometry can then be obtained by loading the geometry until the Christensen's failure criterion approaches one. This value can then be transformed into a design value depending on the load duration (short or long-term loading).

The load will be applied with a prescribed deformation, the analysis therefore is displacement controlled. The supports applied at the displaced faces then yield a support reaction equal to the maximum characteristic load the shear locks can convey through the bricks.

As the shear locks in the design will need to convey the load from wall to wall, and the peak stresses are expected in these locations, the scope of this chapter will limit to the shear capacity of the interlocking brick. As discussed in Section 4.4. it is expected the top bricks to be normative, due to the occurring of uplifting.

5.1.2. Element choice and mesh settings

For each finite element problem it is important to choose the right mesh settings and elements. As the goal of the model is to evaluate the 3D curved geometry of the interlock, the model will consist of solid elements.

This however result in longer calculation times (as the number of elements and nodes increase in 3D elements) and larger files when saving the DPF-files including the mesh. It is therefore advisable to save the model before meshing as a DPF-file, and after meshing merely export a DAT-file. This will save disk space and allows for later editing of the file in DPF, while being able to calculate the DAT-file on a calculation server.

Solid elements

For solid elements there are limited choices. They can be distinguished as pyramids, wedges and brick elements. Each can be subdivided by refinement, with either linear, quadratic or third order interpolation. This choice basically determines the amount of mid-side nodes and therewith the amount of results calculated per element. An overview of all these elements and their nodes are shown in Figure 83.

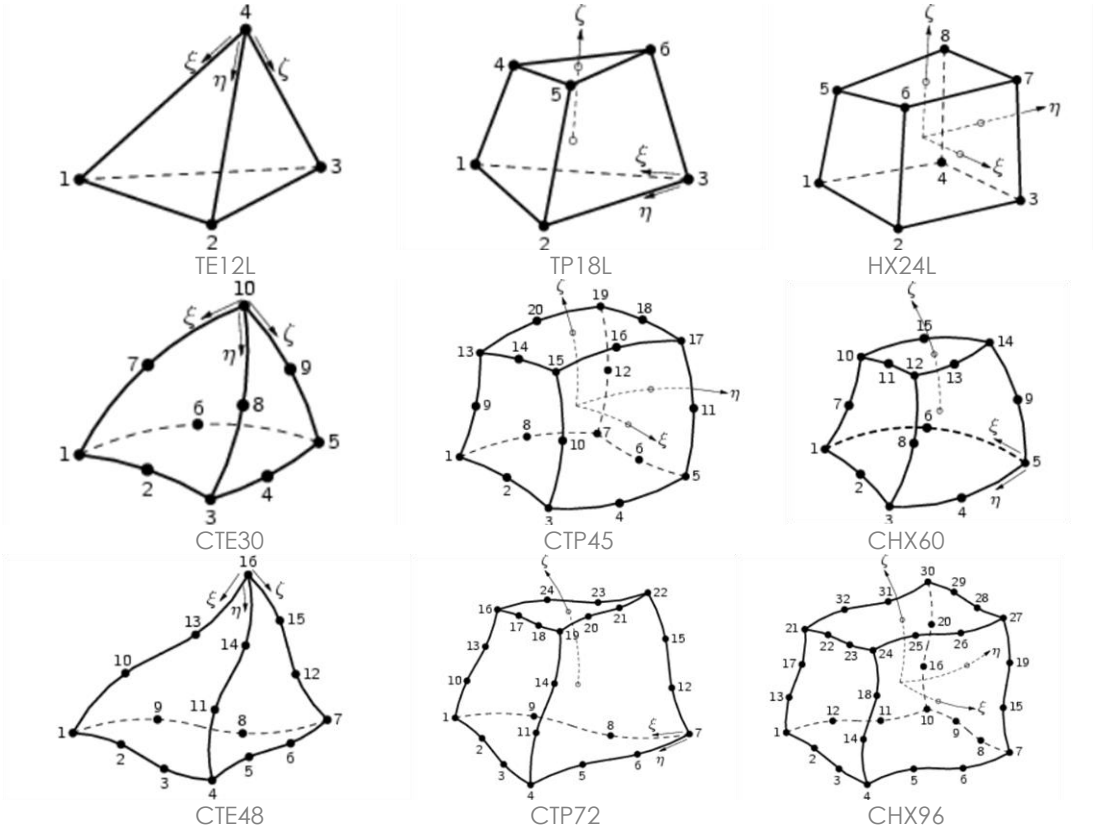

Figure 83: Solid element node schemes for pyramid, wedge and brick elements with linear (top row), quadratic (middle row) and third order interpolation (bottom row). Reprinted from (DIANA FEA, 2009).

A choice for the element used is based on the geometry to mesh, the calculation time and the refinement of the results obtained. In general more nodes result into a longer calculation time but a higher refinement of results. The third order interpolated elements are ruled out as it would result in too long calculation times and processing power needed.

For meshing complex geometries triangular elements are preferred, as they are more flexible while meshing. A comparison model between pyramid elements and a combination of brick and wedge elements showed that calculation and meshing time increased when using the combination of bricks and wedges. This was partly caused due to the increase in nodes to

calculate (with the same mesh refinement) and partly due to difficulties of creating a gradual mesh. Due to the complex geometry therefore is chosen to use triangular elements.

Triangular elements are however prone to locking, especially when linear elements are applied or when using incompressible materials. When locking occurs the elements react stiffer than which would be realistic. To take preventive measures against locking quadratic pyramid elements (CTE30) are chosen. Using a finer mesh for the incompressible materials could also proof beneficial. The material properties of the incompressible PU interlayer should however be recalibrated before calculations can be run.

Interface elements

The touching surfaces of the PU interlayers and the glass should be defined adequately, and its settings will be discussed in the next paragraph (5.1.3.). The interface elements themselves are selected in accordance with the chosen solid elements. Due to connectivity these elements should be triangular as well as quadratic. Therefore CT36I-elements will be applied, here shown in Figure 84.

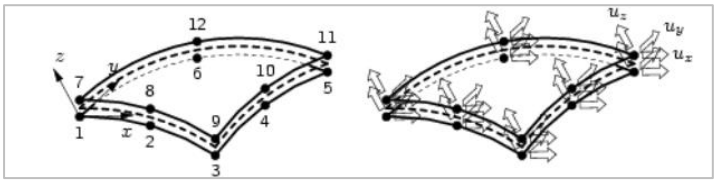

CT36I

Figure 84: CT36I plane triangle 3D-element. Reprinted from (DIANA FEA, 2009).

5.1.3. Non-tensile behaviour of the interface and Coulomb friction

An interface element describes the behaviour between two geometrical faces in the same plane; in this case two touching faces of two solids of different materials. By absence of interface elements the software will recognise the geometry as two connected solids.

This effect is non-realistic for an interlocking system model. The contact between the glass and polyurethane should be able to slide and have no tensile capacity (i.e. the faces should disconnect when tensile stresses occur).

Within the software there are several solutions to simulate these kinds of interface behaviour. To illustrate some of them, the interface elements were tested on a little cube of glass resting on a layer of polyurethane. Four different interface conditions were tested.

Firstly a null-variant without the application of interface elements. The two solid bodies therefore are connected completely.

The second variant features no geometry for the PU layer, but merely models the whole layer as an interface. This interface is given properties to allow no tensile stresses. Hence when tensile stresses occur the geometry splits at the interface.

The third interface applied is a non-tensile layer in between the solid geometries of the PU and the glass. Therefore this interface does not allow tensile stresses either.

Lastly a Coulomb friction interface is applied, which features more parameters to also simulate friction besides non-tensile behaviour. Besides gap opening when subject to tensile stresses, the geometry is now also allowed to slide when a certain threshold is reached.

The four models are subject to three load cases to illustrate the behaviour of these interface elements. All loads are applied with prescribed displacements, except for the dead weight which is added as a global load. The interface elements are hence tested under tension, compression, and shear, which will be discussed individually below.

Tensile stresses in the interface

To illustrate the behaviour when under tension the glass element is lifted from the polyurethane as shown in Figure 85. All interface elements behave as expected, lifting up the glass cube without creating a pulling effect on the polyurethane geometry. This in contrary to the null-variant, which is connected. Here the polyurethane layer is 'glued' to the glass and stretches. This stretching effect can be contributed to the difference of the Young's modulus, which is significant lower for PU. Hence the PU deforms while the glass remains intact.

The bottom row of images in Figure 85 show the tensile stresses in the interface (StNz) red, or in the case of compression or no stresses at all blue. For the connected case the bottom side of the glass geometry is shown (SZZ).

Considering tensile stresses in the interface, all three interface variants simulate the effects of a non-tensile connection well. It is moreover clear that adding no interface at all would result in tensile stresses in the bottom of the brick. Hence this would influence the Christensen's output negatively, as these stresses would be added to the leading tensile stresses on the glass geometry, therefore yielding wrong results.

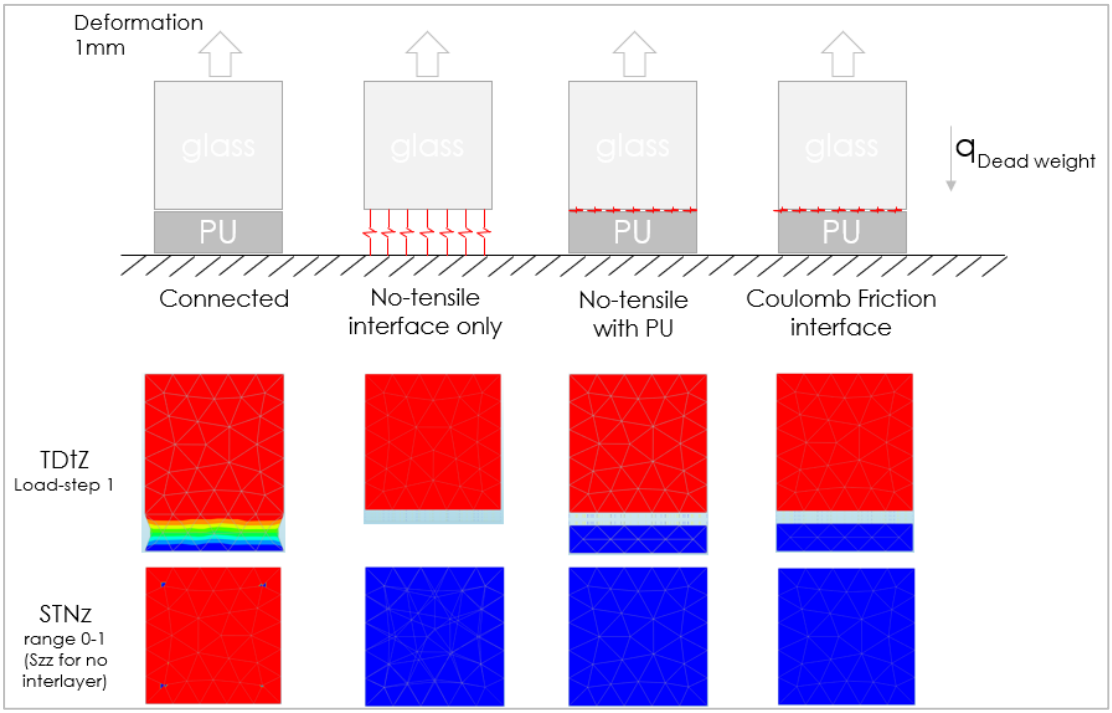

Figure 85: Tension results of the interface element experiments.

Compression

A downward prescribed deformation is applied to simulate compression of the system. This load case is illustrated in Figure 86. When applying no geometry for the PU interlayer and merely applying non-tensile interface elements (second test results) it can be observed that the glass brick itself is being compressed, with no deformations at the interface elements which represent the PU interlayer. Stresses therefore build up in the glass brick, which also lead to inaccurate results for the future model.

The models consisting of a solid PU interlayer act according to the expectations. The PU bulges out on the edges and due to the lower Young's modulus deforms, whereas the glass cube retains its shape. The Coulomb friction model moreover shows horizontal movement as well, as the geometry is allowed to slide. This also can be expected, and is hence more realistic.

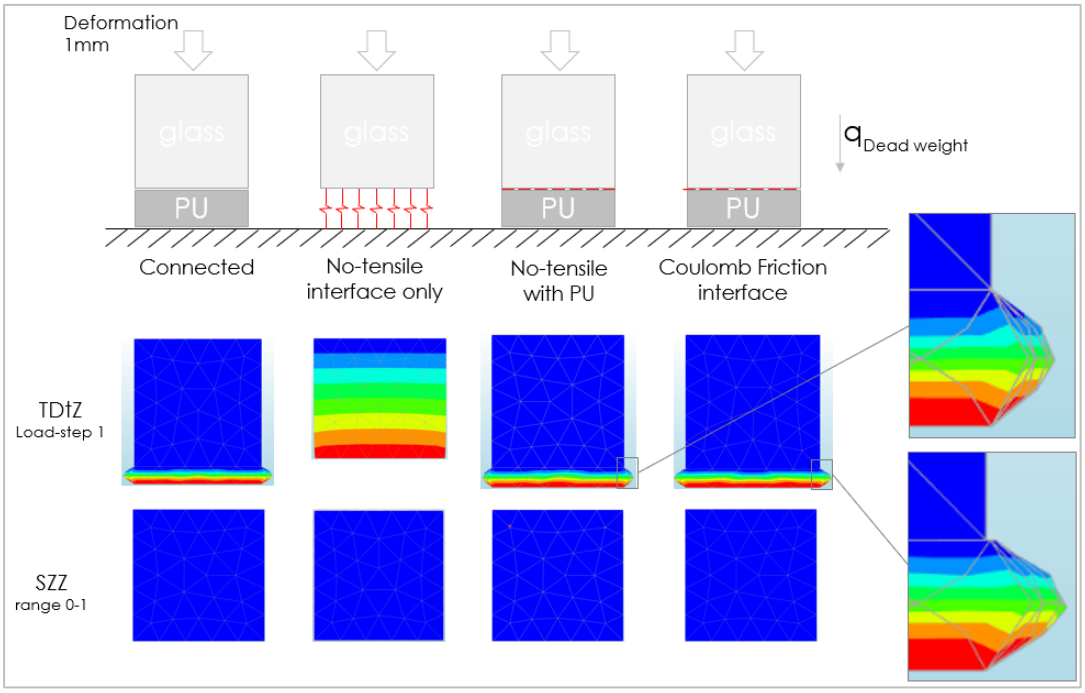

Figure 86: Compression results of the interface element experiments.

Compression and shear

Lastly a two-stepped load case is applied, in which first the geometry is compressed, and where the glass cube is then moved horizontally (see Figure 87). The results for no PU geometry again proof unrealistic, for the same reasons as before.

For the latter two tests the interfaces both display viable results. The non-tensile interface dispatches as soon as tensile stresses occur on one side, whereas the Coulomb friction interface exhibits sliding. Both result in minor tensile stresses near the right-hand-side edge and some peak stresses on the left. Due to the possible sliding behaviour of Coulomb friction this interface is used in the numerical model.

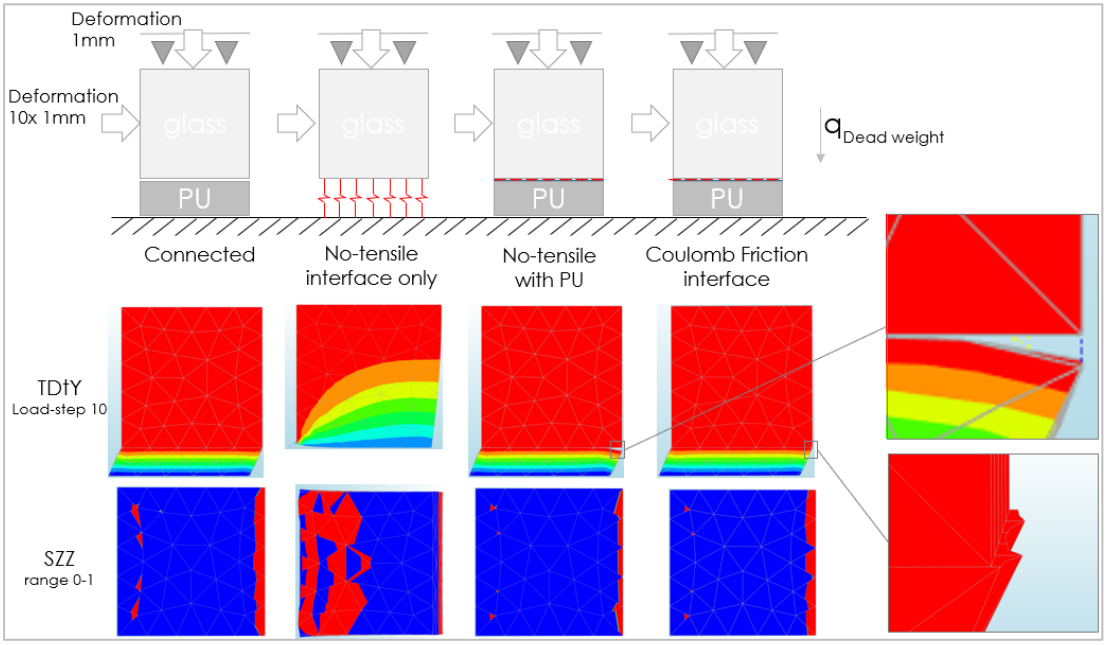

Figure 87: Compression and shear results of the interface element experiments.

5.1.4. Calibration of Young's Modulus PU

As mentioned before in Section 2.2.2. the Young's modulus of polyurethane is highly dependent on the load applied and the direction it is applied in. When under compression the Young's modulus can be determined by applying a shape factor to the initial value. With higher shape factors the stress-strain curve becomes steeper, until a point it can be considered almost linear. This (constant) steepness can then be interpreted as the Young's modulus of PU under compression.

To limit the scope the best performing polyurethane interlayer in Aurik (2017) will be used as an interlayer (PU ShA70). The theory discussed in Section 2.2.2. and the experimental data from Aurik will be used to calibrate the Young's modulus of PU. With regard to finite element analysis it should be noted that, as discussed in Section 5.1.2, the model can be prone to locking of the elements when a triangular mesh is applied or when (nearly) incompressible materials are modelled. In this case both are included in the model and therefore the model might act excessively stiff.

From literature and test results the following values were retrieved for PU70 (summarised in Table 9 and retrieved from Section 2.2.2.). The initial (tensile) Young's modulus was calculated to be about 8 MPa. Calculated Young's modulus according to the literature were either 137 MPa (exact calculation) or 125 MPa (linear assumption). Test results in Aurik (2017) however showed a Young's modulus of 336 MPa, and was assumed linearly. Test results furthermore showed a deformation of Δw=0.13 mm at a compressive stress σ=10.88 MPa.

Table 9: PU70 Young's modulus results.

PU[ShA]	$E_{initial}$	Shape factor	$E_{test\ results}$ Δw=0.13	E_{exact} Δw=0.13	E_{linear} Δw=0.13
PU70	8.63	13.125	336	137	125

Remedies for locking effects include the use of quadratic elements and a finer mesh near the incompressible locations. Quadratic elements are already being applied, as discussed in Section 5.1.2. The PU interlayer should furthermore be meshed finer than the surrounding glass elements.

To calibrate the Young's modulus of PU to a realistic value, part of the test set up used in Aurik (2017) is modelled in DIANA FEA. A fine mesh with element size of 2mm is applied on the PU interlayer, and to limit calculation time and file size the mesh size is gradually increased to 20mm. Only a quarter is modelled due to symmetry, additional supports are added in symmetry directions. A compressive distributed load of 10.88 MPa is applied on the top glass face, conform the test setup discussed in Aurik (2017). See Figure 88a for meshing pattern, loading and support conditions. The Young's modulus is then varied until a deformation of 0.13mm is found, corresponding to the result of the laboratory test. Poisson's ratio is set to v=0.48, to allow a certain degree of compressibility.

Various calculations were performed with several values for the Young's modulus, including the values presented in Table 9. The higher values (125-336 MPa) resulted in an overly stiff PU interlayer with deformations smaller than the aimed 0.13mm, while lower Young's moduli (8) resulted in too compressible behaviour with larger values. The results shown in Figure 88b were obtained after an iterative process, at a value of E=50MPa.

As the shape factor in the Aurik-test (S=13.125) and the shape factor of the initial design (S=12.5) are close to one another, it is assumed that this value for the Young's modulus can be applied on the initial design model as well, provided the shape factor remains the same and mesh settings are identical. Further research and laboratory experiments are needed to validate this assumption prior to using the results in this thesis in practise.

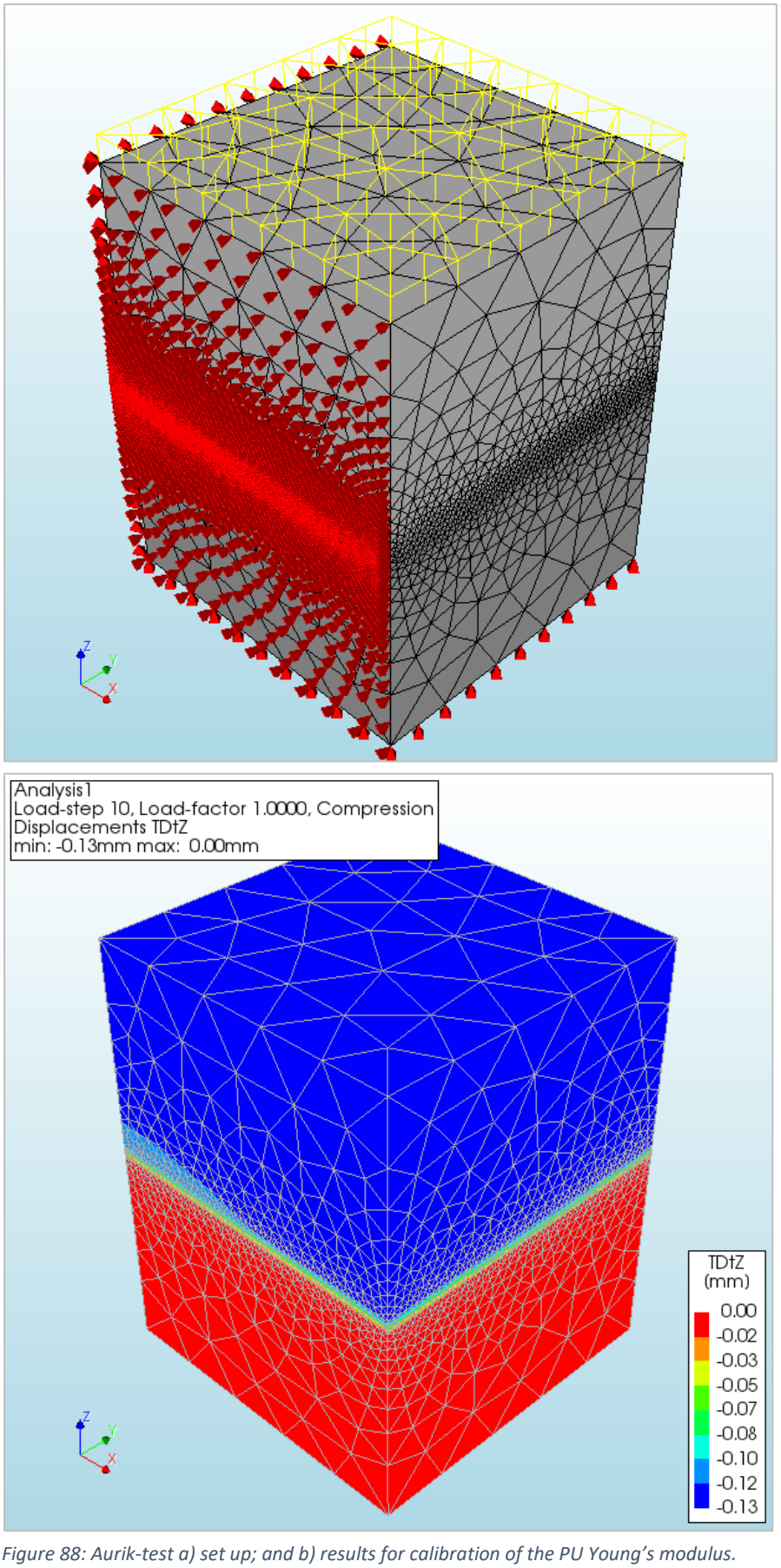

Figure 88: Aurik-test a) set up; and b) results for calibration of the PU Young's modulus.

Section 5.2. Model input properties

For replication purposes and gaining an understanding of the results it is important to take notice of the model input properties. This section therefore discusses the finite element model set up, from importing the geometry to output values requested from the software.

A finite element model is merely a representation of the reality, an approximation gained by often a simplification of the true values. This section therefore provides insight in which stage assumptions are made and how these assumptions are substantiated.

In many cases further research might provide an improvement of input values for future calculations. Especially repeated laboratory tests on interlocking cast glass elements and on PU interlayers might provide additional input to refine the modelling procedure.

5.2.1. Data exchange GH to DIANA FEA

The brick geometry is modelled in the Grasshopper plug-in for Rhinoceros. By rearranging cut parts of the geometry the testing set up is obtained which will be further discussed in the next paragraph.

For exchanging geometry data from Rhinoceros to DIANA FEA there are two export options supported by both software. On the one hand this is the IGES or IGS-files, however these were found to be unable to carry solid geometries, which resulted in them being imported into DIANA FEA consisting of merely faces. On the other hand there are the STP or STEP-files. These are able to carry solid geometries to DIANA FEA, however tolerance problems may occur. These will result into connectivity problems between matching faces.

To bypass these tolerance problems one can import the geometry into MIDAS FX+, a pre- and post-processor for DIANA FEA. Meshing is generally easier in DIANA FEA, however importing the geometry automatically scales the geometry with a factor thousand, one therefore should be careful using MIDAS FX+ and check carefully after importing geometries.

Another way to bypass the tolerance problems is to lower the “coincidence tolerance” input in DIANA FEA. This can be done under the advanced option in the project settings menu (only is available after creating a new project, but before importing the geometry). It basically changes the coinciding node tolerances.

In this thesis the latter option is used, and the coincidence tolerance is set from 1e-09m to 1e-05m. For some variations in the geometry it was necessary to lower the coincidence tolerance input even more.

In general it is best practice to start a new project, set model size to 1 meter, then edit the coincidence tolerance input by going back to project settings and reduce it with a factor 10.000. Next the geometry can be imported. Make sure your units are set in meters, as the STEP file will carry the dimensions of your geometry in meters (regardless of your Rhinoceros settings).

5.2.2. Geometry set up

The geometry obtained from the GH-file already is set into the numerical calculation position. By using the symmetry of the brick design the whole model could be reduced to merely a quarter of its original size. This leads to fewer elements and a more efficient calculation time, as well as a lower impact on storage space. Figure 89 shows how the brick geometry is transformed into the DIANA test set up.

There are six solids in the numerical calculation set up. Two four-millimetre-thick PU interlayers and four glass half bricks. The middle two geometries will be meshed as one, without any interface elements in between. This geometry is merely cut to provide for additional mesh seed edges, applied to reduce total element count.

To mimic a shear test, one quarter of a brick is held in between two eighth bricks. The middle geometry will yield the final results, while the top and bottom geometries introduce the prescribed deformation. A full-scale principle is shown in 2D in Figure 90. A rough indication of the same set up for a 3D quarter brick is indicated in Figure 89.

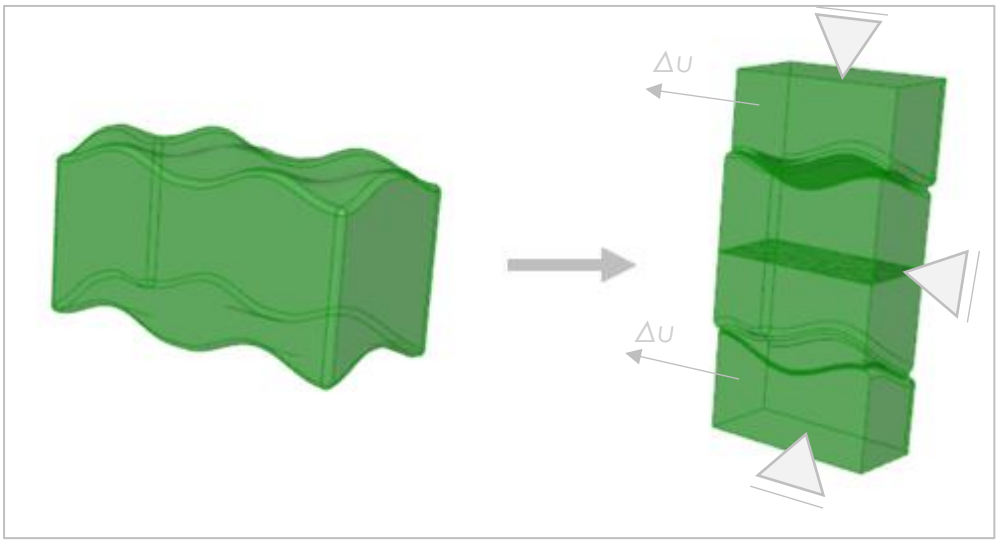

Figure 89: From brick geometry to DIANA test set up geometry, including rough indication of calculation principles.

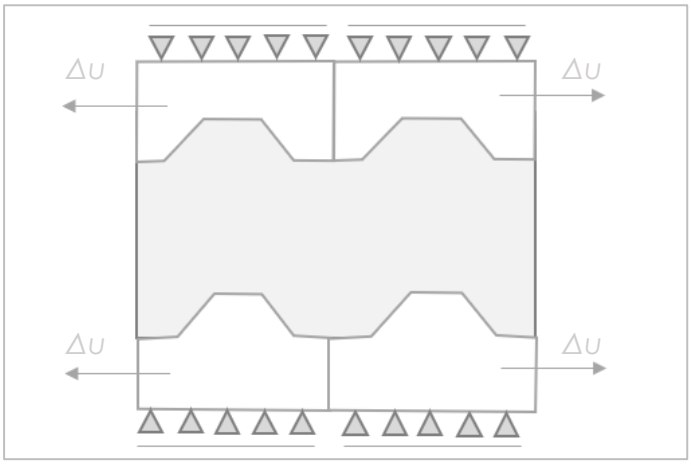

Figure 90: 2D Full scale principle of the model.

5.2.3. Material settings

In the model three materials can be distinguished: glass, polyurethane and the Coulomb friction interface elements modelled in between the two materials. These will be briefly discussed below. To be able to create the Christensen's output all materials need to receive additional information as well. These parameters will be discussed individually.

Glass

The material glass behaves linear elastic until it fractures. As discussed in the theoretic framework it is a linear elastic isotropic material and therefore can be modelled as such. Its input values are given in Table 10.

Polyurethane

Polyurethane can be considered an isotropic material, but officially has no standard Young's modulus. It instead varies under load conditions, shape factor of the specimen and hardness of the material. From Section 2.2.2. and Section 5.1.4. it can however be concluded that for high shape factors the Young's modulus of PU under compression can be considered linear as well.

For application in practice it is however important to extensively test any PU applied. Each mixture of components and each hardness can have different effects, and an extensive study of these effects can generate more detailed input for the finite element analysis as well. This however is not part of the scope of this thesis and therefore the PU interlayer is considered an isotropic linear elastic material. Its input properties are given in Table 11.

Coulomb Friction dummy elements

The interface elements are given Coulomb friction properties. Being a 'dummy' element the properties are determined quite arbitrary to simulate a certain behaviour, such as no allowance for tensile stresses or the introduction of frictional properties.

It is important that the deformations of the interface elements are minimised relative to the deformations of the adjacent solid elements. Its normal stiffness is therefore assumed to be a factor thousand larger than the highest adjacent Young's modulus. The shear stiffness is assumed a factor ten smaller than the normal stiffness.

Ideally the cohesion and tensile strength values are set equal to zero, as that would ensure complete loose behaviour when tensile stresses occur. However for numerical reasons this can lead to numerical errors, especially when no compressive load is present. The values for these parameters are therefore chosen very small. The friction angle is derived from the friction coefficient as discussed in Section 2.2.3. A complete overview of its input properties is given in Table 12.

These parameters combined create the Coulomb friction model as shown in Figure 91. With low values for cohesion c and tensile strength gap criterion f_t the Coulomb friction model will almost start in the origin, hence allowing only very small cohesion and minor tensile stresses. Certain small peak values of tensile stresses are therefore expected in the interface elements.

Additional properties

To generate the Christensen's failure criterion output each material needs to get its tensile and compressive strength assigned. As there is no material model yet to represent both these parameters, the values are introduced manually by altering them in the DAT-file.

It is hence important to export the model firstly as a DAT-file, enter TENSTR and COMSTR in each material model and import the materials back into DIANA FEA. For the analysis to run, all materials should be assigned these additional properties. As in this thesis the scope is on the glass brick, the values for glass are inserted for each material. Results of the Christensen's output in other materials than glass can therefore be ignored.

Table 10: Material properties glass (O'Regan, 2015).

Parameter	Value	Unit
Density ρ_{glass}	$2.5*10^{-9}$	T/mm^3
Poisson's ratio ν_{glass}	0.22	-
Young's modulus E_{glass}	70 000	N/mm^2

Table 11: Material properties polyurethane interlayer.

Parameter	Value	Unit
Density ρ_{pu}	1.1*10-9	T/mm^3
Poisson's ratio ν_{pu}	0.48	-
Young's modulus E_{pu}	50	N/mm^2

Table 12: Input properties of interface elements.

Parameter	Value	Unit
Cohesion c	0.001	N/mm^2
Normal stiffness modulus Z	70 000 000	N/mm^3
Shear stiffness modulus X	7 000 000	N/mm^3
Shear stiffness modulus Y	7 000 000	N/mm^3
Tensile strength gap criterion f_t	0.0005	N/mm^2
Friction angle ϕ	1.10715	rad
Dilatancy angle	0	rad
Interface opening model	Gapping model	-

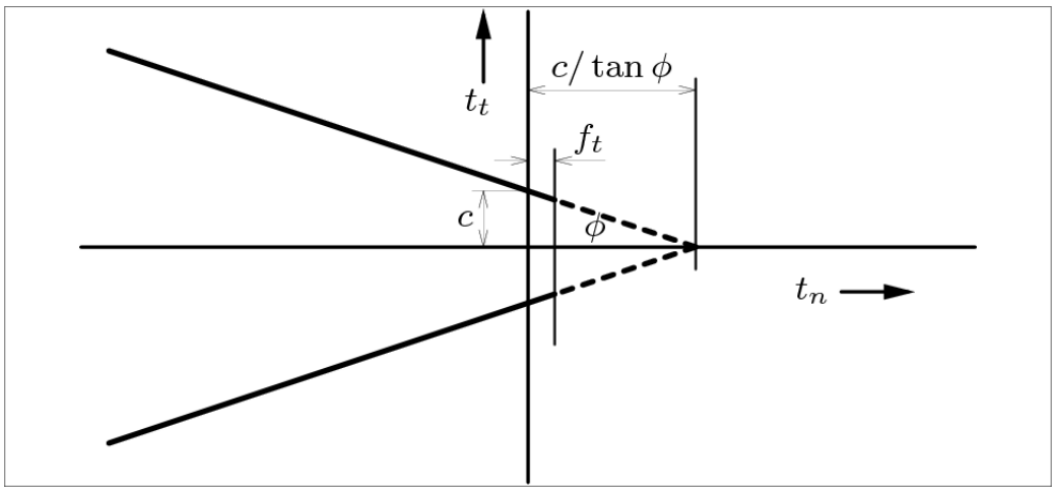

Figure 91: Coulomb friction model. Reprinted from (DIANA FEA, s.d.).

5.2.4. Support conditions

To simulate the model correctly, adequate support conditions should be applied to the model. The main intention of the model is to calculate the shear capacity of the interlocking geometry. The most critical brick is moreover expected to be in the top of the masonry wall, as there the fewest vertical loading is present (lower layers are loaded by the weight of the upper layers). Hence one desired result of the model is to obtain the force necessary to prevent uplifting to occur.

The model therefore should yield results in both vertical Z-direction (uplifting) and in horizontal X-direction (shear loading direction).

To evaluate the uplifting behaviour, the upper and bottom planes of the sliding bricks are therefore restraint in Z-direction, as is shown in Figure 92a. As due to the shear loading it is expected that parts of the geometry will want to move upward, creating different reaction forces across the planes.

In Y-direction supports should be added to simulate the symmetry of the geometry of the brick. The whole sliced face is therefore restraint in Y-direction, as is shown in Figure 92b. These supports therefore simulate the symmetric geometry, and the model therefore will behave as if the whole brick was there.

For the X-direction a similar support is needed for the middle brick, here shown in Figure 92c. One vertex is supported here which is tied to shaded faces. Basically this means that any deformation set in any future node on these faces will have the same deformation as the master node. All reaction forces are summed into this master node, which enables easy access to the desired value for the characteristic shear strength of the geometry.

In X-direction two more supports are moreover added for the top and bottom bricks. Their purpose is to accommodate the prescribed deformation loads, discussed in next paragraph. Again the nodes are tied to the future mesh nodes on the corresponding surface, which all therefore gain supports and the same prescribed deformation.

These support conditions are therefore of vital importance in gaining the envisioned results. The top surface reaction forces will indicate uplifting tendency and the symmetry support of the middle geometry will yield the characteristic shear strength of the interlocking geometry.

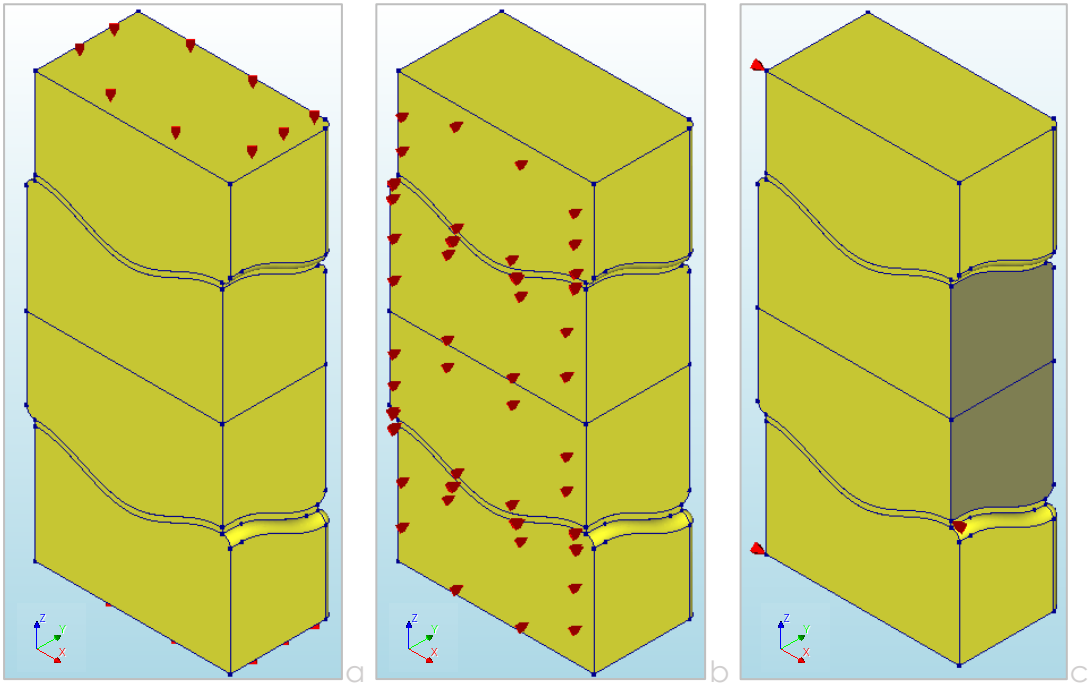

Figure 92: Supports conditions in a) Z-direction; b) Y-direction; c) X-direction

5.2.5. Loading conditions

As mentioned earlier on, a prescribed deformation will be applied to the top and bottom bricks. Due to the sliding support on top and bottom, these geometries are free to move, with only the interlocking geometry as an obstacle. The applied load hence must be conveyed through the PU interlayer geometry to the middle brick, which will then display the resulting stress concentrations according to Christensen's failure criterion.

The load is applied on the previously discussed supported vertexes, which due to the tying will copy the same deformation to any of the nodes on the tied surface. A prescribed deformation of $\Delta u = -0.1$mm is applied to both vertexes. This allows for choosing a wide variety of load step sizes when calculating the models.

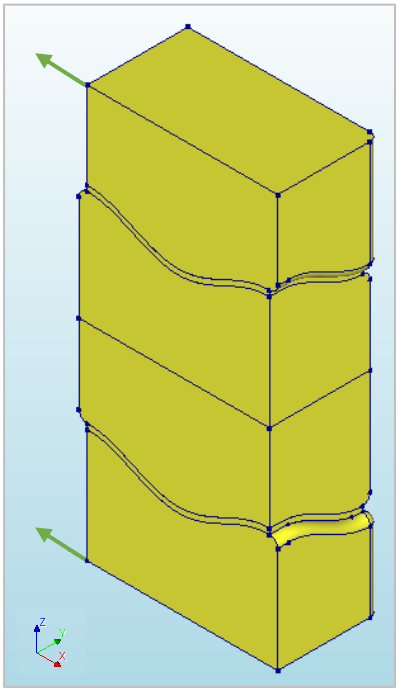

Figure 93: Loading conditions, tied vertexes loaded with a prescribed deformation load.

5.2.6. Meshing properties

For proper results a mesh needs to be properly defined. Earlier in Section 5.1.4. the Young's modulus of PU was calibrated using a reference calculation of the Aurik (2017) test results. It was concluded that the mesh settings and refinement near the PU interlayer affect the rate of locking of the quadratic triangular elements. Consequently the same mesh seed settings needs to be applied on the interlocking geometry models, to simulate the same extra stiffness introduced by these effects.

The PU interlayer therefore is meshed with element length of two millimetres. As the most crucial and complex geometry is in this area, the finer mesh is also beneficial for evaluating the results.

From preliminary calculations with other mesh seeds it became evident that the results in the middle of all solid geometries are not as interesting as what happens near the interlock, and therefore a coarser mesh is chosen for the parts in the geometry showing smaller resulting gradients. This benefits calculation time and file size, however takes more time to set up.

The horizontal edges therefore are given a mesh seed of 20mm length. The vertical edges were given a gradual mesh seed to create a smooth mesh between 2 and 20-millimetre mesh seeds. Smoothness factor was therefore set to 0.25, and preferred mesh size to a length of 20 millimetres. The mesh seed is given in Figure 94a, and the resulting mesh in Figure 94b.

The effect of the tying now also becomes evident, which is visualised in Figure 94c. All the nodes of the mesh in the tied surfaces are automatically linked to the master node. All nodes therefore have the same deformation and supports as the master node, and all reaction forces are summed and displayed in the master node only.

Lastly it is worth to mention some basic meshing settings. Due to the complex shape it is important to use mid-side node location 'on shape' for the quadratic elements and toggle on the option to adapt element size near curvatures. The mesh generation will otherwise fail or result in an ill-connected mesh.

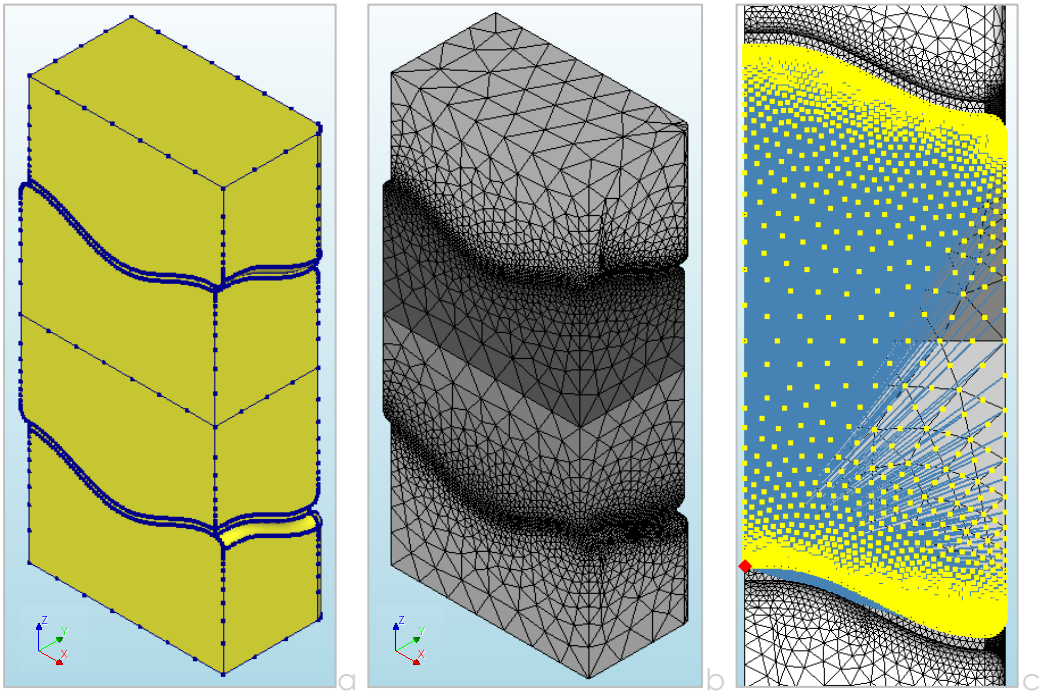

Figure 94: Meshing properties: a) Mesh seed; b) mesh; c) tying of nodes to master node.

5.2.7. Structural nonlinear analysis settings

Below the analysis settings will be briefly discussed.

Nonlinear effects

The only nonlinear effects applied in the analysis are the physical nonlinear effects of the interface elements. Due to the addition of the TENSTR and COMSTR material properties, these properties might have been read by the software as nonlinear material properties. Hence all other nonlinear effects are toggled off prior to analysis.

Load-steps

The prescribed deformation load is set to Δu = -0.1mm. After some initial testing a load step setting of 0.5(11) seemed adequate for most models. This means the load is applied eleven times with a load factor of 0.5. Within this range most models achieved a Christensen's output of one, and therefore was set as initial input. For some variations, such as the Young's modulus and Poisson experiments, this value had to be altered, either with lower increments or a larger range.

Iteration method and convergence criteria

As an iteration method the Secant iteration procedure is used, which in preliminary analyses gave faster results than the Regular Newton Raphson or Modified Newton Raphson. This however comes at the cost of a certain degree of precision, as the method works only faster for larger force convergence tolerances. The imbalance of forces is however sufficiently small to allow such deviations, as will be further elaborated in the next chapter. The analysis is set up to have energy convergence (0.001) and force convergence (0.025) simultaneously.

The Broyden method is applied on the Secant iteration procedure and the tangent is taken from the previous iteration. This method is known to require more storage space for each iteration, however due to swiftly reaching convergence this effect is limited. The principle of the Secant iteration procedure is shown in Figure 95. The method does not set up a new stiffness matrix, but instead uses the previous iteration and its out-of-balance force vectors to predict a new solution (DIANA FEA, 2010).

Output

Besides the conventional outputs (displacements, reaction forces, global Cauchy stresses and global strains) also the Christensen's output is selected, as well as the principal strains and stresses, and the traction strains and stresses. All stresses and strains are moreover reviewed in the local and global axes, and furthermore evaluated in the nodes and element centres.

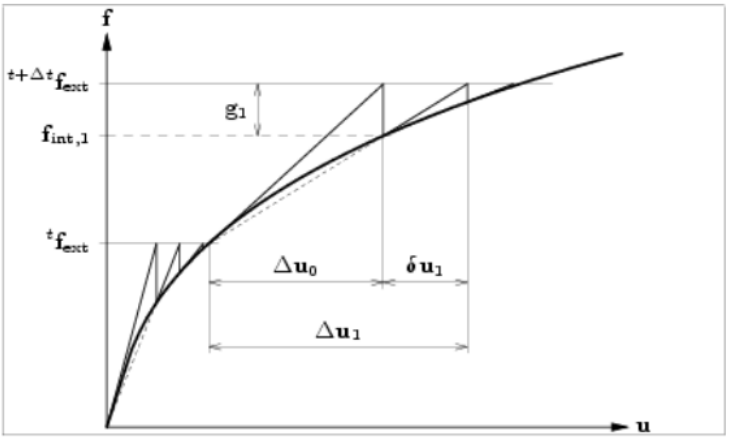

Figure 95: Quasi-Newton iteration procedure, also called Secant iteration procedure. Reprinted from (DIANA FEA, 2010).

Section 5.3. Validity of the model

As mentioned before many of the input properties are based on assumptions. This section reviews if the model is working correctly according to the input and convergence criteria provided. In the following subsections certain important aspects of the model will be reviewed.

5.3.1. Young's modulus of PU

To review the Young's modulus of PU a compressive deformation load is applied on the top face of the test set up. The input value of the polyurethane was a Young's modulus of 50 MPa, determined in Section 5.1.4. If the model works correctly the PU interlayer should behave stiffer than this input value.

A prescribed deformation of 0.10 millimetres is applied. This leads to a deformation of both polyurethane layers of 0.05 millimetres, as is evident from Figure 96. The reaction force on the top surface yields a value of Fc = 37400 N. The following simple calculations can then be made to determine the Young's modulus of the PU:

$$\varepsilon = \frac{\Delta l}{l} = \frac{\Delta t}{t} = \frac{0.05}{4} = 0.0125$$

$$\sigma = \frac{F}{A} = \frac{37400}{150 * 75} = 3.324\ MPa$$

$$E = \frac{\sigma}{\varepsilon} = \frac{3.324}{0.0125} = 265.92\ MPa$$

The resulting Young's modulus is as expected significantly higher than the input provided. It is however in the order of magnitude as was the case in the experimental results by Aurik (2017). It is therefore assumed to be a realistic approach of modelling the polyurethane. The difference between the two values can be a result of the almost incompressible chosen value for the Poisson ratio or due to locking occurring in the interlayer. In any case it behaves similar to the tests performed in Section 5.1.4.

The effect of the incompressibility is clearly visible when evaluating the bulging out behaviour of the material in a cross section of the model, here shown in Figure 97.

It could be interesting to investigate the influence of different values for the Young's modulus or Poisson's ratio on the model. These parameter variations are therefore included in the variation study in the next chapter.

For the Young's modulus a range of 8 – 350 MPa will be evaluated, as the theoretical value starts at 8 MPa and the experiment values yield a value of 336 MPa.

The Poisson's ratio will be evaluated for values approaching incompressibility (ν = 0.50). Therefore a range will be investigated from 0.475 to 0.4999.

Expectations are that the higher the Young's modulus or the closer the Poisson's ratio to 0.50, the stiffer the material will react. Hence the allowed deformations will be smaller and therefore the sensitivity to deviations in the geometry greater.

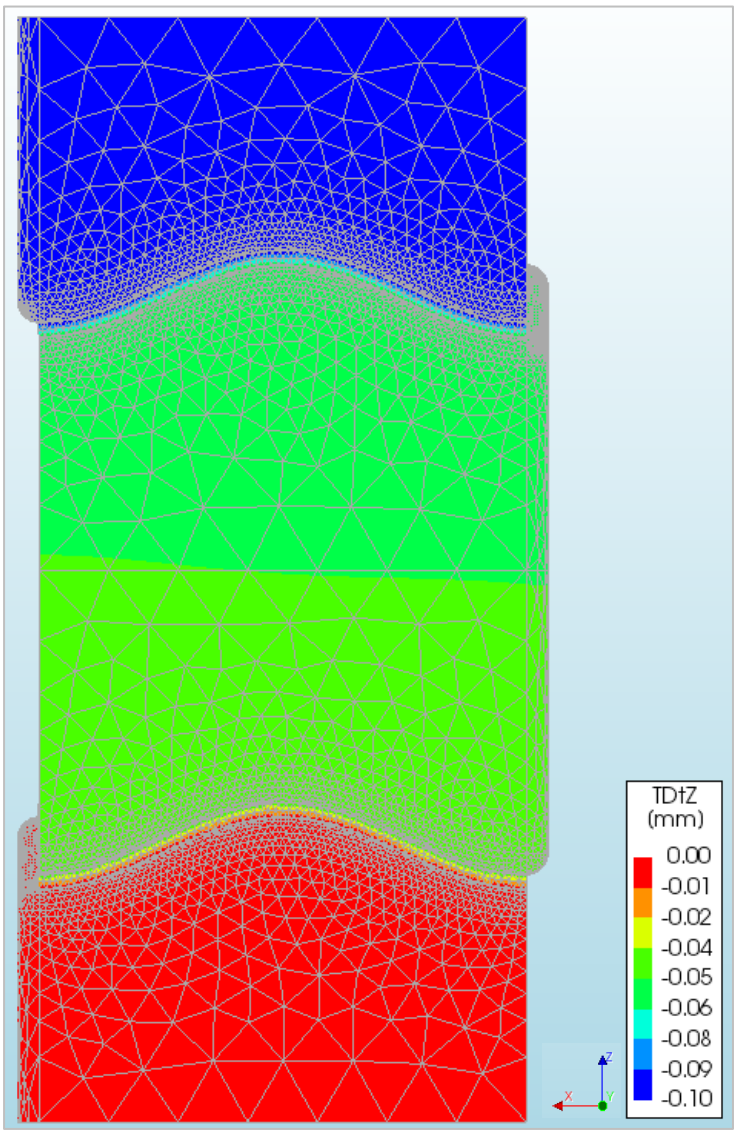

Figure 96: TDtZ results showing deformations in the global Z-direction under a prescribed deformation load of 0.10mm.

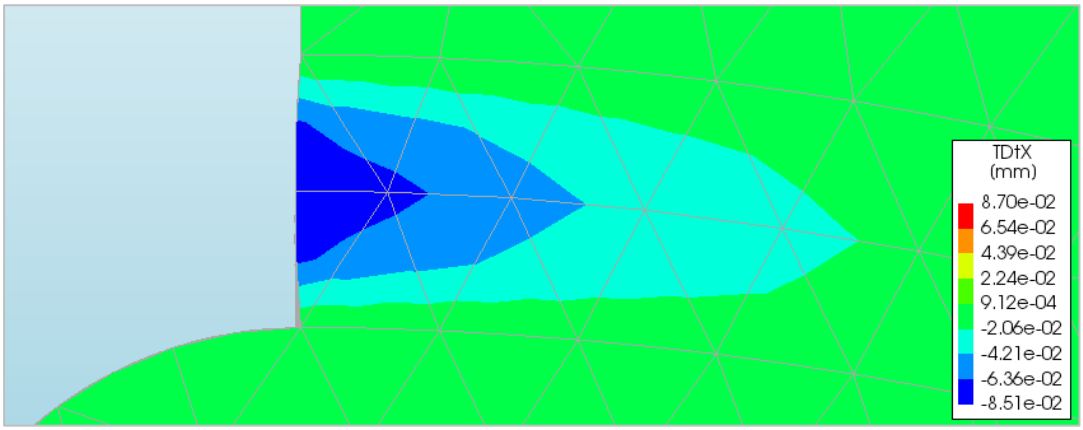

Figure 97: Minor local bulging out of the material.

5.3.2. Validity of the interface elements

It is important to check if the input properties of the interface elements behave as intended. Relative displacements should therefore be low, tensile stresses minimal and the stiffness input should be checked compared to the element results. These properties are checked for the regular shear tests as described in the previous section.

As the interface elements are dummy elements and therefore have no thickness, relative displacements should be kept to a minimum. Reviewing the results, the relative displacements are in an order of magnitude of 1e-07 to 1e-08 millimetres, which is sufficiently small to conclude the interface elements are working sufficiently stiff.

The interface properties moreover dictate that no tensile stresses are allowed to occur in the elements, however local peak stresses always occur in these analyses, but should be kept to a minimum. Hence the results for the local normal stresses StNz are reviewed to check if and where these local invalid peak stresses occur. To visualise this, the results are plotted for zero stresses or lower (in blue) and for 0.1 and up (in red) in Figure 98.

Small peak stresses can be observed along the shorter edges and across the interface. These are however occurring in the nodes, which are determined by interpolation between results obtained from the adjacent elements. When reviewing the results in the element centres, all results are non-tensile, as is shown in Figure 99.

The interface elements therefore appear to work correctly, with some local peaks occurring in the nodes. The overall behaviour is however non-tensile, which was the intention of the interface elements.

Lastly it is important to check if the element stiffness is working according to the input provided. For this the stresses and the relative deformations of an element are reviewed in its element centre. The corresponding stiffness is then calculated to evaluate if the stiffness is in the same order of magnitude as the input provided. The results of the element reviewed are shown in Figure 100.

$$K_n = \frac{StNz}{DUNz} = \frac{-11.76}{-1.68 * 10^{-7}} = 7.00 * 10^7$$

$$K_{t;x} = \frac{StSx}{DUSx} = \frac{1.11}{1.58 * 10^{-7}} = 7.03 * 10^6$$

$$K_{t;y} = \frac{StSy}{DUSy} = \frac{-0.14}{-1.97 * 10^{-8}} = 7.11 * 10^6$$

The values of the normal and tangential stiffness correspond with the input values; hence it can be concluded that the interface elements behave as expected and according to the input provided.

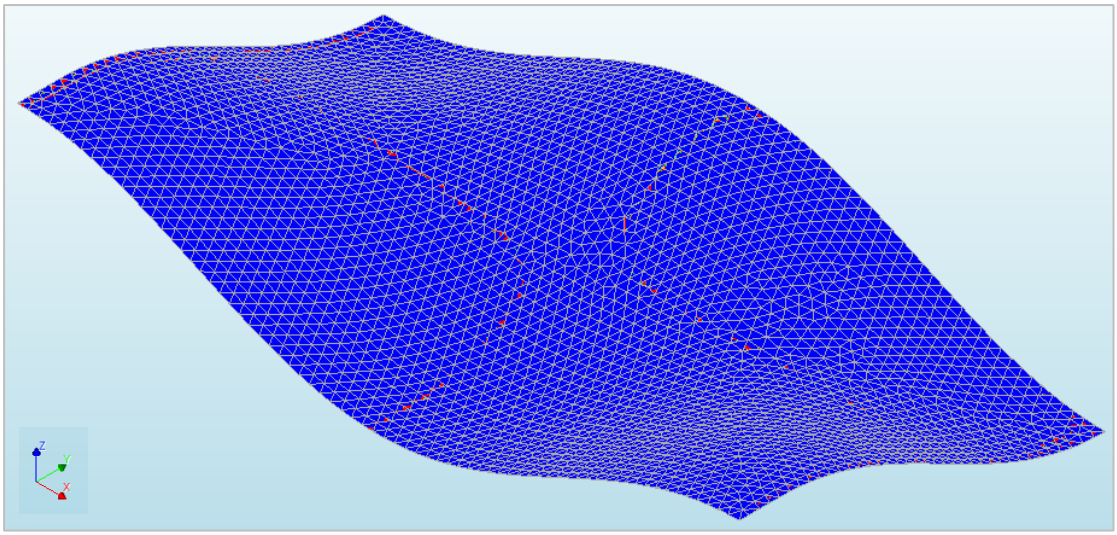

Figure 98: Tensile peak stresses StNz, in the nodes which are minor calculation mistakes in the interface elements. Results are plotted from 0 (blue) to 0.1 (red).

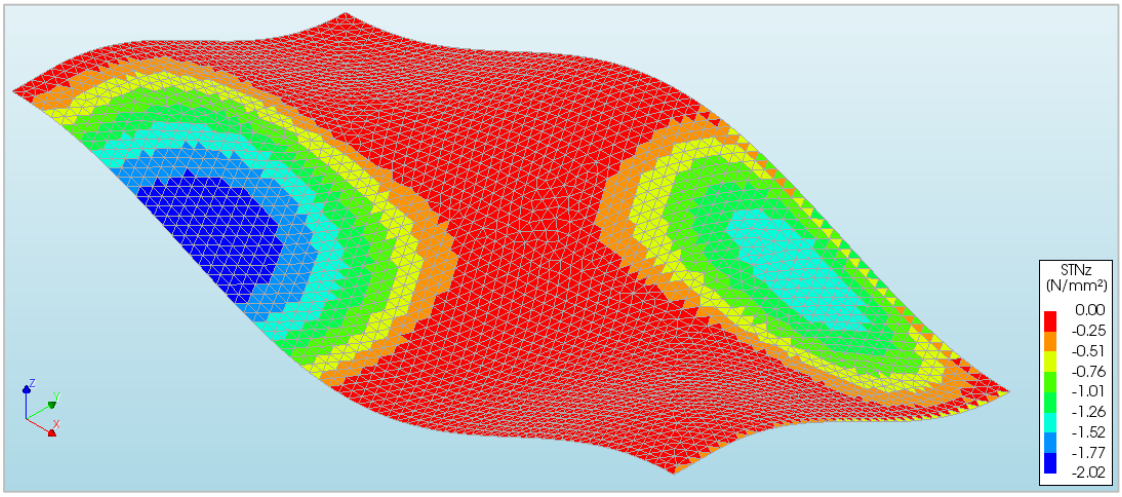

Figure 99: StNz results in the element centres, no tensile stresses are observed.

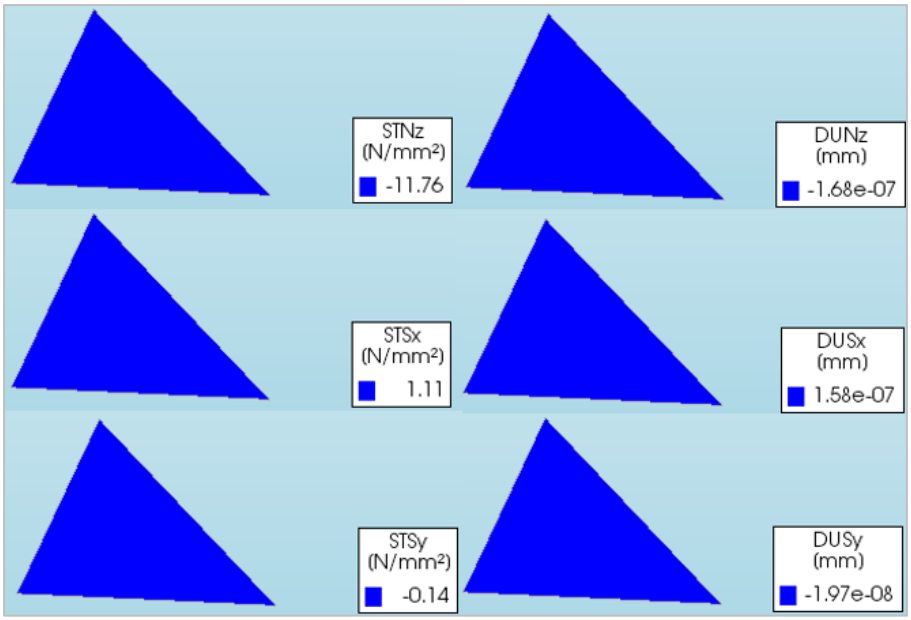

Figure 100: Evaluation of one wedge element in the compressed area, for stresses and deformations in the local direct axis directions.

5.3.3. Validity of the Christensen's failure criterion output

The new Christensen's failure criterion output is essential for evaluating the geometry on the sensitivity of flaws in the geometry. To check if the output is correct it is evaluated here by checking a glass element located on the contact area. Both an element in tension and one in compression is evaluated. The location of these elements on the geometry is shown in Figure 101. Results for the individual elements are given in Figure 102 for the tension area and in Figure 103 for the compression area.

Filling the values in Equation 5.1. yields for an element in the tension area:

$$\left(\frac{1}{45}-\frac{1}{360}\right)(20.59+16.36+10.32)+\frac{1}{2*45*360}[(20.59-16.36)^2+(16.36-10.32)^2+(10.32-20.59)^2]=0.924$$

And for the compression area:

$$\left(\frac{1}{45}-\frac{1}{360}\right)(-2.38-12.73-19.54)+\frac{1}{2*45*360}[(-2.38--12.73)^2+(-12.73--19.54)^2+(-19.54--2.38)^2]=-0.660$$

Hence both values are calculated and displayed correctly in the model.

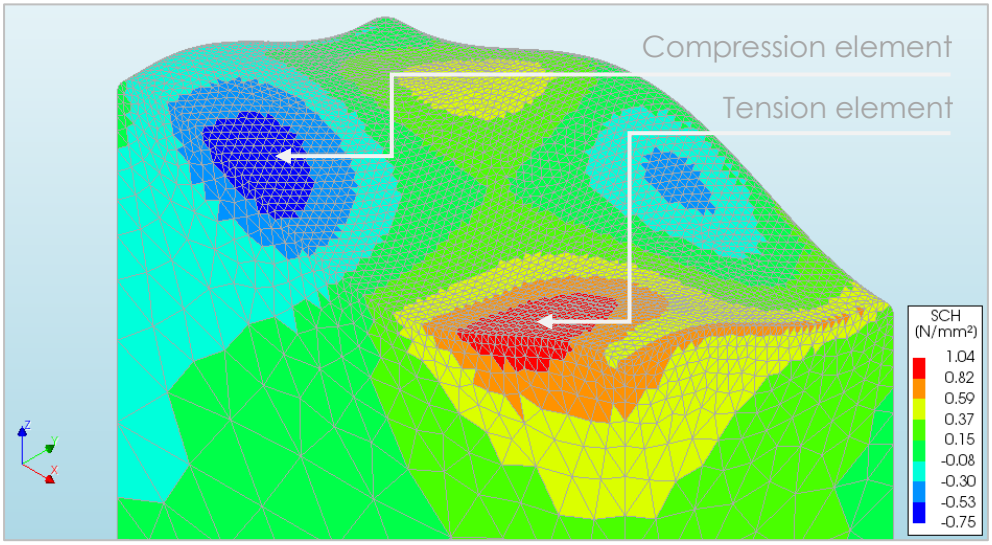

Figure 101: Middle brick Christensen's output, indication of the elements analysed.

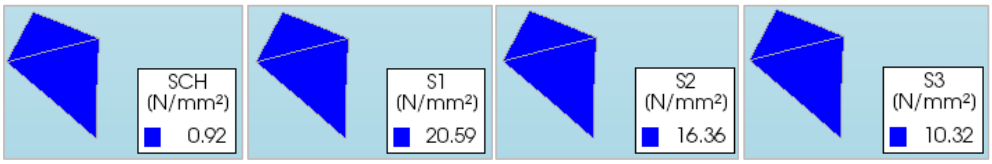

Figure 102: Christensen's output and principal stresses results in the element centre for a single element in the tensile area.

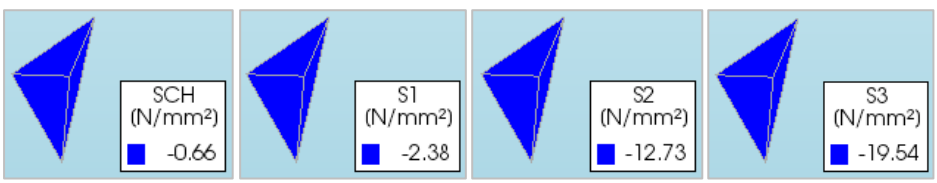

Figure 103: Christensen's output and principal stresses results in the element centre for a single element in the compression area.

5.3.4. Imbalance of reaction forces

For the analysis a quite coarse convergence criterion was set. Therefore it is important to check the imbalance of reaction forces to make sure this is justified.

Below the reaction forces in x, y and z-directions are evaluated. For the x-direction the reaction forces working in the ties are shown. In the y-direction the result is shown from a summation of all supported nodes of the symmetric faces. Lastly the z-direction reaction forces show the difference between the summation of reaction forces at the top and bottom sliding supports.

$$\sum R_x = 83435 - 41967 - 41509 = -41\ N$$

$$\sum R_y = -\ 4 * 10^{-12}\ N$$

$$\sum R_z = 1442 - 1437 = +5\ N$$

It can be concluded that the imbalance is merely a fraction of the reaction forces.

Chapter 6.
FEA results and parameter variations

The results of the analysis of the initial design and its parameter variations are discussed in this chapter. FEA results are compared with earlier derived expectations in Chapter 4. Qualitative remarks considering tolerance sensitivity are discussed and design values for the shear capacity are derived from test results.

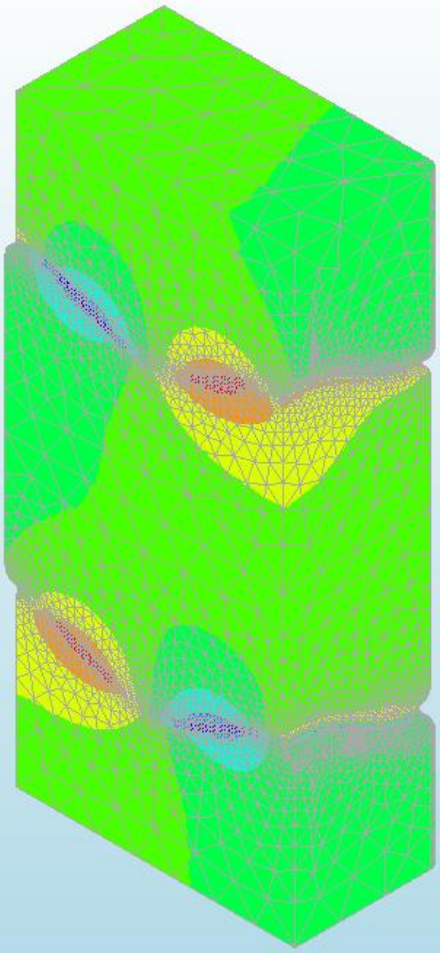

Section 6.1. Initial model results

The initial model design, with overall dimensions of 300x150x150 and an amplitude of 10mm are tested on shear, compression, and a combination of both to review the behaviour of the model and to validate the statements made earlier considering the normative brick. The effects of variations of the Young's modulus and Poisson's ratio are also evaluated, as these are expected to affect the results significantly.

6.1.1. Compression test results

The vertical loading of the bricks is expected to act on the geometry beneficially, putting the geometry in a state of compression. However, it is important to check if this behaviour is true, and if due to the interlocking geometry no other tensile areas are created, which can induce local failure. Hence the model is tested using a prescribed deformation on the top surface instead of the shear deformation used in the shear test set up. All other parameters and settings are equal to the model described in Chapter 5. The load is applied until reaching a Christensen's value of CHR = 1, hence at that point there should be a critical tensile stressed area.

The resulting contour plot is shown below in Figure 104 for CHR = 1. This contour plot is the same for any load-step applied, as the relation between the compressive load and the Christensen's criterion is linear, as is depicted in Figure 105.

Regarding the contour plot in Figure 104, it appears that the interlocking geometry acts like a wedge prying into the underlying geometry. In a way this makes sense. The polyurethane interlayer has limited compressibility, especially in the enclosed areas. When compressed it pushes the convex interlocking geometry outwards, hence resulting in tensile stressed areas in the concave parts of the brick.

Failure due to these tensile peak stresses however is very unlikely to occur. As Figure 105 indicates, the peak tensile stress occurs at a compressive load of approximately 1600 kN. With a brick weight of about 16 kg this is equivalent to the weight of ten-thousand upper layers. Hence this only becomes problematic when constructing a wall with a height of 1500 metres, which is unrealistic and far from the design ambition.

It is moreover important to take notice that these values consider the characteristic strengths. When the bricks are applied into a design, safety factors should be applied according to load duration.

Flaws are moreover not expected to have any effect in the compressed areas, the tensile areas are more prone to these flaws, however the vertical load would have to be significantly high to be of any effect. It is more likely that another failure mechanism would occur. It can therefore be concluded that a failure due to compression is very unlikely and will not be normative for the cast glass interlocking brick.

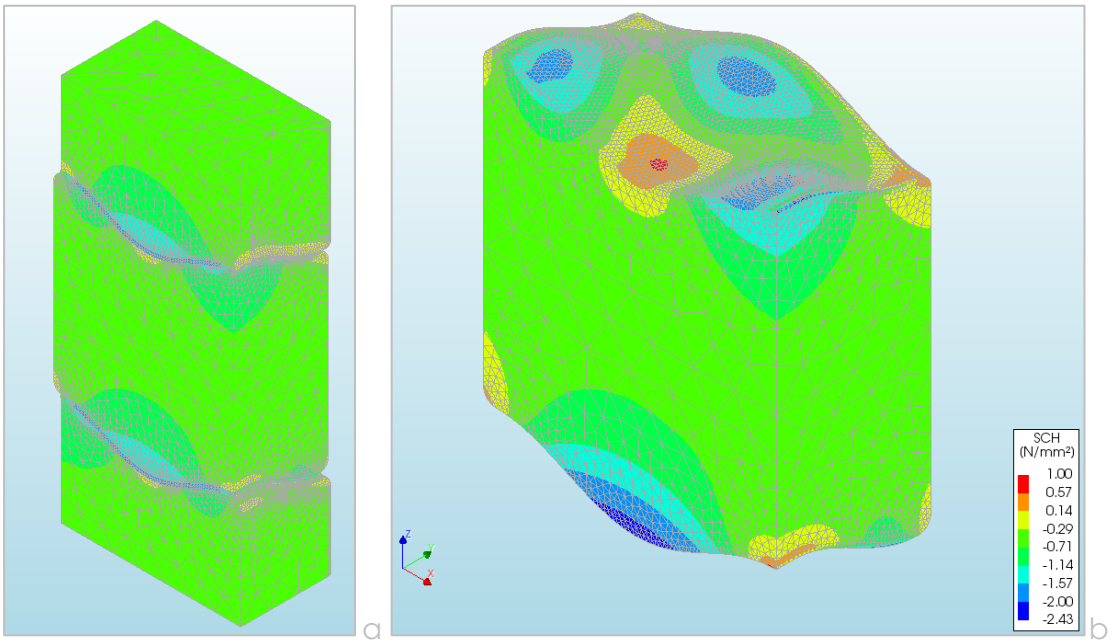

Figure 104: Contour plots of the Christensen's failure criterion for a brick under compression; a) results for the whole test set up; b) results for the individual brick.

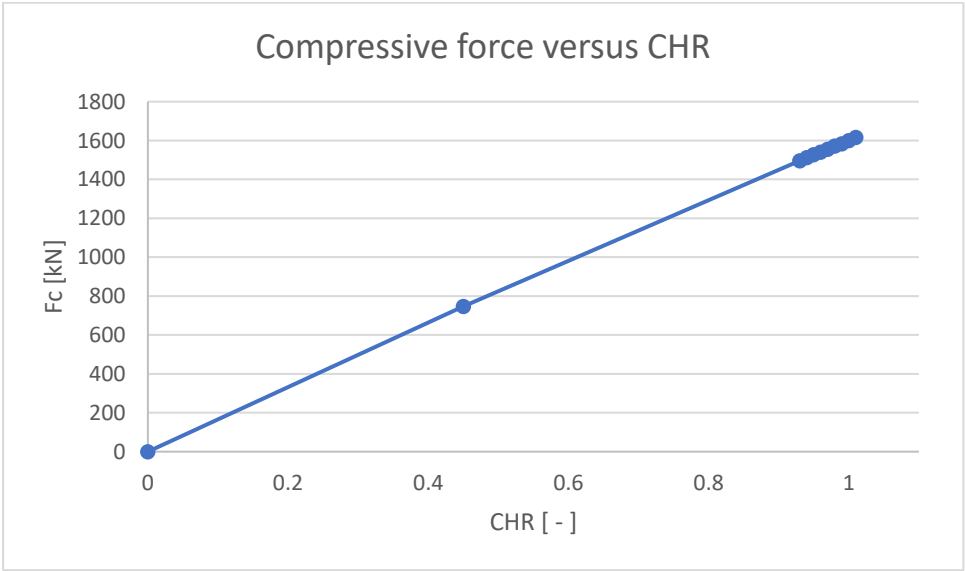

Figure 105: Graph showing relation between Christensen's criterion and the compressive force.

6.1.2. Shear test results

To evaluate the shear capacity of a single brick no other loads are introduced into the model. Any vertical compressive force would prestress the brick beneficially. This principle will be discussed in Section 6.1.3. As discussed in Chapter 5, the top of the test set up is modelled with sliders, hence also uplifting effects will be discussed.

Christensen's failure criterion contour plot

The contour plot shown in Figure 106a shows the whole set up and loading direction. By sliding the top and bottom geometries in that direction, the middle geometry will react with tensile (red) and compressive (blue) areas, as shown in Figure 106b. This contour plot is equal for all load steps, the values merely increase with each load step. This is caused by the linear relation between the Christensen's failure criterion output and the resulting horizontal force, as is depicted in Figure 107.

Along the edge of the brick local peak stresses make an appearance in the contour plot (indicated with a striped box in Figure 106b). These are distorted local effects introduced by invalid tensile peaks occurring in the interface elements, which are shown in Figure 108. As these values come forth from invalid tensile peak stresses in the interface elements, they can be disregarded in this evaluation.

The geometry furthermore behaves as expected, with the compressive area being spread over one interlocking geometry and the tensile area spread over the counter-acting geometry. The gradual curve hence spreads the load more evenly over the geometry. To compare this to one of the earlier 4TU restorative glass team designs in Figure 109, it can be observed that due to a sharp transition between interlock and main geometry, tensile peak stresses accumulate around this sharp transition. The gradual interlock hence prevents such behaviour.

More local tensile stresses would occur due to imperfections, which are not taken into account by the model. The more prone areas are however both the tensile and compression areas. In tensile areas a flaw can open due to this loading and hence can propagate throughout the brick. In compression areas a flaw would discontinue the gradual shape and introduce peak tensile stresses around the flaw, which then could lead to an interlock chipping off.

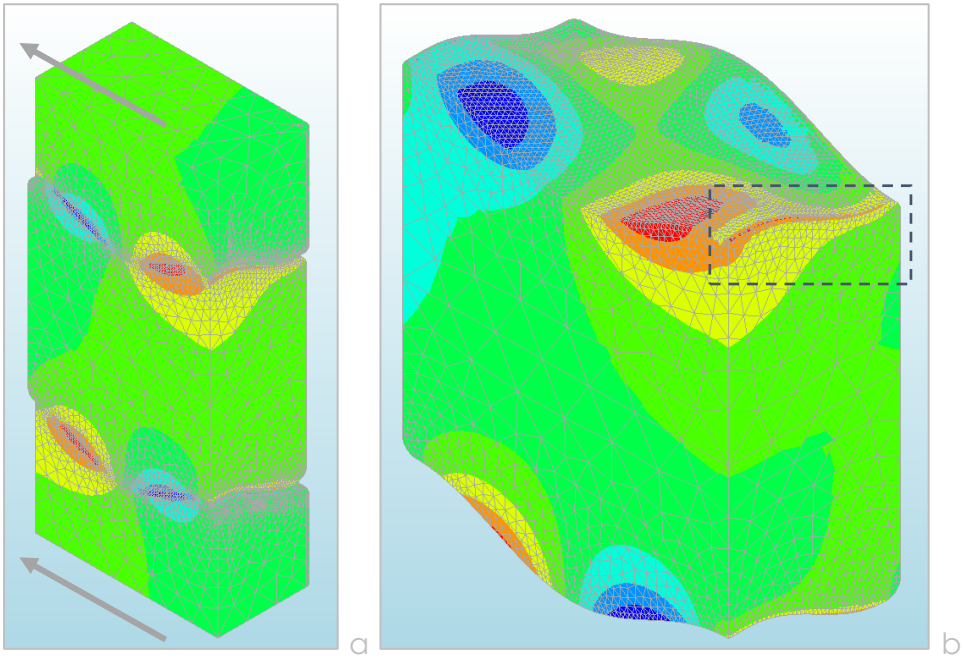

Figure 106: Contour plots of the Christensen's failure criterion for a brick under shear loading; a) results for full set up and arrows indicating loading direction; b) results for the individual brick.

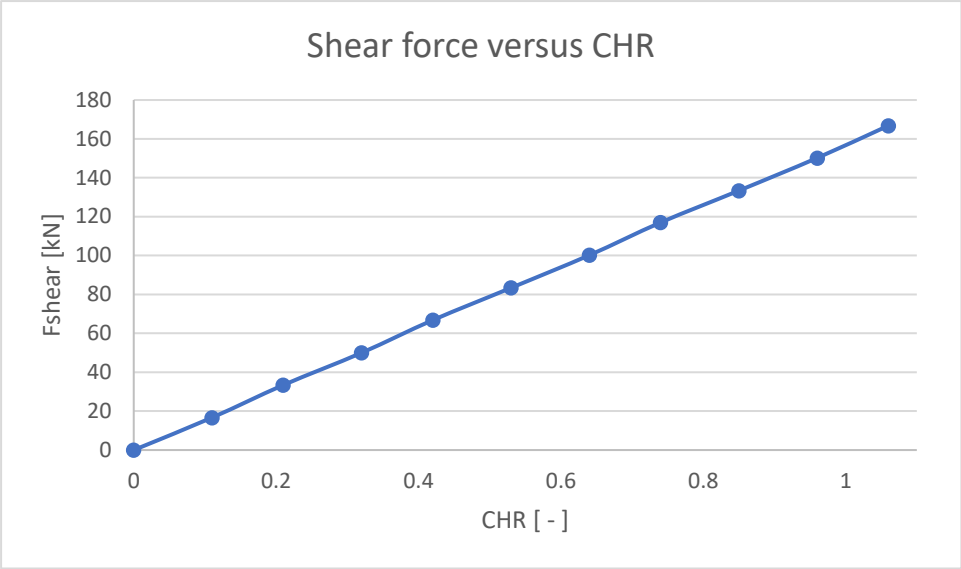

Figure 107: Shear force versus Christensen's output criterion.

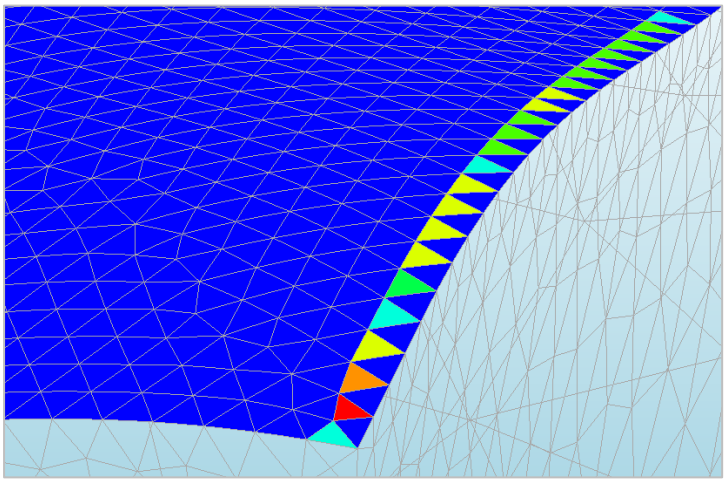

Figure 108: Interface traction results in x-direction (StSx element centre results), which show invalid tensile values near the edge.

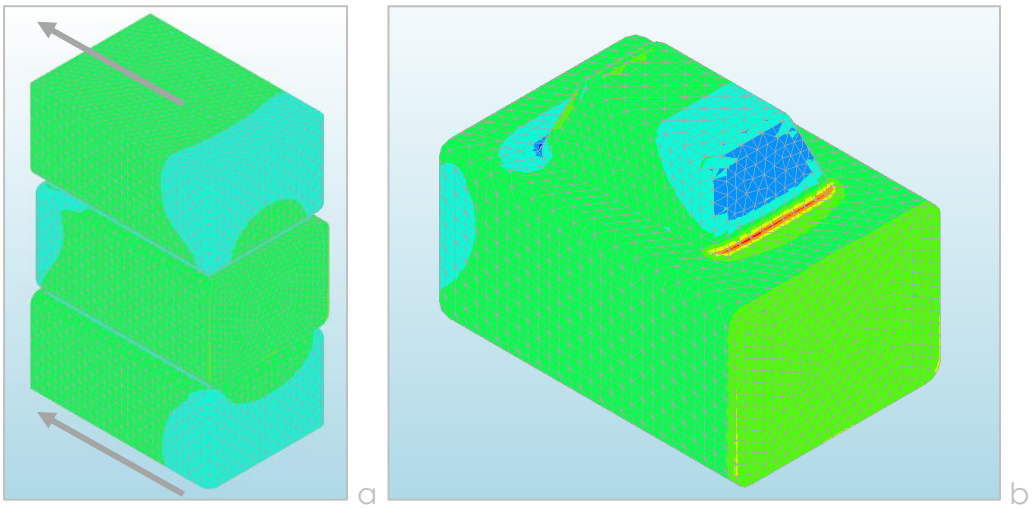

Figure 109: Christensen's output for a previous 4TU Restorative glass design, a) full set up and loading direction; b) results of the middle geometry.

Shear capacity

The shear capacity of the brick can be derived from the graph as shown in Figure 107. Due to the linear behaviour the values for the shear capacity (i.e. at CHR = 1) can be determined by interpolation. For the initial model this yields a characteristic shear capacity of F_{shear} = 156.84 kN. This is somewhat lower than the expected value of F_{shear} = 178.3 kN determined in Section 4.4.1.

Uplifting behaviour

The sliders in the upper geometry mimic the continuous keystone applied in the system. The keystone should have sufficient rigidity to keep the bricks from uplifting and create an initial vertical force to prevent uplifting to occur.

The expectations for the reaction forces are based on uplifting forces coming from the brick. As the top connection in the model is restricted in the global z-direction, a reaction force scheme as shown in Figure 110 occurs. The sum of all these vectors (in an absolute manner) should however still reflect the expected reaction force determined in Section 4.4.2.

The expected value should lie around $F_{reaction}$ = 67.9 kN. The results from the finite element analysis are plotted in Figure 111. At CHR = 1.0 the reaction force can then be determined using linear interpolation, and yields a value of $F_{reaction}$ = 76.9 kN. When not taking the absolute value of all forces, a net force is retrieved of 5.4 kN in positive z-direction.

This net force can be interpreted as the load needed on top of the critical brick to keep the system from uplifting, given its keystone is restricted in the z-direction. Hence when anchoring the keystone itself (and hence restricting it in z-direction), the weight of the keystone and any non-anchored layers should be equal to this net force.

In further analysis this net force will be expressed as a percentage of the shear capacity. Hence for the initial design the vertical force needed when applying an anchored keystone is 3.4% of the total shear capacity.

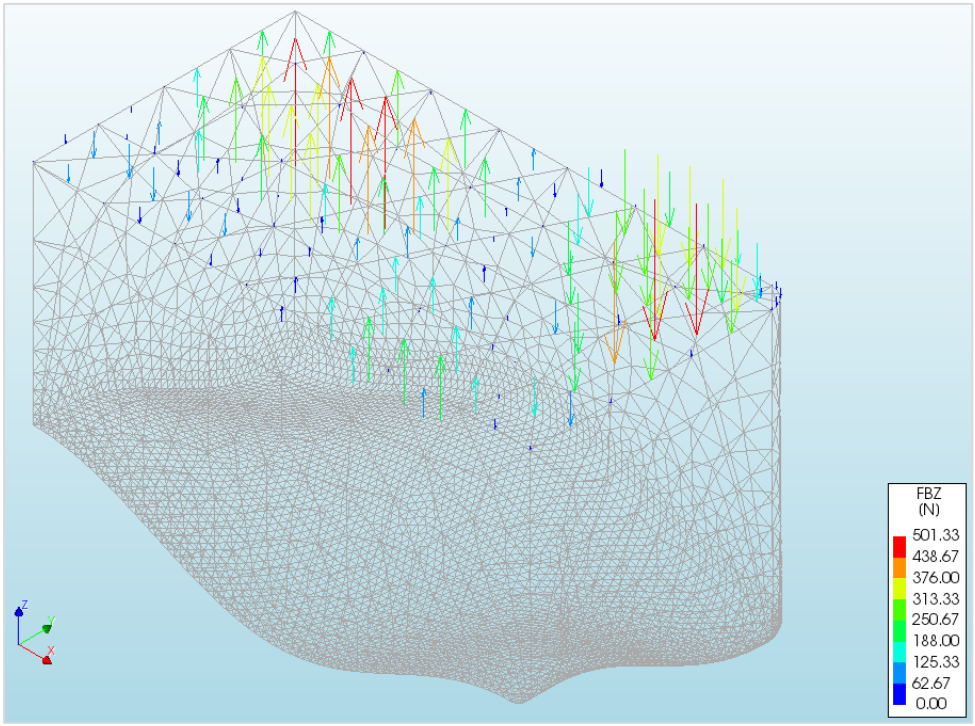

Figure 110: Reaction forces at the sliders restrained in z-direction. Visualisation of the effects of a continuous sliding keystone on the system.

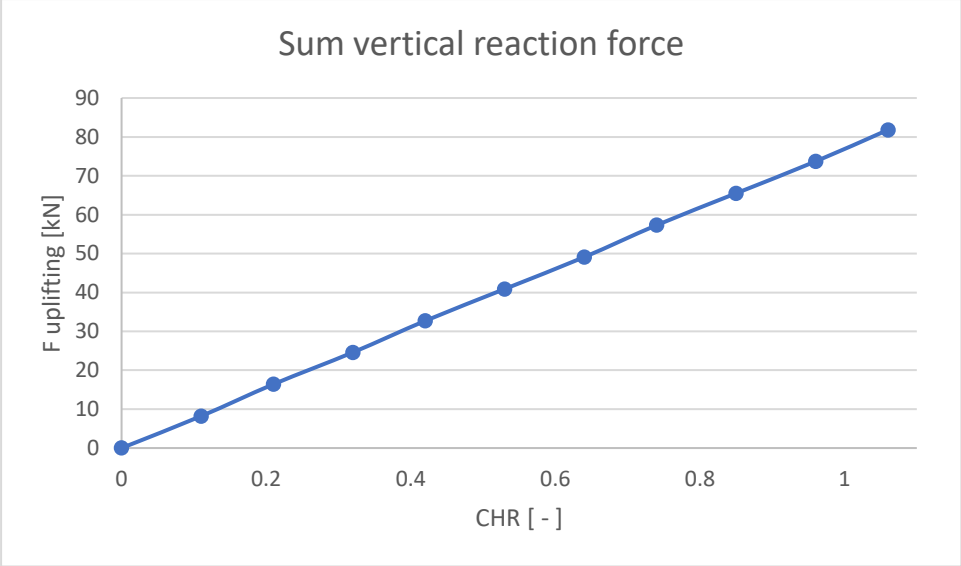

Figure 111: Results of an absolute sum of all reaction forces working on the top plane of the test set up, plotted against the Christensen's failure criterion.

6.1.3. Compression influence on shear capacity

The pre-compression of the bricks is argued to be beneficial for the shear capacity of the interlocking cast glass brick design. To validate this hypothesis, a test is applied with both compression and shear capacity. Hence this test compares a brick in the top of the wall to one in the bottom; or how the wall behaves under added compression.

To visualise this effect first the geometry is stressed with a prescribed deformation of 0.1mm in negative z-direction. After this initial loading the regular prescribed deformations are applied for the shear tests. The resulting forces are plotted in Figure 112 for results obtained in a shear only test (see Section 6.1.2.) and a combination of both. The tensile and compression areas are given for both load cases. This contour plot is constant for the shear only load case, but changes gradually for compression and shear. The complete propagation of tensile and compression areas for this load case is shown in Figure 113.

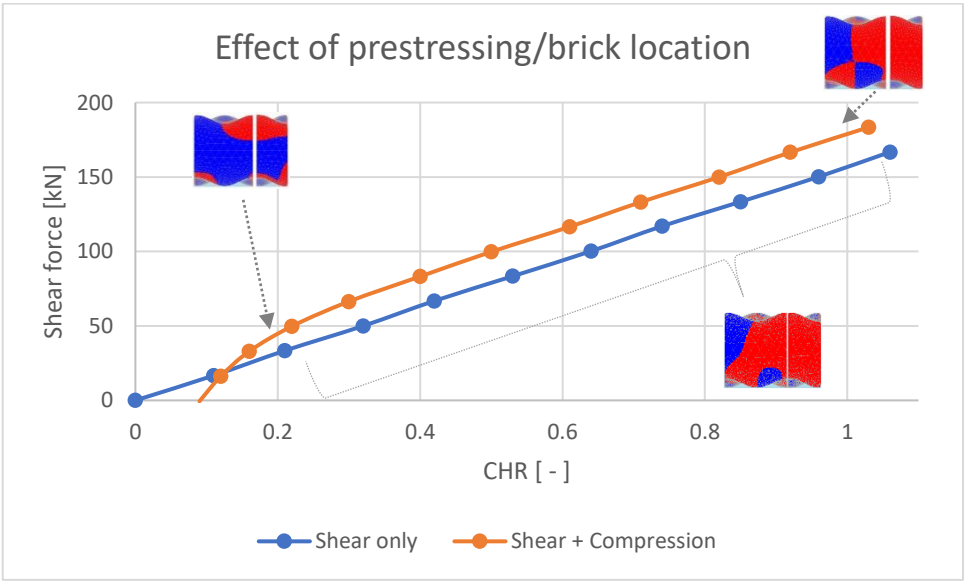

Figure 112: Effect of compression on the shear capacity.

Hence it can be concluded that the normative brick indeed is in the top layers of the masonry system, as any compressive force results into a higher shear capacity. Moreover, applying an extra compressive load can result into a better performing wall.

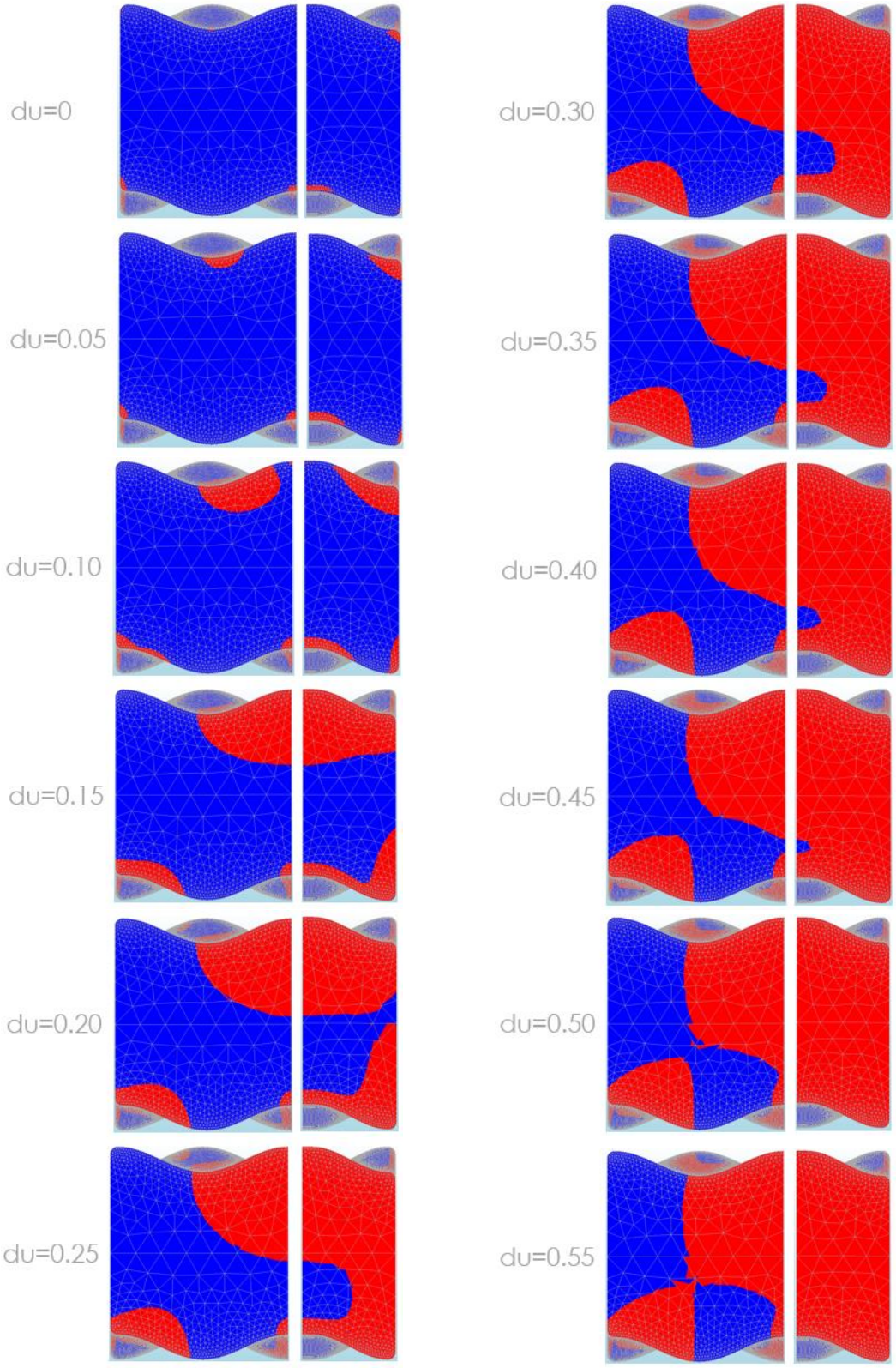

Figure 113: Propagation of tensile and compressive areas through a preloaded brick visualised in both cross-sections, CHR = 1 is passed at a deformation of 0.55mm. du in mm.

6.1.4. Influence of Young's modulus PU

The Young's modulus of PU is dependent on the hardness of the PU chosen. In this thesis a hardness of ShA 70 is chosen, based on laboratory tests performed in Aurik (2017). This value is chosen as these are the only literature results close to the problematic described in this thesis. A Young's modulus hence was derived from these test results, literature and a correction due to locking in the finite element model.

As this merely represents one possible Young's modulus for PU, it is interesting to investigate the influence of this value on the model. As a testing range, Young's moduli from 8 (initial calculated value according to literature) to 300 (value close to the experimental data) will be tested. These values can then be used for future reference, when for instance applying a different PU hardness (which would increase the Young's modulus). It however will always be important to set up a reference test in compliance with experimental results. The results below can however give a first indication.

The shear capacity is highly dependent on the Young's modulus for values below 100 MPa, beyond 100 MPa the shear capacity becomes more or less constant, as can be depicted from Figure 114. This has everything to do with the excessive stiffness resulting from a high chosen Young's modulus. This high stiffness results in small allowable deformations, which principle is shown in Figure 115. For higher values than 100 MPa the interlayer cannot deform much before reaching the capacity.

For very low values of the Young's modulus the interlayer however acts very flexible, with an acceptable deformation of about 2.5 mm before reaching a relative low capacity. A deformation of 2.5mm on a total of 4mm is quite large and not realistic behaviour for a polyurethane interlayer. A PU with 70 ShA is already quite a soft rubbery polyurethane and close to the lower limit of cast polyurethanes (see Section 2.2.2.). Hence it is improbable that a Young's modulus input below 30-35 MPa would yield realistic results in modelling.

The allowable deformation moreover influences the peak stresses occurring on the geometry. Comparing PU025 and PU300, in which the values 25 and 300 correspond with the input value for the Young's modulus, it can be concluded that with more rubbery elastic polyurethanes the peak stresses are more spread out over the surface of the interlock. With increasing rigidity the peak stresses are more localised, as is illustrated in Figure 116. The shear capacity increases hence with higher rigidity, but is also more concentrated in the geometry.

For future reference it can then be stated that when using rubbery polyurethanes as applied in this thesis a realistic choice would lie in between 35 and 100 MPa. For polyurethanes with such a hardness that they can be classified as a plastic, higher values may be possible. These polyurethanes are expected to be more rigid and hence allow fewer deformations.

It is however important that any input for polyurethane in the model is calibrated with experimental results. Hence a more extensive research into the behaviour of polyurethane interlayers is necessary before any application in practice.

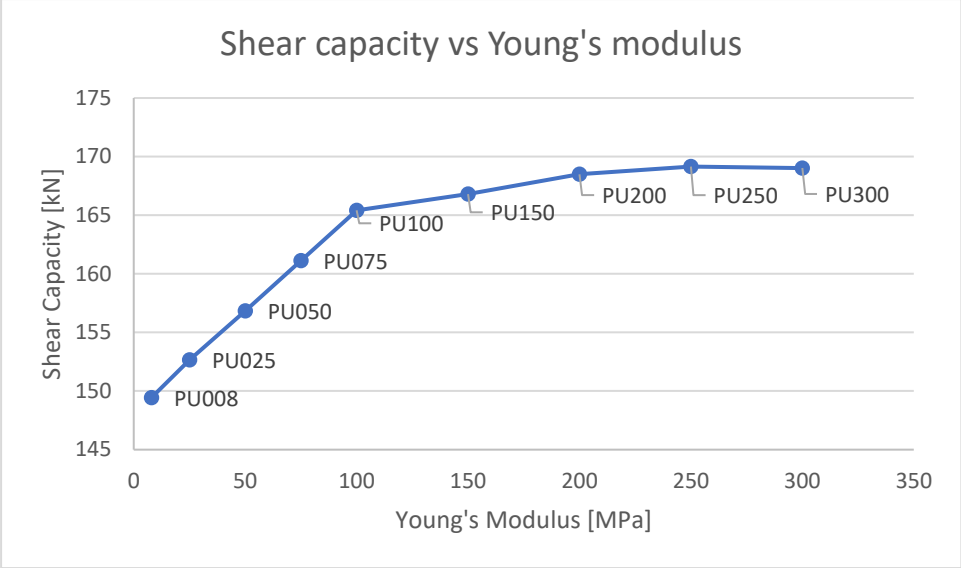

Figure 114: Shear capacity for each tested Young's modulus.

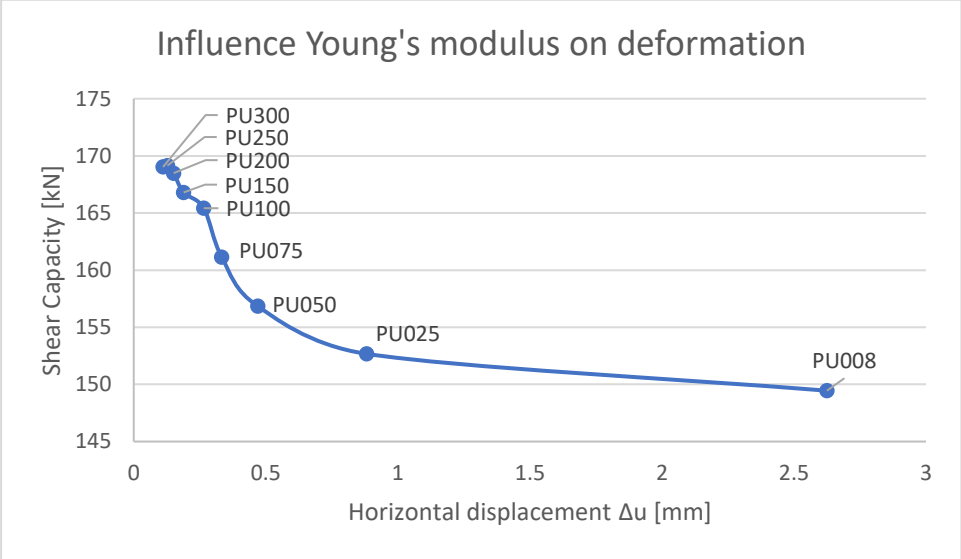

Figure 115: Influence of the Young's modulus on deformation/flexibility of the PU interlayer.

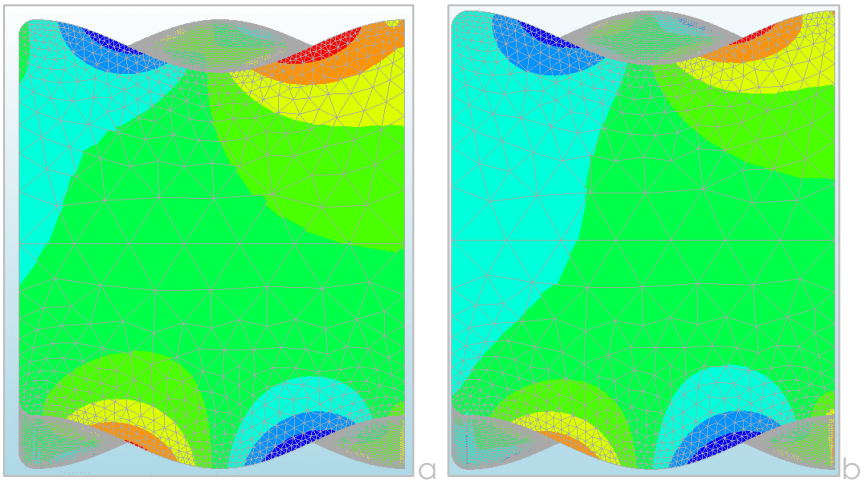

Figure 116: Peak stresses at CHR = 1 for a) PU025; and b) PU300.

6.1.5. Influence of Poisson's ratio PU

Another important parameter in the modelling of the interlayer is the Poisson's ratio. For future reference this value is also evaluated on its effects on the shear capacity and interlayer deformations.

As a rubbery substance, the polyurethane interlayer is nearly incompressible. Theoretically this would mean it has a Poisson's ratio of $\nu = 0.5$. This however leads to modelling problems which are illustrated below in Figure 117. For Poisson's ratios higher than 0.48 the shear capacity gradually drops, and goes into free-fall after 0.499, approaching zero when reaching 0.5. This is a common problem with finite element modelling, and hence should be taken into account when choosing the rubber parameters.

A higher value of the Poisson's ratio moreover limits the deformation capacity of the interlayer, as is shown in Figure 118. In contrary to the Young's modulus variations, this affects the shear capacity negatively. The more incompressible the interlayer is, the more rigid the interlayer acts. In a sense the interlayer becomes so rigid, that it loses its ability to deform and spread stresses as a mediator. Hence it appears as if two rigid bodies collide with the same stiffness, resulting in local peak stresses. For $\nu = 0.4999$ the contour plot is given in Figure 119, which illustrates this behaviour.

Hence it is key to be very careful with using high Poisson's ratios for incompressible materials, especially when using triangular solid meshes. The used value of 0.48 seems appropriate as for any higher value the outcome is affected immediately.

It is however important to calibrate the Poisson's ratio together with the before discussed Young's modulus and relate them to experimental results. Calibrating with a higher value for the Poisson's ratio would likely have resulted into a lower Young's modulus to allow for more deformation and vice versa. However it is not recommendable to use any values getting to close to $\nu = 0.50$, as the above mentioned effects cannot be countered by a sufficiently low value for the Young's modulus.

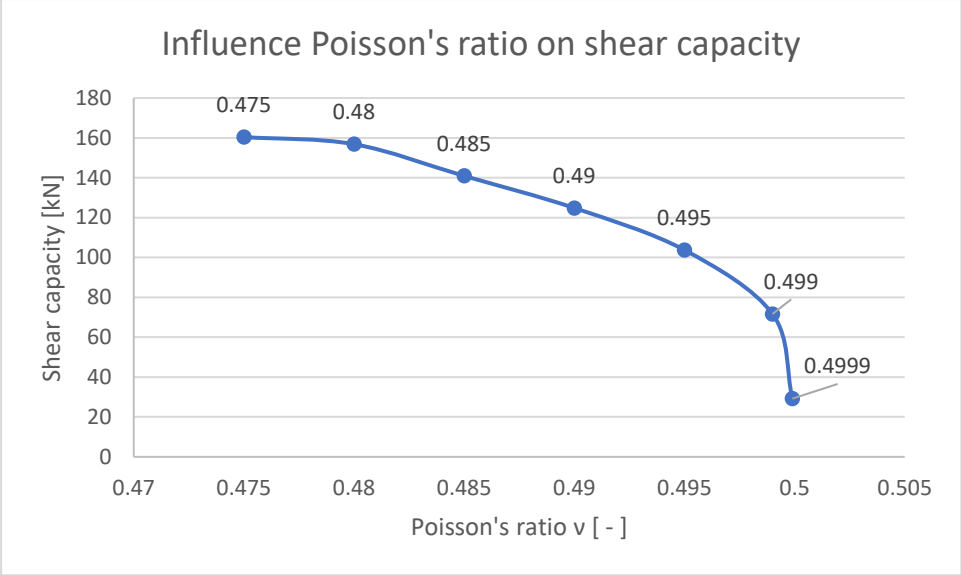

Figure 117: Influence of the Poisson's ratio on the shear capacity results.

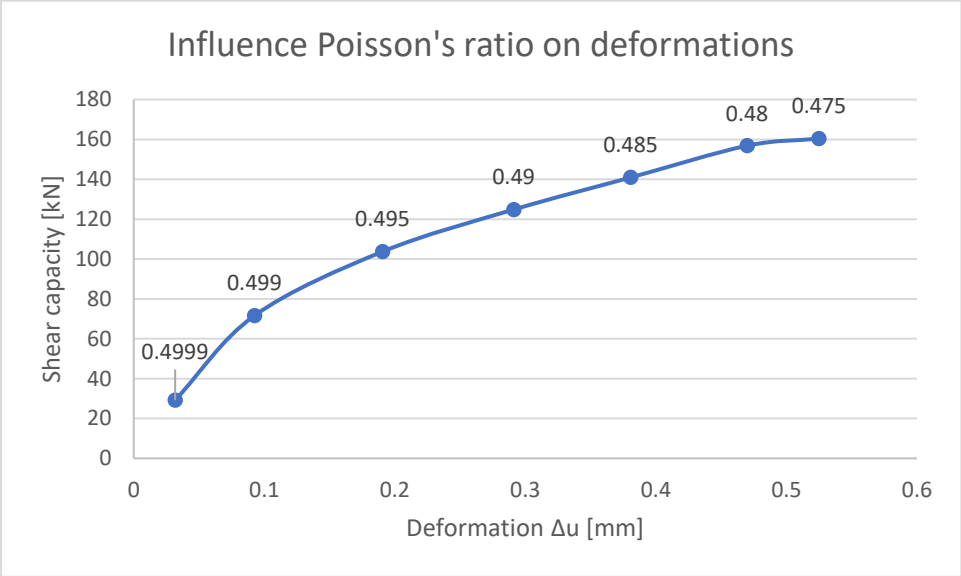

Figure 118: Influence of the Poisson's ratio on deformation of the interlayer versus the shear capacity.

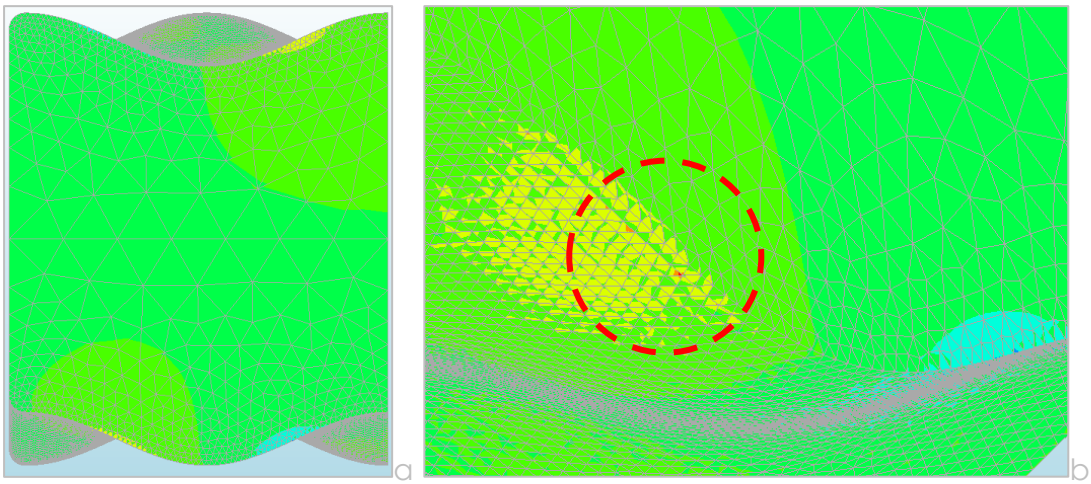

Figure 119: Peak stresses occurring in the v = 0.4999 variation for CHR = 1.

Section 6.2. Variation of brick height

The variation of brick height is expected to be influential on the failure behaviour of the brick. Hence the shear capacity is affected as well. For this parameter evaluation the FEA results are compared with the expectations made in Section 4.4.1.

These results are plotted in Figure 120. Whereas the bending failure expectations are fairly similar to the FEA results, they are showing a slight overshoot in capacity for lower heights. This probably can be dedicated to the 3D effect of the geometry, which was designed to counter-act on deformation tendencies.

From a height of 80mm on the calculated capacity starts to be lower than the expectations. This hence can be seen as a transition phase between the two failure mechanisms. Both failure mechanisms are affecting each other in this transition. Hence both can occur simultaneously. For higher values, such as the initial chosen value of 150mm, the graph seems to indeed approach a horizontal limit value. This means that the chipping off failure mechanism becomes more probable.

The increase in shear capacity can be illustrated with the change in the CHR-contour plots, which are given in Figure 121 for heights ranging 40mm to 120mm. For heights up to 60mm the tensile zone is predominant in the cross-section, hence decreasing the shear capacity. From a height of 60mm on the compression zone at the loaded interlock grows throughout the cross-section, past half the brick height and hence results in a higher allowable stress.

It is however worthwhile to notice that failure in cast glass bricks occurs due to flaw-propagated cracks, introduced by local tensile peak stresses around these flaws. The results however show which kind of crack propagation has a higher probability to occur. An interlock that chips off is hence preferable over the complete splitting of a brick. The more prone areas are both the compression and tensile zones.

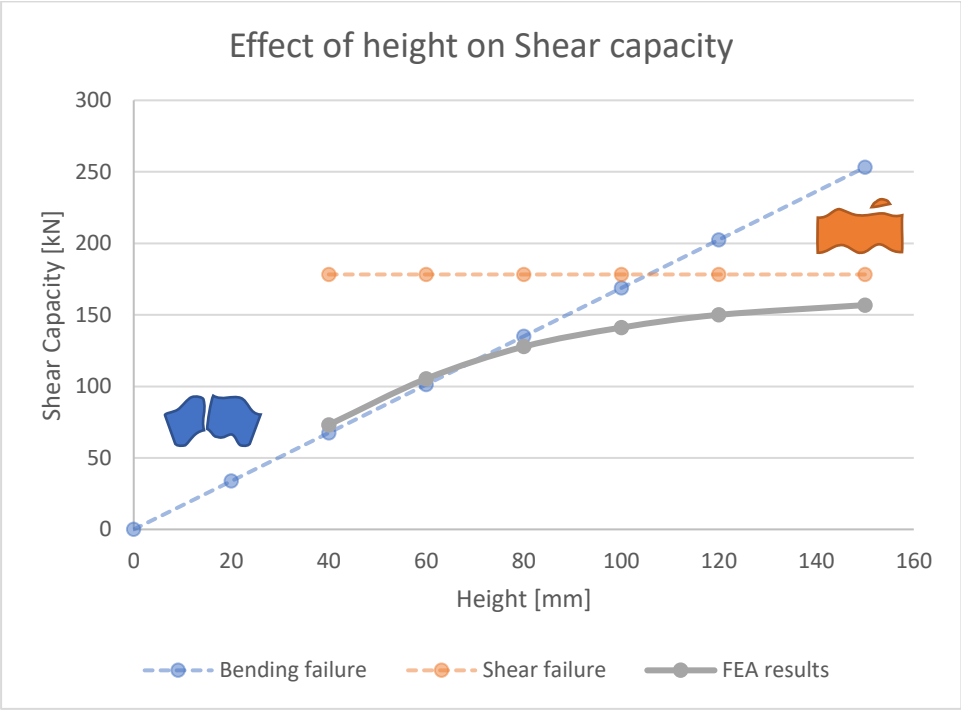

Figure 120: The effect of the height on the shear capacity of the brick, plotted together with the expectations derived in Section 4.4.1.

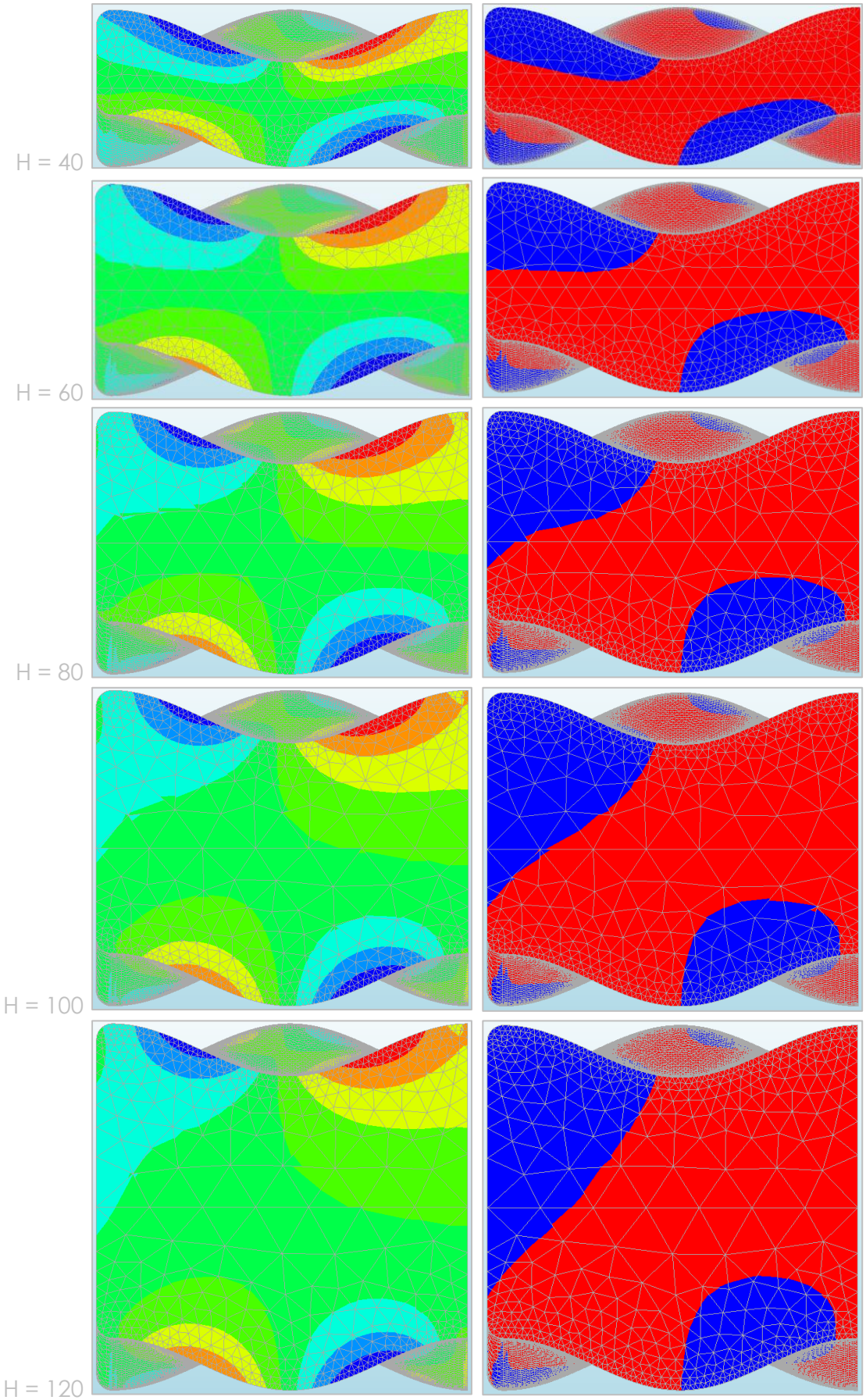

Figure 121: CHR output results (left); and tensile (red) and compression (blue) areas (right) for various heights (in mm).

Section 6.3. Variation of shear key amplitude

Changing the amplitude of the shear keys is expected to have a beneficial influence on the uplifting behaviour of the brick. It moreover is expected that with increasing amplitude, the increase in contact surface will affect the shear capacity positively.

The comparison of the FEA results with the expectations is given in Figure 122. The FEA results differ significantly from the expectations determined in Chapter 4. In order of magnitude the model behaves as expected, however due to influences that were not accounted for in the predictions the curves exhibit a different behaviour.

Moreover, a modelling error in the A = 5mm variant might have distorted the results. Due to the smaller amplitude the model ran into problems in both Rhinoceros and DIANA FEA. Higher tolerances were necessary in order to make the model work. Reviewing the contour plots in Figure 123 the A = 5 variant does not yield proper results. An enlarged image in Figure 124 indicates that the peak stresses occur in the edge of the brick, near the symmetry section plane. Earlier it was already acknowledged that these peaks occur due to small errors in the interfaces.

It may be that smaller amplitude bricks are more affected by this error, as the model will be more affected with friction, which is exhibited in the interface elements. Due to this, no concrete conclusions can be made for lower amplitudes than A = 10.

The behaviour of the model could however well be in the right direction. If a brick would not have any interlock (A = 0) and there would be no vertical force introducing friction, the reaction force and shear capacity curves would approach zero. The uplifting curve, which than is horizontal (parallel to brick interlock) would then be limitless, as the brick than can move freely. Adding this principle results in the graph illustrated in Figure 125. The results of the A = 5mm variant hence could indicate this behaviour, however it could well be that this behaviour sets in with even smaller amplitudes.

In any case the model behaves as expected for the higher amplitudes. Increasing the amplitude increases the shear capacity due to a higher contact surface, while decreasing the relative uplifting effects. This is graphically shown in Figure 126. It is hence beneficial to increase the amplitude to gain a larger shear capacity and lower uplifting effects.

The net value of the needed vertical force to refrain the critical brick from uplifting however increases with the amplitude, as does its ratio to the shear capacity. These values are presented in Table 13. This can be explained by the fact that the uplifting force has a bigger vertical component with increasing angle of the interlock geometry.

A higher amplitude moreover could contribute to beneficial chipping off behaviour. As can be depicted from the contour plots in Figure 123, the tensile and compression areas grow in horizontal direction in the shear keys. This increases the chance of a shear key failure instead of a splitting brick failure.

Table 13: Vertical forces necessary to prevent uplifting when applying an anchored keystone.

Amplitude	Fshear [kN]	Fnet [kN]	Ratio [%]
5	121.7	3.5	2.9
10	156.8	5.4	3.4
11	159.5	5.7	3.6
12.5	165.3	6.3	3.8
15	180.4	7.6	4.2
20	216.4	11.2	5.2

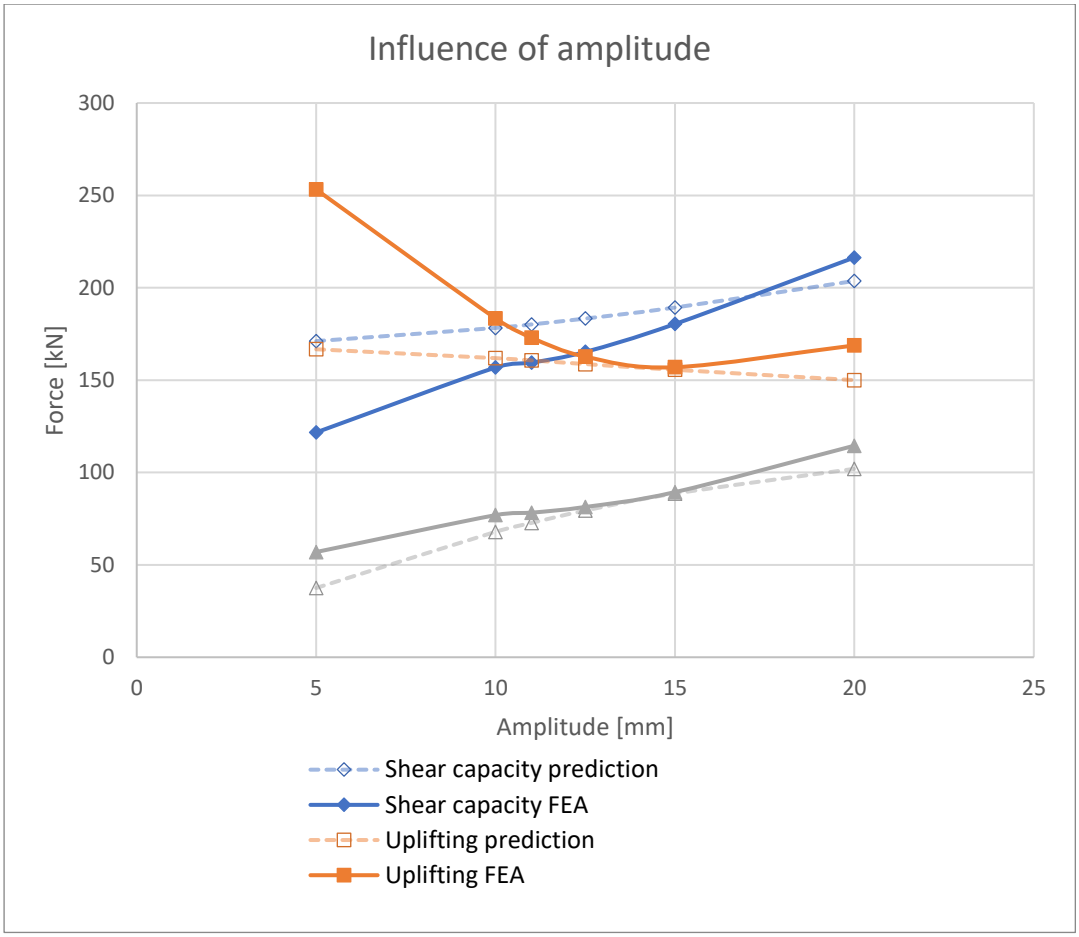

Figure 122: Influence of amplitude on shear capacity, uplifting force (parallel to interlock curvature) and reaction forces on the top.

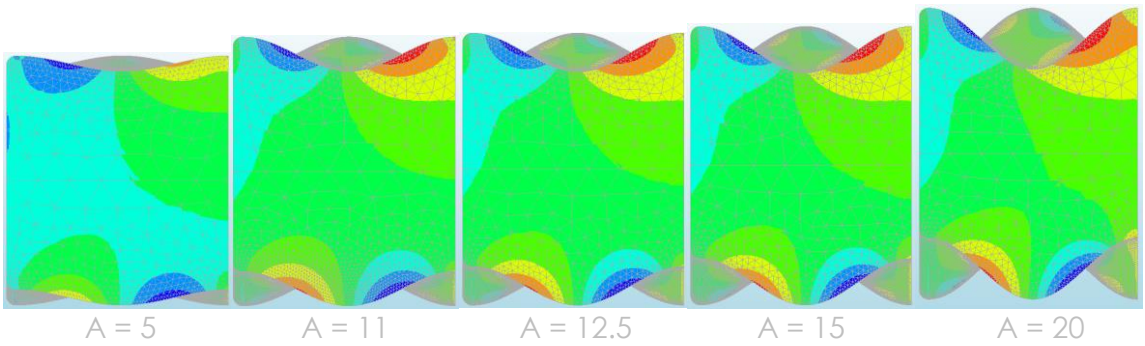

Figure 123: Contour plots for various amplitude variations.

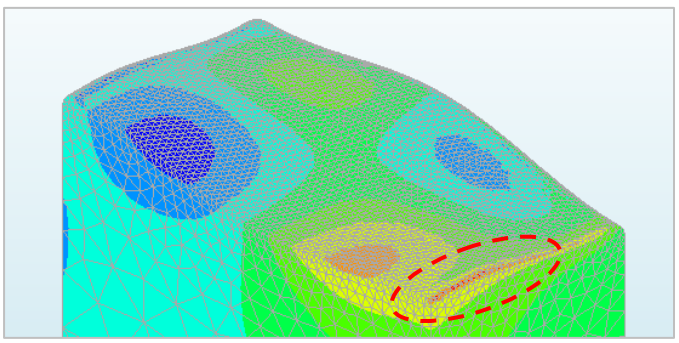

Figure 124: Peak stresses near the edge of the model of A = 5 mm.

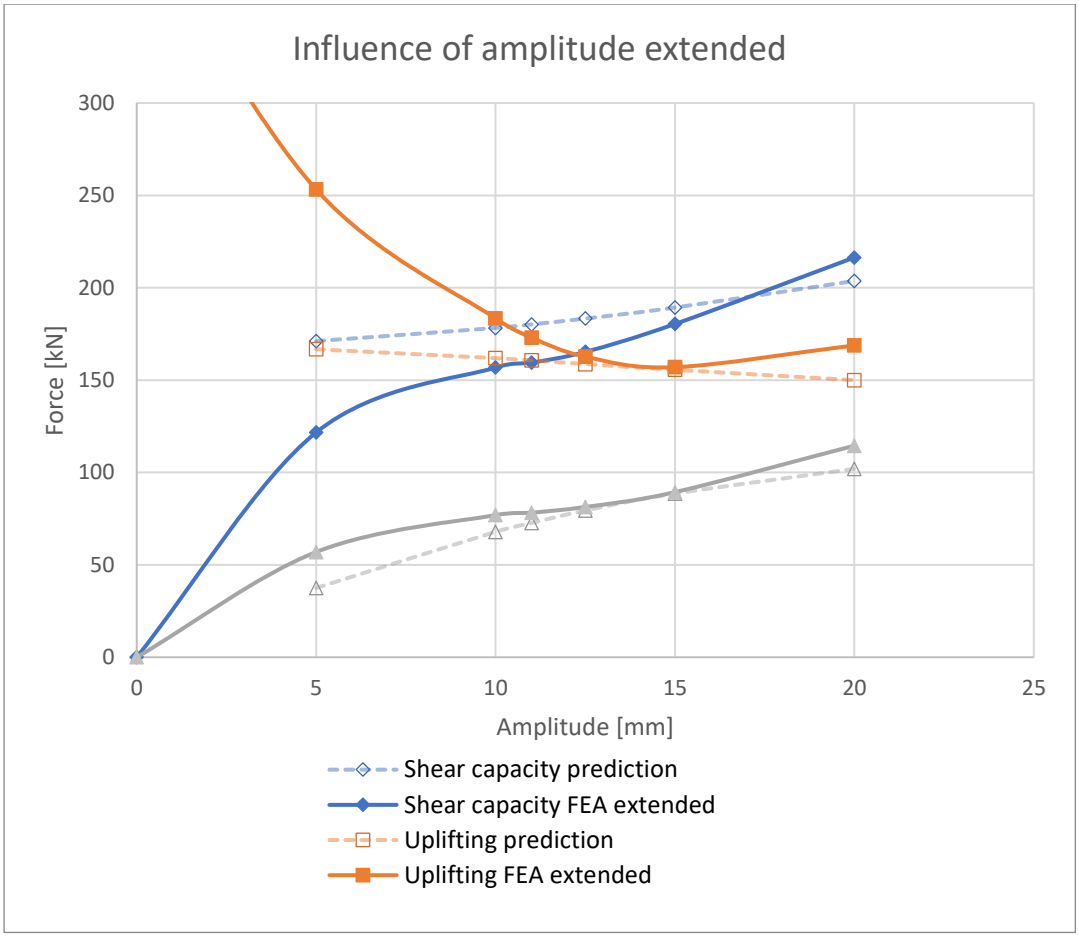

Figure 125: Extended results for the influence of the amplitude.

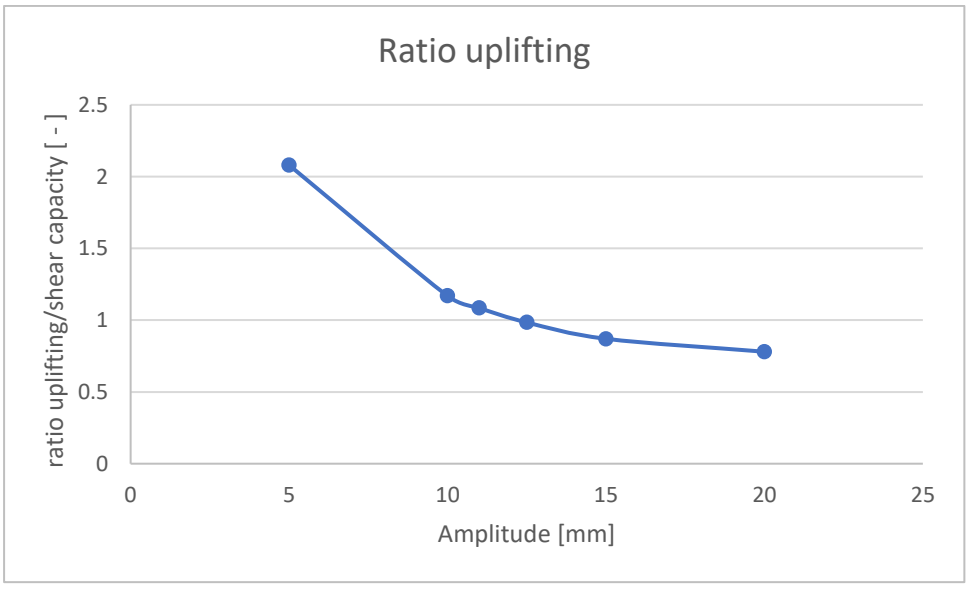

Figure 126: Ratio uplifting/shear capacity versus amplitude [mm].

Section 6.4. Variation of interlock geometry

To simplify the geometry, and hence the manufacturing and post-processing process, the interlocking curve can be combined with a linear function. A small analysis therefore is carried out to illustrate the effects of such a change in geometry.

Limited by the possible shapes exported by Grasshopper three models are tested next to the initial design. The models have approximately the same curvatures halfway the interlock as some of the amplitude variants. Hence these results can be compared to one another. In Figure 127 this comparison is presented graphically according to the curve angle halfway the interlock.

As expected the shear capacity of the new geometry is relatively constant in comparison with the amplitude variation. The uplifting force however decreases compared to the amplitude variant. The brick geometry is hence weaker in shear, but relatively more resistant against uplifting. This consequently can lead to a design choice depending on what the most important parameters are. The manufacturability and the post-processing of bricks are easier for linear-sine combinations, and if uplifting is a bigger problem than its shear capacity, one could choose for the linear-sine combination instead.

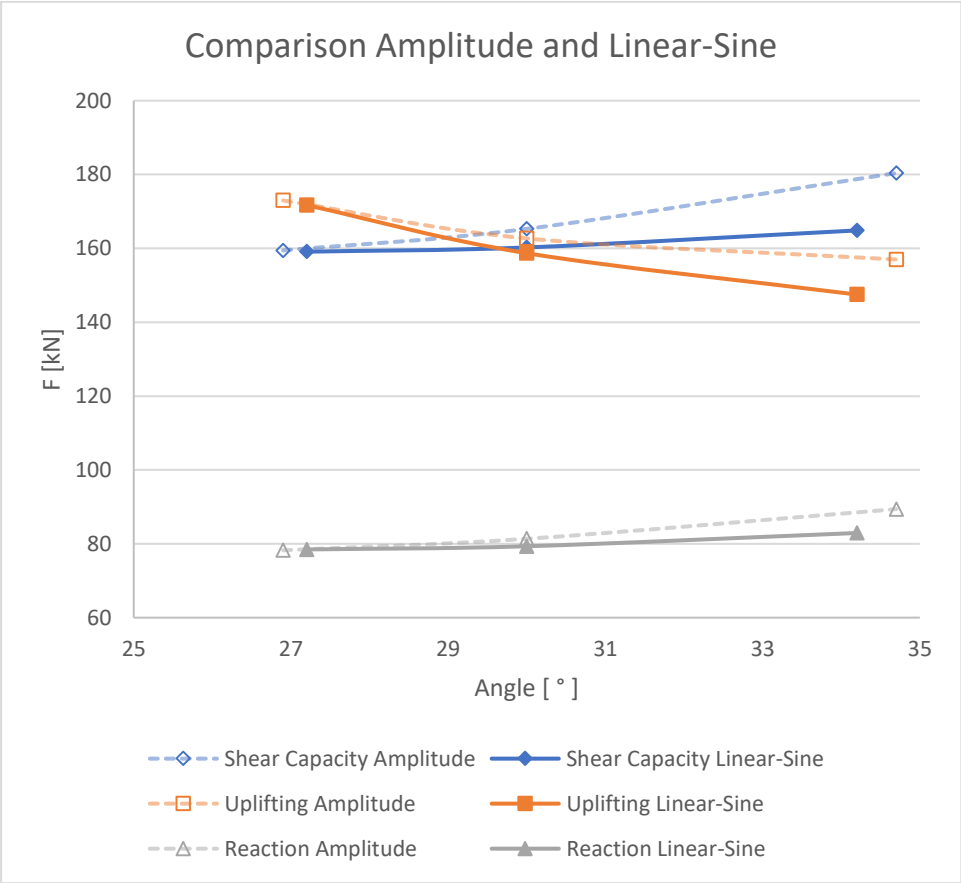

Figure 127: Comparison between amplitude results and linear-sine, plotted on the angle halfway the interlock.

Section 6.5. Acceptable tolerances for all variants

The interlayer deformation affects the allowable deviations of the geometry from its perfect form (i.e. the calculated shape). This principle is illustrated in Figure 128. Two geometries with slight deviations (δ) from the perfect condition have different allowable deformations (Δu) before reaching the shear capacity. Hence the geometry deviation introduces a reduction of the shear capacity, as it claims a part of the allowable deformation as its flaw size (δ). It will introduce a peak stress proportionally, leading to a lower total capacity. These effects are consequently higher in variants that have a smaller allowable deformation. A larger allowable deformation before reaching the shear capacity therefore is beneficial.

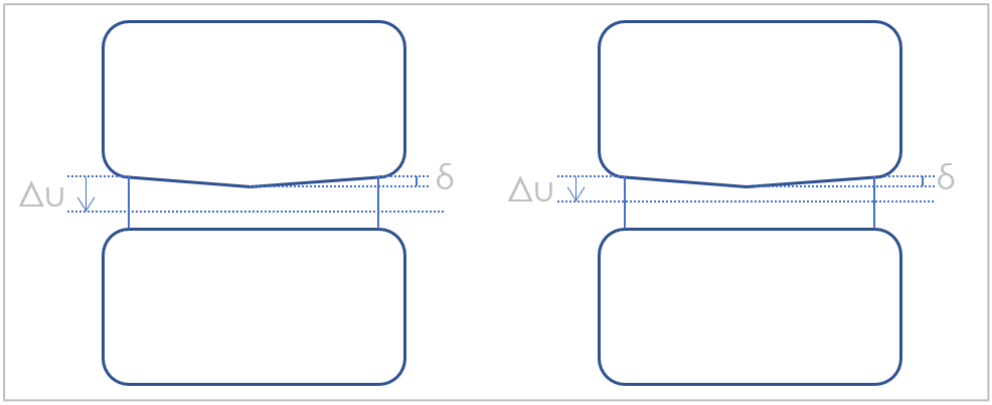

Figure 128: Effect of acceptable deformation on tolerances.

In Figure 129 the results are plotted of the shear capacity of all parameter variations versus the deformations at a Christensen's failure criterion of one.

The most critical results are those of the height parameter variations, here coded as HxA, in which x is the amount of amplitude heights applied in the total height. Results are shown for an amplitude of 10mm. Not only results decreasing the brick height in a reduction of shear capacity, it also occurs at a smaller deformation. Hence geometry tolerances are lower for decreasing brick height.

This effect probably can be related to its failure mechanism. By decreasing brick height, the bending failure becomes more influential. Hence any extra deformation adds to this effect.

Increasing the amplitude increases the shear capacity of the brick. However, it also decreases the allowable deformations in the geometry. Hence it is a trade-off that can be made as a design choice. Lower tolerances versus higher capacity.

For the amplitude variants this effect is probably the result of a larger amount of the interlayer being compressed instead of deformed by shear loading. With a higher amplitude the angle halfway increases, leading to a more vertical contact surface. Therefore the adjacent interlayer is more compressed then sheared, resulting in lower allowable deformations of the interlayer (due to incompressibility).

The Linear-Sine variations gain a slight advantage in shear capacity too, however do also get lower allowable tolerances in return. Topping of the geometry then has a positive effect on tolerances as there is fewer contact area that can be compressed.

Hence tolerances should be significantly smaller than the allowable interlayer deformations. A quantitative value cannot be assigned, however the effect for all variants is given in a qualitative manner. The deviation in the geometry is expected to decrease the capacity proportionally to the allowable interlayer deformation. For quantitative measures further research is necessary, for instance by performing analyses with small deviations and experimental tests.

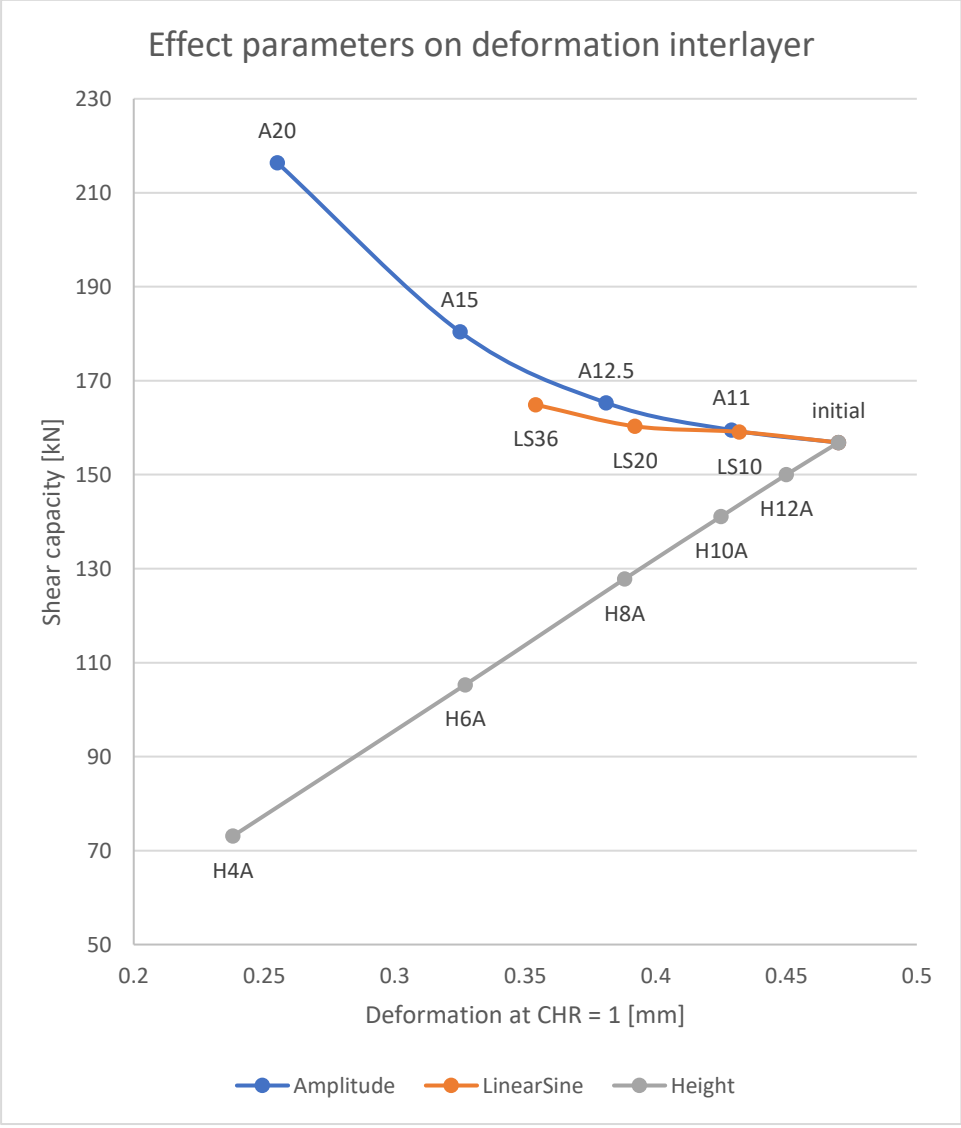

Figure 129: Effect of parameter variations on the deformation of the interlayer.

Section 6.6. Design values

The analyses are performed using the characteristic values of glass. To apply the capacities gained in these tests into a design, hence the design values should be determined. Then from the results certain design rules and diagrams can be derived.

6.6.1. Design values from characteristic results

As an indication of the design value of the results, the values are transformed using safety factors and modification coefficients for allowable tensile stresses according to DIN 18008. The values used are for float glass, and will include a distinction between short- and long-term loading.

$$f_{g;d} = \frac{k_{mod} * k_c * f_{g;k}}{\gamma_{m;g}} \qquad [6.1]$$

In which $f_{g;d}$ and $f_{g;c}$ are the design tensile strength and characteristic tensile strength respectively, k_c a coefficient for consideration of the type of structure (chosen as 1.0); k_{mod} is the coefficient for the load duration of annealed float glass, which is 0.25 for permanent loads, 0.40 for medium loads (snow or thermal expansion) and 0.70 for short loads such as blast impacts and wind; γm;g is the material safety factor for glass (equal to 1.8).

As in the model the characteristic value is used, it is possible to determine the design values for the shear capacity, by substituting $f_{g;k}$ for $F_{shear;k}$ in Equation 6.1.

$$F_{shear;d} = \frac{k_{mod} * k_c * F_{shear;k}}{\gamma_{m;g}} \qquad [6.2]$$

This formula can then be applied on the retrieved results for different load durations.

6.6.2. Design rules and diagrams derived from results

The design rules and diagrams apply for the critical brick in the system. This brick is located near the highest anchoring in the wall system. All other bricks have to either transfer a smaller load, or are more prestressed by the dead weight of the structure. Any compressive stress in this case is beneficial. The compression has a chance to pacify flaws and moreover increases the shear capacity of the brick.

Above the top anchor introducing the load into the glass system an anchored keystone must be applied. Optionally more layers of bricks can be applied to increase the weight. The needed vertical force applied depends on the amplitude steepness and the shear capacity. In total a vertical force of 3-6% of the shear design capacity must act on the critical brick in the system, depending on the amplitude applied. These values are valid up to an amplitude of 20 millimetres, for higher amplitudes further research must be done prior to applying it into a system. This is a conservative value, as all amplitudes required a smaller vertical load and with decreasing amplitude the percentage would decrease as well.

To determine the design shear capacity, the diagrams shown in Figure 130 can be used. For three values of amplitude the values are plotted in the diagram. It is recommended to use higher bricks, preferably in the more horizontal area of the diagram. Tolerances are more beneficial with higher bricks and lower amplitudes.

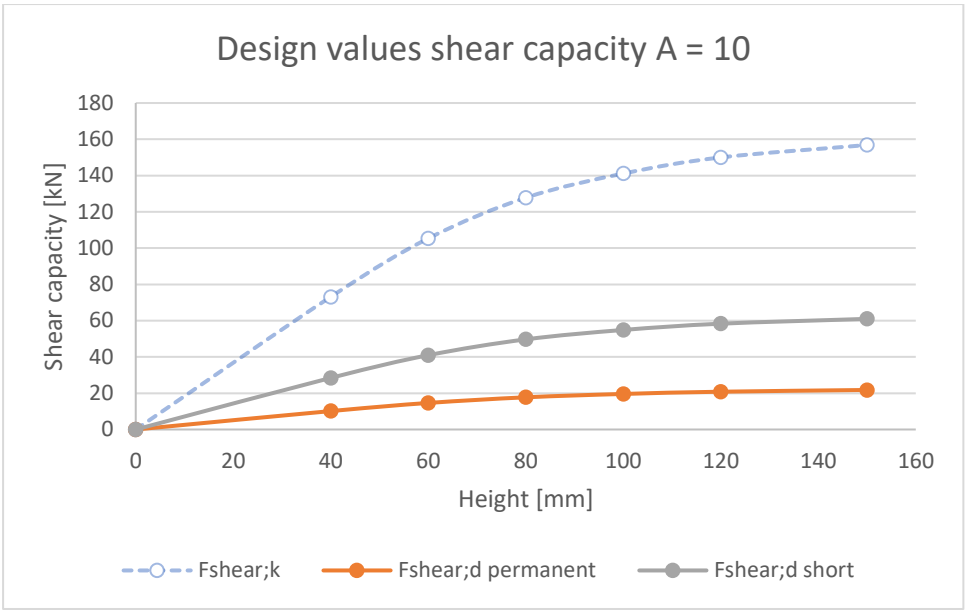

a

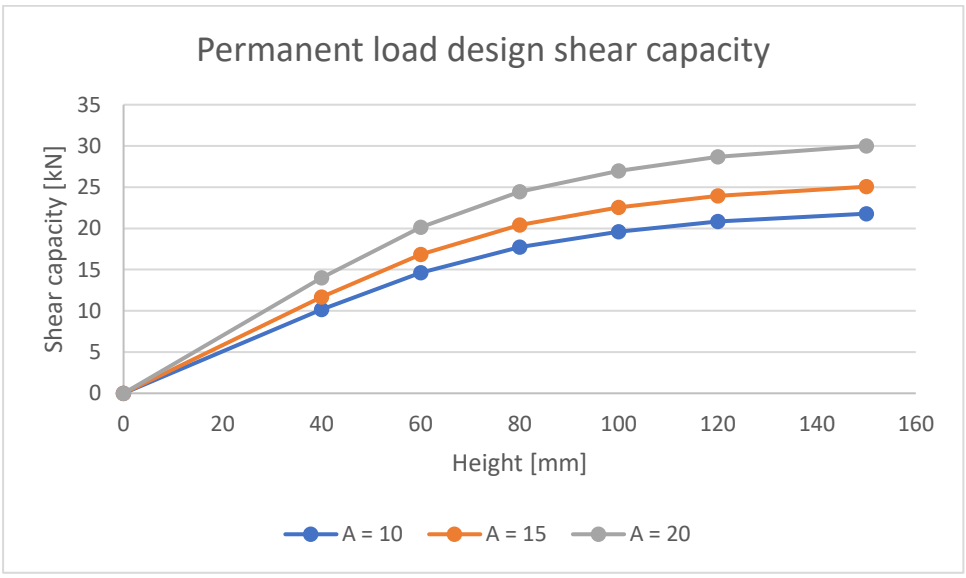

b

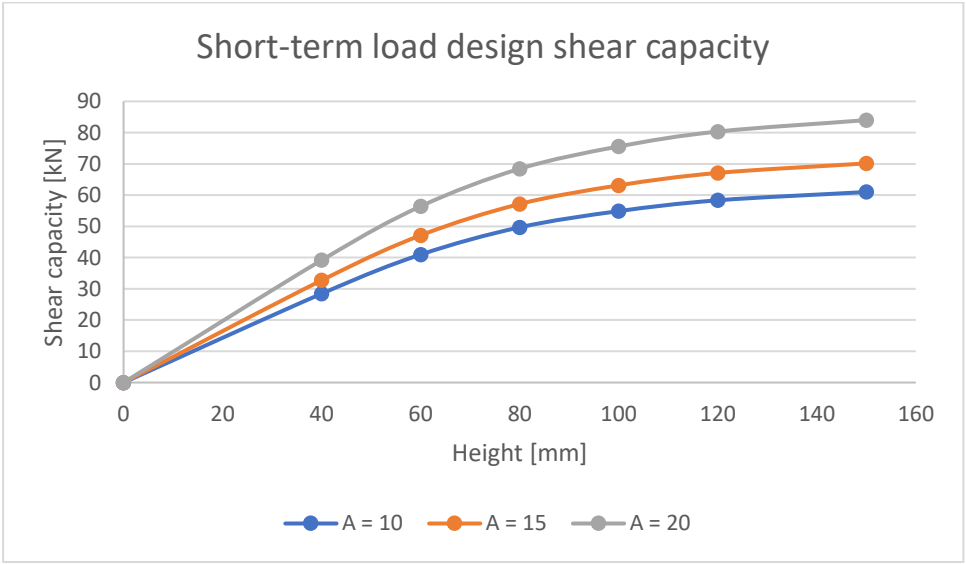

c

Figure 130: Design diagrams for: a) an amplitude equal to 10; b) permanent load design shear capacity for various amplitudes; c) short-term load design shear capacity for various amplitudes.

Chapter 7.

Prototyping of glass interlocking brick

Prototypes of the proposed geometry are made to illustrate potential problems in practice. Flaws, geometry deviations and residual stresses could reduce the capacity of the glass brick, and hence need to be reviewed.

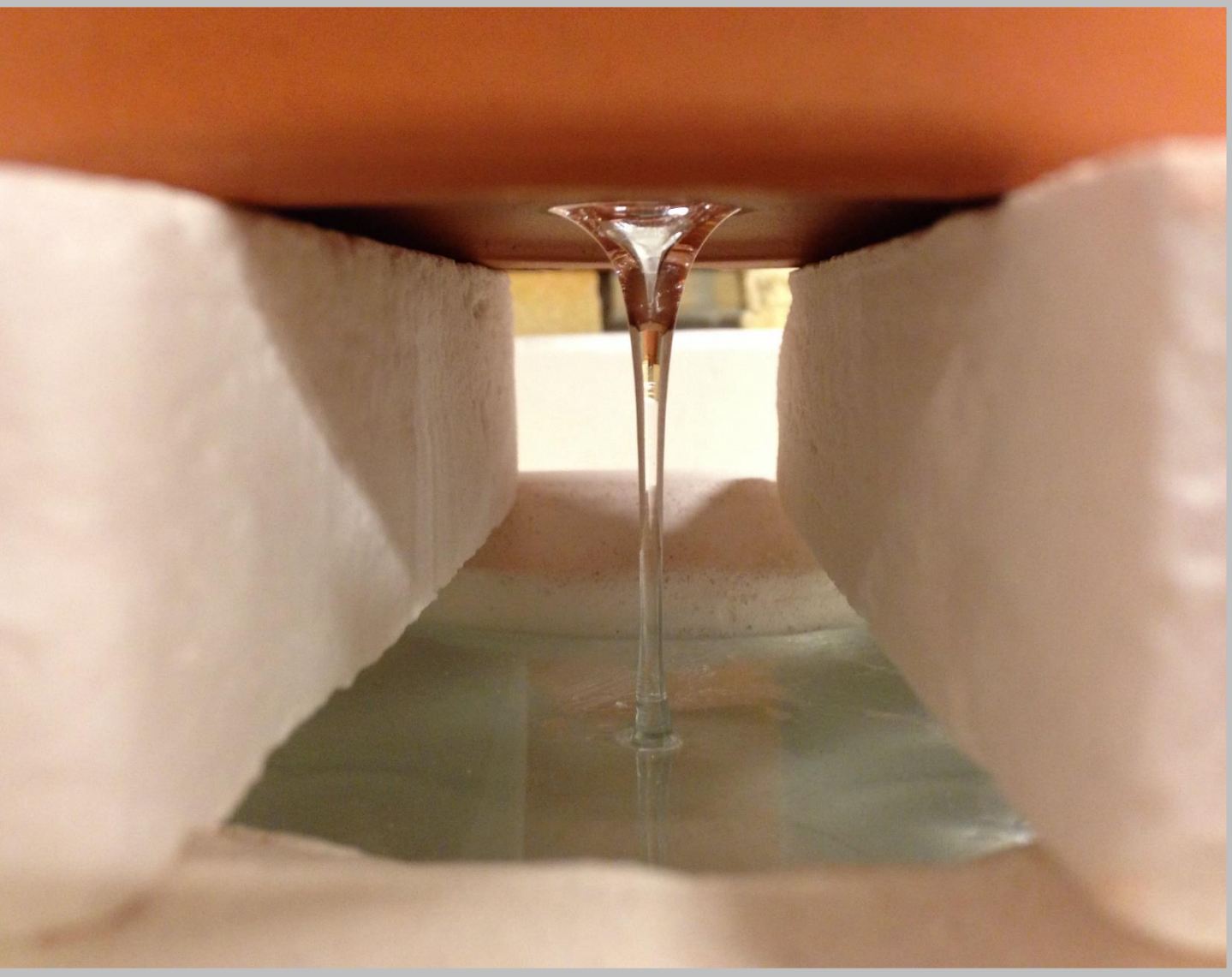

Section 7.1. Prototype goals

For a good fit of the interlocking geometry, it is important to review the effects that the production process has on the geometry. In this thesis the bricks are analysed numerically as if they were perfect bricks, with no deviations from the ideal geometry. In reality this however is never the case.

Casting of glass always results into minor deviations in the geometry, this for instance due to shrinkage while cooling down. Deviations of the mould can moreover introduce imperfections, such as flaws or local excessive material. Impurities in the mould may further result into dirt inclusions, while the pouring of the glass can result in air bubble inclusions. All which can introduce peak tensile stresses when loaded. These effects will be reviewed visually in Section 7.2.

The cooling down process can moreover add other negative effects. When improperly annealing the glass, this can introduce residual stresses in the brick. This will be illustrated using polarised white light and a crossed-polarised filter. Colourful isochromatic fringes occur indicating locked stress concentrations in the glass (Oikonomopoulou, Bristogianni, Veer, & Nijsse, 2017). The evaluation of the bricks on residual stresses will be further discussed in Section 7.3.

The goal of the prototype is to review all these aspects with respect to the geometry, and indicate where problems may occur. The flowerpot-casting method is used to produce the prototypes.

In general this method takes the 3D-printed geometry as a mould, to make a negative of the brick in silicone. This silicone then is filled with wax, to create a positive again of the geometry. Casting a crystal-cast on top of the wax geometry, followed by steaming out the wax gives our final negative for casting the glass in. The brick can then be obtained by dissolving the crystal-glass in water. Below in Figure 131 different stages of the geometry are shown. The whole process is discussed more into detail in Appendix B.

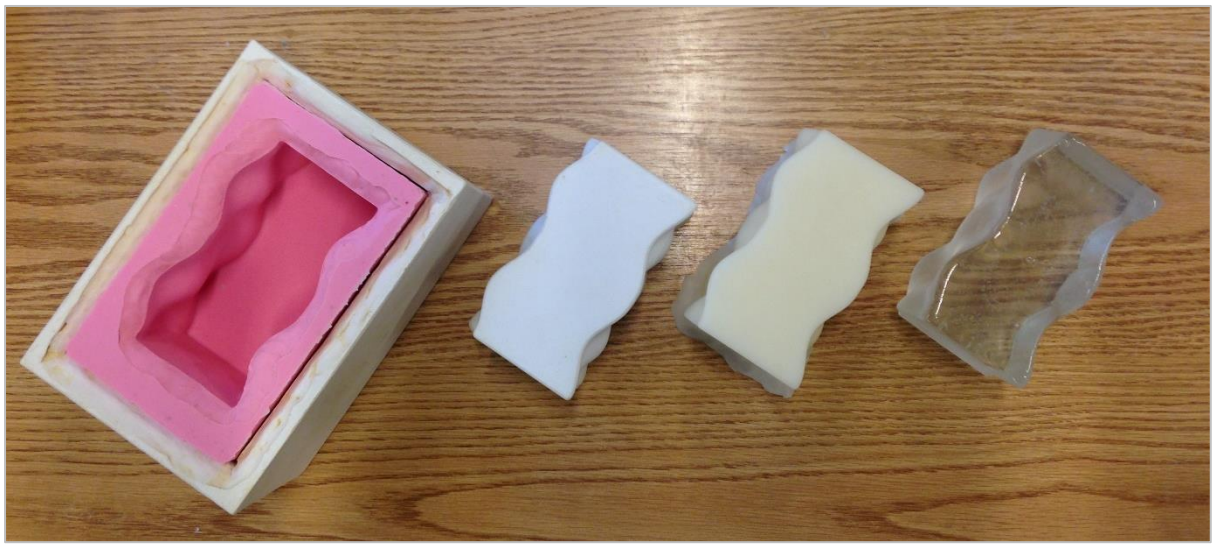

Figure 131: Brick manufacturing stages, from left to right: Silicon negative; 3D printed geometry; wax geometry; resulting glass brick.

Section 7.2. Geometry deviations and flaws

In this section various geometry deviations and flaws will be discussed. These are mostly linked to the manufacturing process, particularly the cooling down and annealing stages. The technique used introduces deviations due to shrinkage, air bubble entrapments and flaws. These will briefly be discussed here with some examples.

Shrinkage

The glass has a certain rate of natural shrinkage when cooling down. The effects are small, but can have influence on the interlocking behaviour. Hence the interlocking geometry of all prototypes was measured.

All prototypes exhibit the same geometry deviations. Interestingly, a slight difference in shrinkage only occurs in the interlocking geometry at the open side of the mould (the cast-in side). This can probably be explained by the difference in cooling rate. Due to the open top, this area will cool down faster than the other areas in the brick, which are enclosed by the crystal-cast mould. Hence the hot brick centre, which takes more time to cool down then its edges, lies not exactly in the middle of the geometry, but somewhat lower. Therefore, the brick does not cool down uniformly, and the geometry will not shrink evenly as well. The hot centre mass consequently pulls more at the cooler top geometry, causing the recorded deviation to occur.

This slight deviation causes the geometries of the bricks to only fit in one configuration properly. Another casting method can prevent that, as mentioned earlier in Section 2.1.3, the Poesia bricks are demoulded prior to annealing, which would prevent this effect from happening.

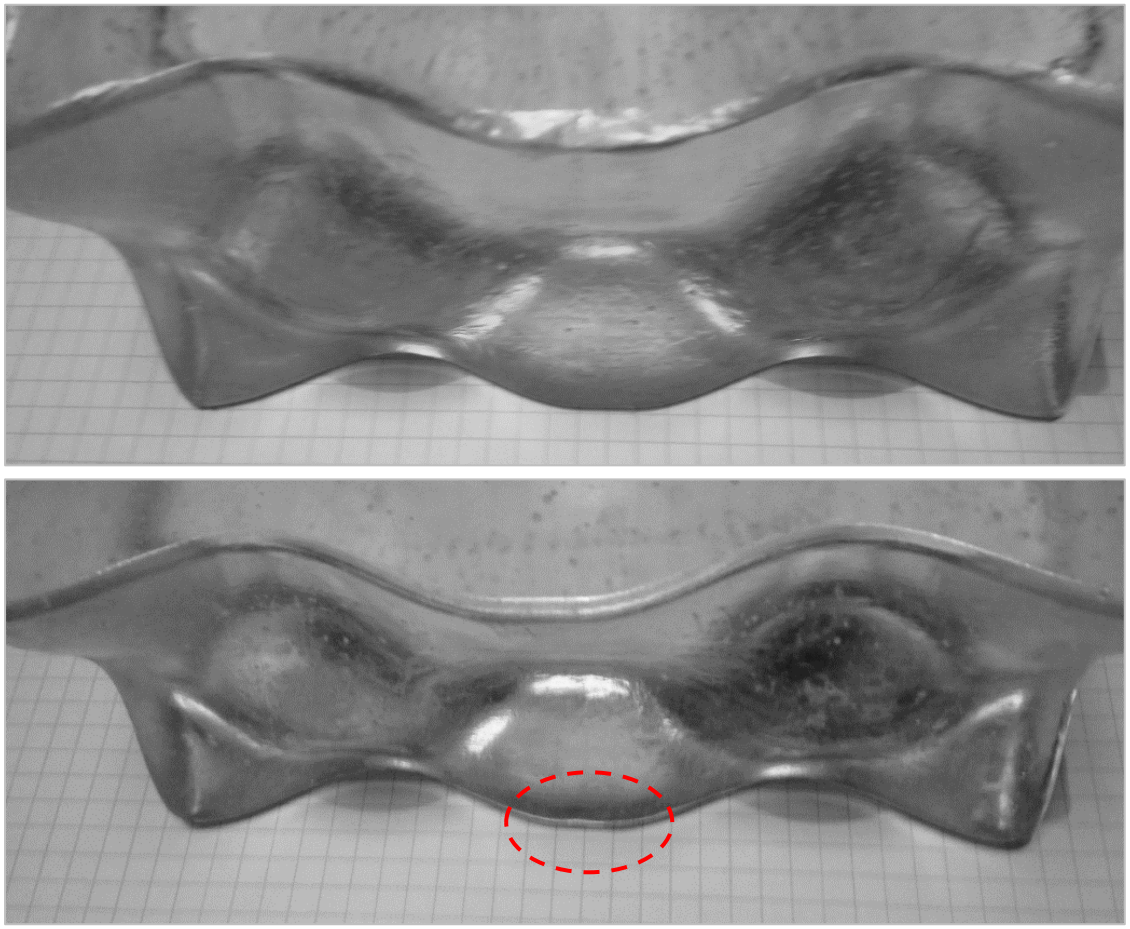

Figure 132: Minor uneven shrinkage effects due to uneven cooling: a) no shrinkage deviations at the side of the brick inside the mould; b) slight deviations in the middle shear key for the side of the brick in the casting side of the mould.

Air bubble inclusions

Using this flower-pot casting technique air bubbles are a result of the slowly melting and casting of the glass. The patterns indicate how the glass has flown into the crystal-cast mould. The images shown in Figure 133 show a clear ellipsoid pattern for prototype A (Figure 133a).

This could be due to a higher spacer distance in the firing set up, here shown in Figure 134. The glass flow could be more constant with a higher spacer height, resulting in evenly distributed air bubbles.

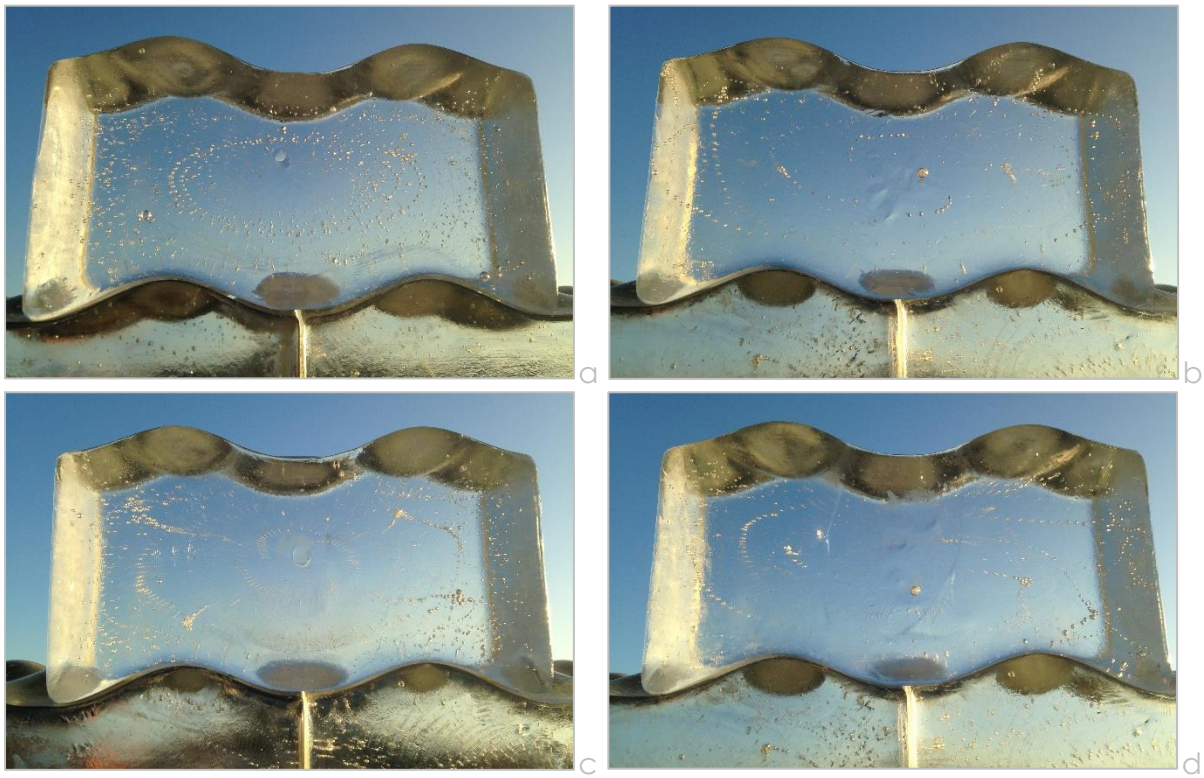

Figure 133: Air bubble entrapment in prototypes A to D, respectively in images a to d.

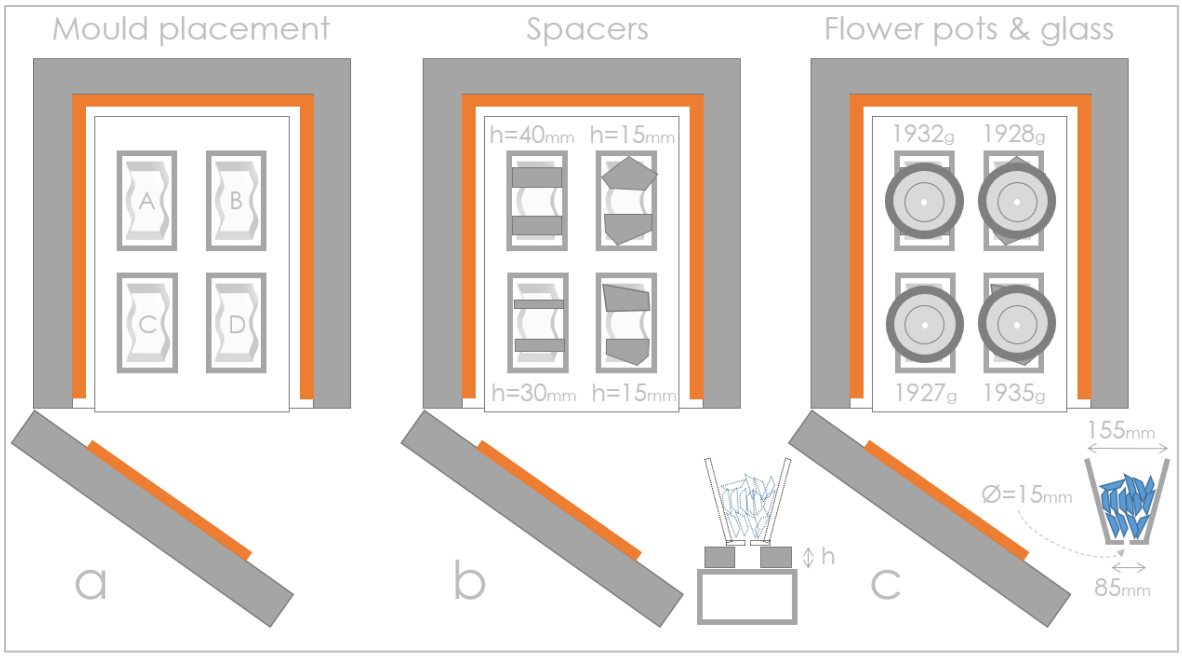

Figure 134: Firing set up: a) placement of moulds in the oven; b) applied spacers with different heights; c) Flowerpot placement and weight of glass for each prototype.

Flaws & dirt inclusions

All manufactured prototypes exhibit various flaws throughout their geometries. These will now be discussed with the examples shown in Figure 135.

At certain edges of the geometry some deviations from the desired curvature occurred. An example is shown in Figure 135a. These flaws most probably are the result of imperfections in the mould, such as residual wax or a flaw in the wax that was imprinted on the mould.

Especially around these edges and in the interlocking geometry these flaws could lead to early failure. The contour plots in earlier chapters indicate where peak tensile stresses would be most influential. Any flaws in these regions would result in a loss of brick capacity.

Due to a less controlled cooling down (further discussed in the next section) crystallisation may occur if the geometries are not cooled down fast enough. This is for instance visible in Figure 135b. This results into a rougher surface, which is moreover not transparent. Rough patches may furthermore be the result of a rough surface inside the crystal-cast mould.

This rough surface is moreover sensitive for dirt inclusions, which could lead to earlier failure when loaded. Besides the flaws introducing peak tensile stresses, the dirt inclusions can act as a wedge prying open the geometry. These dirt inclusions, which settled in the geometry after casting, are shown in Figure 135c.

Lastly an air bubble in the mould resulted in an excess of material on prototype D, shown below in Figure 135d. A deviation like this would result into peak stresses, especially here where it is located in the interlocking geometry.

By polishing and cleaning, most flaws could be smoothened to decrease their effects on peak stresses.

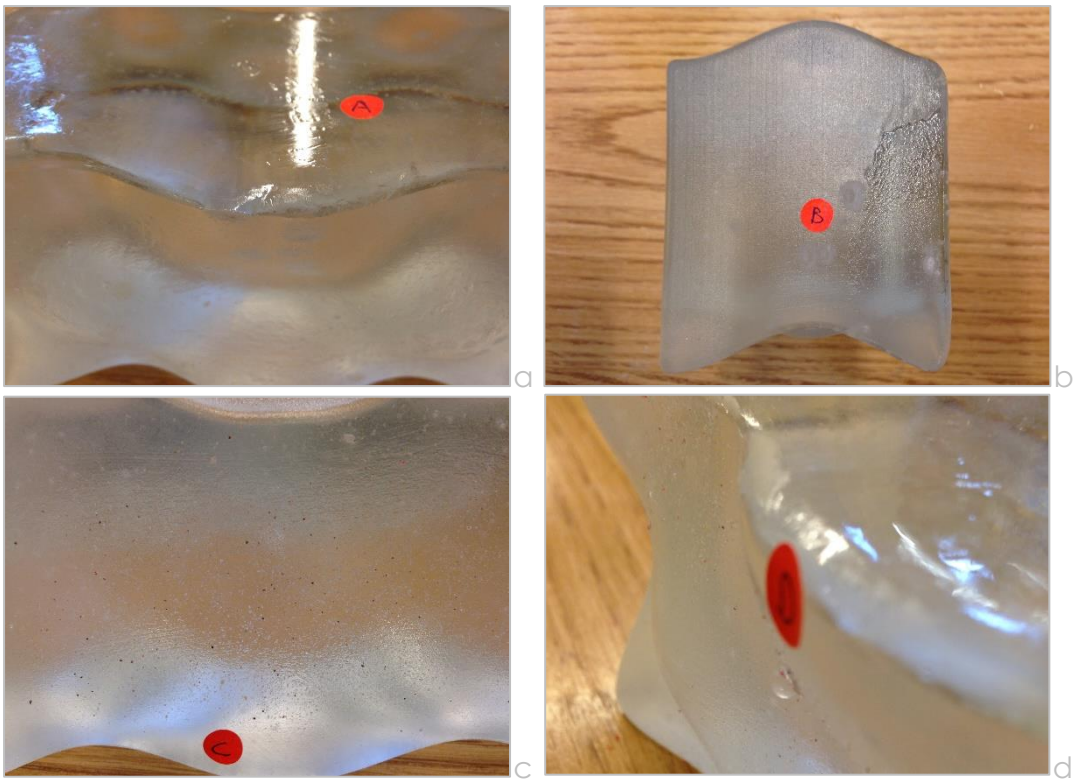

Figure 135: Various flaws across different prototypes: a) edge deviation; b) crystallisation marks; c) dirt inclusions in rough crystallised surface; d) Extra glass bubble due to pore in mould.

Section 7.3. Residual stresses

As discussed earlier, residual stresses can be evaluated qualitatively by placing the prototypes between a LCD-screen (emitting polarised light) and a cross-polaroid film. Stressed areas will occur colourful for higher stresses, and white/grey for relatively small stresses (Oikonomopoulou, Bristogianni, Veer, & Nijsse, 2017). This is because glass on its own is not birefringent, but when it is stressed (or in this case contains residual stresses) the stressed areas do exhibit birefringent behaviour. Hence colourful isochromatic fringes occur in those areas.

For the manufactured prototypes this results into the images shown in Figure 136. To understand these residual stresses, it is needed to look into the firing and annealing process first. The firing, cooling down and annealing process is shown in Table 14.

Due to the oven being unable to cool down rapidly enough on its own, this must be done manually by opening the door with certain time intervals. This hence is a less controlled process, at a crucial stage in the cooling down process. Too slow cooling down can allow crystallisation to occur, while cooling down too fast can lead to passing the strain point of glass, which would lock residual stresses into the glass.

Hence it is expected a certain amount of crystallisation to occur, and for the prototypes closer to the door to cool down faster, which then are more prone to passing the strain point and locking in residual stresses.

However, when evaluating the residual stresses shown in Figure 136. We see that the highest rate of residual stresses occur in prototype B and D. Prototype D indeed was close to the door opening and hence more influenced by the rapid cooling down. Prototype B however was set up in the back of the oven. Hence there might be another effect influencing the residual stresses locking in the brick.

The cause might be found in the firing set up itself. This is shown schematically in Figure 134. The prototypes A and C, both indicating few residual stresses, had higher spacers compared to the other two specimens. A higher spacer height hence might contribute to a better cast and less residual stresses in the glass.

Table 14: Firing, cooling down and annealing scheme.

Time elapsed [h]	**Firing scheme**	**Temperature**	**Notes**
Firing up			
0	+50°C/h	25°C - 750°C	
14.5		750°C	Remain for half an hour
15	+50°C/h	750°C - 850°C	
17		850°C	Remain for an hour
18	+30°C/h	850°C - 940°C	
21		940°C	Remain for 8 hours
Cooling & annealing			
29	-380°C	940°C - 560°C	Manually by opening door
44	-2°C/h	560°C - 510°C	Annealing
59	-1°C/h	510°C - 480°C	Annealing
66	-30°C/h	480°C - 25°C	
82		25°C	

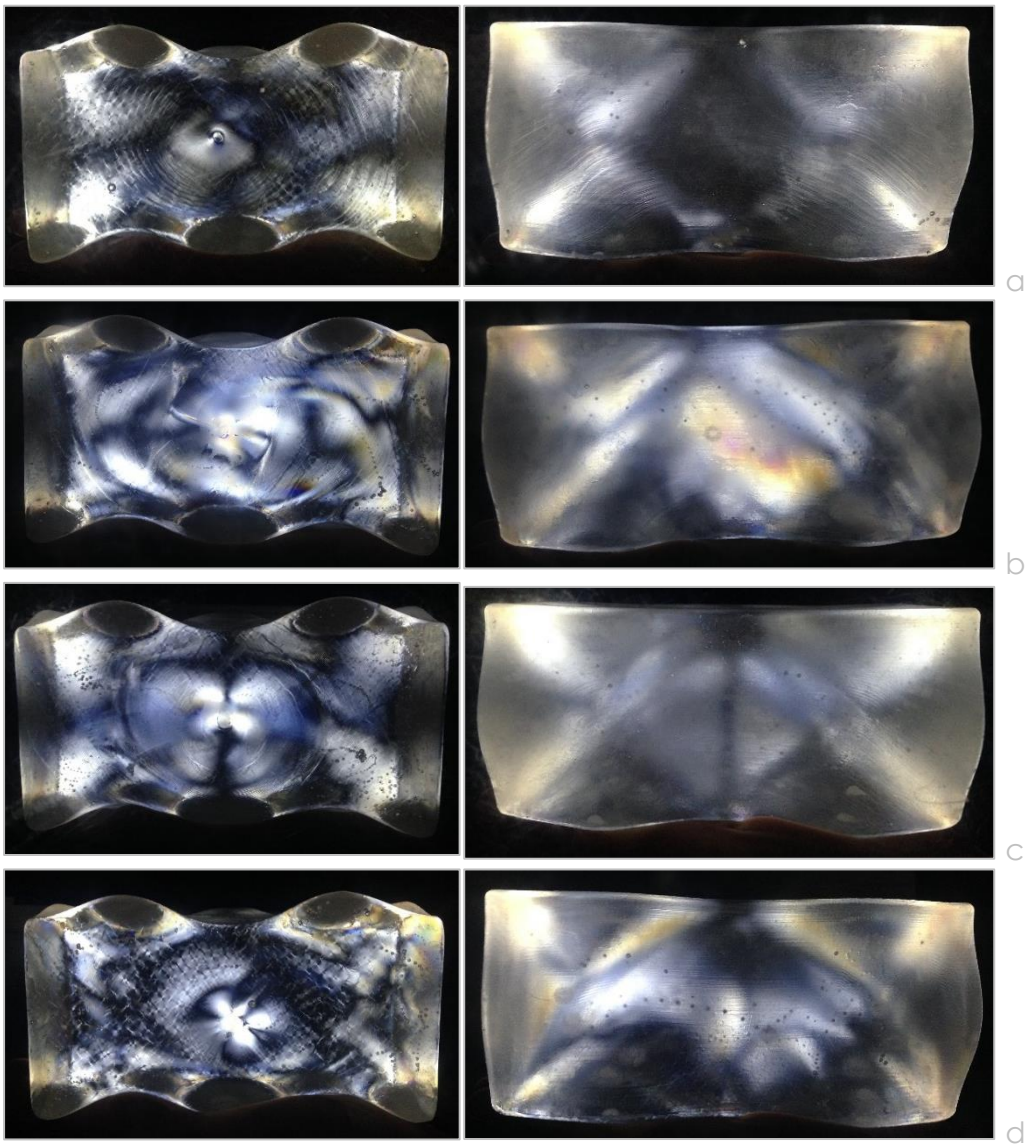

Figure 136: Evaluation of residual stresses of prototypes A to D in images a to d.

Chapter 8.

Concept – A glass-reinforced Lichtenberg

A concept for consolidating the Lichtenberg Castle ruin is drawn up, discussing the applied geometry chosen from the earlier derived design values. Both the system design, as well as the proposed connection designs are discussed. Lastly the glass consolidation capacity is compared with the current consolidations applied in the tower and various load cases acting on the tower.

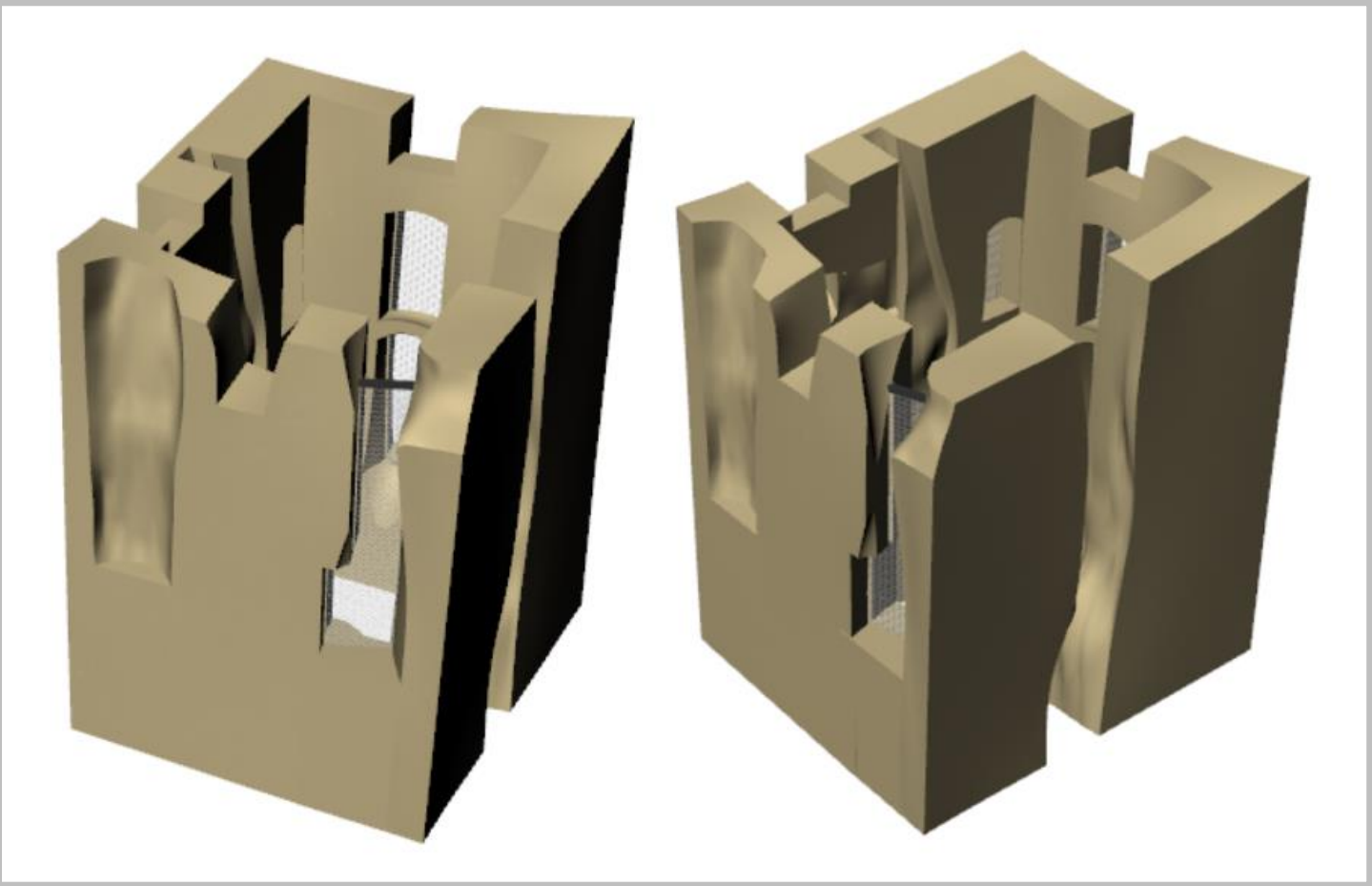

Section 8.1. Chosen brick geometry

From the design diagrams it can be determined that the increase of height from 120mm to 150mm does not contribute much to the design shear capacity. The increase in sensitivity to geometry deviations is acceptable too, as it is relatively small difference. Decreasing the brick size makes assembly easier as the weight of the brick decreases, from 16.8kg to 13.5kg, when comparing it to the initial design.

The amplitude is kept the same as the initial design, with A = 10mm. Hence the tolerances can be kept in check, as for higher amplitudes the allowable deformation of the interlayer decreases. This results into a shear capacity of 20.8kN for the system applied. Hence a vertical force of 3.6% must act on top of the upper shear key, in this case equal to 0.75 kN. The dimensions of the chosen geometry are presented in Figure 137.

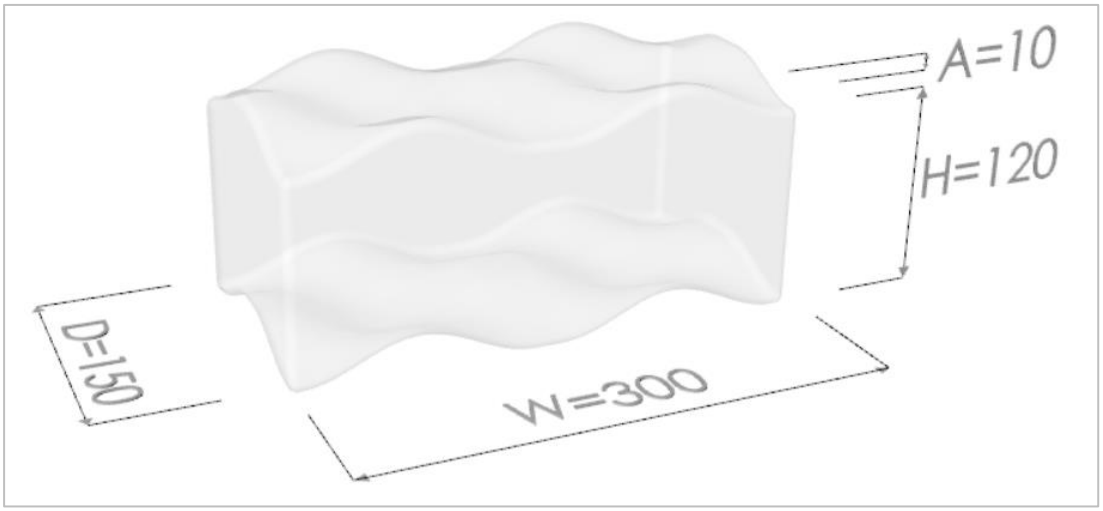

Figure 137: Chosen geometry measurements, in millimetres.

Section 8.2. Cast glass interlocking system design

The chosen geometry can be applied in a cast glass wall system. The thickness of the interlayer is set to four millimetres, as the results could only be validated for this interlayer thickness (from experimental results presented in Aurik (2017)). This thickness is applied both in the horizontal seams (between interlocking surfaces), as well as between the vertical seams (between adjacent bricks). Only the horizontal interlayer has a structural purpose of conveying and spreading loads from brick to brick. The vertical interlayers are merely to cushion the blow in case of for instance an earthquake, and to prevent any glass-to-glass contact. These vertical interlayers then can be applied with a slightly thinner softer rubber. All seams will be made water- and airtight with a transparent silicone sealing agent.

The system itself is completely reliable on its boundary conditions. A failure of one of its boundaries could result into an early failure of the system. Hence the connection to the existing structure is of high importance. These connections will be discussed in the next couple of sections, leading up to a conceptual consolidation design.

8.2.1. Wall connection design and assembly

The connection between the cast glass interlocking system and the monumental tissue is a critical part of the design. The connection should have sufficient capacity to ensure that if failure occurs, this occurs in the glass system and not in the monument. Hence a possible connection design will be drawn up. For application certain parts of the connection should be tested experimentally, especially the behaviour of the chemical anchor in the limestone wall.

As a potential connection anchor channels are applied in combination with a chemical injection anchor bolt systems. The connection will be explained in order of assembly.

Preparation of the wall and applying anchor channel

Within the wall a groove is created, which is slightly larger than the depth of the brick. Holes are drilled within this groove to fit the chemical injection bolts. To reach a sufficient capacity, which is higher than the design capacity of the glass interlocking bricks, it is chosen to apply 145 M 16 chemical anchor bolts, which have a diameter of 16 millimetres and a length of 145 millimetres. Its strength is 29.9 kN in tension, which is the design value for cracked C20/25 concrete (Halfen, 2010). For masonry limestone no values are found in literature and hence the anchors should be tested in a laboratory prior to application. For this specific case longer anchors might proof necessary.

The anchor length allows anchor spacing to be a minimum of three times its length. With this anchor it can hence be repeated every 435 millimetres. This means the wall can be anchored every four layers of cast glass brickwork (4*(120+4) = 496 millimetres).

After drilling the holes, the anchor channel can be fixed into the wall groove using the chemical bolts. For the ruin this is shown in Figure 139. The chemical bolts are placed every other 496 millimetres, in the same spacing as the brick connections will be placed.

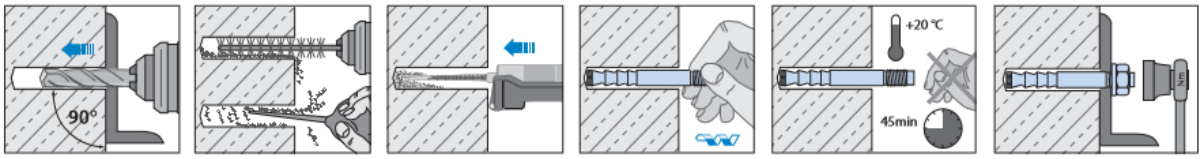

Figure 138: Applying the chemical injection bolt. Reprinted from (Halfen, 2010).

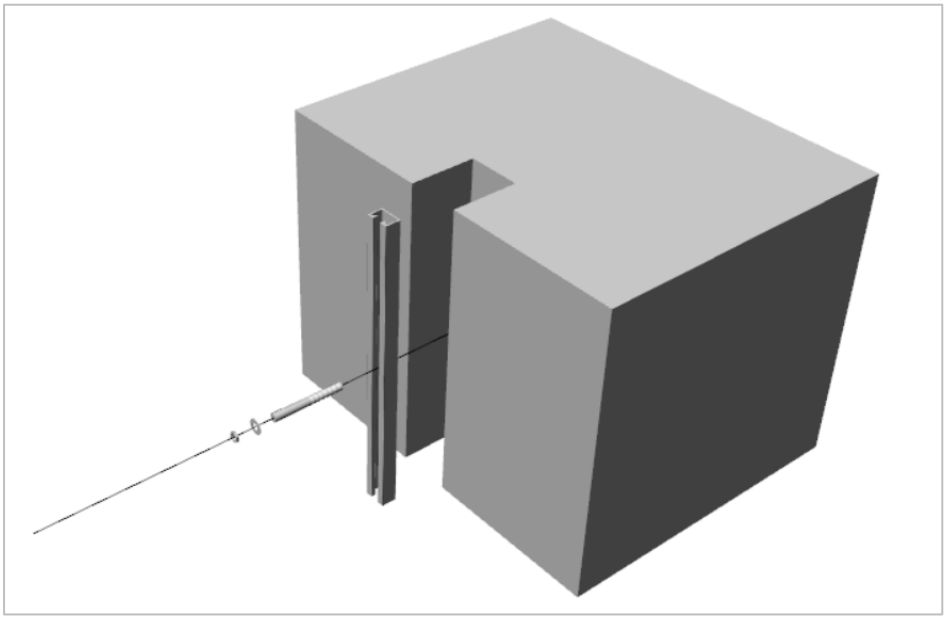

Figure 139: Installing the anchor channel into the wall groove with chemical bolts.

Anchor channel bolt and aluminium interlocking half-brick

The anchor bolts can be fixed into the channels in three ways: a sliding connection, a locked connection and a fully interlocked connection. These three connection types are displayed below in Figure 140. As small vertical movements should be allowed by for instance compression of the interlayer or creep effects, it is chosen to apply the sliding connection.

To fix the cast glass structure with these bolts to the anchor channels a half interlocking brick of aluminium will be used, which has a bolt channel for fixing purposes. This principle is drawn in Figure 141. The exploded view shows the fixing of the chemical anchor bolt onto the channel, followed by the parts needed for the fixing of the aluminium half-brick.

Assembly is quite straightforward; one builds up the wall layer by layer, and attaches an aluminium half brick every four layers on both sides of the wall. By turning the bolt inside the aluminium half-brick the brick locks into the channel, and can transfer tensile loads.

The bolts have the highest capacity of the system, leading up to a capacity of 78.4 kN (when applying HM 72/48 framing channel in combination with M20 8.8 bolts) (Halfen, 2014). The maximum load bearing capacity of the channel due to loads in the bolt direction is equal to 65.8 kN (Halfen, 2014).

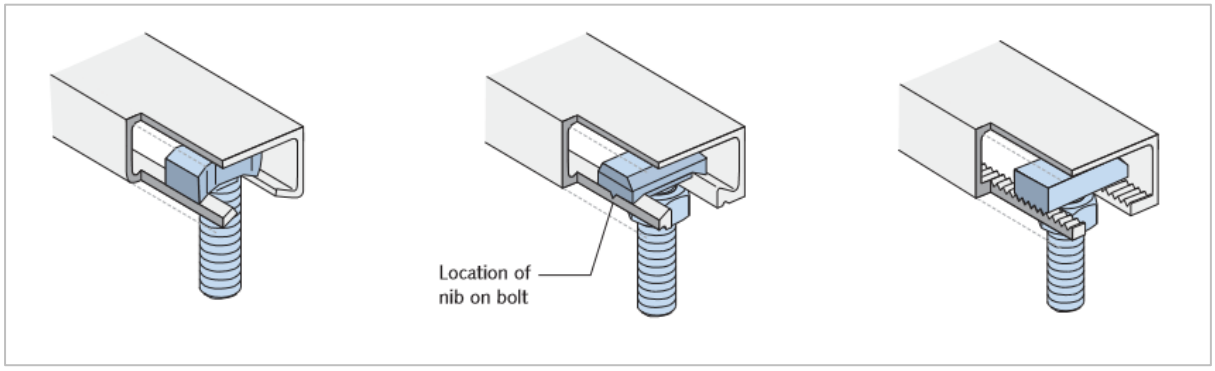

Figure 140: Three options for bolt fixings in the anchor channel. Reprinted from (Halfen, 2014).

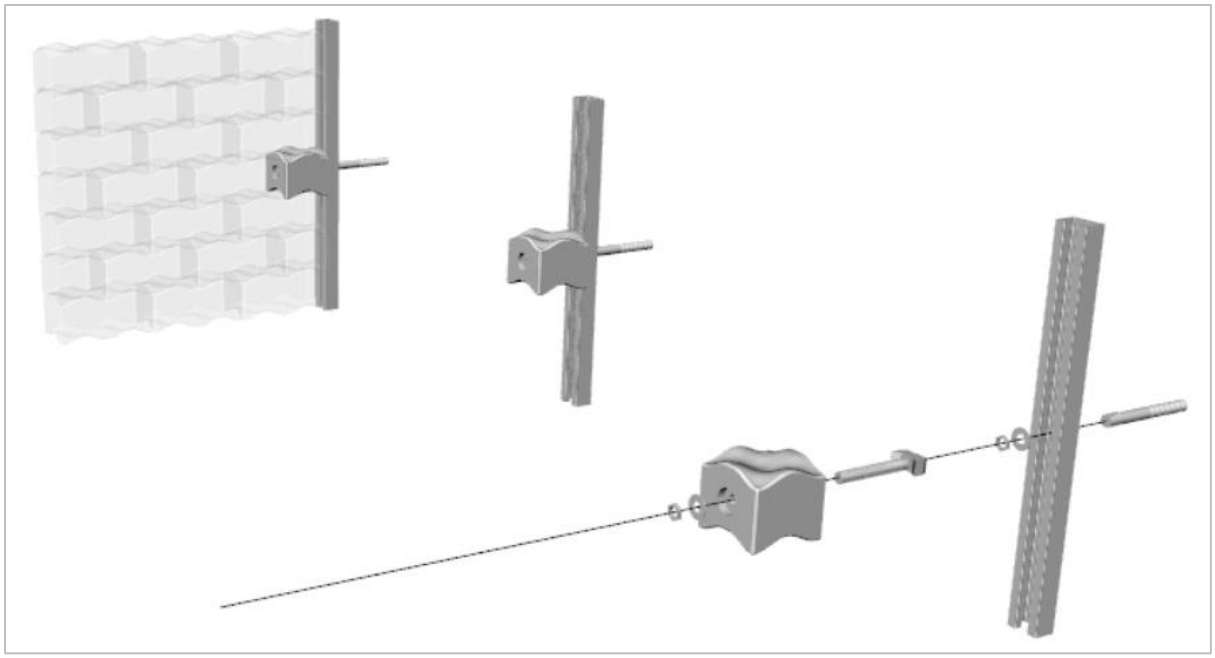

Figure 141: Aluminium half-brick fixing principle in exploded view and after fixing.

Final connection design

The final connection design is shown in Figure 143. Preferably a half-size brick-depth is applied for the groove, as to make the connection less visible. Transparent rubber spacers are used around the glass bricks in the groove, as to prevent them touching the anchor channel or the adjacent monument brickwork.

The groove depth is however dependent on the location in the crack, as the crack itself has an irregular profile. Moreover, the wall should be investigated to see how deep this groove is allowed to penetrate the wall, as it is unknown how the quality of the wall is at these locations.

Hence the connection will most probably show in certain parts of the intervention. A glass connection instead of an aluminium connection could be investigated as well, however it is safe to say that this brick then would be the critical element in the structure, as peak stresses around the bolted connection are inevitable.

For a proper convey of the load it is moreover important that the application of the bolted fixing is near the application of the chemical anchor. With increasing distance from the anchoring, the connection will experience increasing eccentric loads.

Lastly it is worth to mention that the design shear capacity used for this consolidation design, is for a single brick. As the connection introduces the load from the wall into two bricks through the top and bottom shear lock, the load will be divided among these two bricks as well. Due to tolerances or a miss-alignment it can however occur that this load is not divided proportionally. Hence as a worst-case scenario it could happen that only one adjacent brick has to transfer the full load. For this reason, the design shear capacity is assumed at each anchor location.

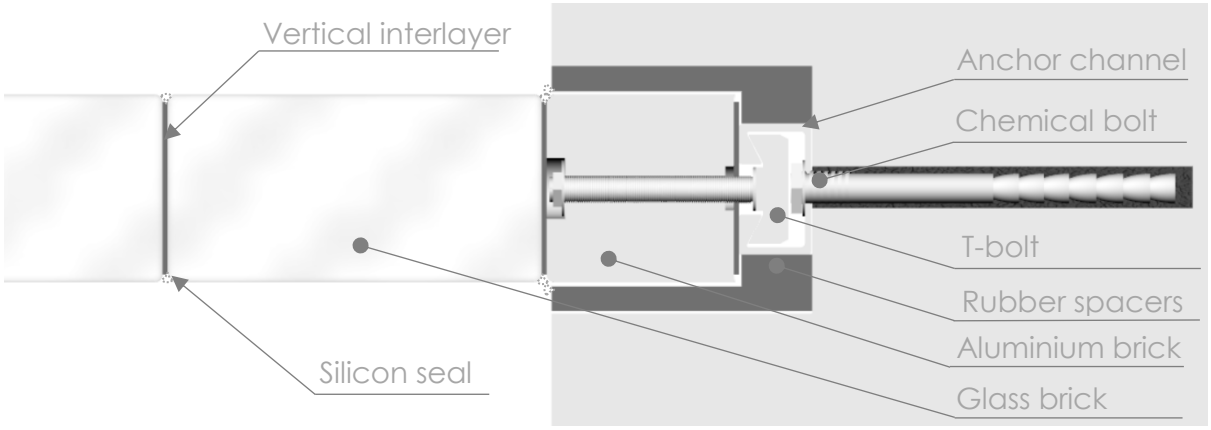

Figure 142: Detailing of the connection between historic wall and glass system (shown through a cross-section of the aluminium half-brick).

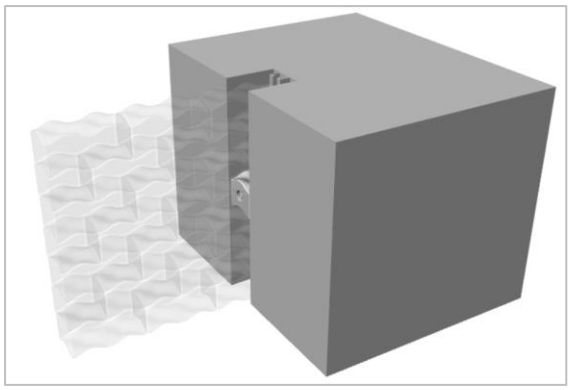

Figure 143: Final connection design embedded connection.

8.2.2. Top and bottom constraints

The boundary conditions of the system are for an interlocking system of extreme importance. With the anchoring in the adjacent walls covered in the previous section, only the top and bottom constraints remain.

Top constraint: Anchored keystone

The keystone can be anchored in various ways. In all cases the keystone should be prevented from moving upwards. Hence there are different alternatives, with different capacities regarding uplifting. This will only be discussed in a qualitative sense, as the scope is limited to a conceptual design. Further detailing, prototype testing and computational modelling should be done before applying in practice. Especially with respect to the quality of the materials used in the monument and the effect new connections would have on existing damages.

Using a connection like the anchor channel system discussed in the previous paragraph could be applied here as well. A 3D sketch is shown in Figure 144a. A steel U-profile, with rubber lining at the inner surfaces of the geometry, is applied on top of the cast glass brickwork. Special bricks are used, which have no interlock in the top surface. Hence, they are allowed to slightly move inside the U-profile due to for instance thermal expansion. A corner element fixes the keystone to the anchor channels in the wall. A more detailed view is shown in Figure 145.

This is the most minimalistic connection possible to constrain the keystone. Its resistance against uplifting is equal to the capacity of either the steel elements (failure of the bolts or anchor), or the material in which it is anchored (crack propagation in the limestone). Assuming using the larger profiles available, the shear resistance of the anchor channel appears to be the weakest, whilst still allowing 72kN as a design value (Halfen, 2014). Probably the material of the monument is the weakest link, and should therefore be further investigated.

The connection could be strengthened by adding more weight to the keystone (heavier steel profile) or adding a weight on top of the connection (adding limestone brickwork on top of connection). Another way to strengthen the connection is to apply a larger anchor plate, and anchor the keystone with more anchors. This all however depends on the need of the current structure, which should be further investigated.

There are of course more options that could be applied and further investigated. One of which is shown in Figure 144b. When adding more glass layers until the top of the structure is reached, allows for a keystone fixing in the top of the structure and hence the system can be anchored vertically. Adding more glass layers increases the self-weight of the system, and hence enhances its capacity as well as restrains more uplifting behaviour. Multiple anchors can be applied and spread over a larger area of the top of the structure. This connection concept costs more material, and the anchor(s) could potentially create a vertical inner crack in the limestone wall (due to pulling of the wall).

Another way to restrain the system is to apply post-tensioned cables. These could be applied internally (as shown in Figure 144c) or externally. This is the most visual of the connection options, but potentially least impacting the current structure. Internal cables would be applied through the brickwork, essentially affecting the bricks capacity negatively. Even in compression, peak tensile stresses would occur due to a wedge-effect. This implicates that a compression prone area in the brick would become more sensitive under compression, while the post-tensioned cables would increase the compressive stress in the system. Hence an external cable system would be preferable, however this would lead to applying even more cables, as the compressive load should be applied symmetrical into the system. In literature it was moreover found that using such a system would affect the damping behaviour of the system during an earthquake (Ali, Briet, & Chouw, 2013).

More research is needed to explore this kind of detailing and the effect on the capacity of the brick. For now, the horizontal anchored detailing will be chosen as a conceptual solution.

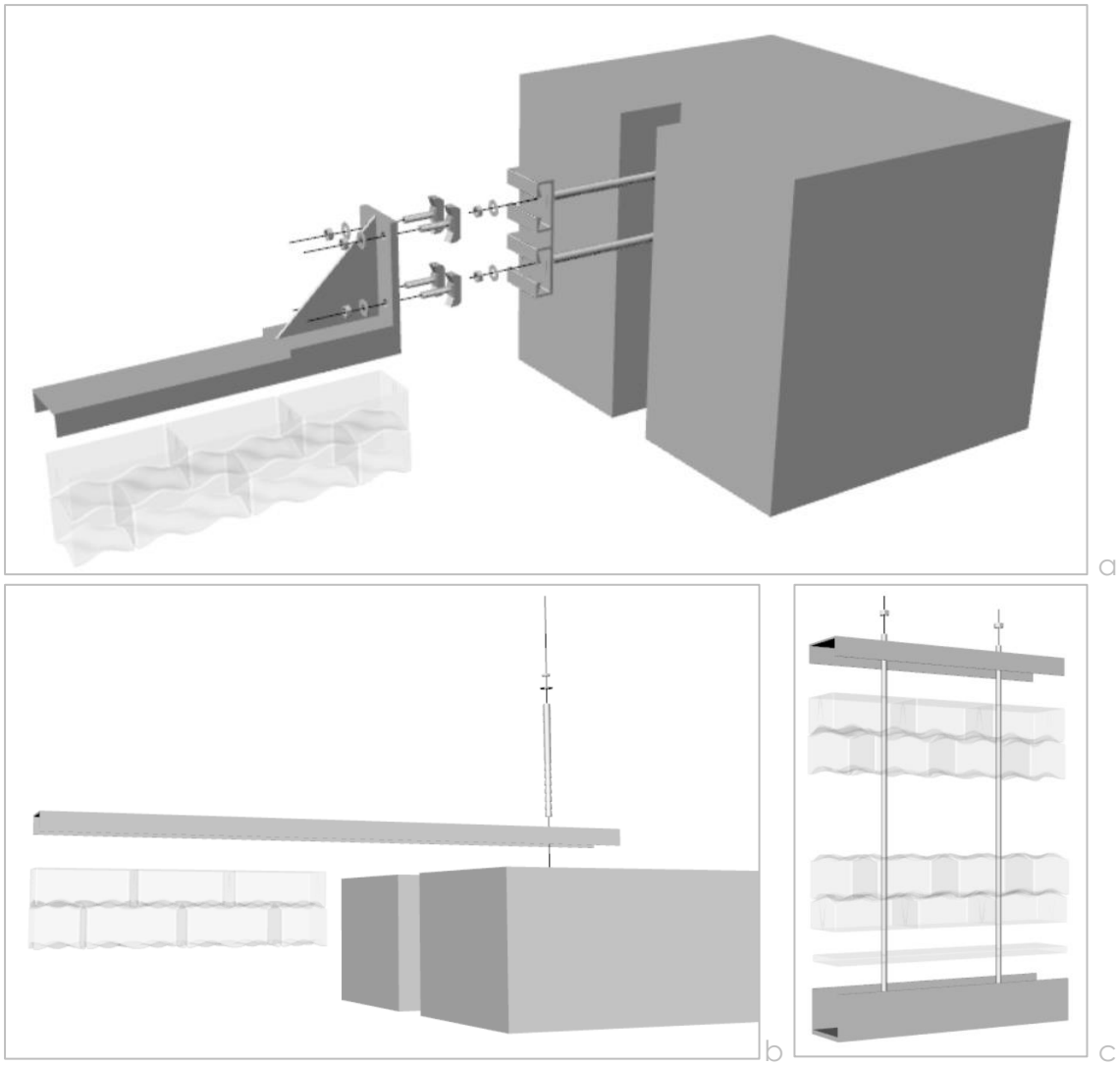

Figure 144: Possible top constraint connections: a) Horizontal anchoring into the wall; b) Vertical anchoring into the wall; c) post-tensioned tendon system.

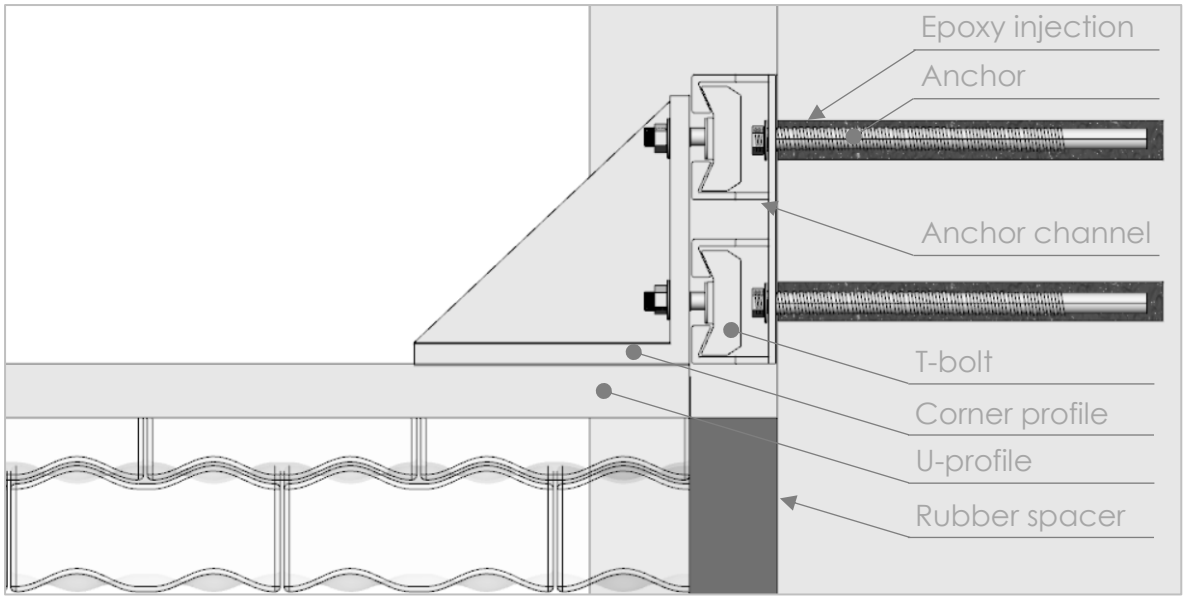

Figure 145: Detailed view of top connection.

Bottom constraint

The bottom constraint features a similar principle, with glass half-bricks and a steel profile foundation. Depending on the soundness of the lower structure vertical anchors can be applied to make sure the bottom constraint remains horizontal. This principle is shown in .

The vertical anchors are grouted into the existing structure, and hence act as a sort of pile foundation for the glass system. The underlying structure however should be evaluated on existing cracks and other indications of further damaging of this part of the structure. These then should be repaired and strengthened prior to applying the anchors.

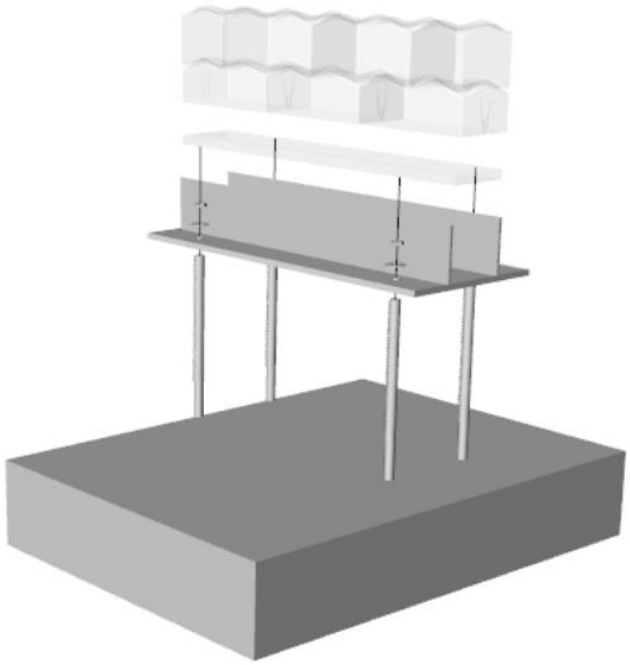

Figure 146: Bottom constraint design principles.

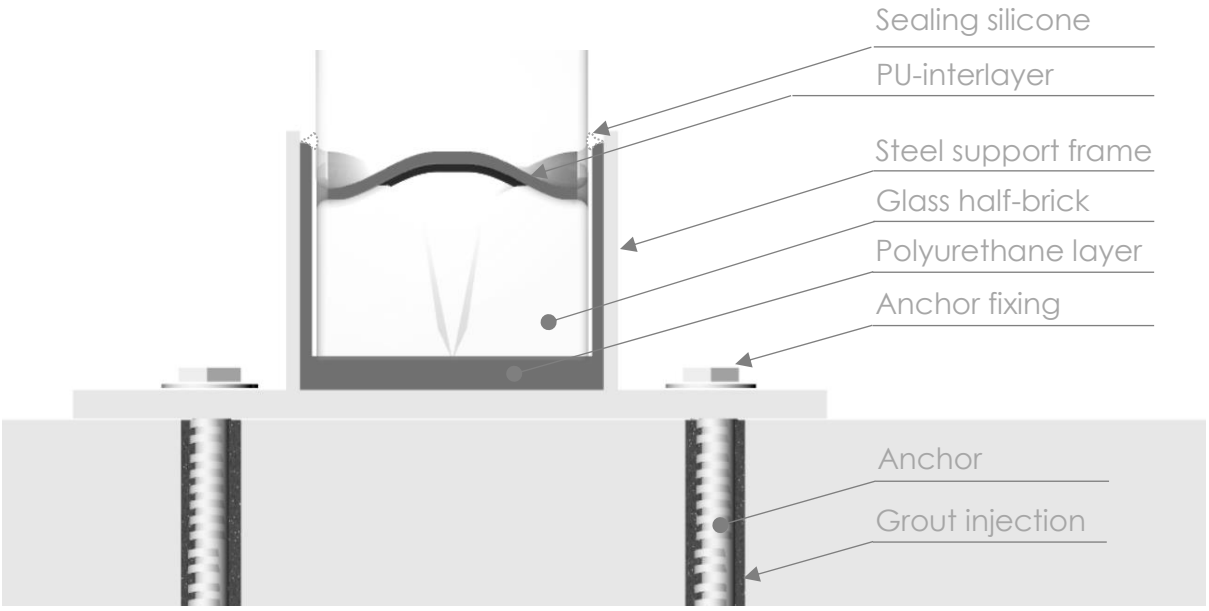

Figure 147: Conceptual detailing bottom constraint

Section 8.3. Conceptual consolidation design

It was determined that the new system should have equal capacity as the current applied interventions. In Section 3.4.2. a conservative value was derived, which indicates a capacity in the rotational centre of the wall of 2.0 MNm.

From a height of 4.6 meter and up the cast glass system will be applied. Every fourth layer is anchored into the wall, resulting into additional capacity of the system with ongoing layers (calculated from the rotational centre of the wall). This results into the curve shown in Figure 148. This figure indicates furthermore horizontal lines representing the capacity of the steel structure and certain load cases (including safety factors according to the Eurocode).

Hence it can be concluded a minimal amount of approximately 48 layers is needed in the glass system to reach the same capacity as the current steel interventions. However, it should be noted that in this case the shear capacity is taken as the capacity at the anchor. In reality, the anchor will distribute the load onto two bricks through the aluminium half-brick, and hence the real capacity is actually greater than described here. With this conservative statement, the unfortunate case is taken into account when a brick has zero capacity (due to failure or misalignment of bricks).

According to the results gained from the finite element analysis, a load on top of the critical brick is needed of at least 3.4% of its shear capacity. This is equal to the dead load from six bricks on top of the last anchored brick. Hence the total layers applied is equal to 54, of which the last six layers are not anchored. The keystone is the last anchored element of the system, and hence also contributes to the capacity of the whole. This results into the scheme drawn in Figure 149a and the system is visualised in Figure 150.

Moreover, it should be taken into account that the glass wall is designed under an angle of 20° (on the location of the former limestone wall closing the gap). This is marked blue in the top view in Figure 149b. Most of the former steel interventions are anchored in this section of the wall (marked in orange). Due to this angle the cast glass system slightly works in a different direction, hence the component working perpendicular to the wall is slightly smaller than the calculated capacity, about 19.5 kN (20.8*cos (20)).

Calculating the total capacity of the wall then results in a capacity of 2.15 MNm (relative to the rotational centre). Hence the ruin can be consolidated with a cast glass system, even when all values are chosen most conservatively.

Comparing this to the load cases applied, this is quite over-dimensioned. Even for the earthquake load combination (including its initial tilt and safety factors) this is still quite conservative. However, it should be taken into account that dynamic effects are not accounted for and hence this load case should be further investigated. The opposing wall could move with different frequencies, resulting in an even higher load then accounted for. One moreover must take into account that this concerns a monument, with already considerable damages and weaknesses. Safety and preservation of the monument is priority, and hence conservative choices are preferred.

Hence the conceptual design provides the same capacity as the current steel interventions. Further research is needed for the application of the anchoring systems in limestone walls and the behaviour of the material in combination with chemical anchors. Furthermore, the dynamic behaviour should be investigated of the cast glass interlocking masonry system and the ruin, as this is the leading load case for structure.

In Figure 151 some visualisations of the design are shown, which is also implemented in the opposing wall. These walls are expected to be less problematic, as the adjacent ruin masses are more stable.

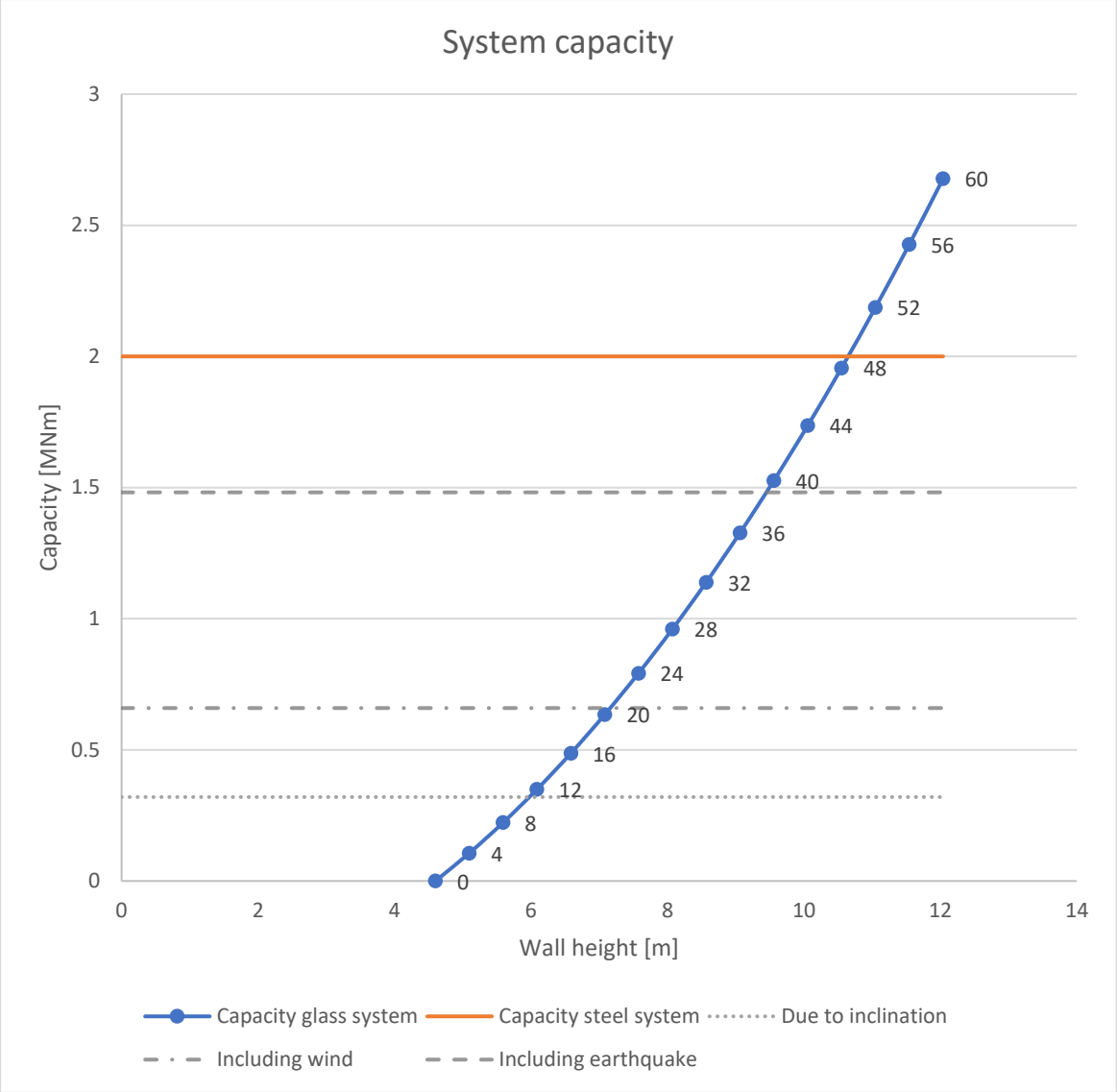

Figure 148: Graph indicating the capacity of the glass system and the capacity of the steel system. Furthermore, load cases for own weight, wind and earthquake loading are included.

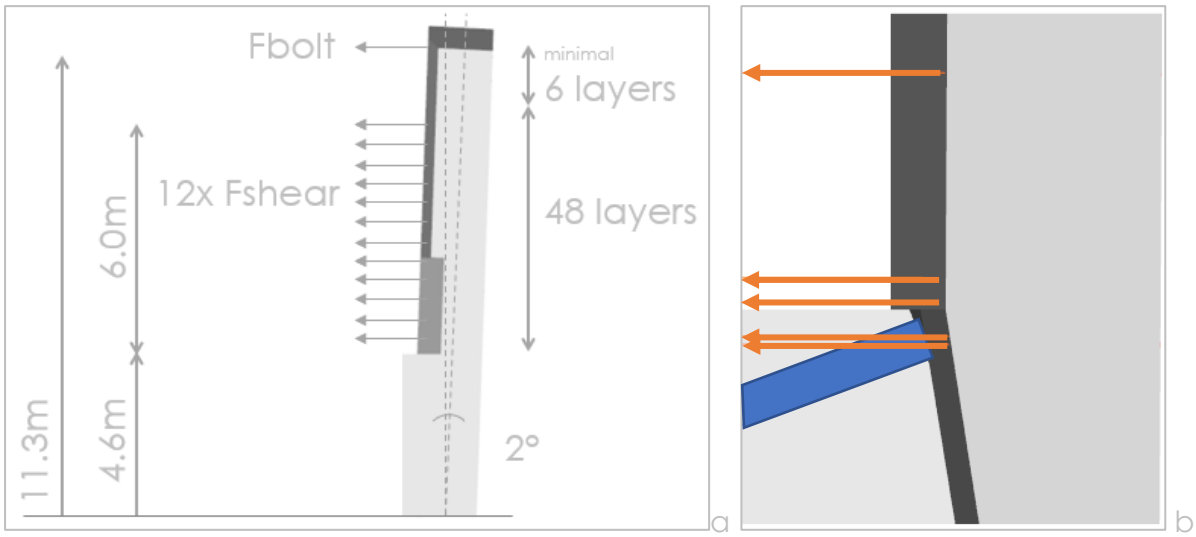

Figure 149: a) Applying a cast glass system with equal capacity as the steel interventions; b) cast glass wall in blue, former steel interventions in orange.

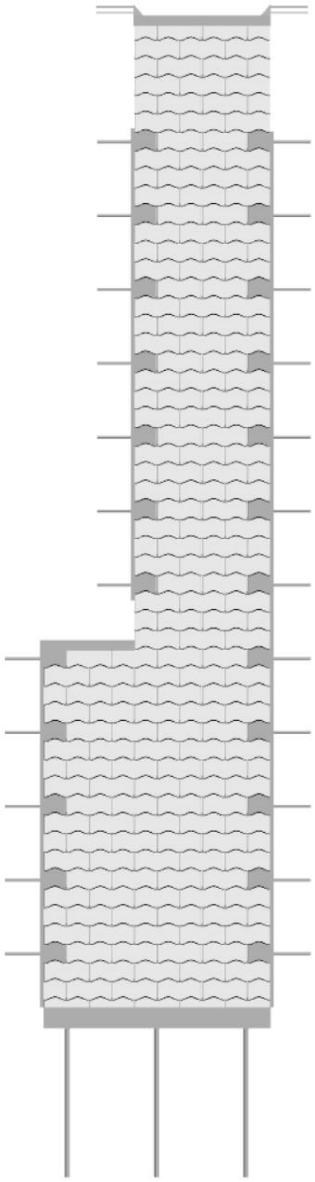

Figure 150: Full system schematic with indicated location of anchors and aluminium bricks.

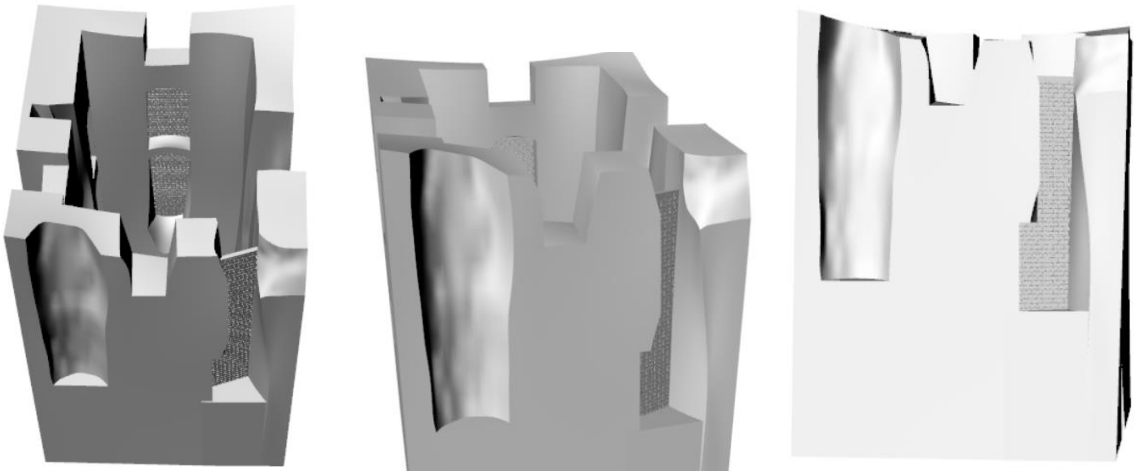

Figure 151: Impressions of the cast glass integrated into the ruin.

Chapter 9.

Discussion

The results and methodology presented in this thesis will be discussed here. The focus lies on the FEA strategy, its results and its relation to the reality.

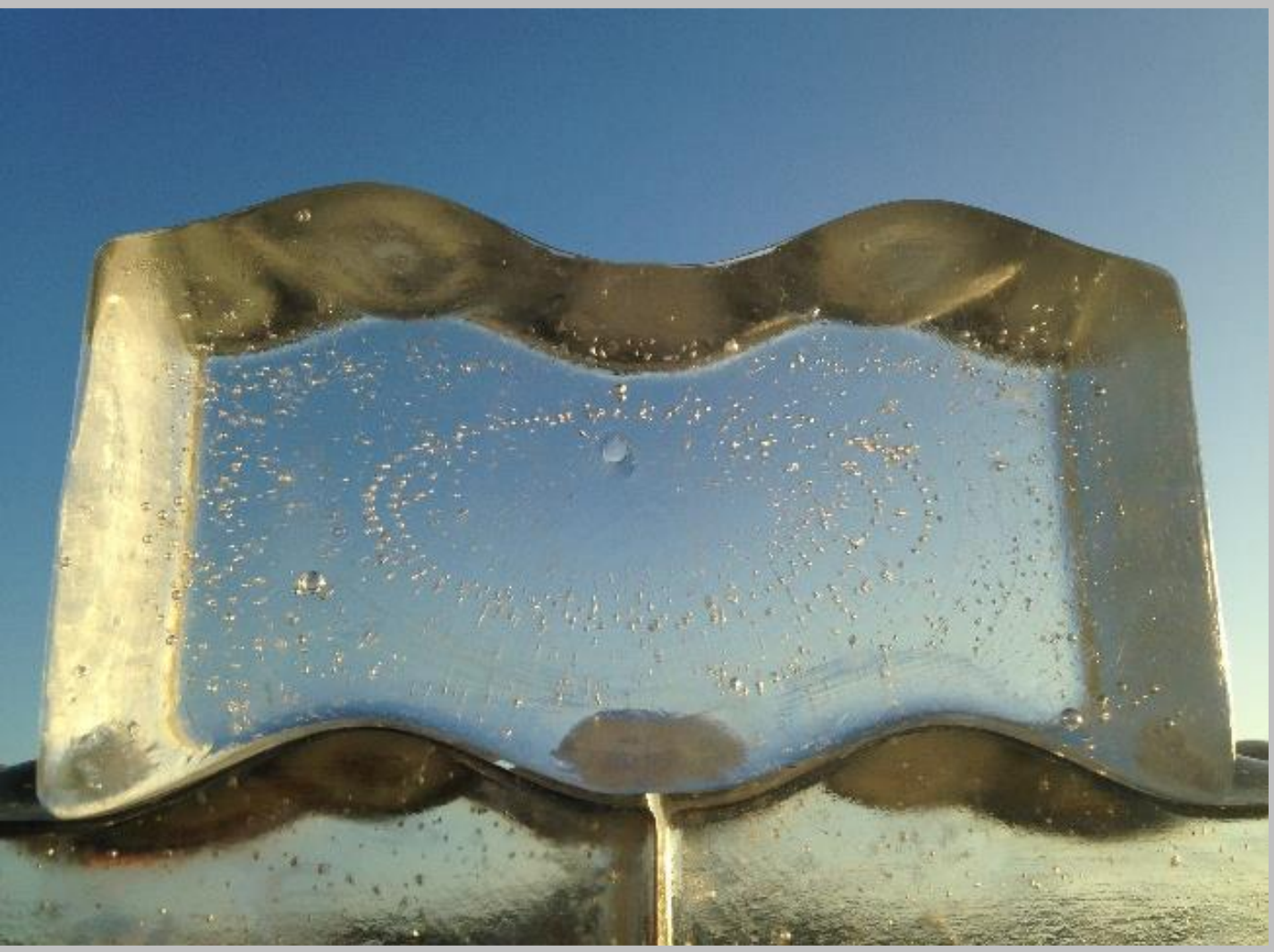

Section 9.1. Finite element analysis methodology

The methodology used, by examining complex geometries with the Christensen's failure criterion output in DIANA FEA was designed to retrieve the shear capacity of this interlocking brick. No compression was applied, as it was expected and proved that this would work beneficially for the shear capacity. The normative brick, located in the top of the wall near an anchor point hence was tested by restraining the top surface of the test set up.

Consequently, the polyurethane interlayers were locked in between the glass bricks, hence the effects of friction and uplifting could not be modelled adequately.

Friction occurs when a vertical load is applied, and results into resistance to slip. As there was no vertical load applied, this phenomenon only exhibited in the curved parts of the interlock, where compression was present due to stresses acting normal to the geometry. Near the edge, on the horizontal parts of the geometry, this results into invalid peak stresses. The dummy input values for the interface apparently did not prevent this from happening (or might have caused them). Hence from a friction point of view not much can be said when analysing the FEA results.

Uplifting of the geometry is also not possible in the model, due to the top constraint. Hence little can be said on this behaviour, other than that the absolute sum of the reaction forces was in the same order of magnitude as the expectations. From the results assumptions are derived considering the resulting net force when restricting the actual keystone in vertical direction as well. This behaviour however needs to be validated.

Essentially uplifting could be evaluated in a different finite element model set up, given an acting load on the glass brick. The goal of the model used in this thesis was however to gain an insight in the shear capacity of the interlocking glass brick, which need it served well.

Moreover, the model illustrates the Christensen's failure criterion output clearly and indicates where stress concentrations occur and how they are expected to spread over a certain geometry. Small invalid peaks occur due to invalid values in the interface elements, either caused by the absence of vertical loading or a too stiff definition of its stiffness parameters. Hence these values can be tweaked, however this would have more meaning after elaborate testing of the material properties of the polyurethane interlayer in combination with the complex geometry. The input parameters of polyurethane (e.g. non-linearity of the Young's modulus) and of the interface (frictional properties and stiffness) can then be related to the experimental results. Due to the limited data available only the Young's modulus was calibrated with experimental data. Other input values were taken from literature and hence might not be completely applicable to this specific case (as for instance the current frictional properties).

For future reference the input values of polyurethane are analysed to observe their influence on the shear capacity. Using harder or softer polyurethanes will result into different values for the Young's modulus. From the results it can be depicted that the shear capacity increases linearly from 150 MPa to 165 MPa between E = 8 MPa and E = 100 MPa. The deformations recorded for the lower values of the Young's modulus is however unrealistic large. For higher values of the Young's modulus the interlayer becomes too rigid to efficiently spread the load onto the geometry. Hence an input value of 25 MPa to 100 MPa is recommended, to benefit from its rubbery elastic properties.

The Poisson's ratio was also reviewed to validate the results in this thesis. As an incompressible rubber this ratio should approximate 0.50, however this leads to modelling difficulties. A value of 0.48 has proven to be a good assumption, to prevent the interlayer from becoming too stiff to work properly. Values nearing 0.5 should not be used, as they distort the results completely.

Section 9.2. FEA results versus reality

The finite element model calculates perfect geometries and hence does not consider any flaws or discontinuities which would be evident in the real cast glass bricks. It however gives an insight in where the highest compressive and tensile stresses occur. Both of which can be sensitive to flaws.

Whereas tensile areas can open the flaw further, in compression areas this will highly depend on the location and direction of the flaw itself and how well the interlayer fits in between. If the flaw is compressed due to the acting forces the crack probably will not propagate.

Beside flaws, the natural shrinkage when cooling down also plays a role in geometry deviations. For this specific brick design the top surface of the brick was more influenced by this shrinkage due to eccentric location of the hot brick core. Hence on one side of the brick, the edges are slightly higher than the shear keys located in the main body of the brick. This deviation consequently changes the interlocking geometry to a less perfect fit. This probably can be solved using a more professional manufacturing method.

Other flaws observed during prototyping also would probably have not occurred using different production techniques. The other techniques, which for instance were used in the Crystal Houses project are however costly, as is the equipment needed. For properly evaluating the interlocking bricks this however is necessary, as its geometry is key to its capacity and fit. Any flaws or differences in shrinkage coming forth from the production process hence influences any prototype testing negatively, giving skewed results.

Section 9.3. Parameter variations

The most interesting parameter variations were explored with DIANA FEA. As the width and length are fixed in a certain ratio (for multifunctionality purposes) and the PU interlayer properties can only be validated for the used shape factor, this parameter variation was left out of the sensitivity study. It is however quite straight-forward that with a smaller brick size, capacity decreases. For completing the design diagrams, the research can be multiplicated for smaller brick sizes after a more thorough research on the PU interlayer.

The more interesting parameter variations include a brick height variation, an increase in amplitude and a more simplified geometry called the Linear-Sine combination.

The brick height variations resulted in the expected behaviour. Up to a certain height bending failure was the dominant failure mechanism, which would result in splitting of the brick. Gradually both failure mechanisms influenced one another and for higher bricks shear key failure became dominant. The expectations were calculated using its characteristic strength in one dimension (45 MPa) while in reality the combination of the three principal stresses (3D) generally results in earlier failure.

While no quantitative value could be assigned to the acceptable tolerances, the variations could be evaluated qualitatively. Failure of the brick occurred with smaller deformations for smaller brick heights. Hence a small brick height is twice as disadvantageous. Not only has the brick a smaller shear capacity, any deviations from the perfect geometry would also have a larger impact.

The amplitude variations showed an increase in shear capacity when increasing the amplitude. This was the expectation as well due to a larger contact area; however it comes at the cost of a relative tolerance compared to smaller amplitude variations. This can be explained by a larger area of the interlayer being compressed rather than deformed due to the increase of interlock angle.

The increase of the amplitude is hence a design choice, trading in tolerated geometry deviations for extra shear capacity.

The Linear-Sine combination geometry was evaluated due to its easier post-processing compared to the all curved geometry. It includes more flat surfaces and hence can be polished easier to perfection. Its results were as expected, the shear capacity was expected to remain relatively constant compared to the amplitude variations, but had a slight increase in capacity. This can be dedicated to a slight increase in contact surface area. This variation is moreover less prone to tolerances compared to the amplitude variations. This again can be explained by its smaller contact area of the interlock.

Tolerance problems in both Rhinoceros and DIANA FEA restricted the choice of geometry variations. For analysing lower amplitudes tolerance problems arose in Rhinoceros, which exhibited in ill-conditioned meshes in DIANA FEA. Hence certain brick variations could not be analysed.

Section 9.4. Consolidation of Lichtenberg Castle ruin

The new consolidation design for the Lichtenberg castle ruin is designed conservatively, replacing the current steel interventions by a cast glass interlocking system. The permanent load design value is used to apply the cast glass shear capacity, as the glass system needs to hold the tilted wall into position. For other actions on the wall the cast glass bricks have a higher design capacity.

The loads are introduced into the system through the anchors embedded in the limestone walls. These anchors are still a point of uncertainty, as tests should be performed on local limestone to determine the anchor behaviour and capacity.

The capacity of the rest of the connection system is larger than the design capacity of the glass bricks. Hence failure is predicted to occur in the glass system, due to peak stresses near a flaw or deviating geometry. To a certain level this also has been taken into account by the design. The design shear capacity is calculated for one brick near the anchored aluminium half-brick. In reality this aluminium brick will transfer the load to both adjacent geometries through their shear locks. The shear capacity however is calculated in this aluminium block, to take into account severe misalignment causing one brick to take the full load.

A simple earthquake calculation shows that this is the most troublesome load case due to the large mass of the wall. In combination with the current tilt a load of about 1.5 MNm is calculated. However, dynamic effects and the other adjacent wall are not included in this simplistic calculation. If its movements are in the opposite directions at certain points during the earthquake the glass wall system would be subject to an even bigger load. The behaviour of the wall system itself has not been accounted for as well. Hence an extensive research should be performed to calculate these effects and to determine if the new intervention is earthquake proof. For this moreover the soil and quarries near the ruin must be investigated on stability and marks of erosion.

For the other walls the system behaves less critical, and hence the same brick size can be applied here as well.

The ruin geometry retrieved from the point cloud and transformed into a solid geometry can be imported into DIANA FEA using a STEP-file. Hence the ruin geometry can be analysed in DIANA as well, however some meshing problems would have to be solved first. However due to time limitations this and its structural evaluation is not included in this thesis.

In any case, it is worth to notice that what could be done for a complex brick is also possible for total structures, using the methodology described in this thesis. Hence any complex geometry can be calculated using DIANA FEA. Some tolerance problems in both software packages might have to be improved for full compatibility.

Chapter 10.

Conclusions

The results of this thesis are here concluded, considering the FEA methodology, parametric geometry, the consolidation design and the Lichtenberg Castle ruin.

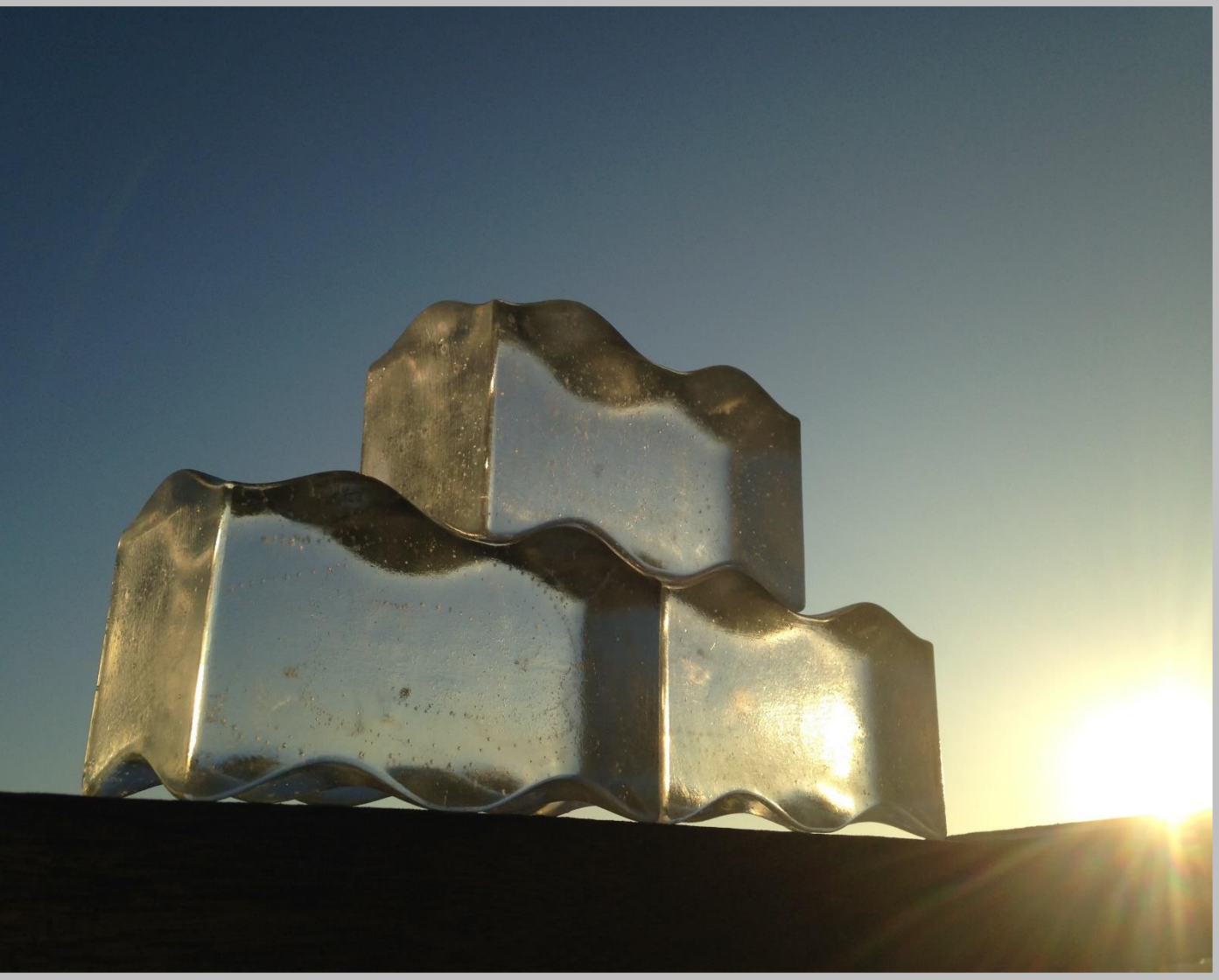

Section 10.1. On finite element analysis methodology

The following conclusions can be drawn considering the finite element analysis methodology applied.

General methodology

In general, the applied method to evaluate the parametrically designed brick can now be applied on other geometries as well. This is not limited to cast glass elements, but can be applied for complex geometries all together. From free-form structural elements to complete 3D laser scanned buildings. Pre-processing could however be automated, by for instance programming certain steps in the process.

Christensen's failure criterion

The Christensen's failure criterion output can be used to successfully predict peak stress concentrations in optional brick geometries, it moreover allows to calculate the characteristic shear capacity of a cast glass brick, which then can be transformed into a design value.

Input values for polyurethane

The correct modelling of the polyurethane interlayer is an essential part of the simulation. However due to locking of triangular elements and the incompressible behaviour of the material it is difficult to determine adequate parameters.

The hardness grade determines the Young's modulus of the PU chosen, and must be calibrated simultaneously with the assumed Poisson's ratio. This calibration should be done according to laboratory experiments, to mimic the real behaviour.

For the Poisson's ratio 0.48 seems a good practice, however values up to 0.49-0.495 are expected to work fine, given that the Young's modulus can be adapted to fit the needs. Values approaching 0.499-0.50 should be avoided, as these values would result in excessive stiff behaviour of the interlayer, resulting in invalid peak stresses and early failure.

Friction and uplifting behaviour

No definitive results can be derived from the simulations made, interpretations made in this thesis need experimental validation.

Importing geometry

The only way to exchange solid geometries from Rhinoceros to DIANA FEA is through STEP-files. Prior to importing the geometry, the coincidence tolerance needs to be changed in DIANA FEA to prevent mismatching of the geometry.

Section 10.2. On brick geometry

The following conclusions can be drawn from the designed brick presented in this thesis.

Reflection on design criteria

The brick design was based on design criteria from material properties, interlocking geometries and boundary conditions from the case study. Its shape was hence determined to not only transfer shear forces through its interlocking geometry, the design also takes into account ease of assembly and multifunctionality. Hence the brick can be used as a column, a single layer wall or a double layer wall in English or Flemish bond. It was designed for a structure in need of high shear capacity, and hence can be applied anywhere else (in the same or other configurations) where this capacity is not needed.

Parameter influences

Decreasing the height changes the bricks failure mechanism and lowers its shear capacity. For thinner brick designs the brick is more sensitive to bending, while for higher heights shear lock failure is more critical. Both failure mechanisms are however still possible, even for higher bricks, as peak tensile

stresses occur halfway the brick. A flaw in that region could lead to crack propagation normal to this area and hence still propagate throughout the brick. A characteristic contour plot is shown in Figure 152. Another possible failure is a flaw near the compressive zone. Due to the flaw peak stresses can be introduced which would lead to a part of the brick chipping off.

Moreover, decreasing the height lowers its allowable tolerances. Hence it can be concluded that choosing a brick design with sufficient height is preferable in matters of shear capacity and tolerance sensitivity.

Varying the amplitude also includes a loss in allowable tolerances but can be seen as a trade-off for a higher shear capacity. It moreover decreases the uplifting force due to the higher inclination of the interlock. Hence it is a designer's choice.

When easier post-processing is desired, one can choose for a Linear Sine variation geometry. This geometry features more flat areas and hence is easier to polish after manufacturing. This variation comes with a slight increase in shear capacity and tolerance sensitivity.

Design values

The design diagrams for short-term and permanent loads are given in Figure 153 for various values of the amplitude.

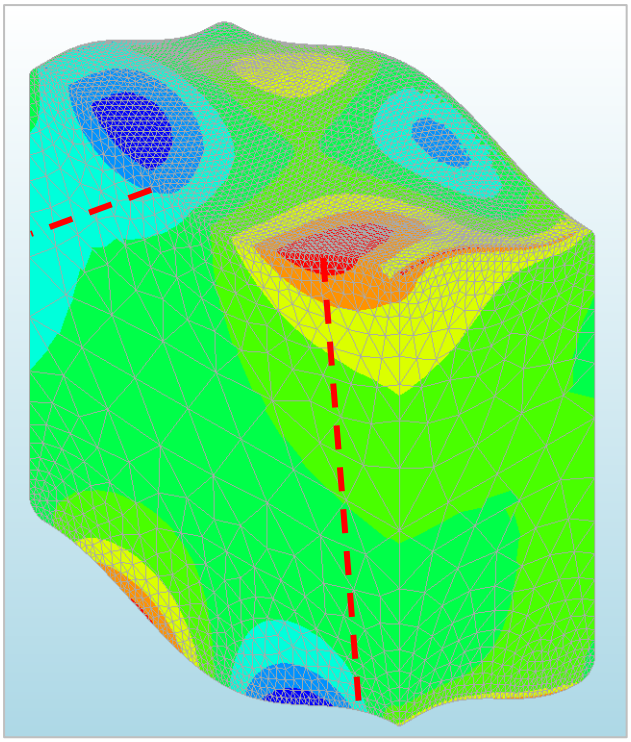

Figure 152: Compression (blue) and tensile (red) areas, visualised with CHR-output. Striped lines indicate potential splitting or chipping of failure mechanisms.

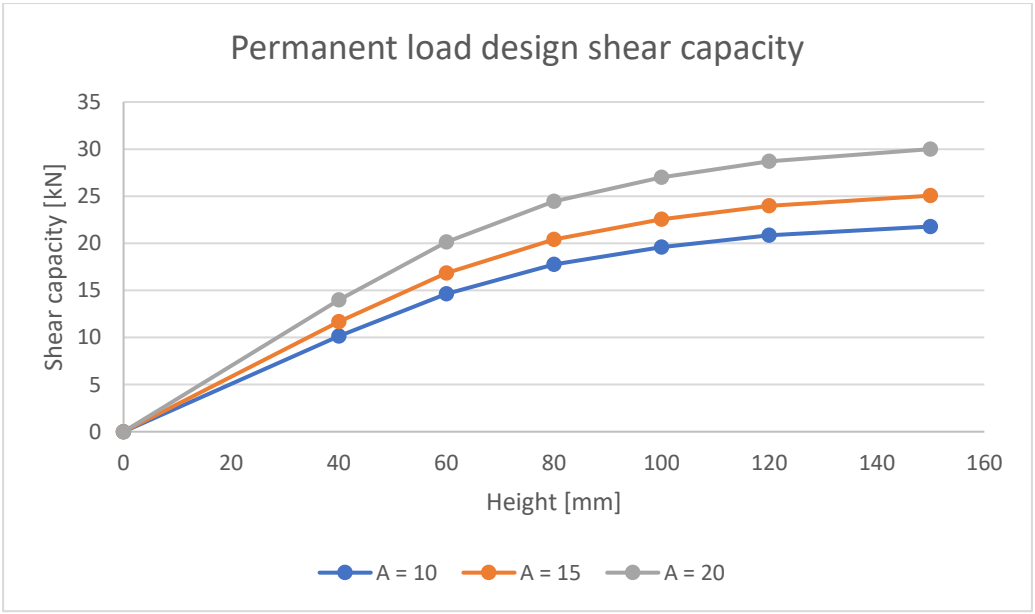

a

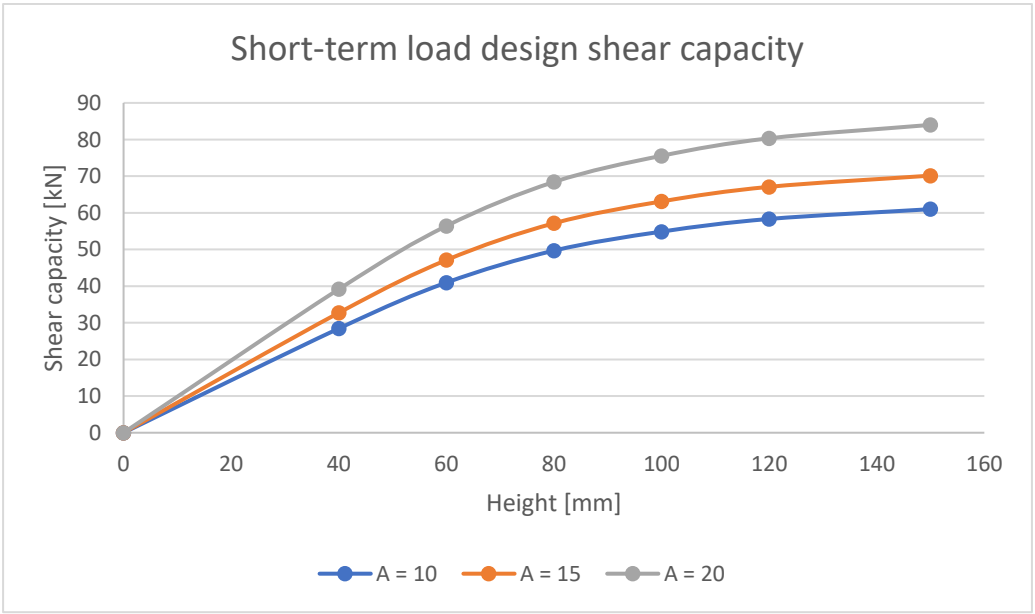

b

Figure 153: Design diagrams for permanent and short-term shear capacity.

Section 10.3. On consolidation design

The consolidation design presented in this thesis is a conceptual proof that the interlocking cast glass brick can be applied to consolidate monuments by replacing previous interventions. The application of anchors should be further investigated for the sensitive limestone brickwork of the Lichtenberg Castle.

In general, the results indicate a wide-spread application for the interlocking cast glass bricks, especially when the system can be compressed, for instance using a post-tensioned cable system. The reviewed case study considers an extreme challenge, and being able to replace the current interventions with a glass system of the same capacity is hence promising for other applications as well.

The proposed connection makes assembly and disassembly easy, as all anchors can be in place prior to building up the masonry wall. The locking bricks in the anchor channel are then applied as the wall is erected. Moreover, the channels can be anchored or embedded into freshly cast concrete. Hence the connection has applicability in not only monumental consolidations, but also in new construction designs.

The proposed design is a concept and should be worked out further to optimize its application. The conservative assumptions hence could be re-evaluated when this system is further researched.

Section 10.4. On ruin Lichtenberg Castle

The former shape of the castle could be determined through historical analysis of archived images. The larger masses of the castle used to be attached to the nowadays ruin. On one side a large sinkhole is located where part of the castle used to be, on the other is an artificial cliff, created by ENCI However historic images indicate that part of the mountain already disappeared before the excavations by ENCI. The current farm seems to be built on top of the foundation of other buildings belonging to the castle, as is depicted in Figure 154. Due to the missing or instable adjacent areas a full restoration of the castle is impossible.

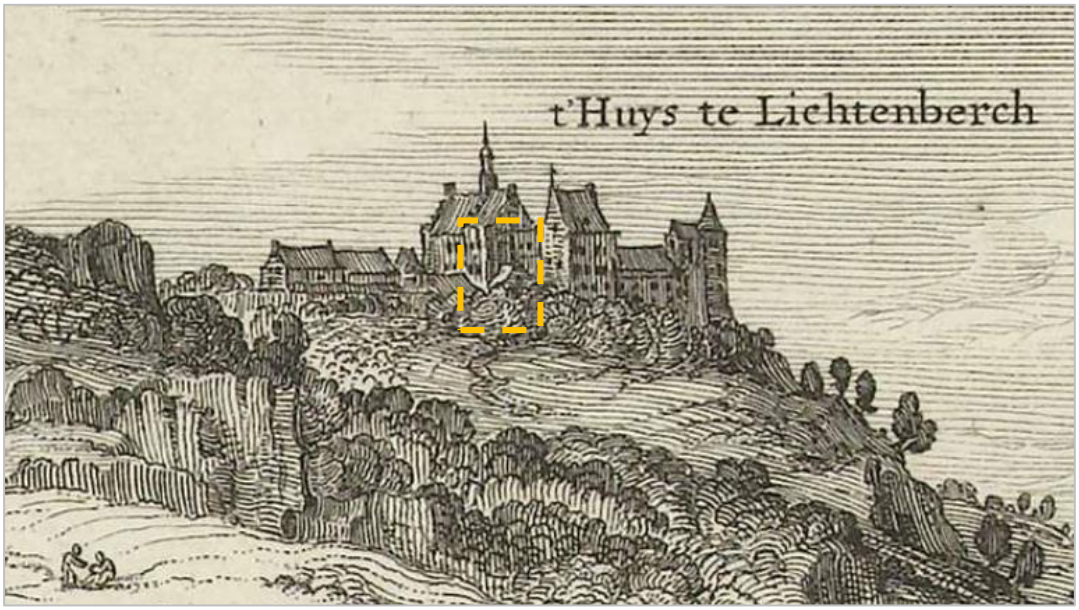

Figure 154: Former appearance of the castle, here depicted on a decorated war map from 1633. The nowadays ruin is marked in the picture. Reprinted from (Visscher (II) & Cletcher, 1633).

Chapter 11.

Recommendations

This chapter discusses continuations on the topic presented in this thesis. Moreover feedback on the Christensen's failure criterion output is discussed for TNO DIANA FEA. Lastly some recommendations are stated considering the case study of this thesis: The Lichtenberg Castle ruin.

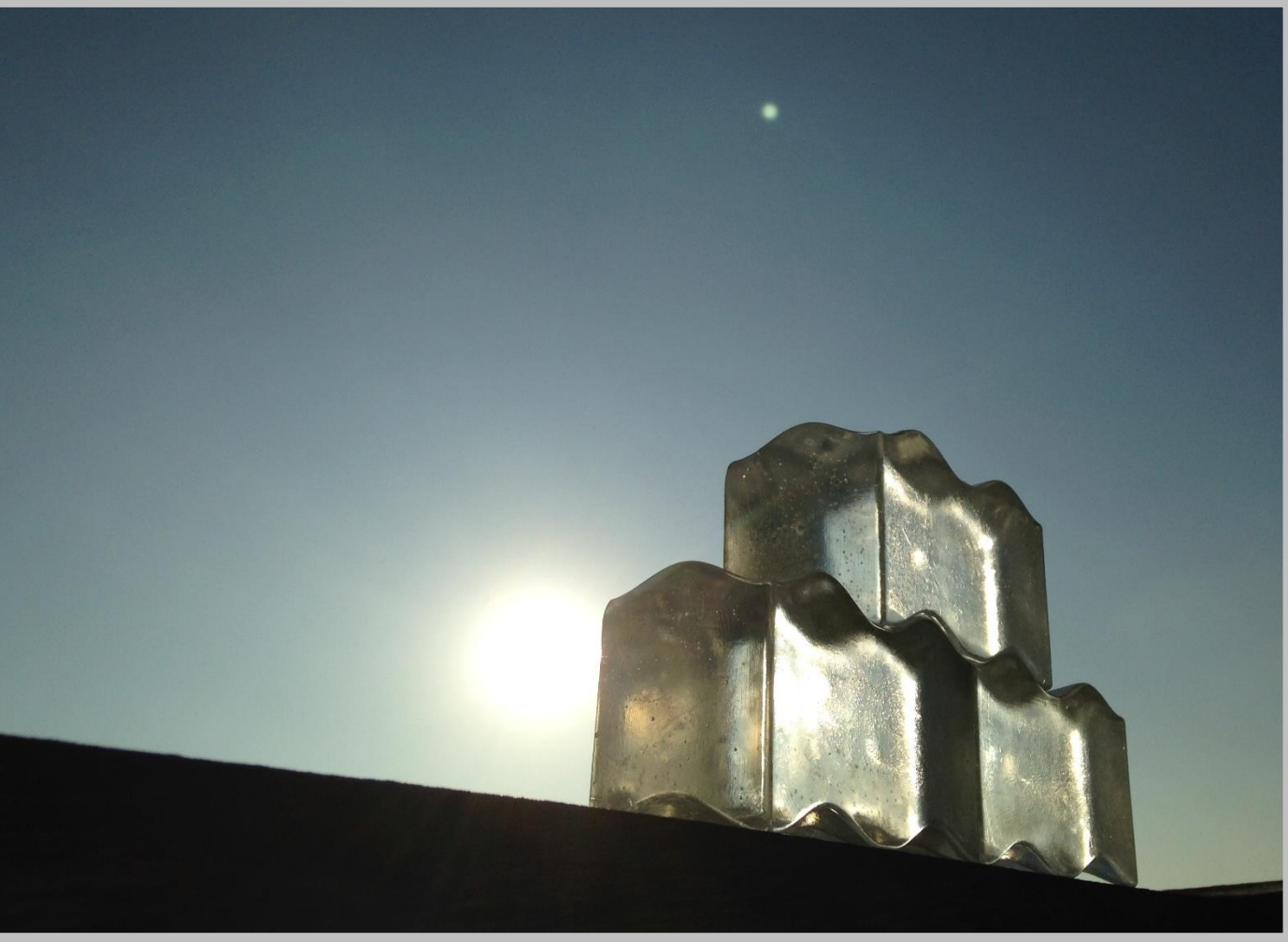

Section 11.1. Further research possibilities

Below some recommended extensions of the research presented in this thesis will be discussed, which build forth on the problematic of the subject.

Development of new (PU) interlayers

Polyurethane is due to its incompressibility not the best choice as an interlayer. Due to the thin sheet applied the material cannot bulge out sufficiently to allow much geometric deviations without introducing peaks stresses. Increasing its shape factor, i.e. by making its bulging out area bigger, would increase its adaptability to the applied glass geometry. This for instance could be done by applying perforated or semi-perforated PU sheets.

Experimental data on compressibility, deformation and friction are still largely missing in the literature for applicable shape factors. To further calibrate the input of the interlayer material it is therefore recommended to do extensive research on thin sheets of cast polyurethane.

Other materials could be explored as well for interlayer application.

FEA research to the effects of flaw size and flaw location

Discontinuities such as surface flaws or enclosed bubbles could be modelled into the brick design to test the effects of flaws in the geometry.

FEA research on cast glass interlocking wall behaviour

As this thesis focuses on the capacity of a single brick, modelling the behaviour of the wall or wall segment is a logical next step to take in the line of research. Hence eccentric loads, wind-loads and dynamic responses due to earthquakes can be reviewed.

Explore cast glass systems with post-tensioned cable systems

From compression results it could be determined that any compression works beneficially, even on the tensile areas in the brick. Hence an internal or external cable system could be applied to strengthen the glass system.

Structural evaluation of a 3D building geometry

It could be interesting to structurally evaluate the tower geometry retrieved from the point cloud into DIANA FEA. A more precise and fast method of translating the point cloud into a solid could also be an interesting topic to further research. Its earthquake response could then also be evaluated in DIANA FEA.

Experimental and FEA research to cast glass elements and anchoring channel systems

The concept of the channel anchoring connection design could be applied in many other applications. It is easy to assemble and has minimal impact on the original structure.

Section 11.2. On restoration Lichtenberg Castle

Finding out what actually happened to the Lichtenberg Castle ruin was a tough nut to crack. With newly gained insights, details and other parts could be restored. Hence here recommendations are stated considering the monument's restoration and consolidation.

Monument restoration

It is deemed impossible to reconstruct the castle on its original location, as in the length of both the original building masses the soil conditions are not preferable or non-existent. This on one side due to a large sinkhole (which is still considered unstable) and on the other side due to excavations done by ENCI.

There is furthermore too few information available to fully restore the castle to its former glory. Proper sources of information considering its floor plans, or even the location of windows, are still missing. Hence no valid restoration can be done for the full castle.

Certain detailing however could be brought back into the monument, such as the gothic niches or the floor beams and girders. This could be done using cast glass elements or using limestone from the region.

To still remind people of what once stood high and proud on top of this hilltop, it is proposed to engrave historical drawings in sheets of glass and position them around the area. Looking through the glass one then can see the castle standing proud on top of the mountain. This moreover might attract more recreational hikers to come and see the ruin.

The idea was taken from an existing piece of art in *Schimmert* by artist *Vera H.J. De Haas*. She immortalised a historical monastery in a sheet of glass, after a fire destroyed the monument. This memorial is shown in Figure 155.

In this research various archives were consulted, see bibliography for more information. More information might be found doing archaeological research near the sinkhole, as I suspect rumble of the old castle or household items might still be hidden underneath the upper soil layers.

Monument consolidation

To properly consolidate the monument an extensive investigation should be carried out considering the soil and quarries below. Moreover, an adequate earthquake analysis should be performed. For implementing a cast glass interlocking system, the dynamic response of the cast glass system should also be evaluated. Not taking into account the dynamic response, the monument could reintroduce its former windows and doors with a cast glass interlocking system.

Figure 155: Monastery engraved in glass to commemorate a lost monument. Art piece by Vera H.J. De Haas, photograph by author.

Bibliography

4TU Bouw. (2017). Re3 glass. *Re3 glass - A Reduce/Reuse/Recycle Strategy.* 4TU Bouw. Retrieved July 27, 2017, from https://www.4tu.nl/.uc/i70/23b4aa0102b8bbb3002216d501d03c0b0047fcb7020701c43002800180.png

Ali, M., Briet, R., & Chouw, N. (2013). Dynamic response of mortar-free interlocking structures. *Construction and Building Materials, 42*, 168-189. doi:10.1016/j.conbuildmat.2013.01.010

Ali, M., Gultom, R., & Chouw, N. (2012). Capacity of innovative interlocking blocks under monolithic loading. *Construction and Building Materials, 37*, 812-821. doi:10.1016/j.conbuildmat.2012.08.002

Anonymous. (1632). *Belegering van Maastricht.* [Etching/Engraving]. Rijksmuseum. Retrieved March 8, 2017, from http://hdl.handle.net/10934/RM0001.COLLECT.388568 Licensed under CC0 1.0 Universal Public Domain https://creativecommons.org/publicdomain/zero/1.0/deed.nl

Anonymous. (1652). *Belegeringe ende Overwinninge der Stercke Stadt Mastricht.* [Etching], Rijksmuseum, obj.nr. RP-P-OB-91.335. Retrieved March 9, 2017, from http://hdl.handle.net/10934/RM0001.COLLECT.460564

Anonymous. (1881a). Gevelaanzichten en plattegronden. *Kasteel Lichtenberg op den St Pietersberg bij Maastricht.* [Drawing], Rijksdienst voor het Cultureel Erfgoed, obj.nr. BT-021139. Retrieved March 8, 2017, from http://beeldbank.cultureelerfgoed.nl/alle-afbeeldingen/detail/c612f2ba-110b-7003-1da4-cb426bbfe17e/media/fa27473a-2524-adb8-9ff6-1993836b96bf Licensed under CC BY-SA 4.0 https://creativecommons.org/licenses/by-sa/4.0/deed.nl

Anonymous. (1881b). Gevelaanzichten. *Kasteel Lichtenberg op den St Pietersberg bij Maastricht.* [Drawing], Rijksdienst voor het Cultureel Erfgoed, obj.nr. BT-021140. Retrieved March 8, 2017, from http://beeldbank.cultureelerfgoed.nl/alle-afbeeldingen/detail/faec8f93-932d-b75c-36ea-9ea08b216174/media/8d09753f-263c-e190-a7a4-9b6fea7c1741 Licensed under CC BY-SA 4.0 https://creativecommons.org/licenses/by-sa/4.0/deed.nl

Anonymous. (1893a). ruïne Ligtenberg. *Rijksdienst voor het Cultureel Erfgoed.* [Photograph], obj.nr. 17.532. Retrieved March 9, 2017, from http://beeldbank.cultureelerfgoed.nl/alle-afbeeldingen/detail/9de14fb4-70ad-dae2-a704-1f398ccfd8a7/media/4bb043a7-fe89-d64a-63bd-28a04c2f0031 Licensed under CC BY-SA 4.0 https://creativecommons.org/licenses/by-sa/4.0/deed.nl

Anonymous. (1893b). *ruïne Ligtenberg.* [Photograph], Rijksdienst voor het Cultureel Erfgoed, obj.nr. 17.531. Retrieved March 9, 2017, from http://beeldbank.cultureelerfgoed.nl/alle-afbeeldingen/detail/ff3a7644-183a-c59c-76fb-52862f73dae3/media/f6809aff-c6cf-893c-99b4-b0da2ad7e7dc Licensed under CC BY-SA 4.0 https://creativecommons.org/licenses/by-sa/4.0/deed.nl

Anonymous. (1904). *Ruine Ligtenberg.* [Photograph], Rijksdienst voor het Cultureel Erfgoed, obj.nr. 17.533. Retrieved March 8, 2017, from http://beeldbank.cultureelerfgoed.nl/alle-afbeeldingen/detail/35ea3a4d-c17b-d444-5153-01f039ae61fc/media/08d1b7b4-1b50-7cb3-992c-57065a099216 Licensed under CC BY-SA 4.0 https://creativecommons.org/licenses/by-sa/4.0/deed.nl

Aurik, M. (2017). *Structural Aspects of an Arched Glass Masonry Bridge.* Structural Engineering. Delft: TU Delft.

Barou, L. (2016). *Transparent Restoration.* Architecture, Urbanism & Building Sciences. Delft: TU Delft. Retrieved November 7, 2016, from http://repository.tudelft.nl/islandora/object/uuid%3A8aa8ef49-6eb5-43cb-bcff-0a51d52ce4cb?collection=education

BASF. (2011, November). Thermoplastic Polyurethane Elastomers (TPU). Lemförde, Germany. Retrieved October 2, 2017, from http://www.ep-cn.com.cn/up/ad/201112301171074575.pdf

Bassi, A., Casa, F., & Mendichi, R. (1987). Shore A Hardness and Thickness. *Polymer Testing, 7*, 165-175. Retrieved October 3, 2017, from https://ac.els-cdn.com/0142941887900304/1-s2.0-0142941887900304-main.pdf?_tid=27043e5c-a826-11e7-addc-00000aacb362&acdnat=1507026927_fac1b1e8430363fa0036640d03d75cfe

Bosch, E. (n.d.). CO2-doline met geologische orgelpijp in het Vijlenerbos. *Karstverschijnselen in de Sint-Pietersberg.* [Illustration], Naturalis. Retrieved March 13, 2017, from http://www.geologievannederland.nl/landschap/sint-pietersberg/karstverschijnselen-sint-pietersberg

Bosch, E. (n.d.). Ontstaan van instortingsdolines (boven) en erosiedolines (onder). *Geologische afbraak van de Sint-Pietersberg.* [Illustration], Naturalis. Retrieved March 13, 2017, from http://www.geologievannederland.nl/landschap/sint-pietersberg/geologische-afbraak#

Brandi, C. (2005). *Theory of Restoration, I.* Retrieved November 11, 2016, from http://isites.harvard.edu/fs/docs/icb.topic822683.files/Brandi_Theory%20of%20Restoration%20I_sm.pdf

Cartwright, M. (2014, March 13). *Inca Architecture*. (Ancient History Encyclopedia Limited) Retrieved March 22, 2017, from Ancient History Encyclopedia: http://www.ancient.eu/Inca_Architecture/ Licensed under CC BY-NC-SA 3.0 https://creativecommons.org/licenses/by-nc-sa/3.0/

Cervera, C. (2016). *Inca Ingenuity in the Andes.* Ancient History et cetera. Retrieved June 12, 2017, from http://etc.ancient.eu/travel/inca-ingenuity-andes/

Christensen, R. (2013). *Theory of Materials Failure.* Oxford: Oxford University Press.

CMOG. (2011). The Glassy State. *What is Glass?* Corning Museum of Glass, Corning. Retrieved September 25, 2017, from http://www.cmog.org/article/what-is-glass Copyright 2002 - Corning Museum of Glass

CUAD. (2003). *Materials Data Book.* Cambridge: Cambridge University Engineering Department. Retrieved October 3, 2017, from http://www-mdp.eng.cam.ac.uk/web/library/enginfo/cueddatabooks/materials.pdf

De Hoog, G. (1914a). Photographed ink drawing by Josua de Grave 1668. *Foto van tekening van de ruïne Lichtenberg en het klooster Slavante.* [Photograph of Ink Drawing], Rijksdienst voor het Cultureel Erfgoed, obj.nr. 2427. Retrieved March 9, 2017, from http://beeldbank.cultureelerfgoed.nl/alle-afbeeldingen/detail/7fa6fc17-5685-7d54-71c4-

ba6c6634cbc8/media/d83a06bc-41ff-59ba-e89e-16871adebcbd Licensed under CC BY-SA 4.0 https://creativecommons.org/licenses/by-sa/4.0/deed.nl

De Hoog, G. (1914b). Photographed ink drawing by Josua de Grave in 166[?]. *Slavante En Slot Lichtenburg.* [Photograph of Ink Drawing] Rijksdienst voor het Cultureel Erfgoed, obj.nr. 2428. Retrieved March 9, 2017, from http://beeldbank.cultureelerfgoed.nl/alle-afbeeldingen/detail/40bef53c-e32b-b53b-c7e7-7f08d3442bd8/media/dac501df-f910-6bf9-cb2a-75ff004fca60 Licensed under CC BY-SA 4.0 https://creativecommons.org/licenses/by-sa/4.0/deed.nl

De Steunbeer BV. (2012). *Onderzoek herbestemming Complex Lichtenberg.* De Steunbeer BV. Zierikzee: De Steunbeer BV.

Delemarre, G. (1958). Photographed reproduction drawing of Van Gulpen 1850. *Ruines du Chateau de Lichtenburg et Maestricht en 1850.* [Photograph of Drawing], Rijksdienst voor het Cultureel Erfgoed, obj.nr. 52.660. Retrieved March 9, 2017, from http://beeldbank.cultureelerfgoed.nl/alle-afbeeldingen/detail/7325f9fc-a0ec-a2c6-700f-8c7be4f791de/media/c03c3333-b3c3-9b7d-0922-e3b9a4322f0f Licensed under CC BY-SA 4.0 https://creativecommons.org/licenses/by-sa/4.0/deed.nl

Delemarre, G. (1966a). *Photographed drawing of Val. Klotz 1670.* [Photograph of Drawing], Rijksdienst voor het Cultureel Erfgoed, obj.nr. 104.350. Retrieved March 9, 2017, from http://beeldbank.cultureelerfgoed.nl/alle-afbeeldingen/detail/68dee6d2-5d7a-678c-fd12-8ed0157435bd/media/198e54ff-fbca-a36b-ebe1-8b933d9c9759 Licensed under CC BY-SA 4.0 https://creativecommons.org/licenses/by-sa/4.0/deed.nl

Delemarre, G. (1966b). Photographed drawing of Val. Klotz 1670. *Lichten Búrgh 1670.* [Photograph of Drawing], obj.nr. 104.352. Retrieved from http://beeldbank.cultureelerfgoed.nl/alle-afbeeldingen/detail/6d2683d2-d24c-b529-8eea-ef0c374acf11/media/c6ff5136-45ce-ac66-6e9b-b40331323b86 Licensed by

Delemarre, G. (1966c). *Klooster Slavante, tekening van J.de Beyer, 1740.* [Photograph of Drawing], Rijksdienst voor het Cultureel Erfgoed, obj. nr. 104.353. Retrieved October 10, 2017, from http://beeldbank.cultureelerfgoed.nl/alle-afbeeldingen/detail/519c38e7-6a8c-34e8-70d9-235bfe5cc742/media/d5def748-26d7-e935-49f6-5d100d5d6105 Licensed under CC BY-SA 4.0 https://creativecommons.org/licenses/by-sa/4.0/deed.nl

DIANA FEA. (2009). *DIANA User's Manual - Element Library.* Delft: TNO DIANA. Retrieved October 28, 2017, from https://dianafea.com/manuals/d93/ElmLib/node288.html

DIANA FEA. (2010). *DIANA 9.4.3. User's Manual - Analysis Procedures.* Delft: TNO DIANA. Retrieved November 2017, 2, from https://dianafea.com/manuals/d943/Analys/node1.html

DIANA FEA. (s.d.). Coulomb friction criterion. *DIANA-10.1 User's Manual - Material Library.* DIANA FEA. Retrieved August 15, 2017, from https://dianafea.com/manuals/d101/MatLib/node134.html

Douglas, R., & Zallen, R. (2016, April 22). *Amorphous solid*. (Encyclopædia Britannica, inc.) Retrieved September 25, 2017, from Encyclopædia Britannica: https://www.britannica.com/science/amorphous-solid

Dyskin, A., Estrin, Y., Pasternak, E., Khor, H., & Kanel-Belov, A. (2005). The principle of topological interlocking in extraterrestrial construction. *Acta Astronautica, 57*, 10-21. doi:10.1016/j.actaastro.2004.12.005

Felder, W. (1989, November). Kalkstenen uit het Boven-Krijt en Onder-Tertiair van Zuid-Limburg. *Grondboor en Hamer, 43*(5/6), pp. 145-155. Retrieved February 28, 2017, from http://natuurtijdschriften.nl/download?type=document&docid=405425

GAM. (1900). Maastricht. Lichtenbergweg. Zuiden. Overzicht vanaf de Wilhelminaweg met de ruïne "Lichtenberg" en links de uitkijktoren. *Fotocollectie GAM.* RHCL, Maastricht. Retrieved October 13, 2017, from http://rhclimburgpubliek.hosting.deventit.net/detail.php?nav_id=15-1&id=241886&index=69

Gazzola, P., Lemaire, R., Bassegoda-Nonell, J., Benavente, L., Boskovic, D., Daifuku, H., . . . Zbiss, M. (1964). International Charter for the Conservation and Restoration of Monuments and Sites. *The Venice Charter 1964*. Venice: ICOMOS. Retrieved March 8, 2017, from https://www.icomos.org/charters/venice_e.pdf

Haagen, J. v. (1650). *Huis te Lichtenberg bij Maastricht.* Rijksbureau voor Kunsthistorische Documentatie. Retrieved August 1, 2017, from https://rkd.nl/explore/images/224729

Haarhuis, K. (2010). *Cilindrische Schaalconstructies in Glas.* Eindhoven: Technical University of Eindhoven.

Halfen. (2010). *Halfen Anchor Bolt Systems - Product information technics.* Halfen. Halfen. Retrieved November 12, 2017, from http://downloads.halfen.com/catalogues/de/media/catalogues/fixingsystems/hb-e.pdf

Halfen. (2014). *Halfen Flexible Bolt Connections - Technical Product Information.* Halfen. Retrieved November 12, 2017, from http://downloads.halfen.com/catalogues/de/media/catalogues/framingsystems/MT-FBC_14.1-E.pdf

Huntsman. (2010). A guide to thermoplastic polyurethanes (TPU). Retrieved October 2, 2017, from http://www.huntsman.com/polyurethanes/Media%20Library/global/files/guide_tpu.pdf

Intercol bv. (2017). *Specifications*. Retrieved October 3, 2017, from Intercol bv: http://www.clearpur.com/en/specifications.php

IPO. (n.d.). *Aardbeving*. Retrieved February 24, 2017, from Risicokaart: http://www.risicokaart.nl/informatie_over_risicos/aardbeving/

KNMI. (2014). *Seismologie en Akoestiek*. Retrieved February 24, 2017, from Jaarverslag KNMI 2014: http://jaarverslag.knmi.nl/Seismologie/

KNMI. (n.d.). *Aardbeving Roermond 1992*. Retrieved February 24, 2017, from KNMI: https://www.knmi.nl/kennis-en-datacentrum/uitleg/aardbeving-roermond-1992

Kunz, J., & Studer, M. (2006). Component Design: Determining the Modulus of Elasticity in Compression via the Shore A Hardness. *Kunstoffe International*, 92-94.

MacLeod, F. (2014). *Emerging Objects Invents Earthquake-Proof 3D Printed Column.* [Photograph], ArchDaily. Retrieved March 22, 2017, from http://www.archdaily.com/568838/architects-invent-earthquake-proof-3d-printed-column Copyright 2008-2017 by ArchDaily

Montagne, D. (1969). Vuursteen in alle tijden. *International Symposium on Flint* (pp. 133-148). Maastricht: Maastricht Museum of Natural History.

MVRDV. (2016). *Crystal Houses.* [Photographs], MVRDV, Amsterdam. Retrieved March 9, 2017, from https://www.mvrdv.nl/en/projects/crystal-houses

Natuurmonumenten. (2014). *Natuurvisie Sint-Pietersberg 2014-2025.* 's Graveland: Natuurmonumenten. Retrieved October 12, 2017, from https://www.natuurmonumenten.nl/sites/default/files/Natuurvisie_Sint-Pietersberg_2014-2025.pdf

Nederlands Maritiem Museum. (2017). Willem van Oranje voor Maastricht in 1568. Retrieved September 21, 2017, from https://www.nmm.nl/zoeken-in-de-collectie/detail/268173/

Oikonomopoulou, F., Bristogianni, T., Veer, F., & Nijsse, R. (2017). The construction of the Crystal Houses façade: challenges and innovations. *Glass Structures & Engineering*, 1-22. doi:10.1007/s40940-017-0039-4

Oikonomopoulou, F., Veer, F., Nijsse, R., & Baardolf, K. (2014). A completely transparent, adhesively bonded soda-lime glass block masonry system. *Facade Design and Engineering 2*, 201-221. doi:10.3233/FDE-150021

O'Regan, C. (2015). *Structural use of glass in buildings* (2nd ed.). London, United Kingdom: The Institution of Structural Engineers.

Pepi, J. (2014). *Strength Properties of Glass and Ceramics.* Bellingham, Washington: SPIE press monographs.

Precision Urethane. (n.d.). *Cast Urethane Hardness Data*. Retrieved October 3, 2017, from Precision Uterthane & Machine, inc: http://www.precisionurethane.com/hardness-chart.html

Qi, H., & Boyce, M. (2005). Stress-Strain Behaviour of Thermoplastic Polyurethane. *Mechanics of Materials, 37*, 817-839. doi:https://doi.org/10.1016/j.mechmat.2004.08.001

Restorative Glass Team. (2016). *Illustration of the new glass facade.* [Illustration], 4TU.Bouw.

RKD. (2016, August 10). *Joshua de Grave*. Retrieved September 29, 2017, from RKD: https://rkd.nl/nl/explore/artists/33428

RKD. (2016, August 10). *Valentijn Klotz*. Retrieved September 29, 2017, from RKD: https://rkd.nl/nl/explore/artists/44931

RKD. (2017, Maart 30). *Joris van der Haagen*. Retrieved October 10, 2017, from RKD: https://rkd.nl/explore/artists/34834

Schittich, C., Staib, G., Balkow, D., Schuler, M., & Sobek, S. (2007). *Glass Construction Manual* (2nd ed.). (S. Lenzen, Ed.) Berlin, Germany: Birkhäuser Verlag AG.

Shelby, J. (2005). *Introduction to Glass Science and Technology* (2nd ed.). Cambridge, United Kingdom: The Royal Society of Chemistry. Retrieved June 8, 2017, from http://wenku.satipm.com/view_omzwkmq25h2ytimr.html

Spee, J. (s.d.). 6706 13 Slavante J15-12. *MAASTRICHT. St Pietersberg-Slavante. VAK: J15.12 . BAND: Slavante-6. PLATTEGROND: - - . THEMABOEK: ENCI foto's BOVENGRONDSE LANDSCHAPPEN : Opnamen met de uitstekende rots van ruïne Lichtenberg, met op de achtergrond de 4 werkende ENCI schoorstenen. Ook is.* RHCL, Maastricht. Retrieved October 12, 2017, from http://rhclimburgpubliek.hosting.deventit.net/detail.php?nav_id=15-1&id=3354376&index=98

Spilman, H., & De Beyer, J. (1740). *De Slavante van de andere zyde te zien 1740.* [Etching], Rijksdienst voor het Cultureel Erfgoed, obj.nr. G-836.b. Retrieved March 9, 2017, from http://beeldbank.cultureelerfgoed.nl/alle-afbeeldingen/detail/d82fb9dd-db1a-d6df-31c3-b46039fce1cb/media/ae2c7254-fab4-f048-1643-090c1a3e7c71 Licensed under CC BY-SA 4.0 https://creativecommons.org/licenses/by-sa/4.0/deed.nl

Sprenger, J. (1941). De Ruïne Lichtenberg. *Maasgouw*, pp. 1-12.

Tadashi Oshima, K. (2012). *Optical Glass House, Hiroshima, Japan.* [Photograph]. The Architectural Review. Retrieved March 8, 2017, from https://www.architectural-review.com/today/optical-glass-house-hiroshima-japan/8638709.article Copyright 2002-2017 by EMAP Publishing Limited

Tuononen, A. (2016). Onset of frictional sliding of rubber-glass contact under dry and lubricated conditions. *Scientific Reports, 6*(27951). doi:10.1038/srep27951

Universität zu Köln. (2011, October 18). *Erdbebenstation Bensberg*. Retrieved March 2, 2017, from Universität zu Köln: http://www.seismo.uni-koeln.de/meldung/dueren/index.htm

Van Maarschalkerwaart, H. (1996). Ijzer- en staalsoorten 1840-1940. *Bouwen Met Staal*(128), 28-35.

Van Nispen tot Sevenaer, E. (1974a). *De Monumenten In De Gemeente Maastricht. Deel 1.* (2011 (unedited reprint) ed.). (D. i. Erfgoed, Ed.) Arnhem: Gijsbers & Van Loon. Retrieved September 2017, 20, from http://www.dbnl.org/tekst/nisp034monu02_01/nisp034monu02_01.pdf

Van Nispen Tot Sevenaer, E. (1974b). *De monumenten in de gemeente Maastricht. Deel 2.* Arnhem: Gijsbers & Van Loon. Retrieved March 2, 2017, from http://www.dbnl.org/tekst/nisp034monu03_01/nisp034monu03_01_0010.php#313

Vanneste, K., Camelbeeck, T., De Vos, W., Degrande, G., Dusar, M., Haegeman, W., . . . Verbeeck, K. (2009). *Project VLA07-4.2 Compilatiestudie betreffende de seismiciteit in Vlaanderen.* KSB, BGD, KU Leuven, UGent. Retrieved March 2, 2017, from https://www.lne.be/sites/default/files/atoms/files/seismisiteitVLA07_42.pdf

Varshneya, A. (2016, May 10). *Industrial Glass*. (Encyclopædia Britannica, Inc.) Retrieved September 25, 2017, from Encyclopædia Britannica: https://www.britannica.com/topic/glass-properties-composition-and-industrial-production-234890

Verheus, D. (1939). Hoeve van de Lichtenberg. *Aanzicht D - aanzicht E - aanzicht F - aanzicht G.* [Drawing]. Rijksdienst voor het Cultureel Erfgoed, obj.nr. BT-020407. Retrieved March 8, 2017, from http://beeldbank.cultureelerfgoed.nl/alle-afbeeldingen/detail/fef3d341-6d78-a22f-af24-d050b3164d7a/media/d03765f5-2cfc-9d14-82ec-f9535a1f7030 Licensed under CC BY-SA 4.0 https://creativecommons.org/licenses/by-sa/4.0/deed.nl

Visscher (II), C., & Cletcher, D. (1633). *Beleg van Maastricht, 1632.* [Etching], Rijksmuseum, obj.nr. RP-P-AO-16-127, Amsterdam. Retrieved March 9, 2017, from http://hdl.handle.net/10934/RM0001.COLLECT.460553

Wright, P., & Cumming, A. (1969). *Solid Polyurethane Elastomers.* London: MacLaren and Sons Ltd.

List of Tables and Figures

Tables

Figures

Appendices

Appendix A: Parametric design in Grasshopper
Appendix B: Prototype manufacturing

Appendix A: Parametric design in Grasshopper

In this appendix the parametric design will be explained and visualised in detail with Grasshopper (GH) screenshots and resulting geometry. Hence an insight is provided in how the geometry is generated, including its possibilities and limitations. This appendix can be used to recreate and expand the geometry discussed in this thesis.

A full overview of the GH-file is shown in Figure 156. The groups will be discussed more into detail further on in this appendix. In general, the geometry is build up from certain input values, which will form a boundary box in which the geometry will be created. Using the same geometry for each neighbouring segment leads to a perfect fit for finally being able to create a solid (which is a necessary condition for exporting and importing to DIANA FEA).

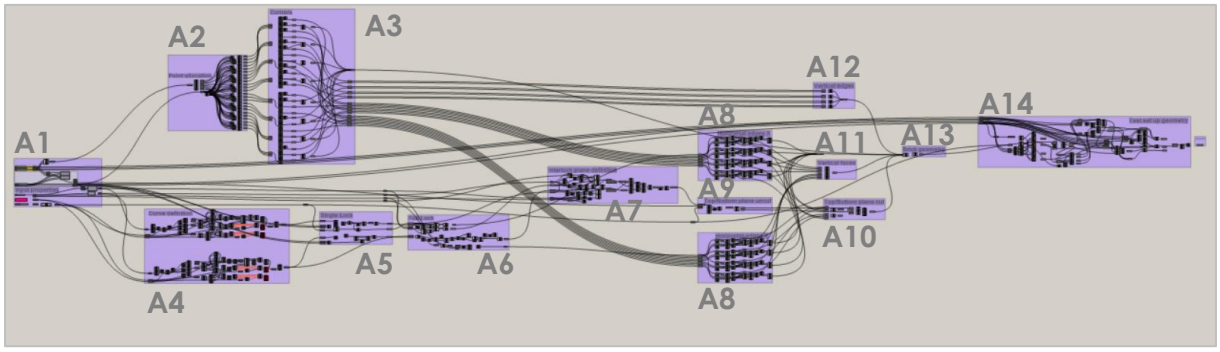

Figure 156: Full overview of the GH-file, which will be discussed in this appendix.

A1: Input of dimensions

The properties for determining the geometry of the brick are the input of the dimensions. The basic properties are the brick width (w), depth (d) and height (h). These properties create an output in the shape of a bounding box, which is used for the generation of its most outward points (see A2).

Other variable properties are the radius of the smooth edges of the brick, the thickness of the interlayer and the amount of interlocks in a direction (nd and nw). In combination with the basic dimensions (w, d, h) these input values generate the partition of the width and depth that will feature the interlock curve (w_{rep} and d_{rep}, as representative values for the width and depth). These are used as input for A4. Other input values are the groove depth (which is twice the amplitude of the interlocking curve) and the division data, which determines the percentage of linear parts in the geometry, both which are also input values for A4.

All parameter inputs are given in Figure 157. Currently, in this thesis, only the interlock deviations and the height are varied (groove depth, linear percentages and h), it however already has been built-in for future extension of the research. For varying these parameters, it however is important to first get a better view on the interlayer properties, and validate its working by laboratory experiments.

A2: Point allocation

From the bounding box, created through parameters w/d/h, its corner points can be generated. These points can be moved in x/y/z-direction using corresponding unit vectors multiplied by the radius of the edges, hence yielding the corner points of the bricks.

This point allocation is shown in Figure 158, and form the backbone of the geometric design. From here arcs can be created and transformed into corner geometry in A3. These arcs then are used to relocate all other geometry generated to create the parametric brick.

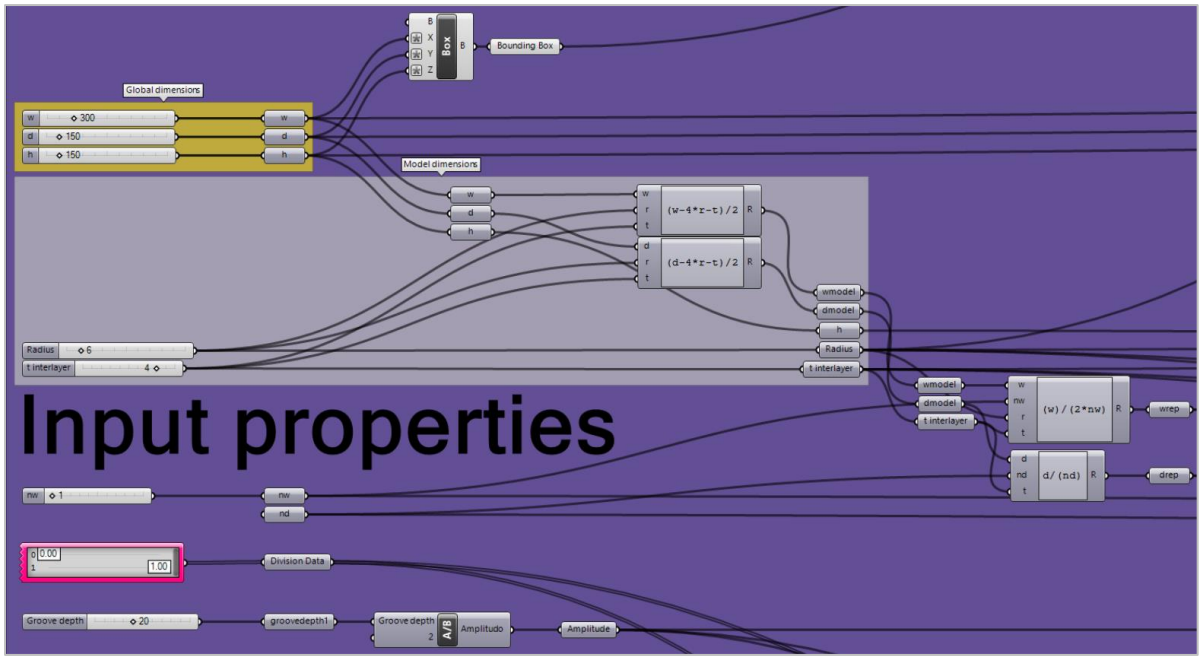

Figure 157: Input properties in GH.

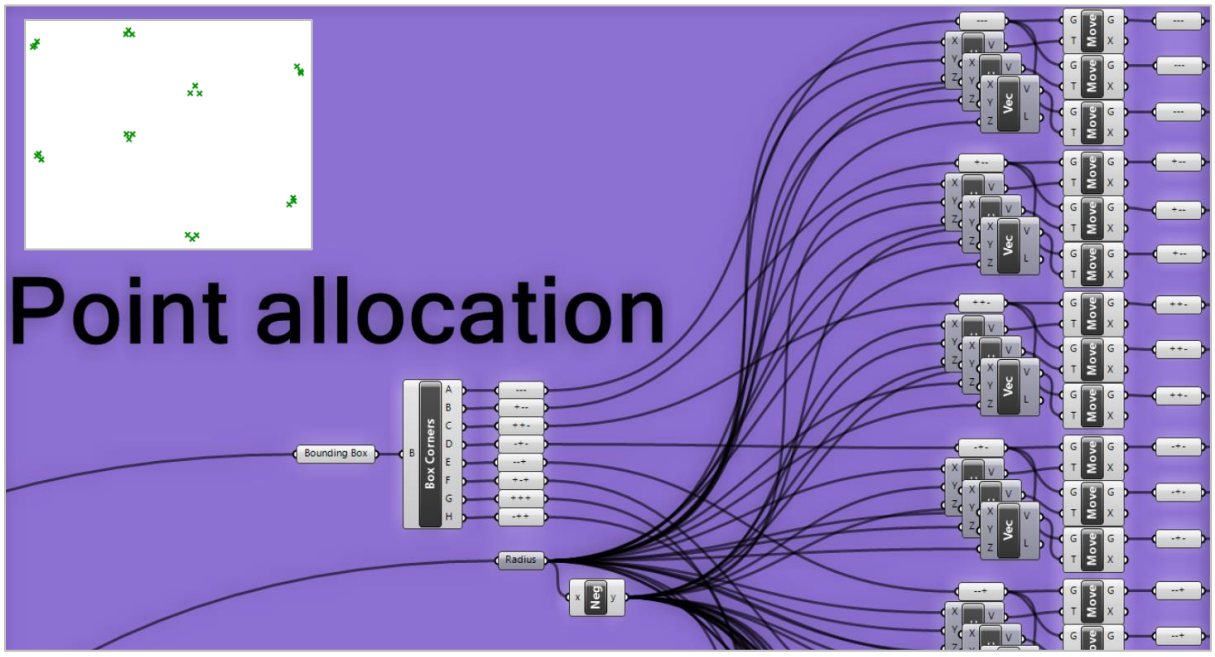

Figure 158: Point allocation of the corners of the geometry, using the radius and the bounding box retrieved from w/d/h parameters.

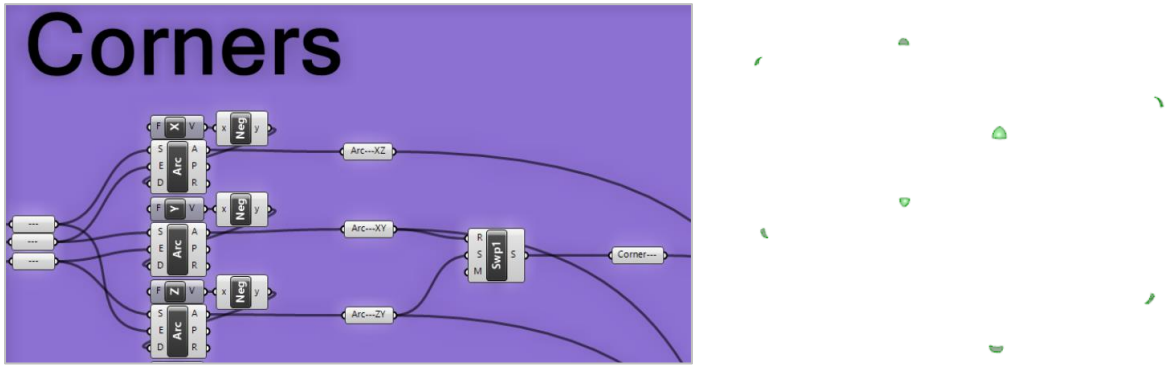

Figure 159: Creating corner arc and surface; visual representation of all corner surface outputs.

A3: Generation of corner geometry

The corner geometries are created using the points generated in A2. They are connected with an arc-command, of which two adjacent arcs create a corner surface using a sweep-1-command. For one corner the GH-commands are shown in Figure 159 and is visualised for all corners.

The arcs are also used as input for other parts of the geometry, for instance for creating the horizontal and vertical edges described in A8 and A12.

A4: Curve definition

The curve definition is created in the origin, and is based on the representative width/depth, the division data (percentage of the linear part) and amplitude. Due to the introduction of the division data, the interlock geometry consists of one, two or three segments (e.g. only a sine curve, a sine curve and a linear curve or two linear curves and a sine curve). Hence data has to be rearranged first and then dispatched to accommodate these geometry variations. For any null values the data tree then has to be cleaned. This principle is shown in Figure 160.

By dividing the curve and applying the sine function below on the resulting points, a curve can be created using the interpolate-curve-command. Depending on earlier choices of parameters there will or will not be linear parts in the geometry. As there are multiple options, the data is collected and cleaned to create a clean curve output, which is used as input for the interlocking geometry.

$$Sine\ function: A * sin((1/(z-y)) * \pi/brep * (x-(y+0.5*(z-y)) * brep))$$

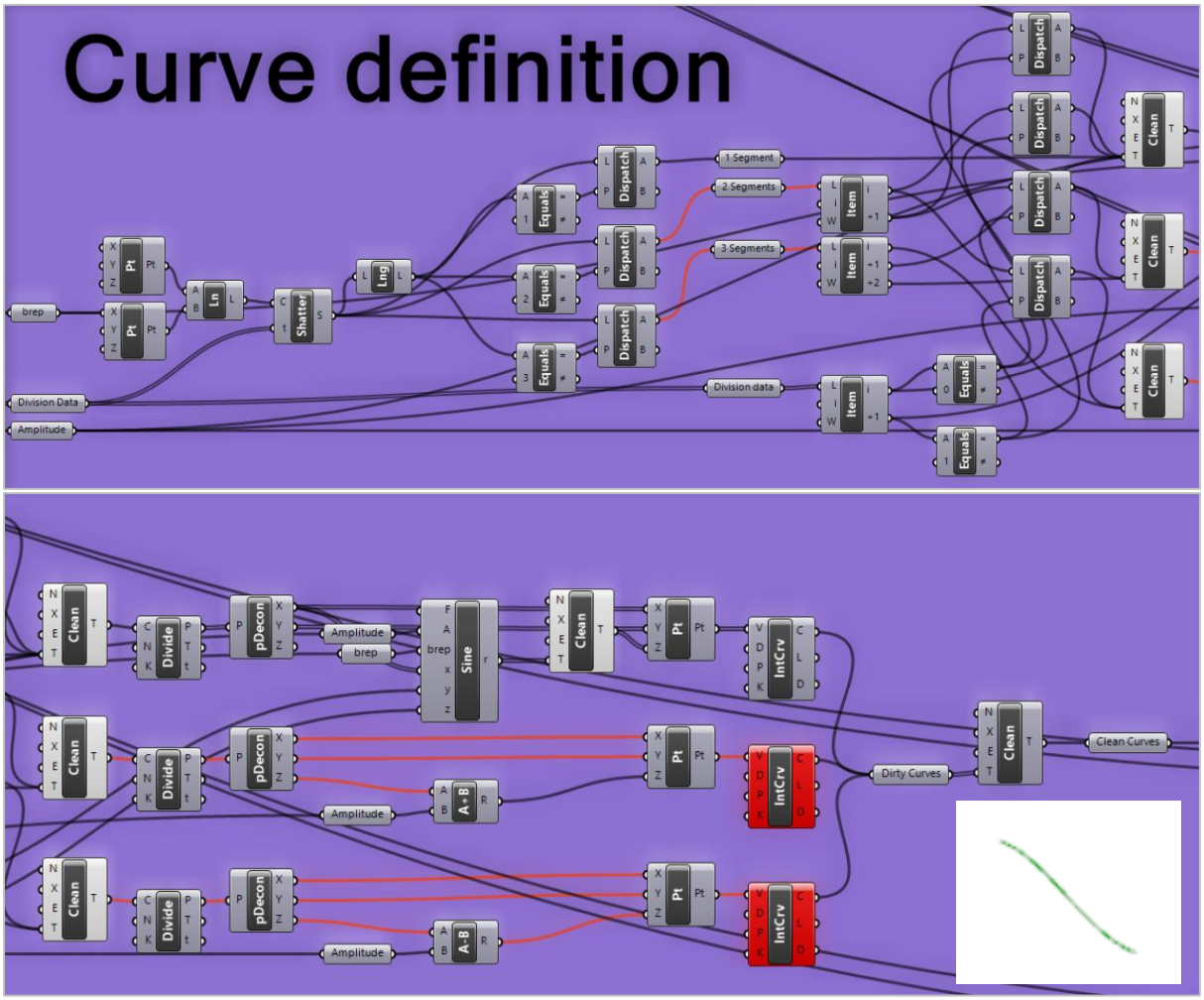

Figure 160: Curve definition, creating the basic interlock geometry which then can be arrayed or mirrored.

A5: Single lock generation

The curve created in A4 is not yet the full geometry. As there are interlayers applied between the geometry, the design should account for these values. Hence first a single lock is created (see Figure 161), incorporating linear parts for the interlayers and also taking into account the radius of the edges. These edges need additional space halfway the brick, as the masonry brickwork will be placed half on half. Mirror commands are used to create the curves which then are joined into a single curve.

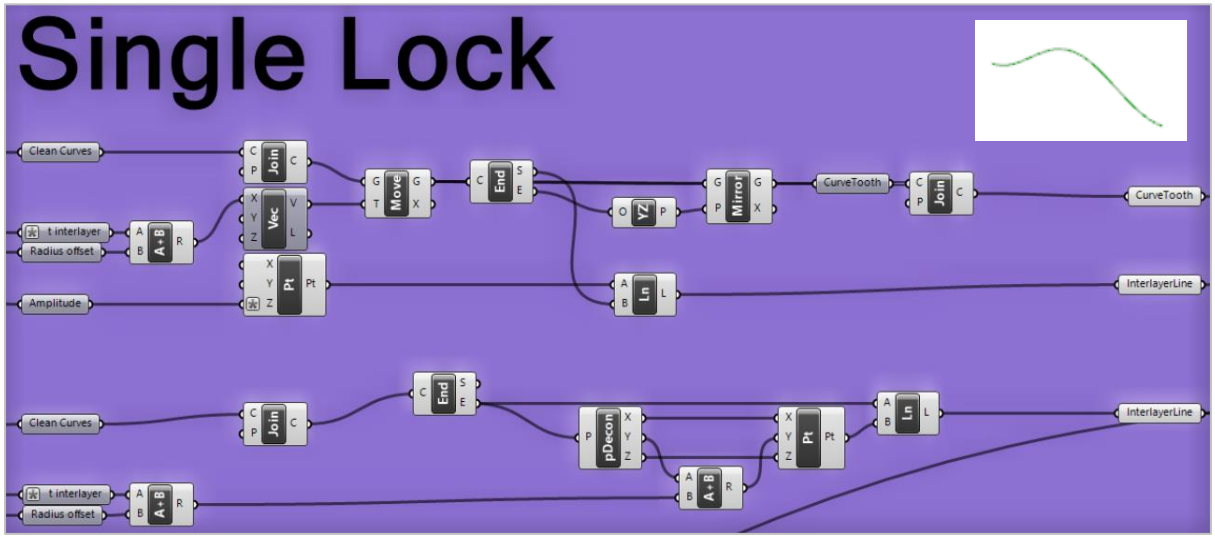

Figure 161: Creation of a single lock.

A6: Full lock generation

Linear arrays and mirroring of geometry is used to create the full lock geometry. For the edges the applied geometry is needed, however for the top and bottom plane, the interlocking geometry is extended. This is needed, as the interlocking faces should fit in the rest of the geometry, hence the curvature should be perfect in the edges. To gain the right curvatures for the method used in A7, longer interlocking geometries are necessary.

Hence this step creates two outputs, for separate purposes. The real geometry is used as input for A8 and the lengthened geometry is used for A7. See Figure 162 for examples.

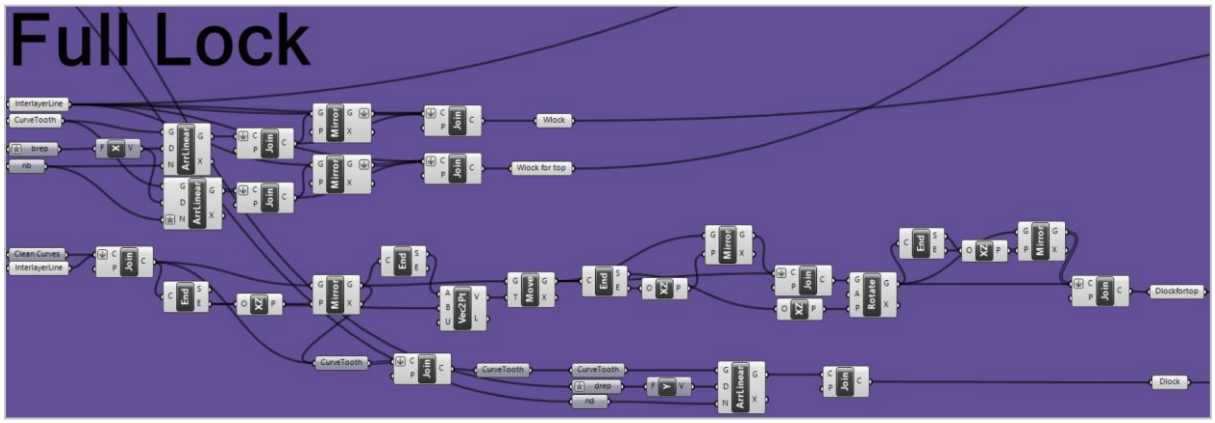

Figure 162: Linear arrays creating locking geometry for both the edge geometries in A8 and the top geometry in A7.

A7: Interlock plane definition

The interlock definition generated in A6 is arrayed and mirrored arrayed to create a grid in both w- and d-direction, taking into account the spacing of the interlocks according to the input properties discussed in A1. The lines have to be rearranged in the correct order, sorting the curves along one of the outer curves. This is essential for using the network surface, which result is shown in Figure 163.

This creates the uncut interlocking geometry, which still has to be moved (A9) and cut (A10). Due to the extended geometry, the cut geometry will have the exact desired interlocking geometry which fits into the rest of the generated geometry.

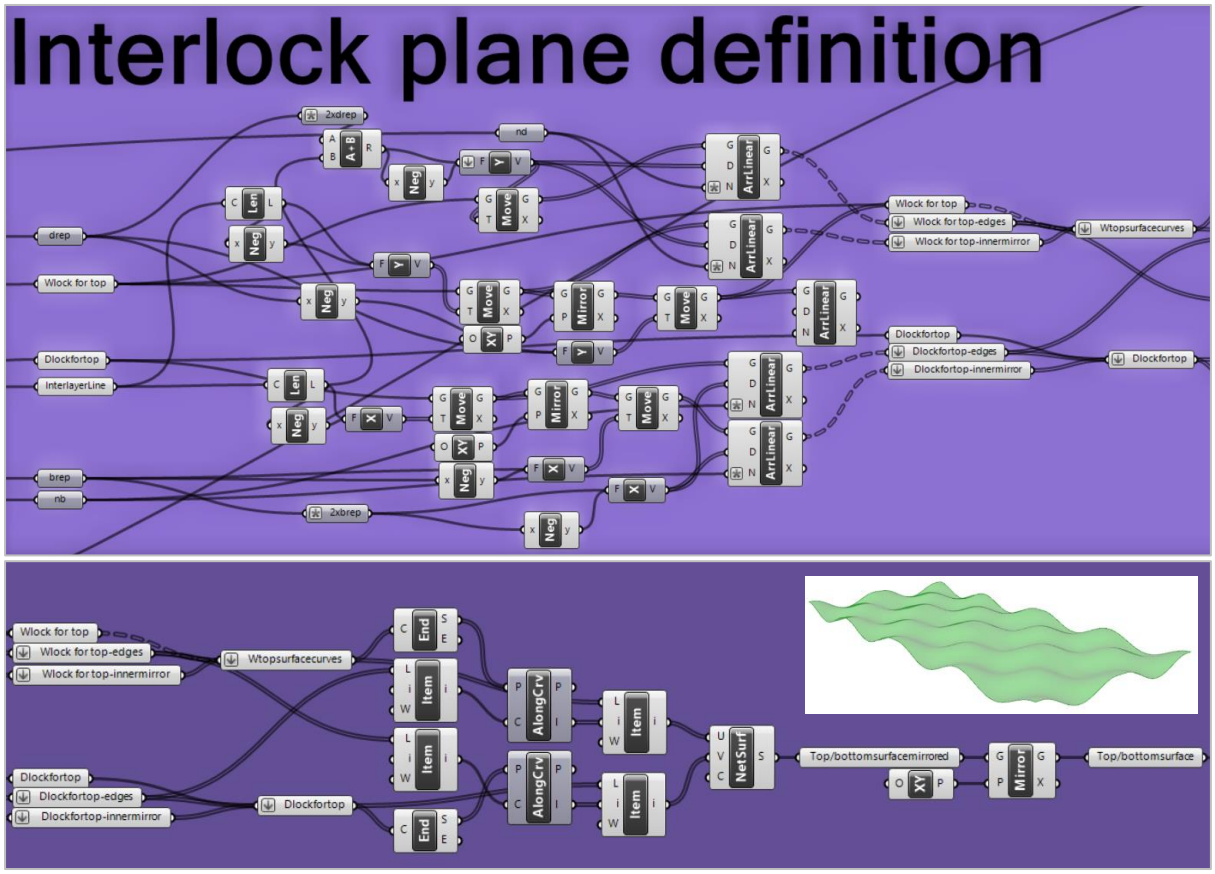

Figure 163: Creating the interlocking surface (uncut).

A8: Creating horizontal edges

The horizontal edges, in both X and Y-directions, is created by firstly moving the lock geometry from A6 to the desired locations. This is done using the earlier derived corner arches (A3). After moving the geometry into the right locations, the arch is swept across the interlock curve using a Sweep-2-command. See Figure 164 for the commands for the horizontal edges in x-direction and the resulting geometry in both directions.

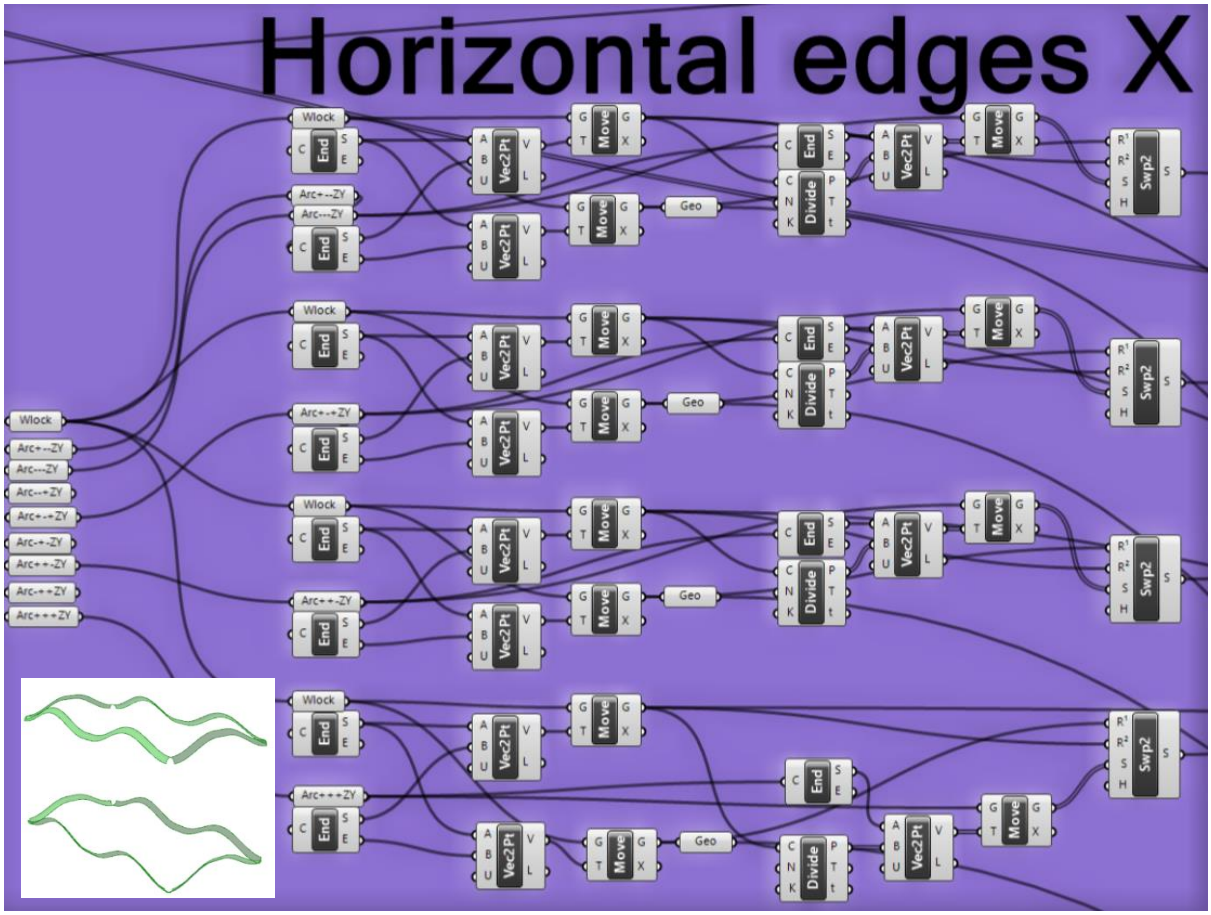

Figure 164: GH-script for creating horizontal edges in X-direction and results for both X- and Y-directions.

A9: Top and bottom geometries

The interlocking surfaces generated in A7 are moved into position using the original input values described in A1. This is shown in Figure 165. These surfaces are now ready to be cut to fit the rest of the geometries.

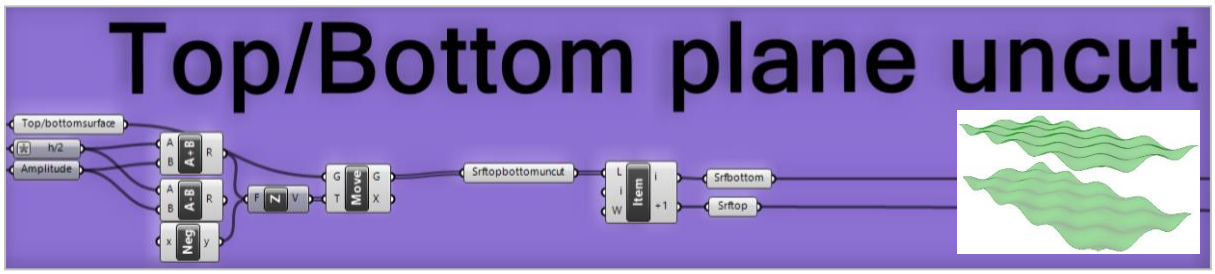

Figure 165: Moving the geometries into position.

A10: Cutting of top/bottom planes

The bottom and top surfaces are cut into the right dimensions using the moved interlocking geometries in A8. This can be done using the command surface-split. This is shown in Figure 166.

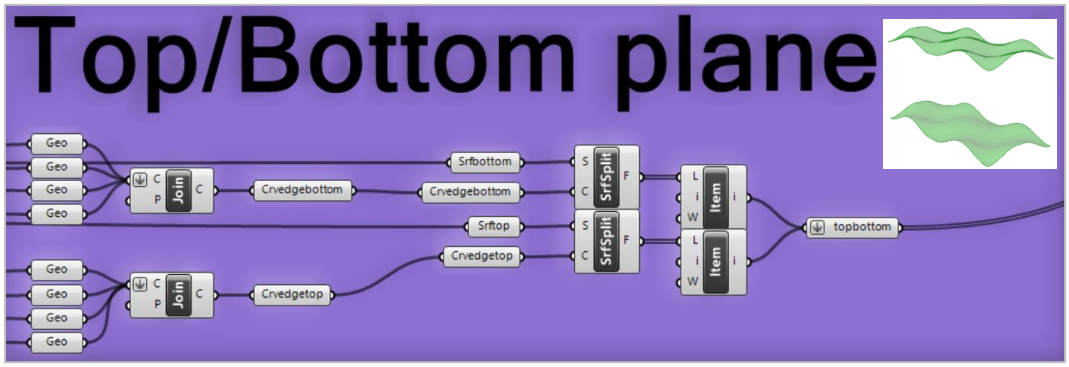

Figure 166: Cutting top and bottom surfaces into the right dimensions.

A11: Vertical faces

From the relocated interlocking geometries in A8 the vertical faces can be created using a loft-command. See Figure 167.

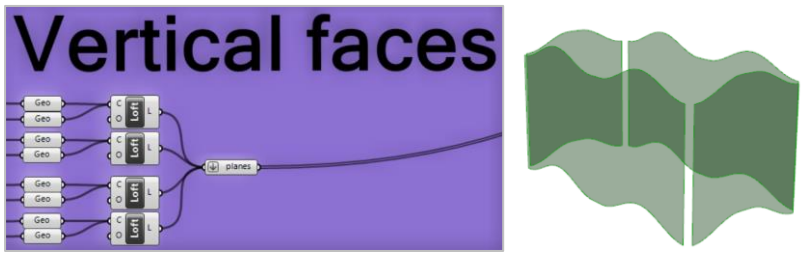

Figure 167: generation of vertical faces.

A12: Vertical edges

Similarly, the vertical edges are created, using the arches generated in A3.

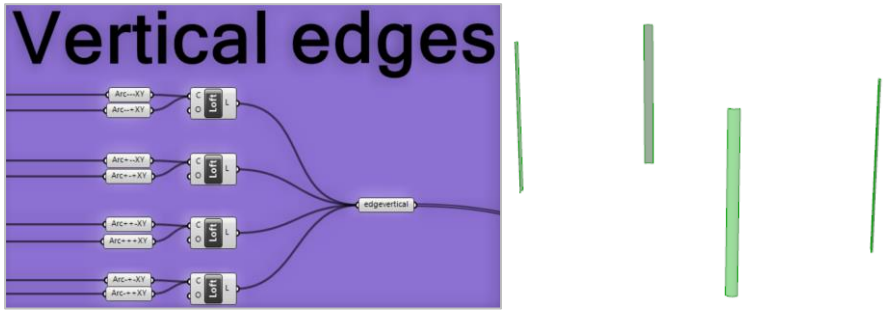

A13: Solid generation

Combining all generated faces, a boundary volume-command can be used to create a solid of the brick geometry. See Figure 168. Perfect connecting faces is key for creating a valid solid.

Figure 168: Using boundary volume a solid is generated of the brick geometry.

A14: Generation of test set up

The test set up is simply generated by splitting the geometry by cutting it with certain faces. Hence the brick geometry can be cut into quarters and relocated into the testing positions with some simple vector translations. A box is created from initial parameters (A1), which is cut with the repositioned brick quarters, resulting in the interlayer geometries (command solid difference). See Figure 169 for commands and geometry output. The output can be baked and exported in a STEP-file.

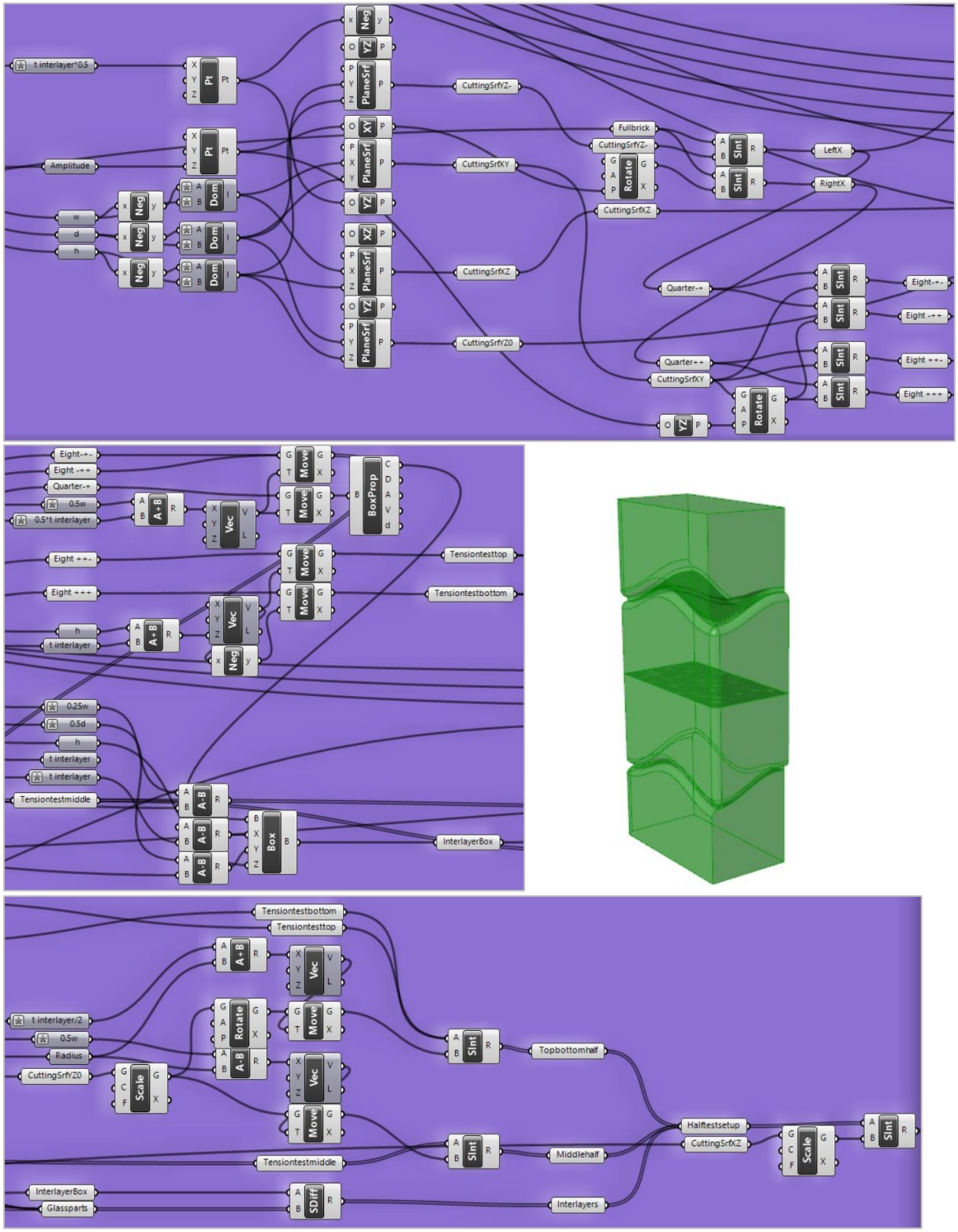

Figure 169: Generation of test set up.

Appendix B: Prototype manufacturing

The steps needed for manufacturing of the prototype will be more detailed explained in this appendix. Firing scheme and schematic oven set up are shown in Chapter 7 and hence will not be covered in this appendix.

The manufacturing process is discussed with a step-wise array of images below.

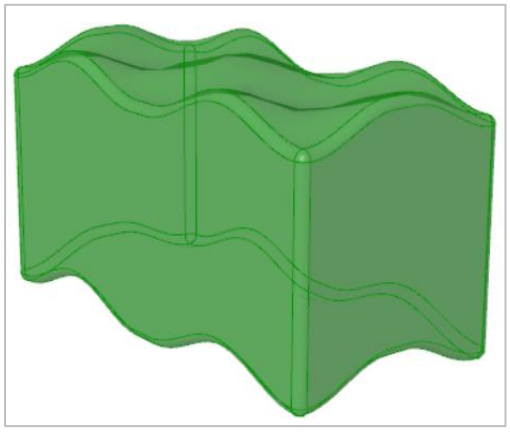

Step 1: Bake geometry in Rhinoceros and add extra geometry for manufacturing purposes.

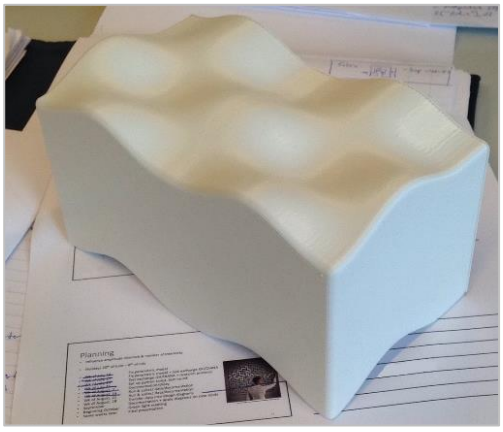

Step 2: 3D print geometry, make sure the printed geometry is a solid. The geometry is printed with a precision of 100 micron and 0.8 nozzle.

Step 3: Filler is applied to smoothen the 3D printed geometry. Otherwise 3D printed layering will show in the glass geometry.

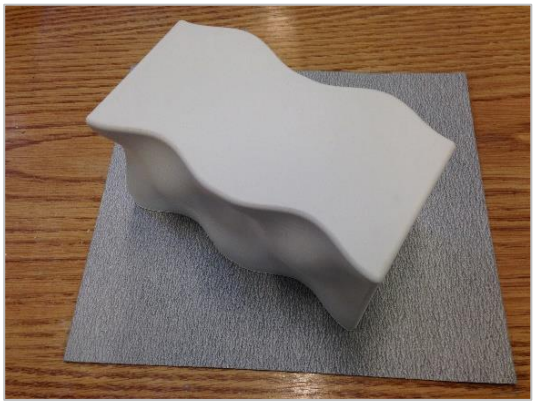

Step 4: Sand excessive filler and repeat step 3 and 4 two more times.

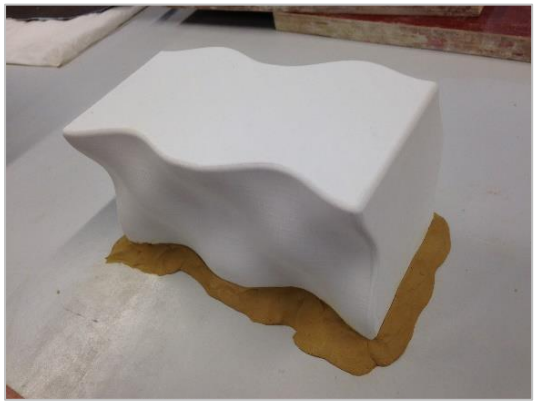

Step 5: Apply a clay edge around the extra added geometry to prevent the silicone mix to flow underneath the 3D printed geometry.

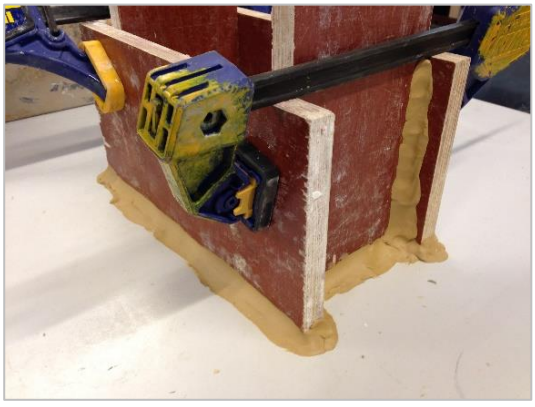

Step 6: Apply formwork and make sure all edges are made watertight by adding clay. Apply some Vaseline inside the mould for better demoulding.

Step 7: Add the two-component silicon mix according to the instructions and make sure to have sufficient mixture to cast on the geometry with a cover of about two centimetres of silicon.

Step 8: Mix the two components thoroughly into an even mixture.

Step 9: Cast the silicone mixture gradually into corner to ensure the geometry is completely covered with silicon and fewer air inclusions.

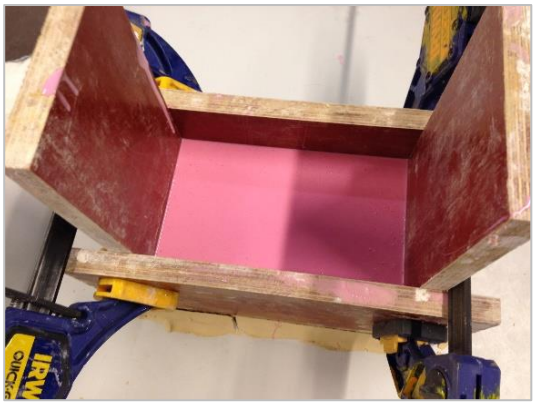

Step 10: Knock on all sides of the moulding to reduce air bubble in the mixture. Wait for 16-24 hours to harden the silicone.

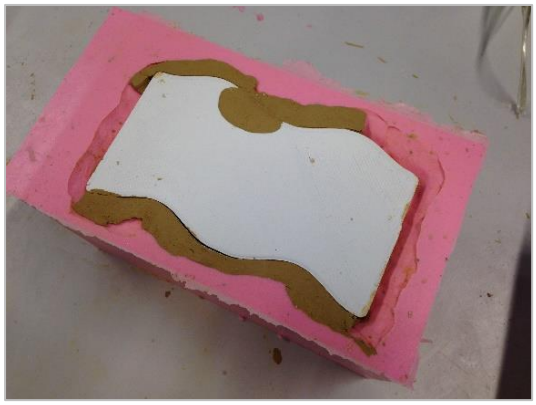

Step 11: Demould, take out the clay but leave the geometry inside the silicone cast. A gypsum cast is needed to restrain the silicon mould for future steps.

Step 12: Mix water and gypsum (ratio 1:1.75), make sure to make sufficient for covering the silicon mould with about an additional 2 cm thickness.

Step 13: Cast the mixture in a corner of the new moulding (all seams again closed with clay).

Step 14: Knock to release entrapped bubbles, wait 45 minutes to an hour for hardening.

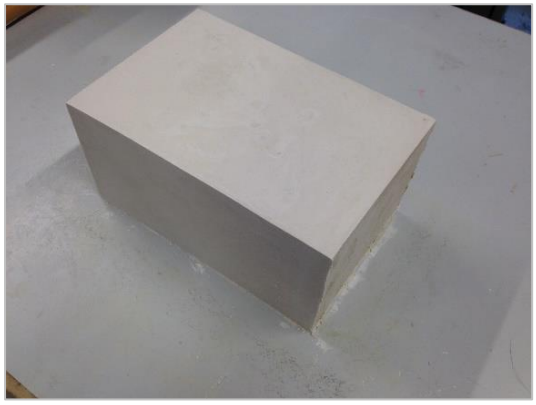

Step 15: Carefully demould the gypsum cast.

Step 16: Remove sharp edges with a spoon to prevent easy breakage of the cast.

Step 17: Disassemble the casts and remove 3D print.

Step 18: Melt wax and place silicon mould in gypsum cast.

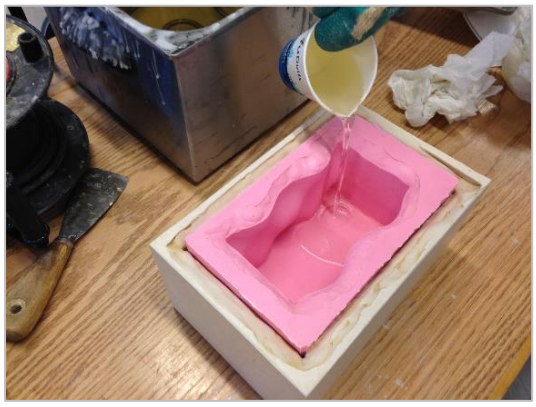

Step 19: Apply wax into the silicon mould.

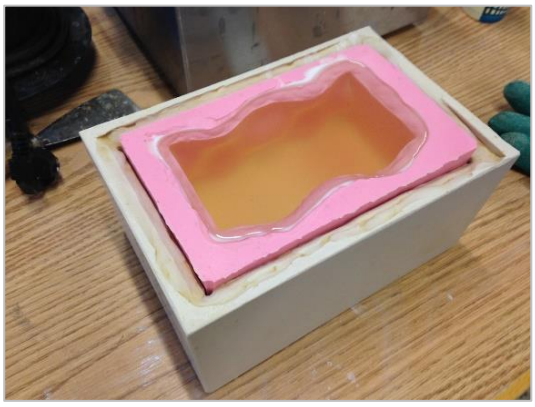

Step 20: Make sure to have some excessive wax for future steps.

Step 21: For speeding up the process one can apply a cut into the geometry and get rid of the molten wax core. This also prevents some shrinkage of the wax geometry.

Step 22: Place the wax geometry on a flat surface, and make sure the geometry is level. Apply some clay on the seams and add some soap for easier release of the crystal cast.

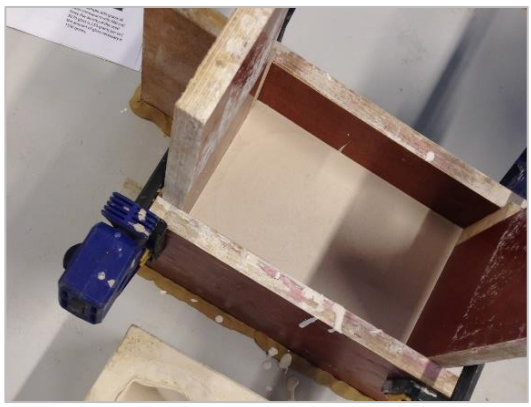

Step 23: Mix a crystal cast with water (ratio 2.75:1) and pour again in a corner of the moulding. Knock the mould to release entrapped bubbles.

Step 24: After about an hour the moulding can be removed.

Step 25: Place the crystal cast in a steaming set up To melt the wax from the crystal cast.

Step 26: Remove any residual wax manually.

Step 27: Clean flower pots with water.

Step 28: Smoothen the rough edges of the bottom hole in the flowerpot for a better glass flow.

Step 29: Weigh the glass and place into the flower pots for the corresponding moulds. The needed glass weight is determined by measuring the volume of water fitting in the mould and calculating the needed glass mass.

Step 30: Place the set up in the oven, see firing scheme in Chapter 7.

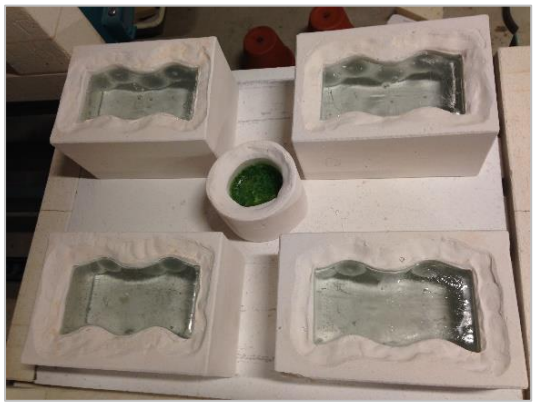

Step 31: After annealing the glass is ready to be removed from the crystal cast.

Step 32: Placing the crystal cast in a bucket of water will dissolve the crystal cast.

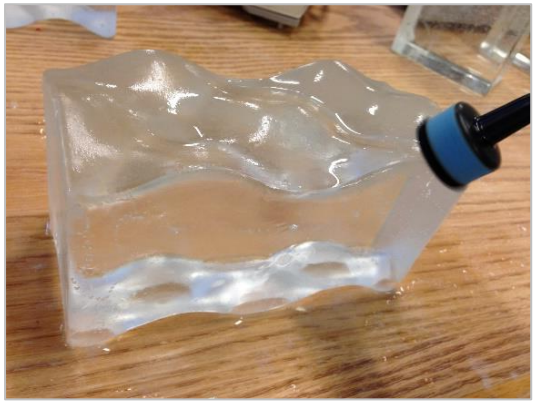

Step 33: Due to impurities and flaws post processing is necessary. Hence the geometry is polished.

Step 34: Final prototype.